Dynamics of Multiphase Gas

Hitesh Kishore Das

München 2025

Dynamics of Multiphase Gas

Hitesh Kishore Das

Dissertation
an der Fakultät für Physik
der Ludwig–Maximilians–Universität
München

vorgelegt von
Hitesh Kishore Das
aus Bareilly, India

München, den 22.05.2025

Erstgutachter: Prof. Dr. Volker Springel
Zweitgutachter: Dr. Celine Péroux
Tag der mündlichen Prüfung: 30.07.2025

Contents

Zusammenfassung

Das astrophysikalische Gas, das den Raum in, um und in Galaxien ausfüllt, wie das interstellare (ISM), zirkumgalaktische (CGM) und Intracluster-Medium (ICM), ist selten einheitlich. Stattdessen ist es oft mehrphasig und besteht aus nebeneinander existierenden heißen, warmen und kalten Komponenten, die mit Turbulenzen und Magnetfeldern wechselwirken. Um den Baryonenzyklus in astrophysikalischen Systemen wie Galaxien zu erfassen, ist es wichtig zu verstehen, wie sich die verschiedenen Komponenten des mehrphasigen Gases bilden, überleben und zerstört werden. In dieser Arbeit werden diese Fragen durch eine Kombination aus idealisierten Simulationen und der Entwicklung von Untergittermodellen untersucht. Die großen Überdichten und kleinen Längenskalen des kalten Gases machen es unerschwinglich, die mehrphasige Struktur durch Erhöhung der Simulationsauflösung aufzulösen. Dies macht den Einsatz von Teilgittermodellen erforderlich, um die unaufgelöste Struktur in einer Simulation zu verfolgen. Ein solches Teilgittermodell wiederum erfordert ein besseres Verständnis und ein physikalisches Modell des Verhaltens von Mehrphasengasen aus idealisierten Simulationen.

Zu diesem Zweck untersuchen wir zunächst die Rolle von Magnetfeldern bei der Gestaltung der Kaltgasdynamik, indem wir sowohl turbulente Strahlungsmischschichten (TRML) als auch turbulente Boxsimulationen mit und ohne Magnetfelder durchführen. Wir stellen fest, dass Magnetfelder die Vermischung in TRMLs unterdrücken, während sie in realistischeren turbulenten Boxsimulationen nur eine begrenzte Wirkung haben. In beiden Fällen wird die Morphologie des kalten Gases fadenförmiger, wenn Magnetfelder vorhanden sind, obwohl die Wachstumsraten insgesamt vergleichbar bleiben. Synthetische MgII-Absorptionslinienprofile aus den Simulationen stimmen in beiden Regimen mit den Beobachtungserwartungen überein, während die Analyse der Feldtopologie eine flussgefriergetriebene Verstärkung in der kalten Phase und verworrene, fraktalartige magnetische Strukturen offenbart.

Zweitens stellen wir ein neuartiges Untergittermodell vor, **MOGLI** (Model for Multiphase Gas using Multifluid Hydrodynamics), das in den Multifluid-Code `AREPO` implementiert wurde. Das Modell berücksichtigt den Luftwiderstand, die turbulente Vermischung und das Wachstum kalter Gase durch physikalisch motivierte Vorschriften mit minimalen freien Parametern. Wir schlagen auch zwei validierte Methoden zur Schätzung der unaufgelösten turbulenten Geschwindigkeiten als Teil des Modells vor. Wir testen und validieren die vollständige und reduzierte Version des Untergittermodells anhand einer Reihe von aufgelösten, mehrphasigen, turbulenten Box Simulationen in `Athena++` als Benchmark. MOGLI reproduziert wichtige Verhaltensweisen wie

die Überlebensschwellen kalter Gase und ermöglicht Simulationen mehrphasiger astrophysikalischer Systeme, die sonst rechnerisch undurchführbar wären.

Drittens untersuchen wir die Kondensation und das Überleben kalter Gase in einer ISM-ähnlichen Umgebung mit Hilfe dreidimensionaler turbulenter Boxsimulationen mit Strahlungskühlung. Anders als im CGM oder ICM haben die heiße ($T \sim 10^4$ K) und die kalte ($T \sim 10^2$ K) Phase vergleichbare Abkühlungszeitskalen, so dass Kaltgaskondensation und -wachstum gleichzeitig von Bedeutung sein können. Wir identifizieren drei Regime: (i) turbulente Kaltgaskondensation, (ii) Überleben von Wolken ohne Kondensation und (iii) Zerstörung von Wolken ohne Kondensation. Wir schlagen ein neues Kondensationskriterium vor, das auf der Abkühlungszeit des komprimierten Gases im lognormalen Schwanz der Dichteverteilung basiert und das die Kondensationsregime in unseren Simulationen genau abgrenzt. Unsere Ergebnisse zeigen, dass in bestimmten Regionen des Parameterraums kaltes Gas nur bestehen bleiben kann, wenn es von außen zugeführt wird. Wir unterstreichen auch die stochastische und nichtlineare Natur der Mehrphasendynamik im ISM.

Zusammengenommen vertiefen diese Studien unser Verständnis davon, wie sich mehrphasiges Gas in turbulenten astrophysikalischen Umgebungen verhält, klären die Rolle von Magnetfeldern bei der Entwicklung von kaltem Gas und bieten einen physikalisch fundierten Rahmen für die Einbeziehung von kaltem Gas in großräumige Simulationen von Galaxien und ihrer Umgebung.

Abstract

The astrophysical gas filling the space in, around and between galaxies, like Interstellar (ISM), Circumgalactic (CGM) and Intracluster medium (ICM), is rarely uniform. Instead, it is often multiphase, comprised of co-existing hot, warm, and cold components, interacting with turbulence and magnetic fields. Understanding how the different components of the multiphase gas form, survive and get destroyed is essential for capturing the Baryon cycle in astrophysical systems like galaxies. This thesis investigates these questions through a combination of idealised simulations and subgrid model development. The large overdensities and small lengthscales of the cold gas make it prohibitively expensive to resolve the multiphase structure by increasing the simulation resolution. This necessitates the use of subgrid models to keep track of unresolved structure in a simulations. Such a subgrid model, in turn, requires a better understanding and a physical model of multiphase gas behaviour from idealised simulations.

Toward that goal, first, we explore the role of magnetic fields in shaping the cold gas dynamics by conducting both turbulent radiative mixing layer (TRML) and turbulent box simulations with and without magnetic fields. We find that while magnetic fields suppress mixing in TRMLs, they have a limited effect in more realistic turbulent box simulation. In both cases, the morphology of cold gas becomes more filamentary when magnetic fields are present, though the overall growth rates remain comparable. Synthetic MgII absorption line profiles from the simulations match observational expectations in both regimes, while analysis of field topology reveals flux-freezing-driven amplification in the cold phase and tangled, fractal-like magnetic structures.

Second, we present a novel subgrid framework, **MOGLI** (Model for Multiphase Gas using Multifluid Hydrodynamics), implemented within the multifluid `AREPO` code. The model accounts for drag, turbulent mixing, and cold gas growth using physically motivated prescriptions with minimal free parameters. We also propose two validated methods to estimate unresolved turbulent velocities, as part of the model. We rigorously test and validate the full and reduced version of the subgrid model against a suite of resolved single-fluid, multiphase, turbulent box simulations in `Athena++` as the benchmark. MOGLI reproduces key behaviours such as cold gas survival thresholds and enables simulations of multiphase astrophysical systems that would otherwise be computationally infeasible.

Third, we investigate cold gas condensation and survival in an ISM-like environment using

three-dimensional turbulent box simulations with radiative cooling. Unlike in the CGM or ICM, the hot ($T \sim 10^4$ K) and cold ($T \sim 10^2$ K) phases have comparable cooling timescales, hence allowing for cold gas condensation and growth to be simultaneously important. We identify three regimes: (i) turbulent cold gas condensation, (ii) externally seeded cloud survival without condensation, and (iii) cloud destruction without condensation. We propose a new condensation criterion based on the cooling time of compressed gas in the log-normal tail of the density distribution, which accurately delineates the condensation regime in our simulations. Our results show that in certain regions of parameter space, cold gas can only persist if introduced externally. We also highlight the stochastic and non-linear nature of multiphase dynamics in the ISM.

Together, these studies deepen our understanding of how multiphase gas behaves in turbulent astrophysical environments, clarify the role of magnetic fields in cold gas evolution, and provide a physically grounded framework for incorporating cold gas into large-scale simulations of galaxies and their surroundings.

1 | A short review of Multiphase Gas

> Nothing in this book is true.
>
> — Kurt Vonnegut, in *Cat's Cradle*

> Writing a review is to science, as golf is to sports.
>
> — Max Gronke, *paraphrasing Volker Springel, while presenting his review paper*

The "Space" is not entirely empty. Apart from the celestial objects like the stellar objects, planets and moons, the "Space" is filled with astrophysical gas. And, this gas does not exist as a uniform, single-phase medium. Instead, it exists in a state known as **multiphase**, where the gas can occupy a wide range of properties (Field et al., 1969; McKee & Ostriker, 1977a). The **phase** in **multiphase** refers to gas that occupies a stable, narrow range of properties, like temperature, density and ionisation fraction. The simplest kind of a multiphase medium is a two-phase gas with a cold ($T \sim 10^4$ K) phase and a hot ($T \gtrsim 10^6$ K) phase (Field et al., 1969). The multiple phases in such a medium coexist, interact, and evolve together. These phases may differ significantly in temperature and density, but often remain approximately in pressure equilibrium. This isobaric nature and significant temperature separation between the phases also results in high density contrasts of $\sim 100 - 1000$. This multiphase character is not only theoretically expected, but ubiquitously observed across a vast range of structures, ranging from galaxy clusters and solar prominences, as shown in Fig. 1.1.

Observational Signatures of Multiphase Gas

Observationally, multiphase gas manifests itself in a wide variety of astrophysical systems. The existence of multiphase gas has been confirmed across vast range of length and timescales. In this section, we cover the observations of multiphase gas, as shown in Fig. 1.1, from the large to small lengthscales, ranging from Mpc to metre size phenomena.

Galaxy Clusters

Galaxy clusters are the largest gravitationally bound structures in the Universe. They typically form at the nodes of the cosmic web, where massive dark matter haloes host numerous galaxies.

At the centre of these haloes resides the brightest cluster galaxy (BCG) (Dubinski, 1998), which is usually a massive galaxy often associated with Active Galactic Nuclei (AGN) jets (Best et al., 2007). Observations have revealed that these jets can propagate into the intracluster medium (ICM), influencing its thermodynamic state. The ICM is predominantly filled with X-ray-emitting hot gas at the virial temperature $\sim 10^7$ K, but it also hosts colder components, such as Hα-emitting filaments at $\sim 10^4$ K, occupying the same spatial regions (Olivares et al., 2025; Mccourt et al., 2012).

A well-studied example is the Perseus cluster, where high-resolution Chandra X-ray images reveal the hot ICM surrounding the BCG, alongside extended Hα filaments tracing the multiphase structure of the cluster core (Salomé et al., 2006; Falceta-Gonçalves et al., 2010). We show a multiwavelength image of the Perseus Cluster's BCG in Fig. 1.1, in top left. The X-ray emitting hot gas is shown in purple and pink, while the Hα emitting cold-gas filaments are shown in red. (Fabian et al., 2008).

Jellyfish Galaxies

As noted in the previous section, galaxy clusters host numerous galaxies within the same dark matter halo, many of which orbit the BCG. Among these, a subset exhibit extended, jellyfish-like structures across multiple wavelengths. These so-called jellyfish or ram-pressure-stripped galaxies are thought to develop such morphologies as a result of gas being stripped from their interstellar medium (ISM) and circumgalactic medium (CGM) due to their motion through the ICM. The stripping of gas is primarily driven by ram pressure and shear forces arising from the interaction with the dense ICM (Vollmer et al., 2001).

Observations have detected X-ray emission from the stripped tails of these galaxies, which gradually blend into the ambient ICM with increasing distance from the galaxy (Sun et al., 2010). In addition, molecular CO (Jáchym et al., 2014) and Hα emission (Merluzzi et al., 2013; Fossati et al., 2016; Consolandi et al., 2017) are observed from the same tails, once again revealing their multiphase nature (Sun et al., 2021).

It remains unclear whether the cold gas in these tails primarily originates from the galaxy's ISM and survives the stripping process, or if it is replenished via in-situ radiative cooling. Understanding the formation and evolution of such multiphase tails remains an active area of research with several open questions. Fig. 1.1 shows an example of such a Jellyfish galaxy, named ESO137-001. It shows a multi-wavelength view of the ram-pressure stripped tail, in CO and Hα (Jáchym et al., 2019).

Galactic outflows

Zooming in to galactic scales, certain galaxies with high star formation rates exhibit strong feedback due to supernovae in the interstellar medium (ISM). This feedback can drive ISM material into the circumgalactic medium (CGM), launching biconical outflows known as galactic outflows (Veilleux et al., 2020a; Scannapieco & Brüggen, 2015; Reichardt Chu et al., 2022).

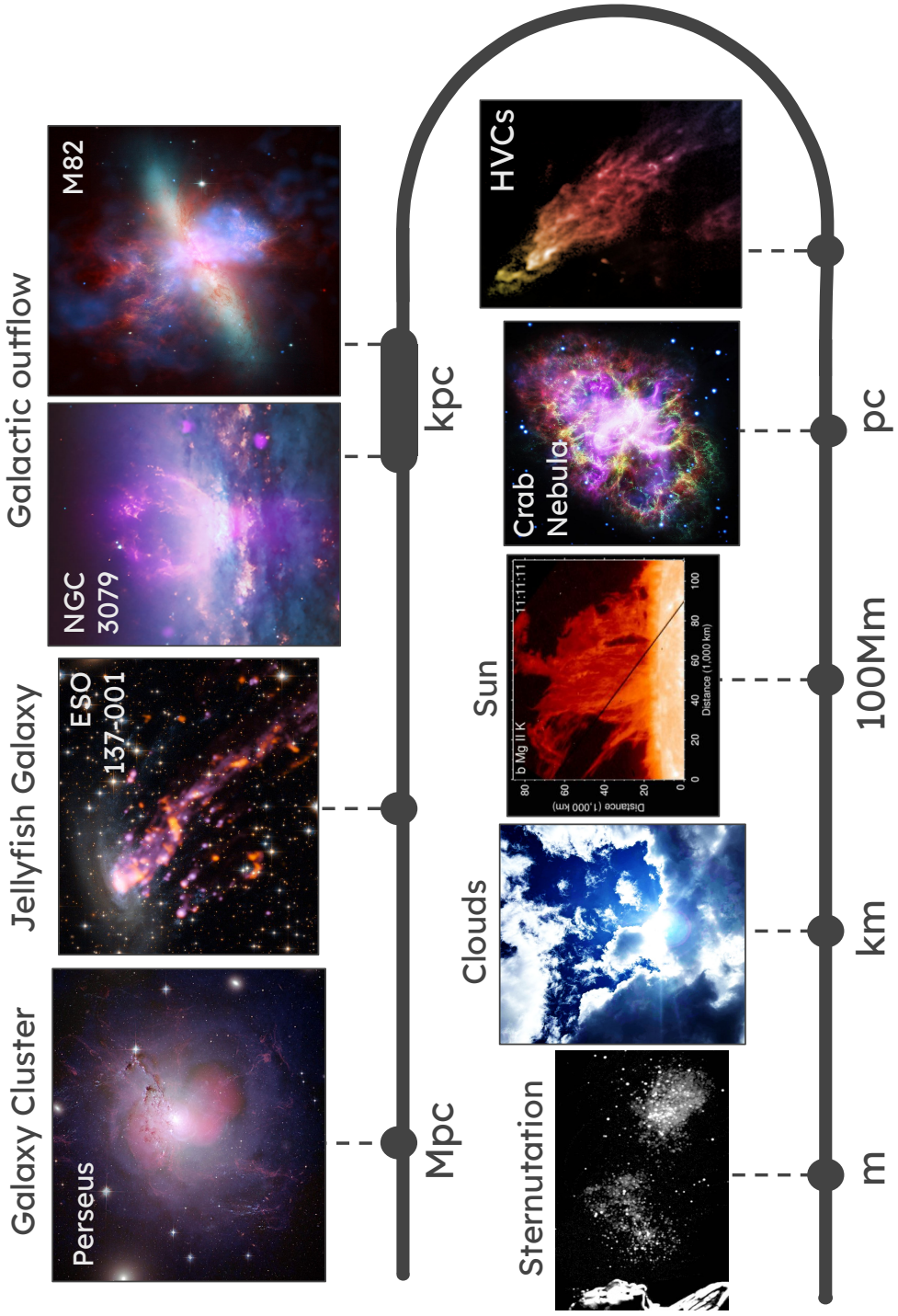

Figure 1.1: Observational evidence for multiphase nature of astrophysical gas across vast range of lengthscales, from Mpc to metre scales. From top left to bottom left: multiwavelength image of Perseus cluster (Fabian et al., 2008), CO+Hα image of ESO 137-001 Jellyfish Galaxy (Jáchym et al., 2019), multiwavelength image of galactic outflows in NGC 3079 (Li et al., 2019) and M82 (NASA/CXC/SAO et al., 2006), Hα image of Smith's cloud (Fox et al., 2016), multiwavelength image of Crab Nebula (Dubner et al., 2017), MgII observation of solar prominences (Hillier & Polito, 2018), Clouds (Image credit: Author) and sternutation, i.e. sneezing (Bourouiba, 2016).

In Fig. 1.1, we show multi-wavelength views of two such galaxies, NGC 3079 and M82 (also known as the Cigar Galaxy)(NASA/CXC/SAO et al., 2006). M82, often regarded as a prototypical example of multiphase galactic outflows, is shown with the stellar disc in green, X-ray-emitting hot gas in blue (Kaaret et al., 2001), and Hα-emitting cold gas in red (Matsubayashi et al., 2013). NGC 3079 similarly exhibits multiphase outflows, with cold gas with Hα emission highlighted in red and X-ray emission from hot gas shown in purple (Li et al., 2019).

These observations illustrate a key component of the baryon cycle, in which volume-filling hot gas and mass-dominant cold gas are ejected from the ISM. However, it remains an open question how much of the cold gas originates from the ISM and how much forms within the outflow via in-situ cooling, thermal instability, or mixing.

High Velocity Clouds (HVCs)

High-velocity clouds (HVCs) are off-plane, fast-moving ($\gtrsim$ 90km/s), Hα-emitting gas structures observed in the Milky Way, embedded within the hotter halo environment (Wakker & van Woerden, 1997) and cover a substantial fraction of the sky. These clouds reflect the complex multiphase structure of the Milky Way's CGM. HVCs exhibit a broad range of metallicities (from studies like Ashley et al., 2024) and velocities (Westmeier, 2018), complicating efforts to determine their exact origins. Proposed origins include galactic inflows from Large Magellanic Cloud (LMC), galactic outflows, or recycled material as part of the Milky Way's baryon cycle (Putman et al., 2012).

In Fig. 1.1, we show an example of an Hα-emitting HVC, called Smith's cloud. The image reveals fine substructures within the cloud, which is embedded in the surrounding hot halo gas, while the hot phase is not visible in Hα. (Fox et al., 2016)

Supernova Remnnant

Turning to the interstellar medium (ISM), we encounter structures such as supernova remnants (Mufson et al., 1986). In Fig. 1.1, we show a multi-wavelength image of the Crab Nebula, a well-known supernova remnant (Hester, 2008). The purple, volume-filling component corresponds to hot, X-ray-emitting gas, while the intricate filamentary structures trace cooler gas emitting at optical and infrared wavelengths (Dubner et al., 2017).

Similar multiphase structures are observed in HII regions and planetary nebulae. Beyond these object-associated environments, the diffuse ISM itself is recognised as inherently multiphase, with components ranging from hot ($\sim 10^4$ K) to cold ($\sim$ 100 K) gas (Inutsuka, 2009). These phases coexist in pressure equilibrium but are shaped by complex processes, including radiative feedback from stars. The ISM remains an active area of research due to its complexity and role in star formation (Field et al., 1969; McKee & Ostriker, 1977b).

Solar Atmosphere

Coming even closer to home, we arrive at our solar system. The Sun and its atmosphere is among the most extensively studied stellar environments, due to both its proximity and continuous monitoring by a range of ground- and space-based observatories across multiple wavelengths. The solar corona, in particular, serves as a valuable observational laboratory for investigating multiphase gas dynamics. Although the solar atmosphere is strongly shaped by magnetic fields, many of the physical processes relevant to other astrophysical systems are also at play.

Two key layers of the solar atmosphere are the photosphere, typically at temperatures of $\sim 10^4$ K, and the overlying corona, reaching up to $\sim 10^6$ K. Energy release events in the photosphere can eject cooler gas into the hot corona, producing a wide range of magnetically structured phenomena, including flares, prominences, and sunspots (Nakagawa, 1970). One prominent example of a multiphase structure is the solar prominence, shown in Fig. 1.1 (Antiochos et al., 2000; Parenti, 2014). These consist of cool ($\sim 10^4$ K) gas emitting in lines such as MgII, suspended within the surrounding million-degree plasma. The dynamics of this material rising, falling, and being reheated are governed by a complex interplay between radiative processes, magnetic confinement, and heating from the underlying layers (Hillier & Polito, 2018).

The high cadence and spatial resolution of solar observations offer a unique opportunity to test theoretical models developed at galactic and cluster scales under more controlled conditions. One such cross-scale concept is thermal instability, referred to in the solar community as thermal non-equilibrium, is invoked to explain the formation of cool condensates in coronal filaments (Antolin, 2020; Antolin & Froment, 2022). This remains an active area of research and represents a promising interface for collaboration between solar physicists and researchers studying multiphase gas in other astrophysical contexts.

Smaller scales on Earth

Back on Earth, we also encounter a wide variety of multiphase phenomena. While the nature of the phases differs from their astrophysical counterparts, both systems present similar modeling challenges due to comparable density contrasts and turbulent environments.

In astrophysical contexts, phase separation typically arises from differences in radiative heating and cooling. In contrast, terrestrial multiphase systems often involve classical fluid phase transitions, for example, liquid water droplets suspended in air, as in terrestrial clouds. Despite the differences in origin, both types of systems feature complex interactions mediated by turbulence between phases with high density contrasts ($\sim 10^3$). (Sardina et al., 2011).

Such behavior is not limited to atmospheric clouds. On smaller scales, turbulence facilitates phase interactions in many day-to-day scenarios. A notable example is sneezing (Sternutation, Bourouiba, 2016), where liquid droplets are dispersed into a turbulent air flow (Faeth, 1996). Similar processes are also studied extensively in combustion physics, where liquid or solid fuel interacts with oxidants, producing multiphase exhaust (Damköhler, 1940; Kuo & Acharya, 2012).

These terrestrial systems have the advantage of being accessible to direct experimentation and

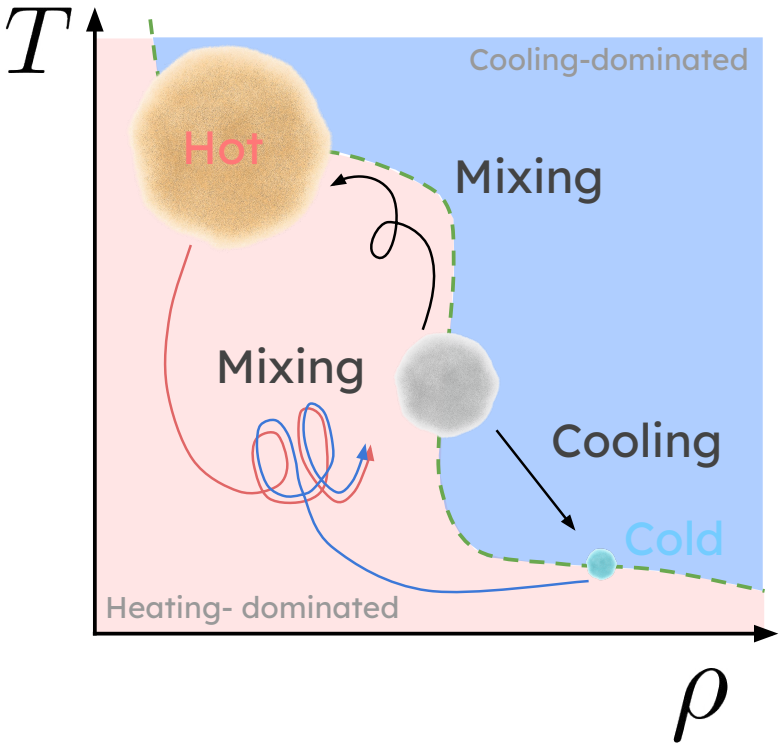

Figure 1.2: Temperature-density phase diagram showing the stable hot and cold phases, as orange and blue blobs, respectively. It also shows the different interactions, namely mixing and cooling, between these phases. The unstable intermediate temperature gas is shown as a grey blob. The green dashed line shows the thermal equilibrium curve, where the cooling and heating are balanced. The red and blue shaded regions correspond to heating and cooling dominated regions, respectively.

controlled study. As a result, they offer valuable insight into multiphase dynamics that can inform our understanding of analogous astrophysical systems, where direct experimentation is not feasible. This presents a promising opportunity for interdisciplinary exchange between astrophysics and engineering disciplines (Tan et al., 2021).

How does multiphase gas form?

A useful way to understand multiphase structure is through the temperature-density phase diagram. When heating and radiative cooling rates are plotted in this space, the equilibrium points define a thermal equilibrium curve, shown as a green dashed line in Fig. 1.2. Stable phases (hot and cold phases) on this curve allow gas to remain in a given phase when slightly perturbed; unstable regions, by contrast, lead to runaway heating or cooling. In general, we can assume that the two phases are isobaric to avoid unbalanced forces at the interfaces (Field et al., 1969). Hence, these stable points align along roughly isobaric contours, giving rise to well-separated cold and hot phases. These features appear in simulation outputs as bimodal

temperature and density distributions, and underlie much of the multiphase dynamics observed (McKee & Ostriker, 1977a).

A medium can become multiphase through several pathways. Previous studies have shown that even a small fraction of seed cold gas can initiate the development of a multiphase structure, depending on the relative timescales of mixing and radiative cooling (Gronke & Peng Oh, 2018; Gronke et al., 2022a). Fig. 1.2 shows an overview of the multiphase interaction between the cold and hot phases. The interaction between the hot and cold phases generates gas at intermediate temperatures, which typically lies in a thermally unstable regime and exhibits short cooling times (Begelman & Fabian, 1990a). If the cooling timescale of this mixed-phase gas is shorter than its mixing timescale with the volume-filling hot phase, it can further condense into cold gas. This leads to a positive feedback loop that enhances cold gas mass and facilitates the emergence of a sustained multiphase medium. In Chapter 3 we extend this understanding to include magnetic fields which can theoretically affect mixing between the phases. For an originally single-phase gas to become multiphase, the seed cold gas has to originate either through external injection, such as from galactic outflows in CGM or Red Supergiant winds in ISM (Larkin et al., 2025), or through in-situ processes like thermal instability or turbulent condensation (Field & Field, 1965; Mohapatra et al., 2022b). In Chapter 5 we investigate the interplay between the two processes of multiphase gas creation, i.e. in-situ formation and multiphase mixing, in a turbulent ISM environment.

Why Should We Care?

The presence of multiphase gas in extended astrophysical environments, such as the CGM and ICM, is crucial due to its central role in regulating the baryon cycle. In the context of galaxy evolution, the multiphase structure has major effects on the processes of gas accretion, feedback-driven outflows, and the subsequent recycling of ejected material over evolutionary timescales of these astrophysical systems (Tumlinson et al., 2017). Fig. 1.3 shows the different components and processes involved in the galactic baryon cycle.

Key observational diagnostics, including quasar absorption line spectra and extended emission features such as Lyman-α and Mg II, are expected to be highly sensitive to the underlying multiphase nature of the CGM. Similarly, in galaxy clusters, the ICM exhibits an analogous multiphase structure that plays a critical role in the thermal regulation and redistribution of baryons across the cluster environment (Donahue & Voit, 2022). Hence, from a modelling perspective, multiphase gas plays a critical role in regulating star formation, metal transport, and the long-term evolution of the gas reservoir within and around galaxies and galaxy clusters. Therefore, any attempt to accurately model galaxy or cluster evolution must account for the multiphase nature of the underlying astrophysical gas.

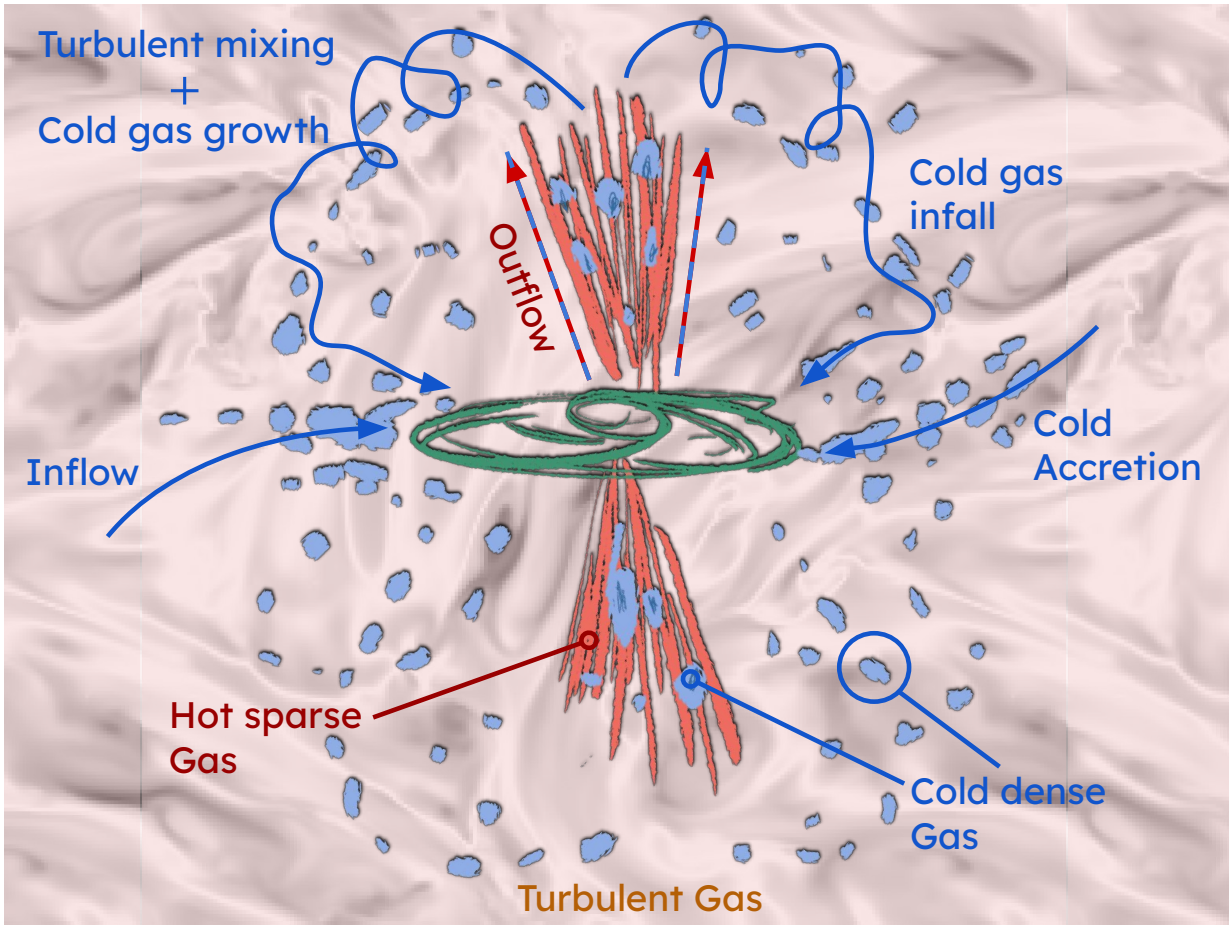

Figure 1.3: Schematic representation of the Baryon cycle of a galaxy. The background structure represents the turbulent nature of the circumgalactic medium. The cold and hot phases are shown as blue and red blobs. It also shows the different flows of gas in and out of the system. Inspired by Tumlinson et al. (2017).

Numerical Challenges and Resolution Requirements

However, modelling multiphase gas is exceptionally challenging due to the vast range of scales involved. Cold gas structures are often sub-parsec in size (McCourt et al., 2018) with more structures for smaller and smaller scales (Gronke & Oh, 2020a; Das & Gronke, 2024a). On the other hand, the domains of interest, such as galaxies or clusters, span tens to hundreds of kiloparsecs, with the associated density contrasts as high as 10^4. Yet, these small-scale structures critically influence large-scale observables, and small-scale effects like the cloud survival, morphology, and kinematics affect CGM diagnostics, star formation, and outflow propagation. Using brute-force computational approaches, such as increasing resolution to directly resolve small-scale cold gas structures, is computationally prohibitive. For instance, simulating a cosmological sample of galaxies with resolution sufficient to capture such cold gas features would require sub-pc resolution. A suite of cosmological simulations like `THESAN` (Kannan et al., 2022) would require an estimated 100 to 1000 years of CPU time on an exascale supercomputer such as *El Capitan*. Hence, capturing this physics without explicitly resolving it necessitates the development of subgrid models.

From a modelling perspective, multiphase gas plays a critical role in regulating star formation, metal transport, and the long-term evolution of the gas reservoir within and around galaxies and galaxy clusters (Tumlinson et al., 2017). Therefore, any attempt to accurately model galaxy or cluster evolution must account for the multiphase nature of the underlying astrophysical gas. In Chapter 4 we develop a subgrid for the multiphase gas using the theoretical understanding from previous studies with small-scale simulations.

2 | A quick introduction to Turbulence

> Let others bring order to chaos. I would bring chaos to order instead, which I think I have done.
>
> — Kurt Vonnegut, in *Breakfast of Champions*

> You can mix anything if you stir hard enough.
>
> — Max Gronke, about *Stirring vs. Mixing*

2.1 Why is astrophysical gas turbulent?

Turbulence, like the multiphase nature of astrophysical gas, is expected to be ubiquitous in astrophysical media. Reynolds number (Re), which is a measure of susceptibility of a flow to become turbulent, is defined as,

$$\mathrm{Re} \sim \frac{uL}{\nu}$$

where u, L and ν are the flow speed, characteristic lengthscale and kinematic viscosity, respectively. A higher Re corresponds to a higher susceptibility of flow to become turbulent (Stokes, 1851; Reynolds, 1883).

The very low values of kinematic viscosity (Spitzer, 1962), along with large characteristic lengthscales in astrophysical environments, result in a very high Reynolds number, with $\mathrm{Re} \sim 10^5 - 10^{10}$. In such regimes, even modest energy injection can give rise to turbulent flows. Consequently, turbulence is expected in virtually any region where energy is being deposited, whether gravitational, thermal, kinetic, or magnetic in origin.

When energy is injected into a medium as kinetic energy, it undergoes a turbulent cascade from the large driving scale down to progressively smaller scales. This cascade continues until the energy reaches the viscous dissipation scale called the Kolmogorov lengthscale (Kolmogorov, 1941), where it is ultimately dissipated as thermal energy. The red line in Fig. 2.1 shows the power spectrum for kinetic energy once this cascade is fully established upto the dissipation length scale, $l_\nu \sim \mathrm{Re}^{-3/4} L$. Due to the massive value of Re, the characteristic (driving) scale (L) and dissipation lengthscale (l_ν) are separated by many orders of magnitudes. This makes it almost infeasible to have a simulation which incorporates both the lengthscales. Hence, simulations without subgrid

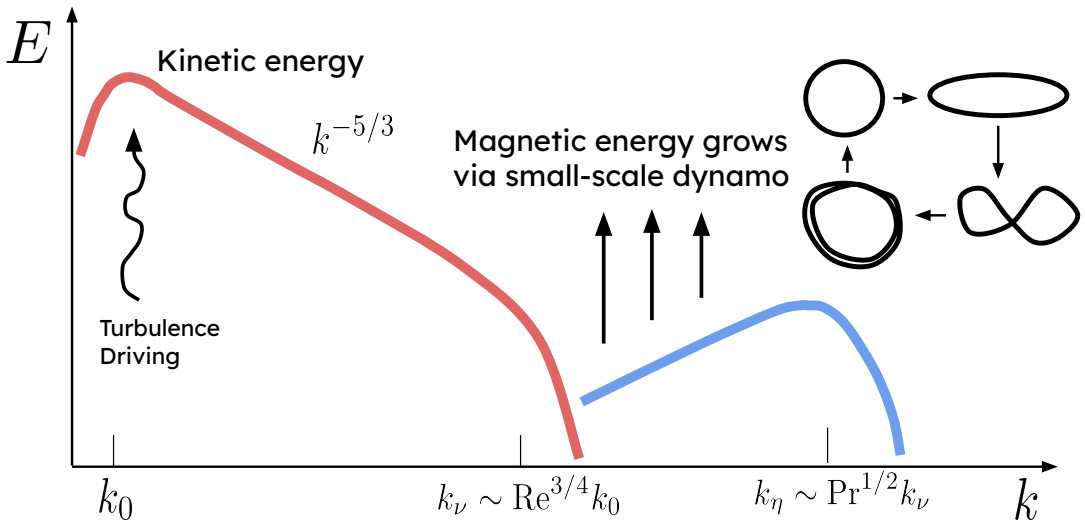

Figure 2.1: Diagram shows the evolution of turbulent power spectrum for kinetic energy and magnetic energy. Replicated from Schekochihin et al. (2001). The series of figures on the right depicts the small-scale dynamo, where a magnetic field loop can be stretched and folded, leading to amplification. k_ν and k_η are wavenumbers corresponding to Kolmogorov dissipation and resistive lengthscale (Kolmogorov, 1941).

turbulence models, either boost ν artificially to enable Direct Numerical simulations (DNS) or leave l_ν unresolved and let dissipation happen numerically at the grid scale. The simulations of the second kind are called Implicit Large Eddy simulations (ILES) and are the most common way of simulating turbulent gas in astrophysical studies, including the ones in this thesis (Pope, 2000).

The eddies of different scales (l) evolve at the eddy turnover time ($t_{\mathrm{eddy}}(l)$) for that scale, making it an important dynamical timescale. According to Kolmogorov's theory of incompressible turbulence (Kolmogorov, 1941), the energy transfer rate across scales is constant. This implies a characteristic turbulent velocity scaling, with lengthscale l as $u(l) \propto l^{1/3}$. This leads to an eddy turnover time scaling of

$$t_{\mathrm{eddy}}(l) \sim \frac{l}{u(l)} \sim l^{2/3}$$

As the eddies of size l evolve on a timescale of $t_{\mathrm{eddy}}(l)$, this scaling implies that smaller eddies evolve more rapidly. Hence, the largest scales typically act as the bottleneck for the overall energy cascade.

Observationally, turbulence has been characterized across a wide range of spatial scales using various tracers. Turbulence in the interstellar medium can be powered by numerous sources, for example, stellar winds, supernovae, inflows, etc (Elmegreen & Scalo, 2004; Scalo & Elmegreen, 2004). Falceta-Gonçalves et al. (2014) quantify the turbulence through the density power spectrum at small scales, revealing its imprint on the structure of the interstellar medium. At galactic scales,

Vidal-García et al. (2021) measure the turbulent energy cascade rate across different regions of a galaxy group using CH+ (1-0) lines. More recently, Li et al. (2022) analyse turbulence in the jellyfish galaxy ESO 137-001, discussed in the previous section, using multiphase emission from CO and Hα, providing insights into the kinematics of the stripped gas tails.

2.2 What about magnetic fields?

In a steady-state turbulent plasma with magnetic fields, we also expect to see a similarly turbulent magnetic field structure, due to the flux-freezing of magnetic fields in the conducting plasma. This leads to exchange of energy between the kinetic and magnetic energy across scales (Grete et al., 2017). Similar to kinetic viscosity (ν) for kinetic energy, there is magnetic diffusivity (η) for magnetic energy, which quantifies the dissipation of magnetic energy to thermal energy. Hence, analogous magnetic Reynolds number (Re_m) and resistive lengthscale (l_η) can be defined as,

$$\mathrm{Re}_m \sim \frac{uL}{\eta}$$

$$l_\eta \sim \mathrm{Re}_m^{-3/4} L = \mathrm{Pr}_m^{-1/2} l_\nu$$

where the magnetic Prandtl number (Pr_m) refers to the ratio (ν/η). With the viscosity and magnetic diffusion values for fully ionised plasma from Spitzer (1962), we can write $\mathrm{Pr}_m \sim 10^{-5} T^4/n$, where T and n are temperature (in K) and number density (in cm^{-3}). A gas with a number density of 0.01 cm^{-3} at 10^6K, typical for CGM, will have a $\mathrm{Pr}_m \sim 10^{21}$, leading to $l_\eta \sim 10^{-10} l_\nu$. As the magnetic field can have structures as small as l_η, magnetic fields structures can be orders of magnitudes smaller than the smallest velocity structure of size l_ν.

In the absence of a strong initial magnetic field, a very low seed magnetic field can be amplified via a small-scale dynamo. Fig. 2.1 shows an intuitive picture (on the right side) of how a magnetic field loop, flux-frozen in a turbulent flow, can be stretched and twisted, leading to amplification. This process happens at the timescales of the $t_{\mathrm{eddy}}(l)$. Hence, magnetic field amplification due to the dynamo is most efficient at the smallest scales, where the t_{eddy} is shortest, as also illustrated in Fig. 2.1.

The vast lengthscale separation between l_ν and l_η, over the existing separation between L and l_ν, makes it practically impossible to simulate magnetohydrodynamic (MHD) turbulence with all the relevant scales included. Hence, similar to hydrodynamic turbulence, the dissipation of magnetic fields is usually left to numerical dissipation at grid scales in astrophysical studies, like the study in Chapter 3. This also implies that the $\mathrm{Pr}_m \sim 1$ in an ILES simulation of MHD turbulence.

3 | Magnetic Fields in Multiphase Turbulence: Impacts on Dynamics and Structure

> Purpose of computation is not numbers, but insight.
>
> — Richard Hamming
> in *The art of doing science and engineering*

> Don't ascribe something to Physics, if it can be explained by a bug.
>
> — Volker Springel

This work has been published in the Monthly Notices of the Royal Astronomical Society, Volume 527, Issue 1, January 2024, Pages 991–1013.

The fact that most of the astrophysical media are multiphase in nature is a well-established one, from observational (e.g. Tumlinson et al., 2017; Veilleux et al., 2020a), numerical, and theoretical investigations (McKee & Ostriker, 1977a; Donahue & Voit, 2022; Faucher-Giguere & Oh, 2023a). The multiphase nature of the interstellar (ISM), circumgalactic (CGM) and intracluster (ICM) medium is also expected to play an important role in the overall evolution of the associated systems, from the general baryon cycle to feedback processes (Veilleux et al., 2005; Péroux & Howk, 2020). However, there are many aspects of multiphase media, like survival and characteristic size of cold media, that are still in question and are an active field of research.

Many forays towards understanding the multiphase gas use an idealised version of the medium. There are studies which focus on the development of the multiphase gas by condensation from an initially static hot ambient medium via thermal instability in 1D (Sharma et al., 2012; Waters & Proga, 2019), 2D (McCourt et al., 2018) and 3D simulations (Gronke & Oh, 2020b). Such studies are a good way to isolate and investigate the role of different factors like magnetic fields (Sharma et al., 2010; Ji et al., 2018), metallicity (Das et al., 2021a), gravity (McCourt et al., 2012), density fluctuations (Choudhury et al., 2019), rotation (Sobacchi & Sormani, 2019) or cosmic rays (Butsky et al., 2020).

It is also well known that the astrophysical media are highly turbulent, due to their high Reynolds number. This has been shown by many observational (Elmegreen & Scalo, 2004;

Falceta-Gonçalves et al., 2014; Vidal-García et al., 2021; Li et al., 2022) and numerical studies (Brandenburg & Nordlund, 2011; Federrath, 2013; Burkhart et al., 2020). Hence, many studies like Mohapatra & Sharma (2019); Gronke et al. (2022a); Mohapatra et al. (2022b,c) investigate the evolution of the multiphase gas in the presence of a turbulent astrophysical media. Turbulence both amplifies and destroys multiphase gas. The density and temperature perturbations in a turbulent medium can enhance the creation of multiphase gas, while the same turbulent motions can mix the existing multiphase gas, which might further cool or mix away depending on the cooling timescale.

Not just astrophysics, multiphase turbulence is also a very relevant topic at more terrestrial scales and is also an active field of research in general fluid dynamics circles, as there are many applications like combustion dynamics, smoke transport and meteorology where multiphase interactions play a crucial role. One seminal result in the field was by Damköhler (1940), where they found that the behaviour of a flame front in a turbulent medium differs depending on the ratio of the reaction and turbulent timescales, i.e. the Damköhler number. Tan et al. (2021) further explore this parallel in the context of hydrodynamic turbulent radiative mixing layers (TRMLs) in astrophysical media.

Generally, there are three stages in the evolution of a turbulent multiphase medium, with many studies examining each. First, the production or presence of seed multiphase gas. The exact mechanism of this can vary from medium to medium. For the CGM, this can either be in the form of multiphase ISM transported into the CGM by feedback mechanism, or via condensations from the hot medium due to thermal instability. The second stage is the growth of one of the phases in the multiphase gas. And, the final stage is the equilibrium or steady state.

In order to understand the second stage of the multiphase gas evolution, Gronke et al. (2022a) study the growth of cold gas in a thermally stable, ambient turbulent medium. They found a critical radius for the size of the seed cold gas cloud in a given turbulent hot ambient medium (akin to the survival criterion previously found for laminar flows Gronke & Peng Oh, 2018; Li et al., 2020; Kanjilal et al., 2021). Their results also agreed with the expectations from the previous hydrodynamics TRML results from Tan et al. (2021), indicating TRMLs might be the principle mechanism for mixing in a multiphase medium.

But, apart from being multiphase and turbulent, the astrophysical media are also known to possess substantial magnetic fields as seed primordial magnetic fields are amplified due to structure formation and other baryonic dynamics (Dimopoulos & Davis, 1997; Subramanian, 2015). There are many observational evidences for ubiquitousness of magnetic fields using techniques like Faraday rotation (Dreher et al., 1987; Kim et al., 1990; Taylor & Perley, 1993; Clarke et al., 2001), dust alignment (Ade et al., 2015), and others (Lopez-Rodriguez et al., 2021). And, many numerical studies also point to a similar prevalence of magnetic fields (e.g., Pakmor et al., 2020; van de Voort et al., 2021).

The presence of magnetic fields can be disruptive to mixing via TRMLs. It is well-known that linearly, the Kelvin-Helmholtz instability is suppressed for specific magnetic field orientation (Chandrasekhar, 1961), while Ji et al. (2019) show that the nonlinear evolution of the instability

with radiative cooling is suppressed for all orientations of the initial magnetic field. [1] Hence, the inclusion of magnetic fields may change the overall evolution of multiphase gas, resulting in different survival criteria and cold gas growth rates. In summary, while it has been shown in recent work that mixing and subsequent cooling can lead to the survival and even the production of cold gas, and thus explain the ubiquitous presence of multiphase gas in turbulent systems – where this cold gas should be destroyed rapidly – magnetic fields might ruin this picture by preventing mixing and hence hindering cooling.

In this paper, we investigate the influence of magnetic fields on the general phenomenon of mixing between the phases in a multiphase gas. For that purpose, we use two kinds of simulations, TRMLs and turbulent boxes, with and without magnetic fields. First, we expand on the parameter space for TRMLs explored in previous studies, to confirm the suppression of mixing for different cooling strengths (and hence different Damköhler numbers). Second, we check for the effects of including magnetic fields in turbulent box simulations similar to Gronke et al. (2022a).

The structure of the paper is as follows. We explain the numerical setups for both TRMLs and turbulent boxes in section 4.1. We present the results from the TRML simulations in section 3.1.1, and the turbulent boxes in section 3.3. Then, we discuss our results in section 3.4 and conclude in section 4.6. The visualisations related to this study can be found here.[2]

3.1 Numerical setup

For our simulations, we use the ATHENA++ code (Stone et al., 2020a). We use the default HLLC solver for our hydrodynamic (HD) simulations and the default HLLD solver for our magnetohydrodynamic (MHD) simulations, with Piecewise Linear Method (PLM) applied to primitive variables, second-order Runge-Kutta time integrator, adiabatic EOS and a cartesian geometry. Similar to Gronke et al. (2022a), we implemented the Townsend radiative cooling algorithm (Townsend, 2009a) for computing the radiative losses, using a cooling curve at solar metallicity fitted using 40 segments of power laws. We also enforce a temperature floor $T_{\rm floor} = 4 \times 10^4$ K.

3.1.1 Turbulent Radiative Mixing Layer (TRML)

Turbulent, radiative mixing layers in the astrophysical context have been investigated in the past (e.g., Begelman & Fabian, 1990a; Slavin et al., 1993; Kwak & Shelton, 2010; Hillier et al., 2023; Fielding et al., 2020). We use the same numerical setup as the one used in Tan et al. (2021) and Ji et al. (2019) to investigate the Turbulent Radiative Mixing Layer (TRML), with a small difference in our coordinates convention. The shear velocity in our simulations is along $\hat{x}$ and the cold/hot interface is normal to $\hat{z}$.

[1] This study was within the slow-cooling regime from Tan et al. (2021).

[2] http://hiteshkishoredas.github.io/research/mhd_multiphase.html

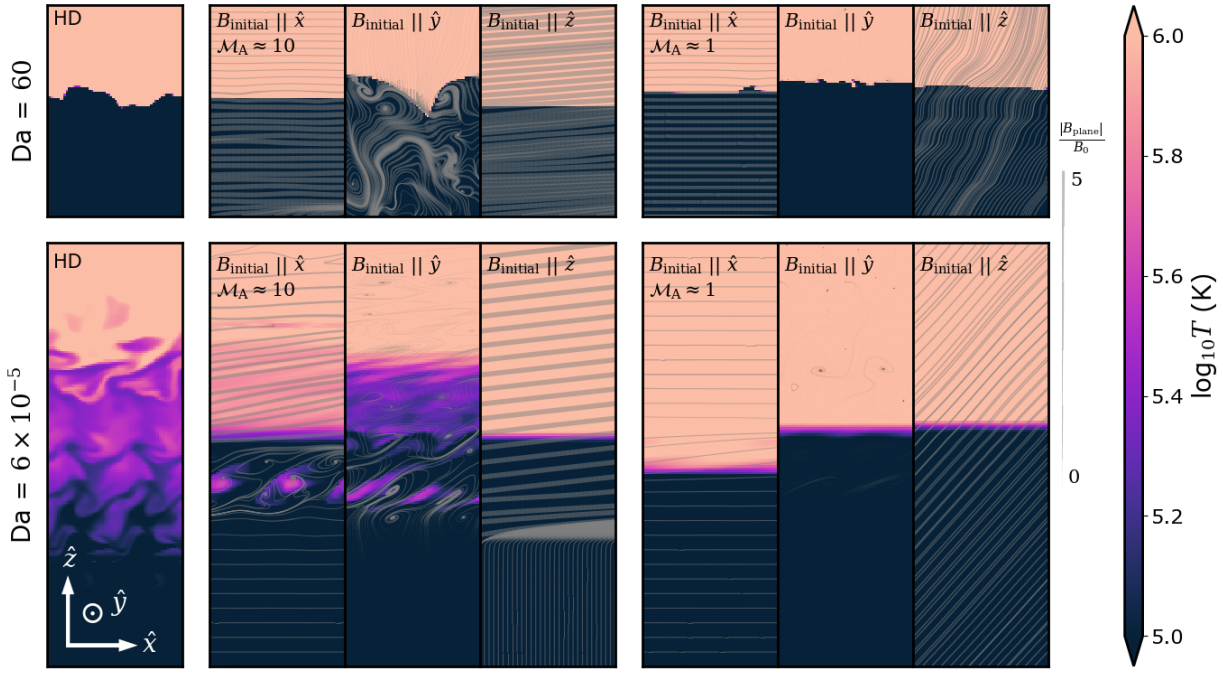

Figure 3.1: Temperature slices for different TRML simulations for $v_{\rm shear} = 100\,{\rm km\,s^{-1}}$ ($\mathcal{M} \approx 0.3$). **First column** shows the hydrodynamic simulations, **2nd to 4th column** show simulations with $\mathcal{M}_{\rm A} = 10$, **last three columns** show simulations with $\mathcal{M}_{\rm A} = 1$. **Top row** shows simulations with strong cooling, Da = 60, **Bottom row** shows simulations with weak cooling, Da = 6×10^{-5}. This shows the different ways magnetic fields evolve for different initial orientations. It also suggests that the cases with the higher magnetic field strength along the shear direction show a lesser extent of mixing.

The different density and velocity profiles are,

$$\rho(z) = \rho_{\rm cold} + \frac{\rho_{\rm hot} - \rho_{\rm cold}}{2}\left[1 - \tanh\frac{z}{a}\right] \tag{3.1}$$

$$v_x(z) = \frac{v_{\rm shear}}{2}\left[1 + \tanh\frac{z}{a}\right] \tag{3.2}$$

$$v_z = \delta v \exp\frac{-z^2}{a^2} \sin k_x x \sin k_y y \tag{3.3}$$

$$B = \frac{v_{\rm shear}\rho_{\rm hot}^{1/2}}{\mathcal{M}_{\rm A}}\hat{B}_0 \tag{3.4}$$

where k_x and k_y are set to $2\pi/L_{\rm box,x}$ and $2\pi/L_{\rm box,y}$ respectively.

We use $v_{\rm shear} = 100$km/s, 50km/s as the shear velocity (corresponding to sonic Mach numbers of $\mathcal{M} \equiv v_{\rm shear}/c_{\rm s,hot} \sim 0.33, 0.16$), $\delta v = 0.01 v_{\rm shear}$, $a = L_{\rm box,z}/20$ for the interface thickness, and $\mathcal{M}_{\rm A} = 1, 10$ as initial Alfvénic Mach number. Furthermore, $\rho_{\rm hot} = 1.6 \times 10^{-4}{\rm cm}^{-3}$ is the

density of hot medium, $\rho_{\rm cold} = 1.6 \times 10^{-2} {\rm cm}^{-3}$ is the density of cold medium, and $\hat{B}_0$ is the initial magnetic field direction. We use a floor temperature of 4×10^4 K, and we stop cooling at temperatures above $0.5T_{\rm hot}$ to emulate the effect of heating, where $T_{\rm hot}$ is the hot medium temperature. We initialise the cold medium at the floor temperature (4×10^4 K), and use a fixed pressure over the whole box to ensure pressure balance in the initial conditions. This corresponds to a hot medium at $T_{\rm hot} = T_{\rm cold}\chi$ with $\chi \equiv \rho_{\rm cold}/\rho_{\rm hot} = 100$ being the overdensity. We impose an outflow boundary condition along the normal to the cold/hot interface ($\hat{z}$), and periodic boundary conditions in all other directions. Note that due to the self-similarity of the solution, the chosen numerical values for ρ and $v_{\rm shear}$ are unimportant (as long as the critical dimensionless quantities are kept constant).

We use a resolution of $64 \times 64 \times 640$ in $\hat{x}$, $\hat{y}$ and $\hat{z}$ directions respectively, and use different box sizes to vary parameters in our simulations, but keep the ratios of box lengths in different dimension fixed, $L_{\rm box,z} = 10L_{\rm box,x} = 10L_{\rm box,y}$. We vary the Damkohler number (${\rm Da} = t_{\rm turb}/t_{\rm cool} = L_{\rm box,x\ or\ y}/(u_{\rm turb}t_{\rm cool})$) in a range of $\sim 10^{-4} - 10^4$ by changing $L_{\rm box}$.

In such TRML simulations, the mixing layer tends to move into the hot medium as it is consumed and more cold gas is created. This can cause the mixing layer to go out of the computational domain, especially for high Da cases. To counter that, we add a velocity to the whole box in the opposite direction to keep the mixing layer inside the computational domain. This velocity is calculated using the difference between the current cold/hot interface position and the original cold/hot interface position ($z = 0$). We verify that this does not affect the mixing rates, and only increases the time the mixing layer spends inside the computational box. We denote the different TRML simulations as `Ma(A)_Bx(B)`, where `A` is the Alfvénic Mach number and `B` is the initial magnetic field orientation.

3.1.2 Driven turbulence boxes

We use a separate simulation setup, similar to the one used in Gronke et al. (2022a), to study the behaviour of cold gas in fully-developed turbulence with (MHD) and without (HD) magnetic fields. We start with a box filled with isobaric gas at uniform density and temperature ($T_{\rm hot} = 4 \times 10^6$ K), with solar metallicity and H-abundance. In our MHD simulations, we initialize the box with a uniform magnetic field. We use the Ornstein-Uhlenbeck (OU) process (Eswaran & Pope, 1988a; Schmidt et al., 2006a) to drive the turbulence at the largest scale ($k = 2\pi/L_{\rm box}$), i.e. the box size. We use driving timescale of 0.001 $t_{\rm eddy}$, correlation timescale $\sim t_{\rm eddy}$ and solenoidal to compressive fraction $f_{\rm sol} = 0.3$. We also maintain a $L_{\rm box}/R_{\rm cloud} = 40$ for all our simulations.

We drive the turbulence for 7 $t_{\rm eddy}$ with the cooling turned off, which gives the setup enough time to reach a steady-state with equilibrium kinetic energy and magnetic energy (when included). We restart the simulation after introducing a dense cloud, with an overdensity $\chi = 100$ and radius $R_{\rm cl}$ in the centre of the box while conserving the kinetic, thermal and magnetic energy density. This results in an isobaric, cold, dense cloud with density $\rho_{\rm cold} = \chi\rho_{\rm hot}$ and temperature $T_{\rm cold} = 4 \times 10^4$ K $= T_{\rm floor}$. As we use an adiabatic equation-of-state, the average temperature can increase significantly by the end of the turbulent driving phase, due to the dissipation of the

turbulent energy. Hence, to bring the ambient temperature back to the required value, before introducing the cloud, we also rescale the internal energy of the whole box by a fixed constant. We also verify that this abrupt rescaling does not have any significant effect on the velocity distribution.

The input parameters for the driven turbulence are the kinetic energy injection rate ($\dot{E}$), the size of the simulation box ($L_{\rm box}$) and the density of the medium (ρ). Given a box size and gas density, we calculate the required $\dot{E}$ for a required turbulent velocity (see, e.g., Lemaster & Stone, 2009), i.e.,

$$\dot{E} t_{\rm eddy} = (\frac{1}{2}\rho v_{\rm turb}^2 + \frac{1}{2}B_{\rm turb}^2) L_{\rm box}^3 \tag{3.5}$$

and assuming equipartition this yields

$$\dot{E} = \frac{\alpha}{2}\rho L^2 v_{\rm turb}^3 \tag{3.6}$$

where, $\alpha = 1$ for hydrodynamic simulations and $\alpha = 2$ for MHD simulations . Following the convention from previous studies, we also use cloud radii normalised by $l_{\rm shatter} = \min(c_s t_{\rm cool})$. This corresponds to the $c_s t_{\rm cool}$ of the cold, dense medium in our simulations, i.e. $c_s t_{\rm cool}(\rho_{\rm cold}, T_{\rm floor})$.

3.2 Results: Turbulent Radiative Mixing Layer

Turbulent Radiative Mixing Layers (TRMLs) are mixing layer simulations that also include radiative cooling for the mixed gas. These have long been studied as an idealised small-scale setup for the mixing between different phases in a multiphase gas (e.g. Esquivel et al., 2006; Ji et al., 2019; Fielding et al., 2020; Tan et al., 2021; Yang & Ji, 2023). In this section, we study the evolution of TRMLs for different cooling strengths and look for differences caused by the presence of magnetic fields.

3.2.1 Gas & magnetic field morphology

Previous studies of linear and non-linear evolution of mixing layers have shown suppression of Kelvin-Helmholtz (KH) instability-induced mixing, in the presence of magnetic fields. In the linear regime, the KH instability is suppressed for cases with magnetic field along the shear direction if $v_{\rm shear} < (v_{\rm A,hot} v_{\rm A,cold})^{1/2} \approx v_{\rm A,hot}\chi^{-1/4}$ (Chandrasekhar (1961); Chapter XI, Eq. 205). While, in non-linear regime, the KH instability is suppressed for all magnetic field orientations (Ji et al., 2019). In this subsection, we reproduce these results and extend them by varying the cooling and magnetic field strength.

Fig 3.1 shows the temperature slices of the different TRML simulations, along with the magnetic field morphology, for different Alfvénic mach number ($\mathcal{M}_{\rm A} = v_{\rm shear}/v_A$, where v_A is the Alfvén wave speed), and initial magnetic field orientation ($\hat{B}_0$). We control the Da $= t_{\rm turb}/t_{\rm cool,mix}$ (where $t_{\rm turb} = L/v_{\rm turb}$ and $t_{\rm cool,mix}$ is the cooling time evaluated at $T = 2 \times 10^5$ K, and $v_{\rm turb}$ is calculated

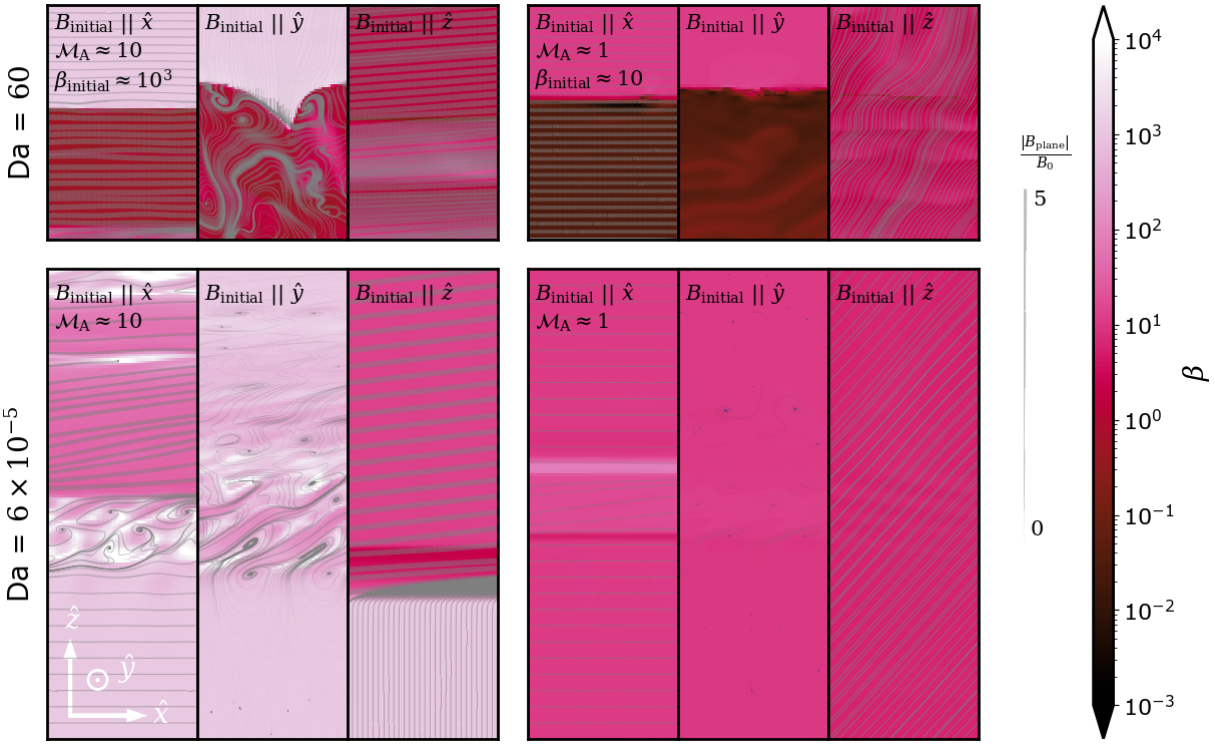

Figure 3.2: $\beta = P_{\text{thermal}}/P_{\text{magnetic}}$ slices for different TRML simulations with $v_{\text{shear}} = 100$km/s (corresponding to the temperature slices shown in Fig. 3.1). **1st to 3rd column** show simulations with $\mathcal{M}_{\text{A}} = 10$, **last three columns** show simulations with $\mathcal{M}_{\text{A}} = 1$. **Top row** shows simulations with strong cooling, $Da = 60$, **Bottom row** shows simulations with weak cooling, $\text{Da} = 6 \times 10^{-5}$. This shows the extent of amplification possible in the different cases. Even with a higher initial β, turbulent motions can amplify the magnetic fields to lower β. For cases with lower initial β strong cooling in the mixing layer can also lead to amplification.

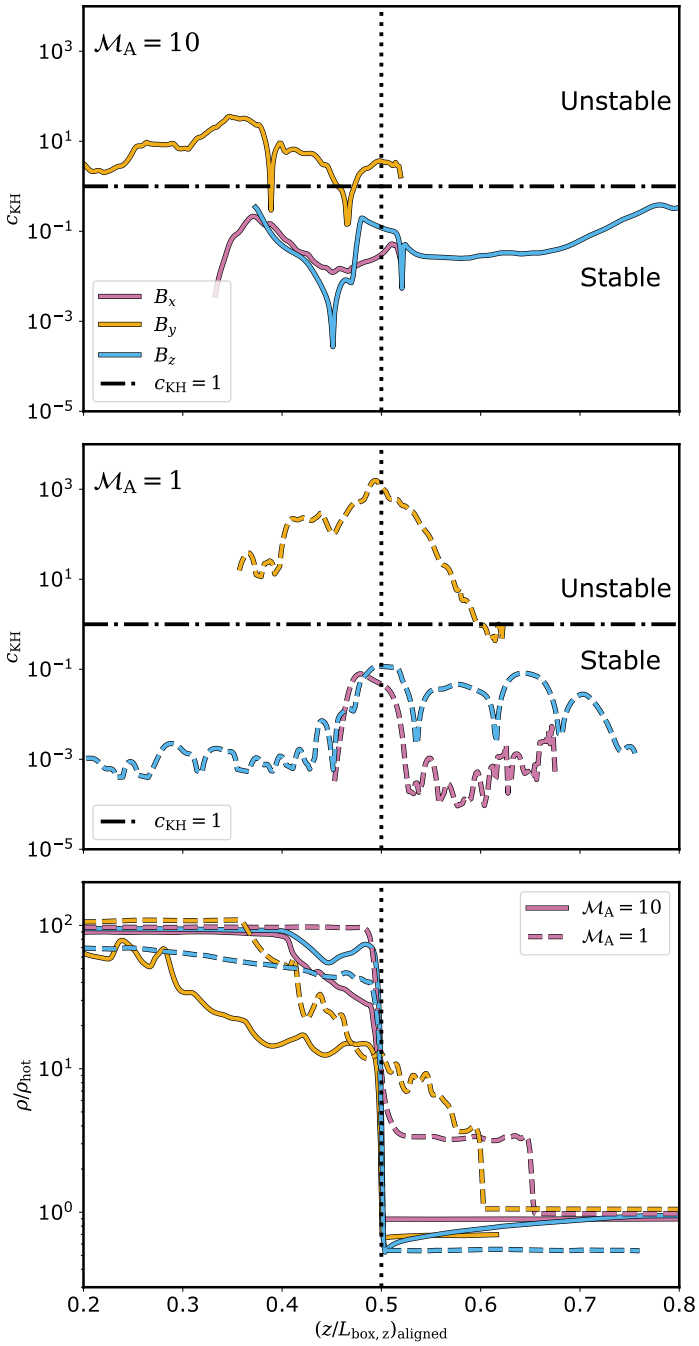

Figure 3.3: **Top & middle** Stability criterion of Kelvin-Helmholtz instability for different initial magnetic field orientations (cf. Eq. (3.8)), **Bottom** Density profile for the different cases shown above. This shows the difference in the stability of the mixing layers for different cases. The cases with higher magnetic field strength along the shear (initial or amplified) are more stable. The density profile shows the extent of the mixing layers.

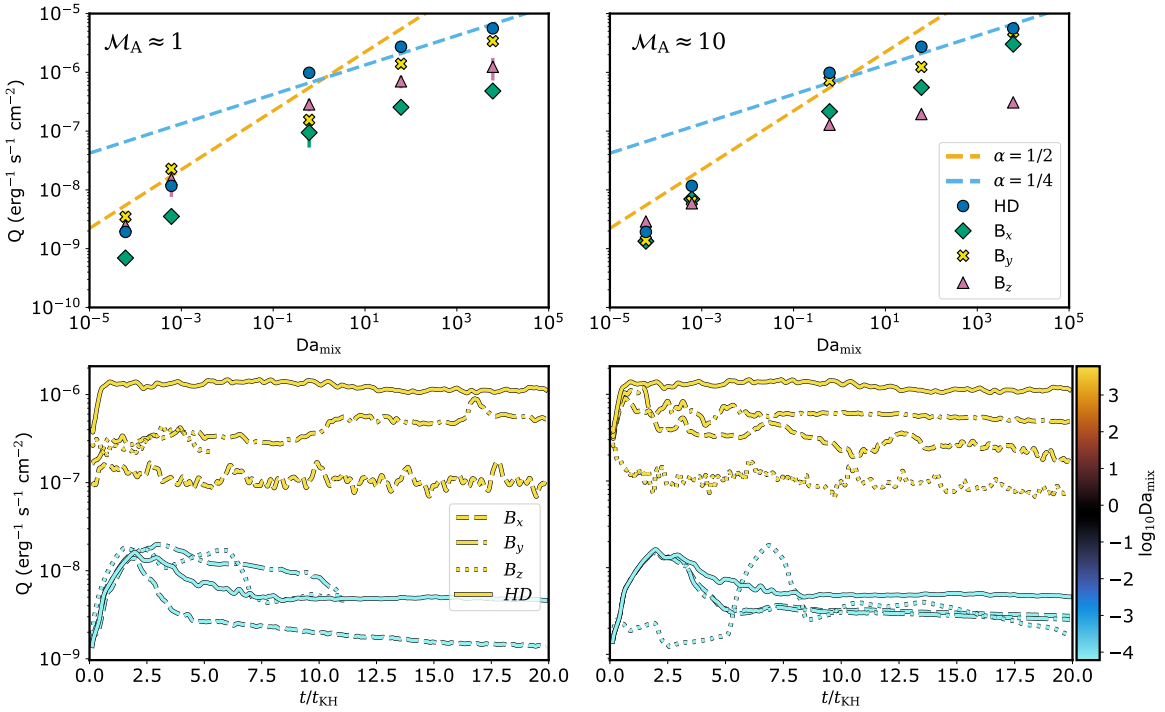

Figure 3.4: **Left column** $\mathcal{M}_A = 1$, **Right column** $\mathcal{M}_A = 10$, **Top row** Stable values of mixing layer surface brightness for different Da, The orange and blue dashed lines on the top row panels are the expected values from hydrodynamic TRML simulations by Tan et al. (2021). This shows clear suppression in cooling rates of most of the simulations with magnetic fields, in comparison to hydrodynamic TRML simulations. We discuss details about the trends in § 3.2. **Bottom row** Evolution of mixing layer surface brightness with time, for different initial magnetic field orientations at two Da values.

using scaling relations from Tan et al., 2021; we will investigate the role of $v_{\rm turb}$ more below) by varying the box sizes, and $\mathcal{M}_{\rm A}$ by changing the initial magnetic field strength, for a given sonic Mach number. We have simulations with $\mathcal{M}_{\rm shear,hot}$ fixed to 0.16 and 0.33, corresponding to a $v_{\rm shear}$ of 50 and 100 $\rm km\,s^{-1}$. We find that the amplification in the magnetic fields is very different depending on the initial magnetic field orientation as we discuss below.

Fig. 3.2 shows the $\beta(= P_{\rm thermal}/P_{\rm magnetic})$ and has layout similar to that of Fig. 3.1. The extent of amplification in the different cases is much clearer in Fig. 3.2, where the darker regions correspond to a higher magnetic field strength and lighter regions to a lower magnetic field strength.

The upper and lower row of Fig. 3.1 shows the fast and slow cooling cases, respectively. On one hand, in the fast cooling (Da $>$ 1) a sharp temperature edge between $T < 10^5$ K and $T \sim 10^6$ K gas is visible, i.e., a true multiphase structure exists, while on the other hand, a large amount of this "intermediate temperature" gas is visible in the slow cooling (Da $<$ 1) case – with the exact amount depending on the suppression of mixing caused by magnetic fields. Unsurprisingly, in the HD case most mixed gas exists and generally in the MHD case with $\mathcal{M}_{\rm A} \approx 1$ the least. What is maybe a bit more surprising is the effect (and the evolution of) the magnetic field topology: in the $\mathbf{B} \parallel \hat{x}$ case the suppression of mixing is easy to understand and expected from linear theory (Chandrasekhar, 1961). However, we also find in all the other cases a (strong) suppression. $\mathbf{B} \parallel \hat{y}$ also has a strong effect, particularly in the $\mathcal{M}_{\rm A} \approx 1$ simulations. This is due to the amplification of the magnetic fields in the direction of the shear, as discussed below. On the other hand, for $\mathbf{B} \parallel \hat{z}$ initially, one can note two distinct effects depending on the value of $\mathcal{M}_{\rm A}$. For $\mathcal{M}_{\rm A} > 1$ the flow bends the magnetic field lines, resulting in a similar situation as in the $\mathbf{B} \parallel \hat{x}$ case; in fact, even larger suppression since the bending of the field lines leads to a $B_x > B_{\rm initial}$. An artefact of this bending can be seen in magnetic field topology in the bottom panel for $\mathcal{M}_{\rm A} > 1$ with $\mathbf{B} \parallel \hat{z}$. We find a kink in the magnetic field moving downwards at the Alfvén wave speed. For $\mathcal{M}_{\rm A} \lesssim 1$, however, the magnetic field lines are so stiff that a bending by 90 degrees is not possible. Instead, we end up with diagonal field lines which, nevertheless, substantially suppress the mixing.

To better understand the exact order of amplification, we first consider the cases where the shear is super-Alfvénic ($\mathcal{M}_{\rm A} \sim 10$) in the hot medium, in the three central ($2^{\rm nd}$ - $4^{\rm th}$) columns of Fig. 3.1 & 3.2, to explain the extent of amplification in the different cases.

- $B_{\rm initial} \,||\, \hat{z} \,||\, \hat{n}_{\rm interface}$ (`Ma10_Bz`): The amplification is the highest for this case. The Alfvén wave velocity in the dense medium is lower by a factor of $\chi^{1/2}$, hence the field lines are more "anchored" in the cold gas, compared to the hot gas. This causes field lines to bunch up near the interface, resulting in high amplification of magnetic fields in the direction parallel to the shear. This amplification is so high that the magnetic field strength can get much higher than the initialised magnetic field strength.

- For $B_{\rm initial} \,||\, \hat{x} \,||\, \vec{v}_{\rm shear}$ (`Ma10_Bx`): As the Kelvin-Helmholtz (KH) instability grows, it gives rise to vortices around $\hat{y}$. Fig. 3.1 shows that vortices can stretch and bend the magnetic fields, leading to their amplification. These vortices can further become turbulent and cause more amplification due to local dynamo effect. All of these put together, result in the second-highest amplification of magnetic fields along the shear direction.

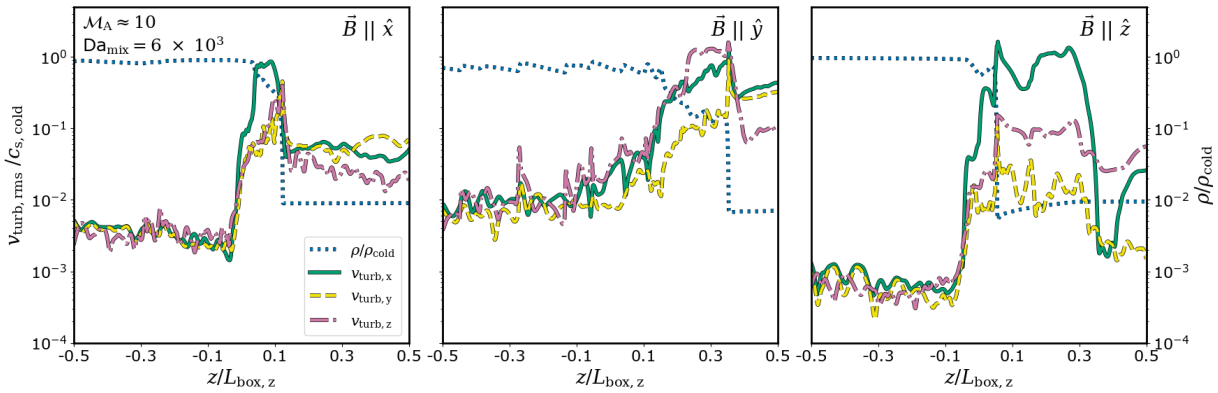

Figure 3.5: u' profiles along $\hat{z}$ for different initial magnetic field orientations. The first two panels from the left show the difference between the direction parallel to magnetic fields versus the other directions. The third panel shows the outlier case of magnetic fields normal to the interface, where both the normal ($\hat{z}$) and shear direction show much higher fluctuations due to the presence of magnetic fields along both these directions. Hence, we choose the directions which free from these spurious fluctuations in these different cases, as denoted in Eq 3.13

- Lastly, for $B_{\rm initial} \parallel \hat{y} \perp \vec{v}_{\rm shear} \perp \hat{n}_{\rm interface}$ (`Ma10_By`): The amplification is the lowest as the only process for amplification of magnetic fields is due dynamo effect from the turbulent motions generated in the mixing layer due to non-linear evolution of the KH instability.

This results in a general order for the magnetic field strength along the shear direction in Super-Alfvénic TRML simulations as: `Ma10_Bz` > `Ma10_Bx` > `Ma10_By`.

Similarly, for the cases where the shear is sub/trans-Alfvénic ($\mathcal{M}_A \sim 1$) in the hot medium, in the three rightmost columns in Fig. 3.1, we again check for magnetic field strength along the shear direction.

- For $B_{\rm initial} \parallel \hat{z} \parallel \hat{n}_{\rm interface}$ (`Ma1_Bz`): As the shear is sub-Alfvénic, the amplified magnetic field in the shear direction is not high enough to surpass the initialised magnetic field in the shear direction for $B_{\rm initial} \parallel \hat{x} \parallel \vec{v}_{\rm shear}$ (`Ma1_Bx`). So, `Ma1_Bz` ends up with the second highest in the order of magnetic field strength along the shear direction.

- $B_{\rm initial} \parallel \hat{x} \parallel \vec{v}_{\rm shear}$ (`Ma1_Bx`) has the strongest magnetic field in shear direction, just due to the high initial magnetic strength.

- This leaves the $B_{\rm initial} \parallel \hat{y} \perp \vec{v}_{\rm shear} \perp \hat{n}_{\rm interface}$ (`Ma1_By`): Due to the much higher overall magnetic field strength, it is harder for the resulting turbulent velocity to cause any amplification.

Hence, we get an order for the magnetic field strength along the shear direction in Sub-Alfvénic TRML simulations as: `Ma1_Bx` > `Ma1_Bz` > `Ma1_By`. In our simulations, we find one exception to this order, at intermediate Da, where the order of `Ma1_Bz` and `Ma1_By` is switched.

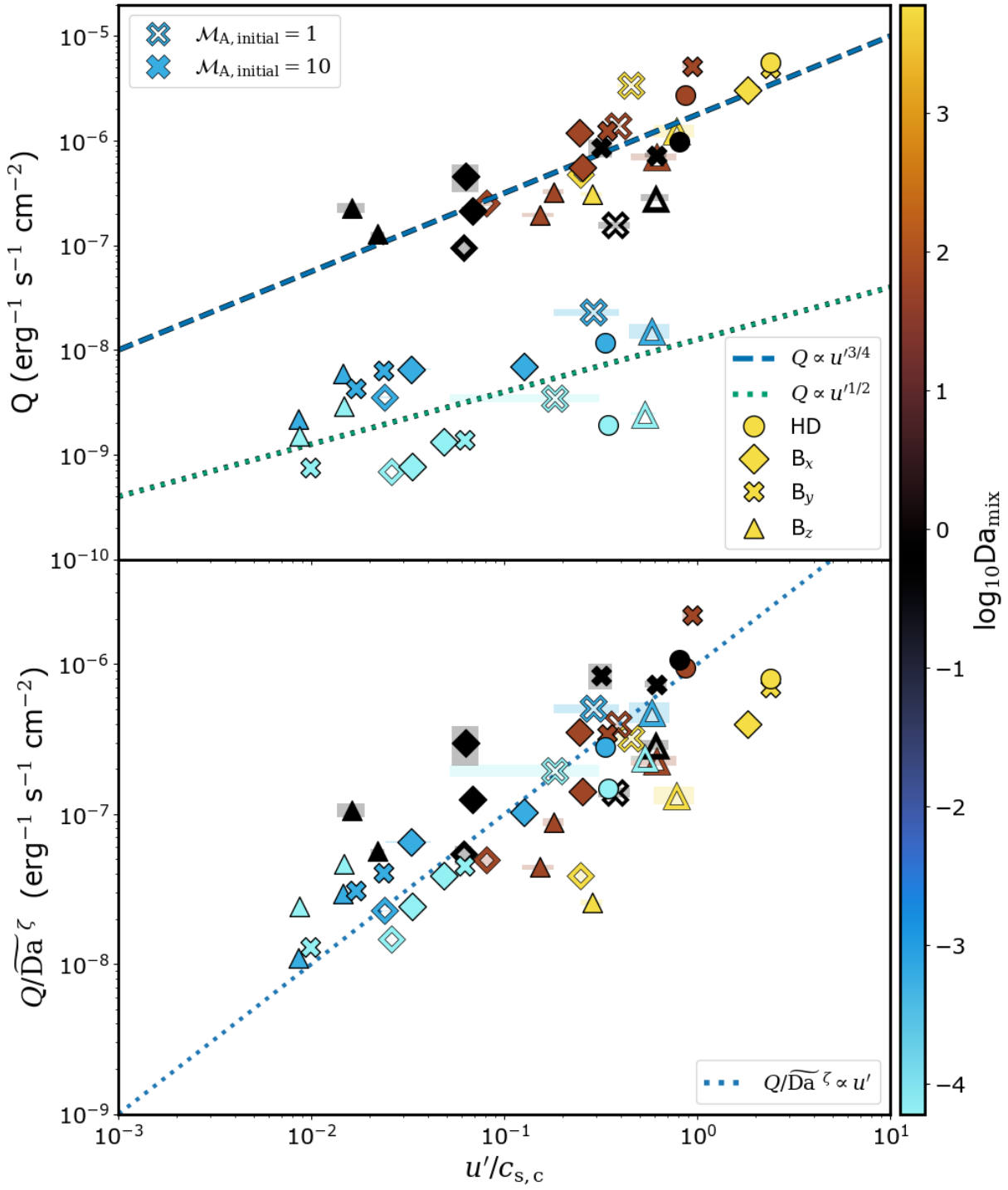

Figure 3.6: **Top panel** Scatter plot of the surface brightness (Q) and turbulent velocity (u') calculated from the simulations. The dashed and dotted lines show the respective strong and weak cooling scaling relation according to Eq. 3.9-3.10. **Bottom panel** Similar to the top panel, after we remove the $\widetilde{\mathrm{Da}}$ dependence. The dotted line shows the analytical expectation from Tan et al. (2021), which they find for hydrodynamic simulations. This suggests that the general relation found in hydrodynamic TRML simulations, between the turbulent velocity in the mixing layer and cooling (and hence mixing) rate, is still valid in the presence of magnetic fields.

3.2.2 Cooling rates

According to the linear KH instability criterion, the stronger the magnetic field in the direction of the shear, the more stable the perturbation gets. This means stronger magnetic fields in the later non-linear phase may disrupt the generation or cascade of further vortices. To test this, we quantify the stability of KH perturbations, using the linear stability criterion (Chandrasekhar, 1961). So, the perturbation is stable to KH instability, if

$$v_{\rm shear} < (v_{\rm A,hot} v_{\rm A,cold})^{1/2} = v_{\rm A,hot} \chi^{-1/4} \tag{3.7}$$

which can be expressed as a dimensionless number

$$c_{\rm KH} = \frac{\Delta v_x \chi^{1/4} \rho_{\rm hot}^{1/2}}{B_x} < 1. \tag{3.8}$$

We calculate $c_{\rm KH}$ using profiles of all the relevant quantities along the normal to the hot/cold interface. This results in a profile of $c_{\rm KH}$, in which a value <1 denotes a tendency towards stability while a value >1 shows a tendency towards instability. Fig. 3.3 shows the profiles of this KH stability criterion at an advanced stage of evolution, for different magnetic field orientations and strengths. The top and middle panels show the KH stability criterion and the bottom shows the corresponding density profiles. We align the profiles so that the hot/cold interface aligns between all the cases. We do not plot the points on the profile which have a $\Delta v < 10^{-2}$ km/s, or if the points are out of the computational domain.

We find that due to the amplification of the magnetic fields in the shear direction, the KH instability is suppressed. The order of the extent of suppression seems to follow the same order as the amplification of the magnetic fields. For both $\mathcal{M}_{\rm A} > 1$ and $\mathcal{M}_{\rm A} < 1$, `Ma1_By` and `Ma10_By` are the most unsuppressed as the $c_{\rm KH}$ is almost entirely in the unstable regime. For the other two directions, the extent of suppression depends on the size of the portion around the mixing layer that is stable. This means, `Ma1_Bx` and `Ma10_Bz` are the most suppressed in $\mathcal{M}_{\rm A} < 1$ and > 1, respectively. This trend in suppression is important as this can affect the cooling rates, which we check next.

We study the cooling rates using the surface brightness of TRML simulations for all the different cases, that is, different values of the Dahmköhler number (Da $= t_{\rm turb}/t_{\rm cool}$), Alfvénic mach number ($\mathcal{M}_{\rm A} = v/v_A$, where v_A is the Alfvén wave speed), and initial magnetic field orientation ($\hat{B}_0$). We define the surface brightness as the total luminosity per unit surface area, that is, $Q = L_{\rm total}/(L_x L_y)$. Fig. 3.4 shows the calculated saturation surface brightness (along with 2σ errorbars) for the different simulations on the top row, along with its temporal evolution on the bottom row.

We find that the order of amplification of magnetic fields along the shear direction, mentioned above, matches the order of suppression of surface brightness, as shown in the right panel in Fig. 3.4. This is due to the higher suppression of KH instability by the higher magnetic field strength along the shear direction, as also expected from the linear theory (Chandrasekhar, 1961). Below, we dive deeper into this correlation.

We also find that the difference in cooling rates, due to this suppression of KH instability, is reduced for the low Da cases with $\mathcal{M}_A \sim 10$, as shown in Fig. 3.4. This might be due to the change in the rate-limiting process. For a low Da the cooling is very slow, so the cooling rate is bottlenecked by the slow cooling rate rather than the mixing rate. This does not happen for $\mathcal{M}_A \sim 1$ because the mixing rate is suppressed to such low values that mixing continues to be the rate-limiting process.

3.2.3 Turbulence velocity profiles

Among the different ways to mix two phases, turbulence is one of the most efficient ones. In this section, we quantify the extent of turbulence in the mixing layer in the above discussed TRML simulations and look for connections of turbulence with the rate of mixing and cooling in the system.

This dependence has been studied before, in the absence of magnetic fields. Assuming a constant pressure and cooling function for hydrodynamic TRML simulations, as shown in Tan et al. (2021), for a strong cooling regime (Da > 0.1),

$$Q \propto u'^{3/4} L_{\rm box}^{1/4} \propto u' {\rm Da}^{1/4} \tag{3.9}$$

and for slow cooling regime (Da < 0.1),

$$Q \propto u'^{1/2} L_{\rm box}^{1/2} \propto u' {\rm Da}^{1/2}. \tag{3.10}$$

Our next step is to check these relations in the presence of magnetic fields. We use the geometric method to calculate the u', similar to Tan et al. (2021). First, we calculate this bulk velocity profile as the density-weighted average of the velocity field along the other two perpendicular axes (i.e. $\hat{x}$ and $\hat{y}$). Then, we subtract the bulk velocity profile along $\hat{z}$, which is normal to the hot/cold interface, from the velocity field to obtain the turbulent component. This turbulent velocity field allows us to compute density-weighted RMS values of this field along the axes perpendicular to the hot/cold interface normal (i.e. $\hat{x}$ and $\hat{y}$), to obtain 1D profile of all three components of turbulent velocity along normal to the hot/cold interface ($\hat{z}$). Fig. 3.5 shows an example of the calculated turbulent velocity profiles for a snapshot where the cooling rate has reached saturation, for different initial magnetic field orientations. There are other methods like Gaussian filtering (e.g. Brereton & Kodal, 1994; Adrian et al., 2000; Abruzzo et al., 2022a) to get these 1D profiles, but we find that the choice of method does not significantly influence the next steps, as shown in appendix 6.5.3.

Unlike Tan et al. (2021), we cannot select a particular direction that is untouched by shear or cooling inflow, as that direction can be aligned with the magnetic field. Hence, we have to calculate the turbulent velocity using different directions for different cases. In addition to that, the turbulent velocity component along the magnetic field can have some contributions from large velocity fluctuations along the magnetic fields, as Fig 3.5 shows. To get around this issue, we calculate the u' using the other two components perpendicular to magnetic fields, except in

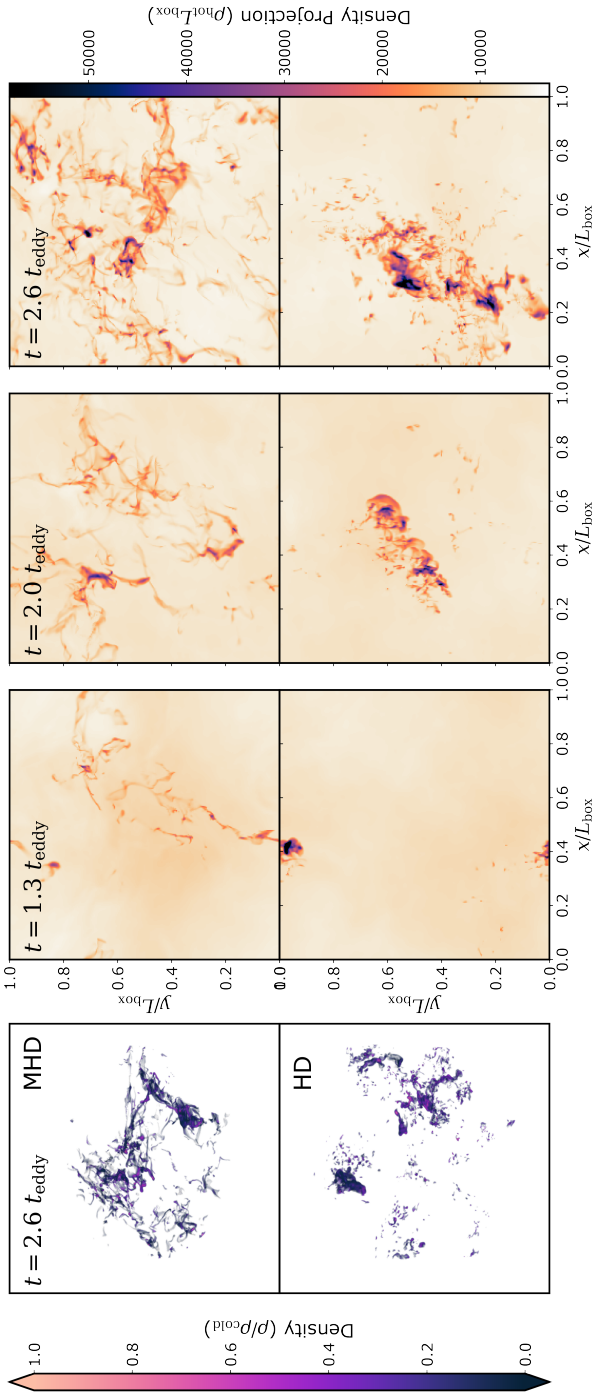

Figure 3.7: **Left column** Density rendering at $2.6t_{\rm eddy}$ after the cold gas cloud of size $310l_{\rm shatter}$ is introduced in a turbulent box with rms velocity of Mach 0.5, **2nd-4th column** Density projections of the same simulation, at 1.3, 2.0 and $2.6t_{\rm eddy}$ after the cold gas cloud is added. The **top row** panels are from the simulations with magnetic fields, and the **bottom row** panels are from the simulation without magnetic fields. These show the clear differences between the morphology of cold gas of gas with and without magnetic fields, while also showing the similarities in the overall evolution of the cold gas.

the case of $B_{\rm initial} \,||\, \hat{z} \,||\, \hat{n}_{\rm interface}$ (`Ma1_Bz`, `Ma10_Bz`). For the exceptions, where the large-scale magnetic field orientations are along the shear and normal to the interface (i.e. $\hat{x}$ and $\hat{z}$), we only consider the turbulent velocity component along the direction perpendicular to those directions, $\hat{y}$. In short, we use the following expressions to calculate the turbulent velocities in the different cases,

$$u'^2_{\hat{\rm B}_0||\hat{\rm x}}(z) = \frac{3}{2}\left(\langle u'_y\rangle^2_{\rm rms} + \langle u'_z\rangle^2_{\rm rms}\right) \tag{3.11}$$

$$u'^2_{\hat{\rm B}_0||\hat{\rm y}}(z) = \frac{3}{2}\left(\langle u'_x\rangle^2_{\rm rms} + \langle u'_z\rangle^2_{\rm rms}\right) \tag{3.12}$$

$$u'^2_{\hat{\rm B}_0||\hat{\rm z}}(z) = 3\,\langle u'_y\rangle^2_{\rm rms} \tag{3.13}$$

We, furthermore, checked that the turbulent velocity components used in the equations above are the ones that have similar profiles among themselves in each case, to ensure the isotropicity of the turbulent components, as shown in Fig. 3.5.

As in Tan et al. (2021), we consider the maximum of the obtained turbulent velocity profile as the turbulent velocity. We repeat this process for every snapshot and consider the mean of the turbulent velocity over the last $5t_{KH}$ as the saturated turbulent velocity (u') and the standard deviation as the error.

Note that throughout we denote the Damköhler number with $\widetilde{\rm Da}$ when the measured u' was used and Da when the theoretically expected u' from the Tan et al. (2021) was used.

3.2.4 Turbulence vs. cooling rates

We use the above obtained u' to check the relations in Eq. (3.9)-(3.10), as shown in Fig. 3.6. The top panel of Fig. 3.6 shows a scatter plot of the surface brightness and turbulent velocities calculated from the simulations. We find the respective strong and weak cooling scaling relation according to Eq. (3.9)-(3.10), regardless of the magnetic field strength and orientation. For a better comparison, we remove the $\widetilde{\rm Da}$ dependence and show the correlation in the bottom panel of Fig. 3.6. We clearly show that regardless of the initial magnetic field orientation or strength, the Eq. 3.9-3.10 holds true, even though the relations originally obtained for hydrodynamic systems (Tan et al., 2021). We also confirm that the method of u' calculation does not affect these results, as shown in Appendix 6.5.3, in Fig. 5.

3.3 Results: Turbulent box

In the previous section, we examined the TRML setup which is considered a more idealized version of Turbulent boxes (cf. §4.1), and found that magnetic fields can suppress the mixing in general, regardless of their initial orientation. If we follow this conclusion, one would expect the inclusion of magnetic fields in turbulent boxes to cause significant differences in the evolution of a cold cloud. This effect can manifest either as a change in the cold gas growth rates or a change in

the survival criteria. In this section, we show results from the "turbulent box" setup in which we place a cold gas clump of size $R_{\rm cl}$ in a turbulent medium, with a turbulent Mach number of $\mathcal{M}_{\rm s}$, either with (MHD) or without (HD) magnetic fields. We then look for the effect of the magnetic fields, not only on the growth rates and survival criteria but also on the morphology and overall behaviour of the cold gas.

3.3.1 Cold gas survival and growth

When cold gas is subject to turbulence, it can either be mixed away in the hot material or the mixed gas cools sufficiently fast to ensure the continuous survival of the cold gas. Gronke et al. (2022a) studied this effect using hydrodynamical simulations and found a relation between the critical value of $t_{\rm eddy}/\,t_{\rm cool,mix}$ (equivalently $R_{\rm cl}/l_{\rm shatter}$) for a given turbulent velocity. However, as we have shown in the last section, magnetic fields can suppress Kelvin-Helmholtz (KH) instability-induced mixing between the hot and cold phases in a TRML. Hence, one could expect a similar significant difference in a turbulent box with (MHD) and without (MHD) magnetic fields.

As mentioned in (cf. §4.1), the initial seed magnetic fields are such that plasma β ($= P_{\rm thermal}/P_{\rm magnetic}$) $\approx$ 100. But, due to the local dynamo effect (Schekochihin et al., 2001), the magnetic field gets amplified to reach equipartition with the turbulent kinetic energy by the end of the driving phase of the turbulence and before the cloud is introduced. We can use the fact that at equipartition, $\mathcal{M}_{\rm A} \sim 1$, and the relation between the sonic ($\mathcal{M}_{\rm s}$) and Alfvénic ($\mathcal{M}_{\rm A}$) Mach numbers as follows, to get an estimate of the final plasma β for a given $\mathcal{M}_{\rm s}$,

$$\beta \sim \frac{2}{\gamma \mathcal{M}_{\rm s}^2} \sim \frac{1}{\mathcal{M}_{\rm s}^2}. \tag{3.14}$$

This means the plasma β at equipartition, when the cloud is introduced, is $\approx$ 16, 4 and 1 for $\mathcal{M}_{\rm s}$ = 0.25, 0.5 and 0.9, respectively.

We study multiple of these turbulent box simulations at different turbulent velocities ($\mathcal{M}_{\rm s} \approx$ 0.25, 0.5 and 0.9) and with multiple cloud radii near the critical radii found in previous hydrodynamic studies (Gronke et al., 2022a). See §4.1 for an overview of the setup.

Fig. 3.7 shows one of the HD-MHD pairs of simulations with $\mathcal{M}_{\rm s} \approx 0.5$ and $R_{\rm cloud} \approx 310 l_{\rm shatter}$, where the upper row shows the simulation with magnetic fields (MHD) and the lower row shows the same simulation but without magnetic fields (HD). The leftmost column shows renderings of the number density with the view in the direction of one of the diagonals of the computational domain, at a time 2.6 $t_{\rm eddy}$ after the cloud is introduced. The three columns on the right show density projections of the same simulations as the first column, but at different times (1.3 $t_{\rm eddy}$, 2.0 $t_{\rm eddy}$ and 2.6 $t_{\rm eddy}$ after the cloud insertion). We can see that in both the HD and the MHD simulation the crude behaviour of the cold gas is similar. The cloud survives and grows in both simulations, and the overall amount of gas in the simulation box also looks roughly similar.

Fig. 3.7 also shows how the gas structure evolves. The cold gas seems to grow as it gets stretched, folded and transported by the turbulent motion in the hotter surrounding medium. We also see the

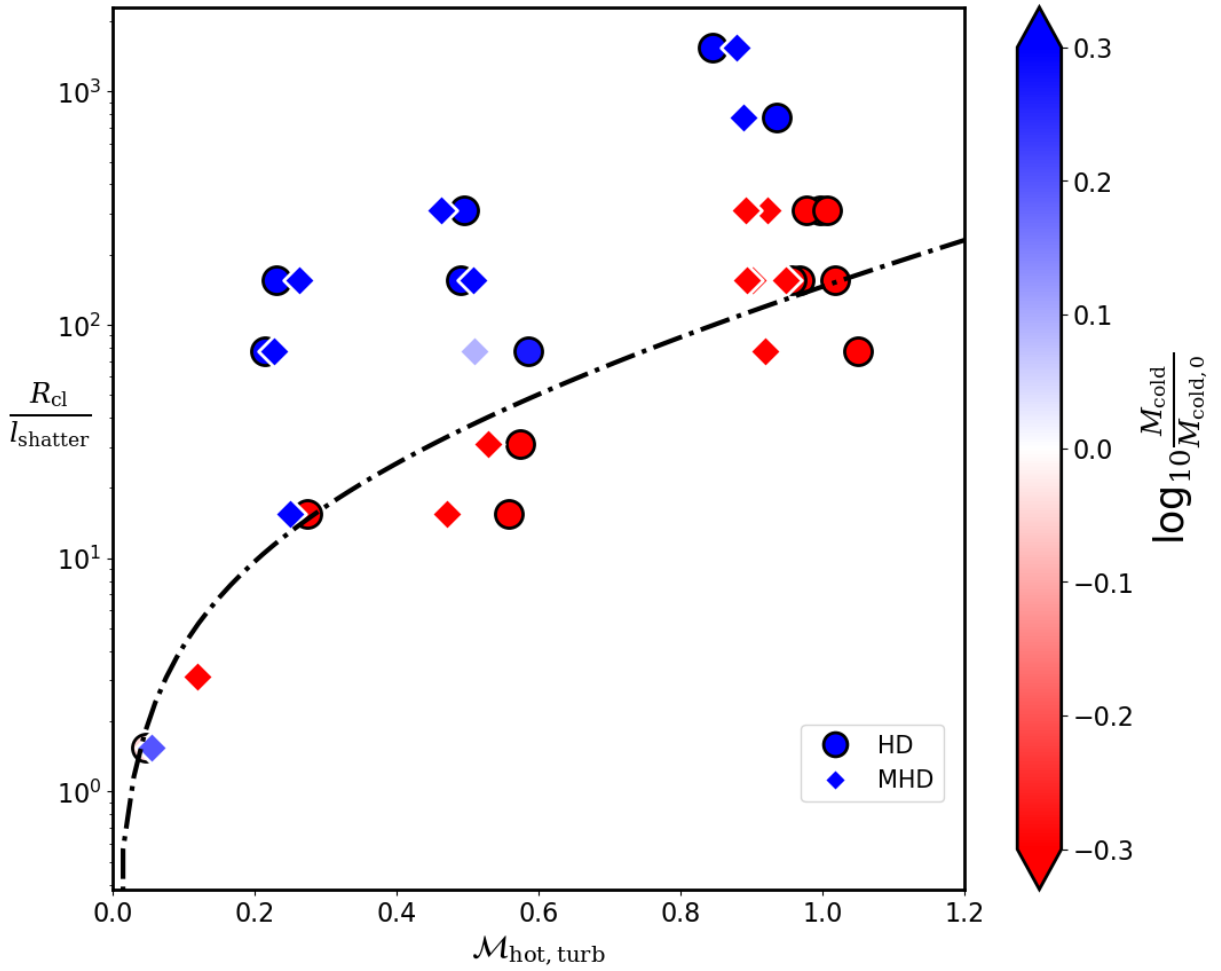

Figure 3.8: Survival or destruction of the cold gas in the different turbulent boxes. The dashed line is the survival criterion from Gronke et al. (2022a). This shows the surprising lack of difference between the survival criterion, with and without magnetic fields. The subsonic turbulent simulations agree well with the previously found survival criterion, with some deviation in trans-sonic turbulent boxes (c.f. § 3.3).

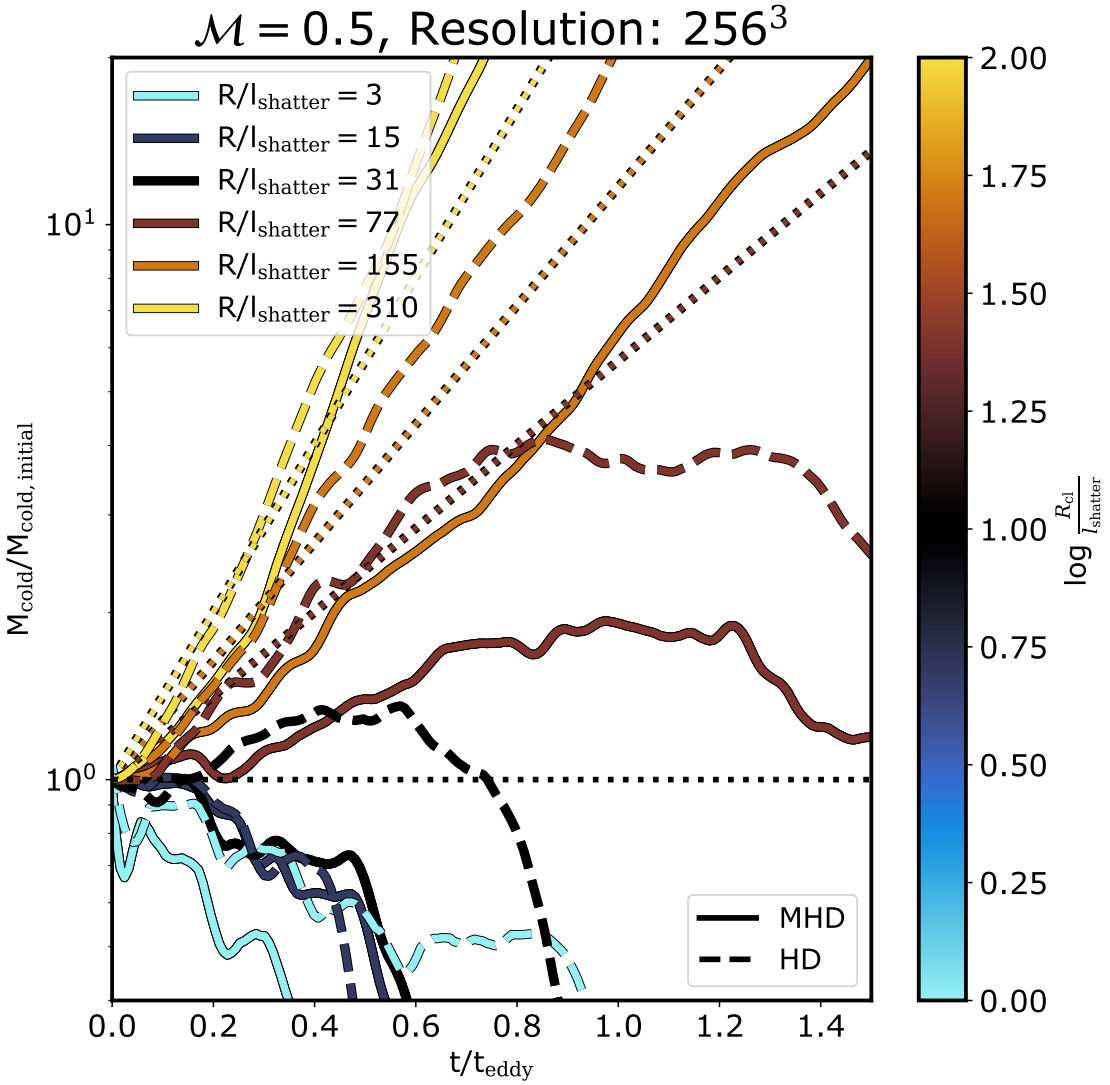

Figure 3.9: Cold gas evolution with time for different simulations initiated with varying sizes of cold gas cloud in turbulence with $\mathcal{M} = 0.5$. Solid lines show the simulations with magnetic fields, dashed lines show the hydrodynamic simulations and the dotted lines show the expected hydrodynamic growth rates from Gronke et al. (2022a). This shows that there are only marginal differences between the growth and destruction rates of the cases with and without magnetic fields, compared to the differences seen in the TRML simulations. The differences further diminish as we consider cases well within the survival regime.

difference in the general morphology of the cold gas in the two cases. The cold gas morphology is much more filamentary in the MHD simulation, while it is very clumpy and less dispersed in the HD simulation. We will discuss the morphology further in § 3.3.2.

Next, we check for the growth (or destruction) of the cold gas in all the turbulent box simulations. We define the cold gas mass as the total gas mass with temperature below 2 $T_{\rm floor} = 8 \times 10^4$ K and normalize the obtained value with the initial cold gas cloud mass. We take the obtained cold gas mass and check for survival or destruction at different Mach numbers and cloud radii. We determine the survival or destruction of the cloud using the final normalized cold gas mass values. The cases with final $M_{\rm cold}/M_{\rm cold,0} > 1 (< 1)$ are considered to show cold gas survival (destruction). We plot this survival or destruction for the different cases as a scatter plot in Fig. 3.8. It clearly shows the lack of difference in survival criteria between the pairs of simulations with (MHD) and without (HD) magnetic fields. This shows that the inclusion of magnetic fields does not affect the survival or destruction of the cold cloud. We also plot the survival criteria found by Gronke et al. (2022a) in Fig. 3.8, given as

$$\frac{R_{\rm cl}}{l_{\rm shatter}} = \mathcal{M}_{\rm hot,turb} \frac{t_{\rm cool,mix}}{t_{\rm cool,cold}} 10^{(0.6\mathcal{M}_{\rm hot,turb}+0.02)}$$

We find that this survival criterion works well for our subsonic turbulent simulations, but our transonic turbulent simulations seem to deviate slightly from this survival criteria. This could be due to the difference between subsonic, transonic and supersonic turbulence due to the presence of shocks in later cases, possibly destroying the clouds which would have survived in the absence of these shocks. Regardless, this does not affect our original conclusion about the lack of significant difference in survival (or destruction) between HD and MHD simulations, hence, we leave the investigation for causes of this discrepancy to future studies.

Another property which can have differences due to the inclusion of magnetic fields is the growth (destruction) rates of the cold gas. For that, we repeat the process of calculating the cold gas mass for each snapshot to obtain the temporal evolution of cold gas mass for all the different simulations with $\mathcal{M} = 0.5$, and Fig. 3.9 shows the same. We find a lack of drastic differences in the growth rates of the simulations that are well within the survival regime. We see slight differences (within a factor of 2) in simulations close to the transition regime, but it is still less than the order of magnitude differences seen in and expected from the TRML simulations. We also plot the expected growth curve for the surviving cases, using $t_{\rm grow}$ from equation (7) in Gronke et al. (2022a) and the mass growth equation for "fragmented" growth, $M_{\rm cold} = M_{\rm cold,0}\, e^{(t/t_{\rm grow})}$, as

$$t_{\rm grow} \equiv \alpha \chi \mathcal{M}_{\rm s,hot}^{-1/2} \left(\frac{R_{\rm cloud}}{l_{\rm shatter}}\right)^{1/2} \left(\frac{R_{\rm cloud}}{L_{\rm box}}\right)^{-1/6} t_{\rm cool,cold} \tag{3.15}$$

where, $\alpha = 0.5$ is a fudge factor.

This lack of significant difference in the cold gas mass evolution and survival criteria between turbulent box simulations with (MHD) and without (HD) magnetic fields is surprising, in view of the results from TRML simulations in the previous (cf. §3.2), where we found that the mixing rates are (highly) suppressed when magnetic fields are introduced into the same simulations. This dichotomy in the results can be confusing, and we discuss a possible solution to this in the discussion section (cf. §3.4.1).

3.3.2 Cold gas distribution and morphology

In the previous subsection, we showed how the presence of magnetic fields seems to have only a marginal effect on the cold gas mass growth and survival. Still, the magnetic fields are not entirely inconsequential. The magnetic fields can affect the gas flow and vice-versa due to effects like flux-freezing. We also saw in the above section that the morphology of the cold clouds is different between the simulations with (MHD) and without (HD) magnetic fields (cf. Fig. 3.7). In this section, we present such differences and quantify these differences in the morphology and distribution of the cold gas.

Turbulent transport has been a long-standing field of research in fluid dynamics. In a turbulent medium, the stochastic motions can transport, break, coalesce or mix the cold gas clouds. This results in a wide variety of cold gas cloud morphology. Gronke et al. (2022a) calculated the cloud size distribution in a hydrodynamically turbulent medium and found a power law, $N(>V) \propto V^{-1}$ (which has also been found in larger scale simulations, e.g., Tan & Fielding, 2023). As we saw a significant difference in the cold gas structure in Fig. 3.7, we check if the visual difference in cold gas morphology between HD-MHD simulations is reflected in cold gas size distributions.

We calculate the cumulative number distribution of the cold clumps in a set of HD-MHD simulations with $\mathcal{M}_{\rm s,hot} = 0.5$ and $R_{\rm cloud} = 310 l_{\rm shatter}$. Similar to Fig. 3.9, we define cold gas as the gas with temperature below $2T_{\rm floor} = 8 \times 10^4$ K and use feature labelling functionality in SciPy's (Virtanen et al., 2020) `ndimage` as the clump finding algorithm to identify the cold clumps. We determine the volume of the obtained clumps and use it to calculate the cumulative number distribution, shown in Fig. 3.10. We find that the distribution is well approximated by a power-law with slope -1, i.e. $N(>V) \propto V^{-1}$, while deviating at the two extremes of the volume range due to resolution limits at lower volumes and statistical under-representation at higher volumes. This matches the results from Gronke et al. (2022a). We also see that the number distribution does not show a drastic difference between the HD and MHD simulations, apart from a slight excess of small clumps in the HD simulation. This means the cold gas clumps in MHD simulation are not significantly smaller or larger in volume than its HD counterpart.

Even though the difference in number distribution is minor, Fig. 3.7 clearly shows significant morphological differences between the cold gas structure in HD and MHD simulations. Visually, the cold gas in MHD simulations has a much more filamentary shape, while it has a more clumpy cold gas morphology in the corresponding HD simulations. We quantify this filamentariness of the cold gas structures as the length of the longest "shortest path" possible within the clump.

To do so, we first identify the individual clouds, as done for Fig. 3.10, and create a "neighbourhood

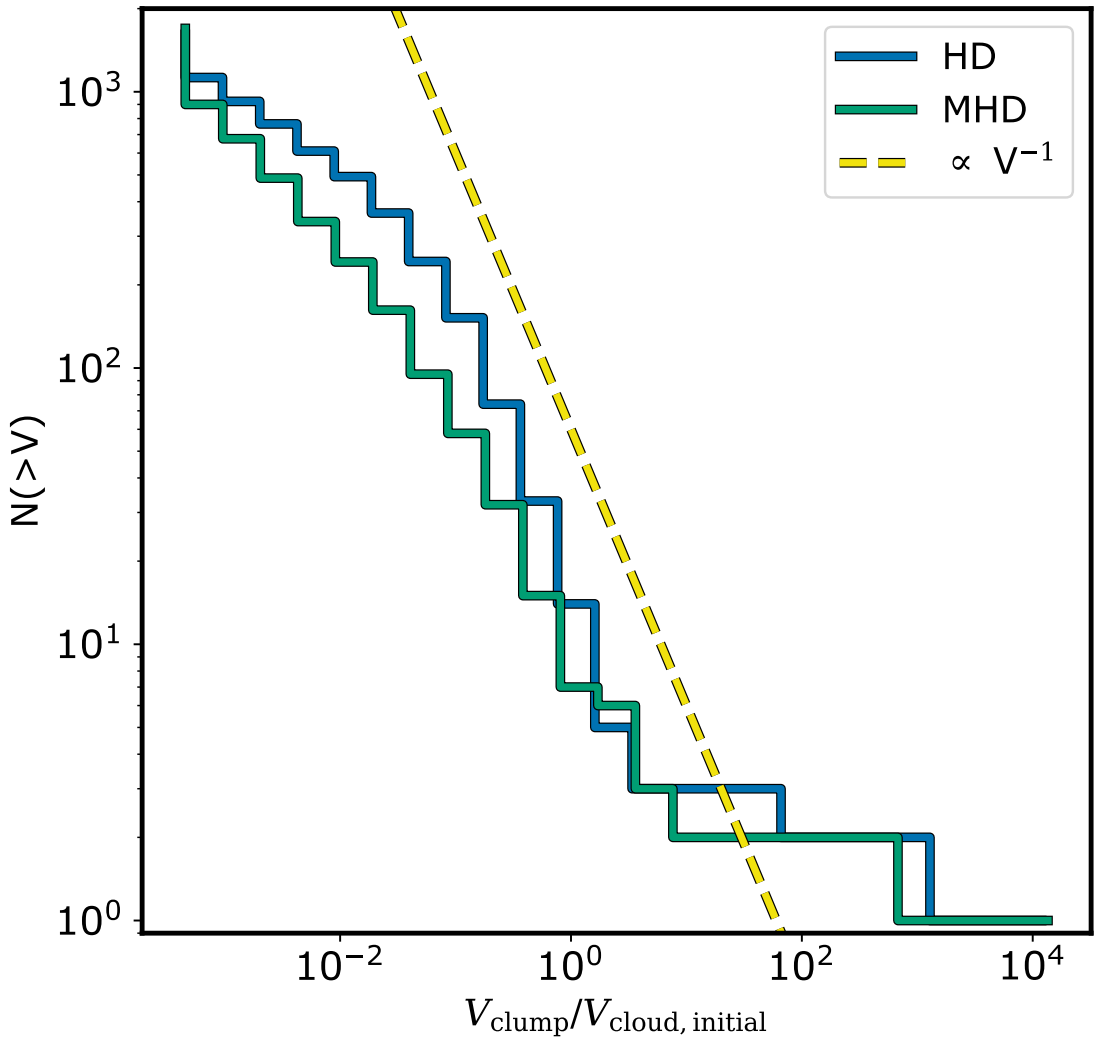

Figure 3.10: Cumulative number distribution for HD-MHD simulation pair with $\mathcal{M} = 0.5$ and $R_{\rm cloud} = 310 l_{\rm shatter}$. This shows the marginal difference in the overall distribution of clump sizes, and also that the distribution matches the distribution of $\propto V^{-1}$, found in previous studies.

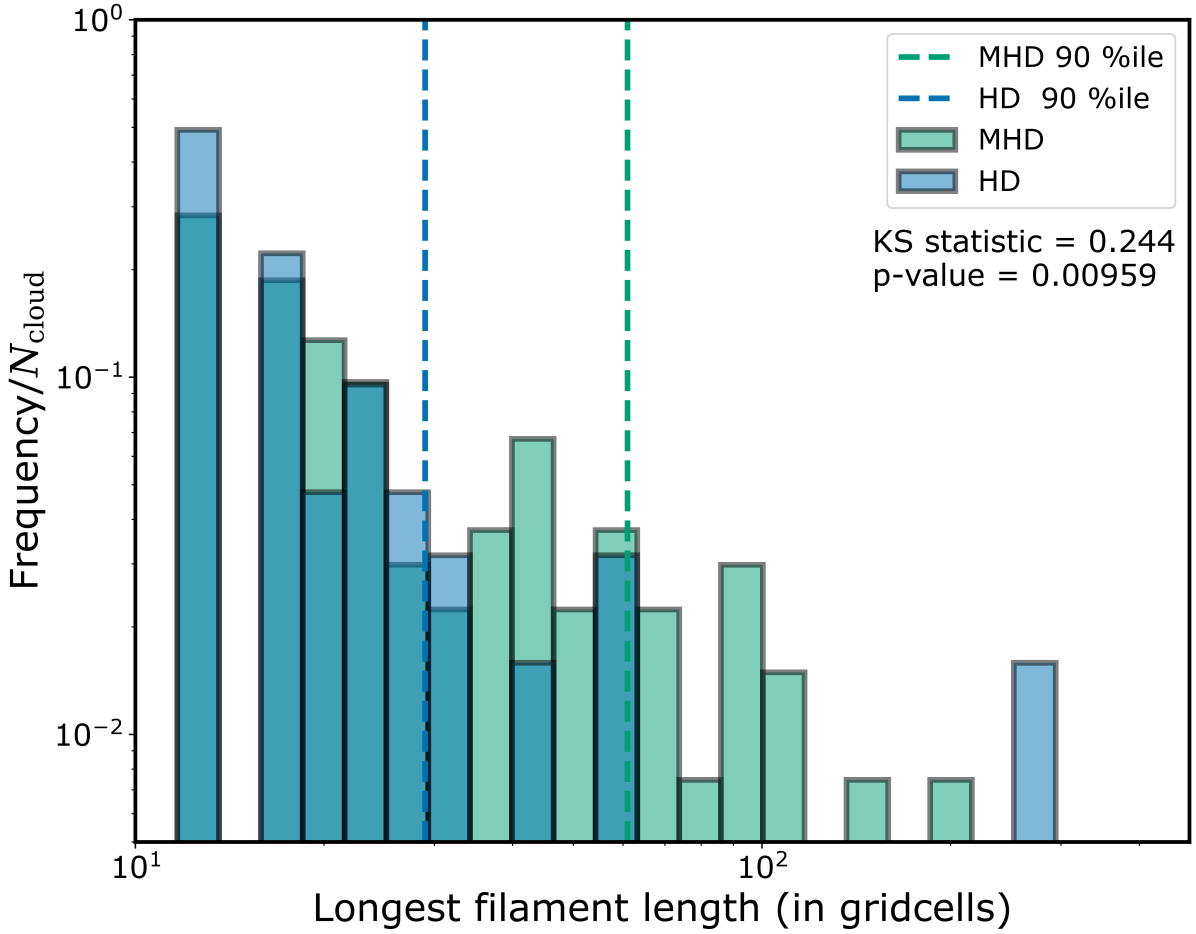

Figure 3.11: Histogram of longest shortest distance in the neighbourhood graph of every clump in a snapshot from the turbulent box at $\mathcal{M}_{\rm turb} = 0.5$, with and without magnetic fields. This figure gives a lower limit on the difference in the filamentariness of the cold gas clumps in the two cases. We find at cold gas clumps can get more filamentary in the presence of magnetic fields, by about a factor of 2.

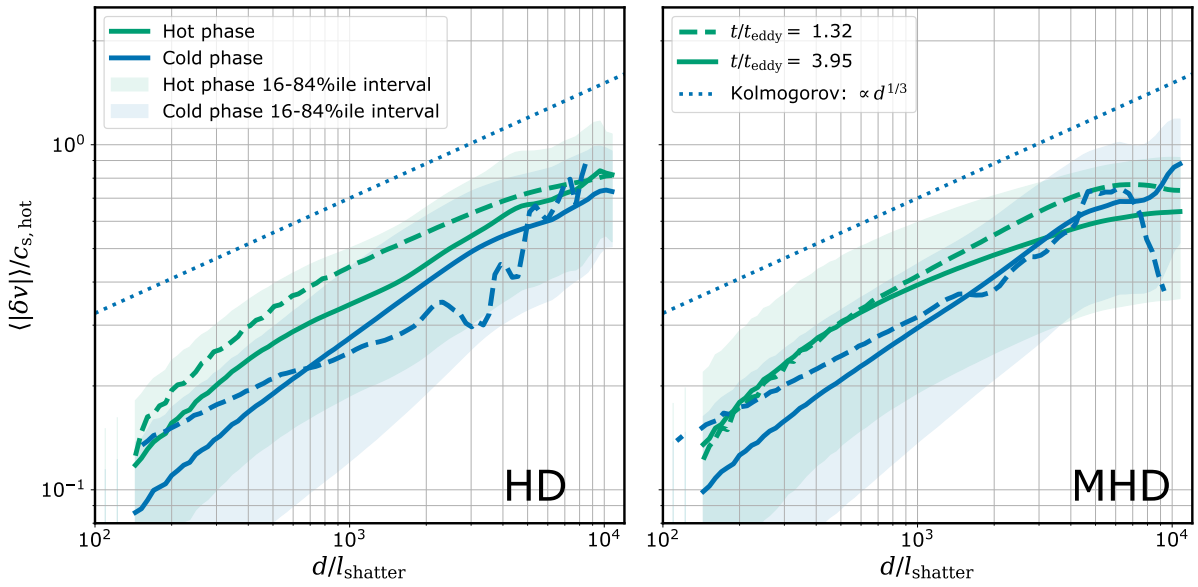

Figure 3.12: Velocity structure function (VSF) for hot (green line) and cold (blue line) gas phases in a set of simulations with (MHD) and without (HD) magnetic fields, at $\mathcal{M} = 0.5$ and $R_{\rm cl} = 310 l_{\rm shatter}$. The dashed and solid lines show the VSF at different times, $t = 1.32 t_{\rm eddy}$ and $3.95 t_{\rm eddy}$ after introducing the cold gas cloud. This shows the decreasing difference in VSF of the two phases with time, in both cases, which means that the two phases are kinematically well-connected. We also find a smaller early-time difference between the hot and cold gas VSF for the MHD simulation, indicating a better kinematic connection in that case.

graph" for each clump using an adjacency matrix. In this "neighbourhood graph", each gridcell inside the cloud is a node and two nodes are connected with an edge if the two share a face. We calculate the shortest path between every node in this neighbourhood graph, and take the longest from this list of shortest paths as the required longest "shortest path". As many of the largest clumps contain $\gtrsim$ 50,000 gridcells, we have to use a faster way which can give a close enough answer instead of using the brute force method. The slowest step of the method is the shortest path calculation among each pair of nodes. Hence, to speed up this step, we only consider every 4^{th} node to identify the two points with the longest "shortest path", and later recalculate the path using the full graph with all nodes to get the final length. This optimised method drastically reduces the number of path calculations and makes this analysis computationally feasible. We also find negligible differences between the full brute force method and the optimised method in our tests. This is because the points with the actual longest "shortest path" is usually in close vicinity, likely within 4 grid lengths, unless the reduced graph is drastically different, which is rare.

We repeat this process for each clump in the MHD and HD simulations with $\mathcal{M} = 0.5$ and $R_{\text{cloud}} = 310\ l_{\text{shatter}}$ and plot the histogram of the obtained longest "shortest path" in Fig. 3.11. We find that the 90%ile of this length distribution for MHD simulations is longer by a factor of 2 compared to the corresponding HD simulation. Assuming, a constant volume of a cylindrical cold gas clump, which is reasonable as shown in Fig. 3.10, an increase of 2 in length corresponds to an increase of ≈ 2.8 in the length-to-width ratio of the clump. This method under-quantifies the filamentariness of the clumps, as the connected filamentary structures that are shorter than the main filament are not included. A full tree-based filament analysis will be the ideal method for this analysis, but we leave the detailed study of filamentariness to future investigations.

We find that the p-value for the two length distributions in HD and MHD is lower than 0.05, which means we can consider the filamentariness of HD and MHD simulations to have different underlying distributions. The KS statistic quoted in Fig. 3.11 quantifies the difference between the two distributions and is linked to the p-value. The higher the KS statistic, the lower the p-value. As our number of samples is limited by the number of clouds in the simulation, we will need a bigger box and longer runtime to improve the confidence level of this conclusion.

So, we conclude that, even though the cold gas clouds in the MHD simulation are similar in volume and its distribution, compared to their HD counterparts, they are significantly more filamentary in their morphology.

3.3.3 Cold gas entrainment

In a multiphase environment, the motion of one phase can affect the motion of another via drag forces or mixing-induced momentum transfer (see, e.g., Gronke & Oh, 2020a; Tonnesen & Bryan, 2021a). This means the phases can be kinematically linked. In addition to that, due to flux freezing in the gas, the magnetic fields can increase the extent of this kinematic link. A good way to check for this is the first-order velocity structure function (VSF). It quantifies the average difference in velocities of gridcells separated by a given distance. The difference in the VSF of

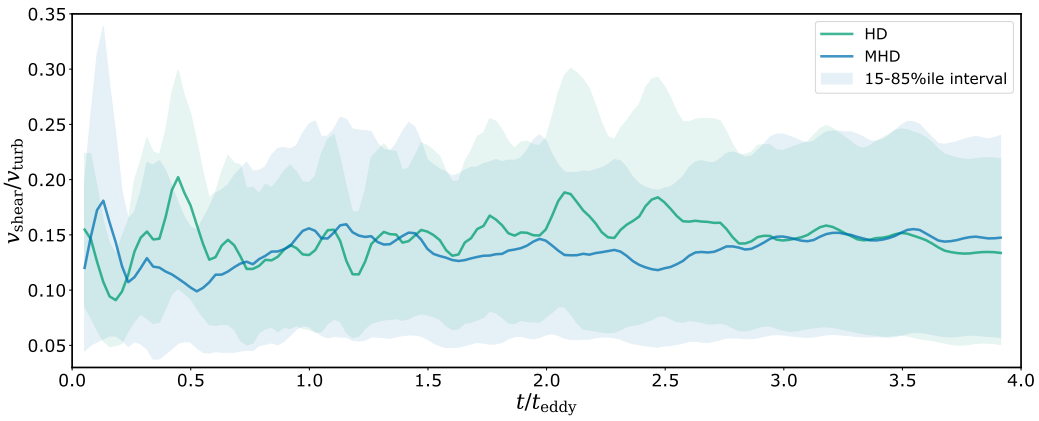

Figure 3.13: Evolution of average shear at clump boundaries in a set of HD and MHD simulations with $\mathcal{M} = 0.5$ and $R_{cl} = 310 l_{shatter}$ (same as Fig. 3.12). The shaded regions show the corresponding 15-85%ile intervals. The figure also shows the shear on the clump boundaries is about an order of magnitude lower than the turbulence velocity in the simulations. Also, on average, clumps in the MHD simulation seem to have a marginally lower, but very similar shear, in comparison to HD simulations.

the two phases corresponds to a lack of link in the kinematics between the two, while a smaller difference corresponds to a greater kinematic link.

We calculate the velocity structure function (VSF) of the hot and cold phases of gas in simulations with (MHD) and without (HD) magnetic fields at different times. First, we calculate pairwise distances and velocity difference magnitudes between each pair of gridcells. Again, due to computational constraints, we cannot use all cells for the pairwise calculations, so we randomly choose 2×10^4 gridcells for this calculation. Then, the list of pairwise velocity differences is binned according to the pairwise distances and we plot the average of the velocity differences in each bin as the VSF in Fig. 3.12. In general, we find a higher value of VSF in the hot gas than the cold gas for both the simulations at all different times in the evolution, as seen in other idealised simulations (Gronke et al., 2022a; Mohapatra et al., 2022a), and even some observations (Li et al., 2022).

For structure function calculations with steep slopes, Seta et al. (2023) had found a 2-point stencil to be unconverged and suggested the use of higher-order stencils. But, the slope of VSF for Kolmogorov turbulence (1/3) is shallow enough for a 2-point stencil to be converged. Hence, we use a 2-point stencil for all our VSF calculations.

This difference between the hot and cold VSF is much larger in HD simulation, on the left panel of Fig. 3.12, while in MHD simulations (right panel of Fig.3.12) the difference is much more subtle with both hot and cold VSF comfortably within 16-84 %ile range of each other. This shows that the cold phase is, in general, better entrained in MHD simulations compared to HD simulations. This is likely due to the flux-freezing of the magnetic fields that can result in a

more efficient kinematic connection between the hot and cold phases, as mentioned before. In presence of flux-frozen magnetic fields, any relative motion between the two phases encounters an enhanced drag force (McCourt et al., 2015). We also find that, even though the VSF of the different phases start off differently in HD-MHD simulations, they end up with very similar hot and cold VSF profiles in both cases. This means, given enough time, both simulations reach a similar extent of entrainment. Still, we do note that the entrainment is faster in MHD simulations, compared to HD, as shown by the faster decreases in the difference between hot and cold medium VSF in MHD simulations. This result indicates high entrainment of cold gas in hot gas, albeit an imperfect one. More importantly, it also points to a more efficient and faster entrainment of the cold gas in the presence of magnetic fields, with both HD and MHD simulations reaching an equivalent entrainment state, given enough time.

Further, we calculate the average shear at the cold gas clump boundaries for each snapshot in the HD and MHD simulations with $\mathcal{M} = 0.5$ and $R_{\rm cl} = 310 l_{\rm shatter}$ using `yt`(Turk et al., 2011). Fig. 3.13 shows the evolution of this average and the 15-85%ile interval of the shear at clump boundaries with time. We find that the shear at the clump boundaries is, in general, about one order of magnitude lower than the turbulent velocity in the simulation. This again indicates a high entrainment of the cold gas. Also, the slightly lower values of average and 85%ile value of shear for MHD simulations suggest a more efficient and faster entrainment in the presence of magnetic fields.

3.3.4 Magnetic fields strength and structure

In MHD simulations, magnetic fields are kinematically very important, as the gas flows affect the magnetic fields and vice-versa. Apart from affecting the kinematics, magnetic field structure can also affect other processes like thermal conduction and cosmic ray transport in an astrophysical media (e.g., Kempski et al., 2023; Ruszkowski & Pfrommer, 2023).

The turbulent motions can result in a local dynamo effect, leading to amplification of magnetic fields in MHD simulations. The extent of this amplification can vary in the different phases due to differences in the Alfvénic wave speed ($v_{\rm A} = B/\sqrt{\rho}$) and turbulent velocities. On top of the dynamo effect, the compression of gas during its cooling can also cause amplification during cold gas formation, due to flux-freezing.

To examine these differences, we check the distribution of magnetic field strengths in the different phases. We define the cold phase as the gas with temperature $T < 2T_{\rm floor} = 8 \times 10^4$ K, hot phase as $T > 0.5T_{\rm amb} = 2 \times 10^6$ K, and mixed gas as the gas with temperatures in between, i.e. 8×10^4 K $< T < 2 \times 10^6$ K. Fig. 3.14 shows the distribution of magnetic field strengths in these three gas phases, for simulations of three turbulent Mach numbers and with two cloud radii. The exact distribution has a non-trivial dependence on factors like the turbulent Mach numbers and cold gas growth rate. But in all cases, the mixed and cold gas magnetic strength distributions are centred at stronger magnetic fields, while the hot gas magnetic strength is centred around weaker magnetic fields, with the dashed line showing the equipartition magnetic field strength. This higher magnetic field strength in cold and mixed gases could be due to three possible processes:

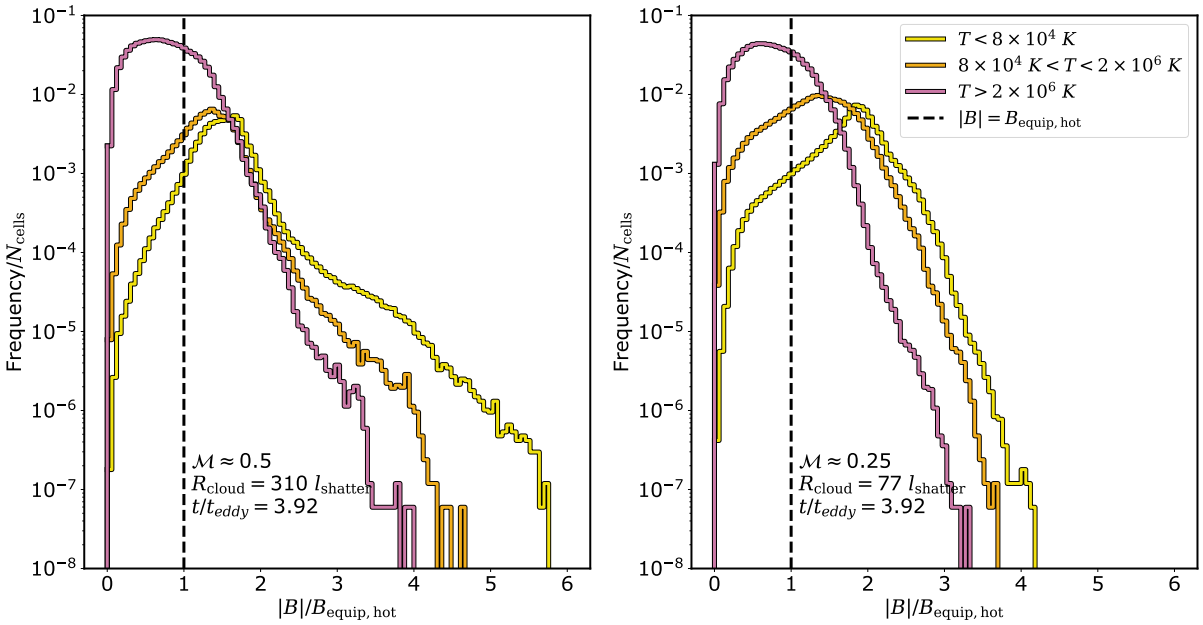

Figure 3.14: Histogram of magnetic field strength in gas within different temperature ranges, namely hot ($T > 2 \times 10^6$ K), mixed (8×10^4 K $< T < 2 \times 10^6$ K), and cold ($T < 8 \times 10^4$ K) gas, for two simulations where the cloud gas cloud survives, $t = 3.92 t_{\rm eddy}$ after its introduction. **Left** $\mathcal{M} = 0.5$, $R_{\rm cl} = 310 l_{\rm shatter}$. **Right** $\mathcal{M} = 0.25$, $R_{\rm cl} = 77 l_{\rm shatter}$. The dashed vertical line corresponds to the equipartition magnetic field strength, achieved in the hot ambient gas at the end of driving the turbulence. This shows that the magnetic fields are significantly amplified as the gas cools down to a lower temperature. We discuss the possible causes of this amplification in § 3.4.2.

turbulent local dynamo in the dense gas as the equipartition magnetic field is higher for a denser gas moving at similar velocities, flux-freezing accompanied by compression due to cooling, and magnetic draping caused by the relative motion between the dense gas and magnetic fields. We discuss more about these processes, and possible order of importance in the discussion section (c.f. §3.4).

Flux-freezing and the turbulent motions can result in a very tangled magnetic field structure. These tangled mangetic fields can have many consequences including reduced thermal conduction and slower cosmic ray transport. Presence of multiphase gas in a turbulent medium can add further complexity to the magnetic morphology, due the magnetic field strength distributions in different phases, as we show earlier in this section. To better understand this, we study the structure of the magnetic fields using magnetic field streamlines. We use `yt` (Turk et al., 2011) to calculate 10000 streamlines for 100 different streamline lengths ($l_{\rm stream}$) between $0.01 - 1 L_{\rm box}$. We calculate the displacement between the two endpoints of the streamlines (l), to get the ratio $l_{\rm stream}/l$. This ratio denotes the extent of entanglement of the magnetic field. A $l_{\rm stream}/l = 1$ indicates a perfectly untangled streamline, with higher values denoting a higher extent of entanglement. We repeat this

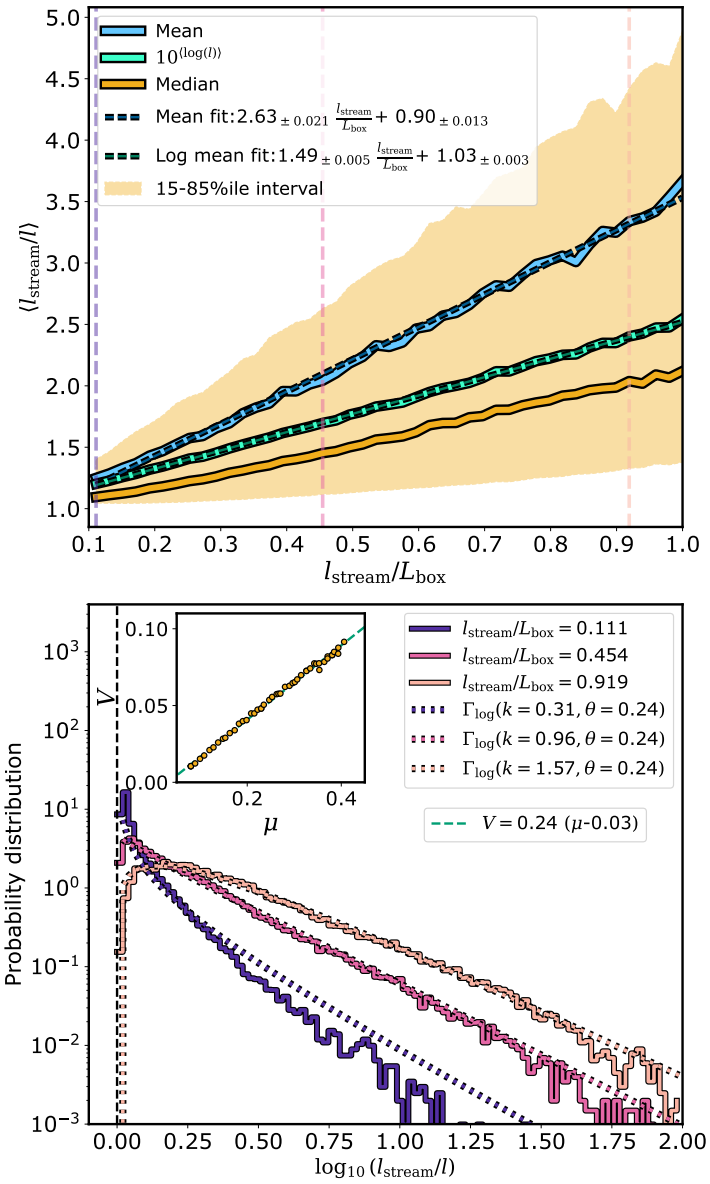

Figure 3.15: **Top** Average, median and $10^{\text{average of logarithm of}}$ entanglement, i.e. $l_{\rm stream}/l$ for different streamline lengths ($l_{\rm stream}$). The dashed lines show the corresponding best linear fits and the shaded region shows the 15-85%ile interval. The general trend of increasing entanglement for longer and longer streamline lengths indicate a fractal-like structure of the magnetic field lines, discussed further in § 3.4.2. **Bottom inset** Points denote the mean and variance of $\log_{10}(l_{\rm stream}/l)$ and the green dashed line shows the linear fit, $V = 0.24(\mu - 0.03)$. We use this relation to calculate the shown probability distribution. **Bottom** Solid lines show the probability distributions of different values of entanglement, $\log_{10}(l_{\rm stream}/l)$, for three values of streamline lengths. The dashed lines show the corresponding calculated Γ distributions, with the parameters mentioned in the legend. This shows the close agreement between the estimated and calculated probability distributions. There are some deviations for the probability distribution of small streamline length, which is discussed further in § 3.3.4.

process for different $l_{\rm stream}/L_{\rm box}$, and obtain distributions of the extent of entanglement ($l_{\rm stream}/l$) for each $l_{\rm stream}/L_{\rm box}$. We calculate the mean, median and mean of the logarithmic lengths in each $l_{\rm stream}/l$ distribution.

The upper panel of Fig. 3.15 shows the trend of mean, median, mean(log) and 15-85%ile interval for each $l_{\rm stream}/L_{\rm box}$ value. We find that all the metrics of ensemble value of the ratio $l_{\rm stream}/l$ increase linearly with $l_{\rm stream}/L_{\rm box}$. The upper panel of Fig. 3.15 shows the close approximation of the linear trend for mean and mean(log). This means the extent of the entanglement increases linearly with the length of the streamline. This property could be a sign of fractal-like behaviour of the field lines down to a certain threshold at small scales. We discuss this further in the discussion section (cf. §3.4). Note that the asymmetrically located 15th and 85th percentiles with respect to the median indicate a long tail towards longer $l_{\rm stream}/l$.

To show this more explicitly, we further choose three different streamline lengths, shown as vertical dotted lines in the upper panel of Fig. 3.15, and recalculate the streamlines for 10× more (10^5) starting points. We repeat the above mentioned process to calculate the $l_{\rm stream}/l$ values and calculate the probability distribution function of the entanglement, $l_{\rm stream}/l$, for these three values. We plot these probability distribution functions as solid lines in the bottom panel of Fig. 3.15. Even though we find some minor deviations at higher entanglement values due to insufficient counts caused by the reduced number of samples, the histogram at lower entanglement values is robust and fairly well converged with the number of streamlines.

Next, we attempt to find an analytic form for the different probability distribution functions (PDF) that we found earlier for the $l_{\rm stream}/l$, in the bottom panel of Fig. 3.15. We calculate the variance (V) and mean (μ) of $\log_{10}(l_{\rm stream}/l)$ and find a strong linear relation between the two as $V = 0.242(\mu - 0.031)$. For a Γ distribution, the variance and mean are given by $V = k\theta^2$ and $\mu = k\theta$, where k and θ are the shape and scale parameters, respectively. This means, our $V - \mu$ relation for $\log_{10}(l_{\rm stream}/l)$ matches the properties of a Γ distribution with $\theta = 0.242$, and $k = \mu/\theta = \mu/0.242$. Using the linear fit for the μ, shown in upper panel of Fig. 3.15, and the equation of the Γ distribution, a fit for the PDF of $l_{\rm stream}/l$ for a given $l_{\rm stream}/L_{\rm box}$ is a Γ distribution for $x = \log_{10}(l_{\rm stream}/l) - 0.031$ with $k \approx \log_{10}(1.5 l_{\rm stream}/L_{\rm box} + 1)$ and the $\theta = 0.242$ mentioned above.

The bottom panel of Fig. 3.15 shows the analytical form with the dotted lines. We find that the analytical form agrees very well with the PDF for long streamlines. But for shorter streamlines, at intermediate values of entanglement ($l_{\rm stream}/l$), it overestimates the PDF at intermediate entanglement values in the tail. This can be an indication towards a different underlying analytic form for PDF, which is equivalent to the Γ distribution at longer streamlines. Or, it can be due to resolution effects as they start to become more important for short highly entangled streamlines. We leave a deeper investigation of this for future studies.

As the charged particles tend to gyrate around and follow the magnetic field lines, analytic form for the magnetic field morphology, similar to the ones we find above, can be used in developement of models for their transport through a multiphase turbulent medium.

3.3.5 Synthetic absorption line spectra

As shown in the results section of turbulent boxes (cf. §3.3), we know that the morphology and details of kinematics can differ significantly between the simulations with (MHD) and without (HD) simulations. This difference can affect observational probes like predicted quasar absorption line spectra, because the column density and Doppler shift, the two major features of lines, can be affected by these differences in morphology and kinematics. We investigate these effects and their observational consequences in this section.

Fig. 3.16 shows the distribution of column densities of cold ($T < 10^5$ K) and intermediate/mixed ($10^5 < T < 10^6$ K) along one of the dimensions of the box for a set of HD-MHD simulation with $\mathcal{M}_{\rm hot,turb} = 0.5$ and $R_{\rm cloud} = 310\, l_{\rm shatter}$, same as Fig. 3.7 and 3.12. Note that because $l_{\rm shatter} \propto n^{-1}$ McCourt et al. (2018) the column densities simulated can be directly compared to observations. We still find that the column density histogram of the cold gas shows a greater extent of difference between the set of HD and MHD simulations, compared to the intermediate gas. We also see that most of the difference shows up at lower values of column density. So, we expect to see some difference between the HD and MHD simulations in observational probes of cold gas, for example, LOS absorption due to MgII, at lower equivalent widths.

In order to investigate the observational consequences of the differences between HD and MHD simulations, we create mock LOS absorption spectra using `Trident` (Hummels et al., 2017) on the same set of HD-MHD simulations as Fig. 3.7, 3.11, 3.12, and 3.16 ($\mathcal{M}_{\rm hot,turb} = 0.5$, $R_{\rm cloud} = 310\, l_{\rm shatter}$). Note that both of these snapshots have similar cold gas volume filling fractions.

We sample $\sim$ 10000 line-of-sight (LOS) spectra along one of the axes of the computational domain on a 100×100 grid. Due to the isotropic nature of the system, the particular choice of the axis should not affect the statistical inferences. We use a $\Delta\lambda = 0.1$Å (corresponding to a spectral resolution $R \equiv \lambda/\Delta\lambda \approx 28,000$) to create the mock absorption features for MgII at uniform solar metallicity. We select spectra which have a maximum absorbed flux of more than 0.1, over a continuum flux of 1.0, so that we are only considering LOS that pass through significant amounts of cold gas. We also exclude the spectra which have saturated features (with a flux less than 0.1) because they correspond to unnaturally large cold gas volume filling fractions, thus, leaving the number of components ill-defined. Next, we calculate the equivalent width (EW) for the MgII line complex and the number of absorption features for each LOS, as the area under the continuum and the number of minima in a spectrum, respectively. Fig. 3.18 shows the 2D distribution of EW and the number of absorption features for the HD-MHD simulations. We also show the fit obtained for the same quantities from observations of MgII absorbers in quasar spectra in Churchill et al. (2020). Interestingly, the more frequent regions of both the 2D histograms in Fig. 3.18 are close to the relation found in Churchill et al. (2020). We also find that, for the same EW, the MgII spectra of the MHD simulation tend to have a slightly higher number of absorption features, compared to the HD simulation, but these differences are marginal.

We repeated this exercise with 10x better spectrum resolution, which is much higher than that of the observed spectra, and we also included an additional CIV 1551Å line. The corresponding distributions, analogous to Fig. 3.18, are shown Fig. 7 and 8 in Appendix 6.5.3). In both cases,

the distributions change, but still roughly follow the observed curve.

3.4 Discussion

3.4.1 Mass transfer rates in a magnetized, turbulent medium

The two results for mixing layers and turbulent box simulations shown in Sec. 3.1.1 and Sec. 3.3, respectively, present a dichotomy. On one hand, TRML simulations show a significant suppression in the mixing of two phases, and on the other hand, the turbulent box simulations show the lack of a similar difference in mixing rate, as shown by the cold gas growth rates and survival criterion.

To resolve this, we need the answer to the question, *what is the primary mechanism of mixing of two phases?* The mixing happens when the multiphase structures get small enough to reach the "dissipation scale" where the molecular diffusion is fast enough to mix the two phases (Obukohov-Corrsin phenomenology; Oboukhov, 1949; Corrsin, 1951). There can be multiple ways to reach such small scales, and one of these is via vorticity. Vorticity or vortices can stretch, fold and transport, in other words, it "stirs" and stretches the structures, eventually reaching the small scales where molecular diffusion can take over and "mix" the two phases (Villermaux, 2019). In theory, this vorticity does not have to be part of turbulence, but in the high Reynold's number of fluids, as is the case in astrophysical mediums, the vortices generally become turbulent. This causes a faster stirring of the multiphase structures, and a more rapid increase in the surface area and decrease in structure width, resulting in more efficient diffusion. Hence, in an astrophysical medium, the main mechanism of mixing is expected to be turbulent mixing. In principle, the mixing should only depend on the turbulence and be independent of the source of turbulence.

In a Kelvin-Helmholtz or TRML setup, the initially structured vortices quickly give way to a turbulent mixing layer. The turbulence in this mixing layer is the key mechanism of stirring and mixing the two phases. This lead to this chain of processes: KH instability $\rightarrow$ Turbulence $\rightarrow$ Mixing. When magnetic fields are introduced in the system, depending on their orientation, they hinder the link between the KH instability and turbulence by slowing down the rate at which the turbulence in the mixing layer is driven. But as we show above, importantly, the magnetic fields do not affect the other link that connects turbulence with mixing. So, we expect to see a tight correlation between the turbulent velocity in the mixing layer and the extent of mixing/cooling that is occurring in the mixing layer, regardless of the magnetic field orientation or strength (cf. Fig. 3.6). Hence, we conclude that suppression of mixing in TRML simulations in magnetic fields is due to the reduced driving of turbulence in the mixing layer, which in turn leads to a reduced mixing of the two phases.

The situation is different in our turbulent box setup. There the system is the driven turbulence that cascades from the largest (box-size) scales to the smallest (gridcell-size) scales. This implies that u' is fixed and since the mixing and cooling rate only depends on u' directly, we obtain similar growth rates in the HD and MHD cases – explaining the unaltered survival criterion and mass transfer rates found (cf. Figs. 3.8 and 3.9, respectively).

We also find direct evidence that the turbulent, cascading u' is responsible for the mixing, and not the (also in the turbulent box present) hydrodynamical instabilities seeding smaller-scale turbulence. Firstly, the velocity structure functions of both the hot and the cold medium follow each other closely (cf. Fig. 3.12) indicating near perfect entrainment of the cold gas. Secondly, we also show explicitly the shear between cold and hot gas (c.f. §3.3.3) being small, i.e., the cold gas is well-entrained in the hot ambient gas. This means the shear is minimal, resulting in a lesser extent of turbulence in the mixing layer between the two phases. If solely the shear would be responsible for the mixing and cooling, we estimate the mass doubling time to be $\sim 5 t_{\rm eddy}$ for the turbulent box with $\mathcal{M} = 0.5$ and $R_{\rm cl} = 310 l_{\rm shatter}$, which is about an order of magnitude longer than actually found in the simulations (using the TRML scaling relations of Tan et al., 2021 for each surface cell on the cold gas clump).

In summary, we find the $u' \rightarrow \dot{m}$ relation to be universal in HD and MHD (and consistent with high-resolution TRML studies; Fielding et al., 2020; Tan et al., 2021). However, magnetic fields prevent instabilities to form in the mixing layer setup leading to a lower u' and thus to a decreased mass transfer rate. When the extent of turbulence is fixed by larger scales – as done in the turbulent box – the magnetic fields cannot suppress the mixing leading to comparable luminosities in the HD and MHD runs.

In realistic, astrophysical multiphase systems such as the ICM, CGM or ISM turbulence is also seeded on larger scales, then cascading downwards. In the ICM, for instance, AGN feedback is believed to play a dominant role in the stirring process leaving a characteristic imprint on the VSF (Li et al., 2022). Similarly, for the CGM where both (AGN and stellar) feedback processes as well as cosmological inflow act on $\sim$ 100 kpc scales 'stirring' the CGM (Chen et al., 2023a). The alternative 'shearing layer' picture might occur in multiphase systems where bulk flows are dominant such as galactic winds and cold streams; however, since also there non-negligible turbulent is present which mixing channel is dominant is still unclear (Schneider et al., 2020; Tan & Fielding, 2023; Rathjen et al., 2023).

3.4.2 Magnetic field amplification and morphology

We find that the magnetic field strengths in cold and mixed gas of our MHD turbulence simulations are higher than their equipartition values in the hot medium (c.f. §3.3.4). As discussed earlier, this higher value in the cold and mixed gas can be due to higher equipartition values in denser gas (as $B_{\rm eq} \propto \sqrt{\rho}$, with the caveat of assuming similar turbulent velocities in hot and cold medium, which we discuss later in the section), due to flux-freezing during compression from hot to cold medium (e.g. Sharma et al., 2010; Gronke & Oh, 2020a), or due to magnetic draping around the cold gas clumps (Dursi & Pfrommer, 2008; McCourt et al., 2015).

It is hard to disentangle these three processes as the extent of amplification in the simulation ($\approx 6 B_0$) can be achieved via all above the processes. The flux-freezing can cause an amplification up to $\chi^{2/3} B_0 \approx 22 B_0$, assuming an isotropic, isobaric collapse from $T_{\rm hot}$ to $T_{\rm cold}$ and conservation of magnetic flux. The local dynamo and magnetic draping can account for an amplification up to $\chi^{1/2} B_0 \approx 10 B_0$, assuming the amplification continues until equipartition is reached, i.e. $\mathcal{M}_{\rm A} \sim 1$,

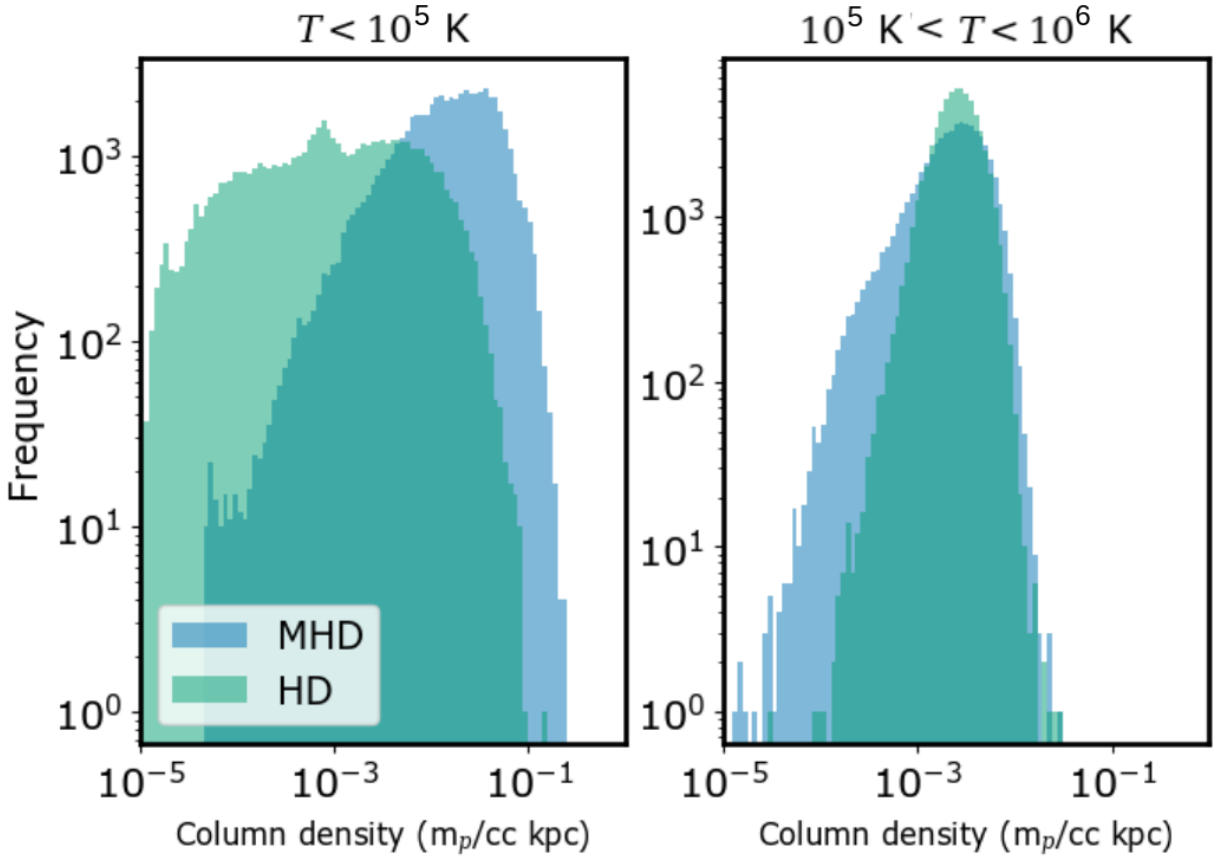

Figure 3.16: Column density distribution of cold ($T < 10^5$ K, left panel) and intermediate (10^5 K $< T < 10^6$ K, right panel) temperature gas in HD (in green) and MHD (in blue) simulations, with $\mathcal{M} = 0.5$ and $R_{\rm cl} = 310 l_{\rm shatter}$. This shows that the column densities for the above cases are within the observationally expected column densities for absorption spectra in a circumgalactic environment. It also shows that the lower end of column density distribution for cold temperature gas has a higher extent of difference between the HD and MHD simulations. This makes an absorption line tracing the cold gas a prime candidate for looking at observational differences between the HD and MHD simulations.

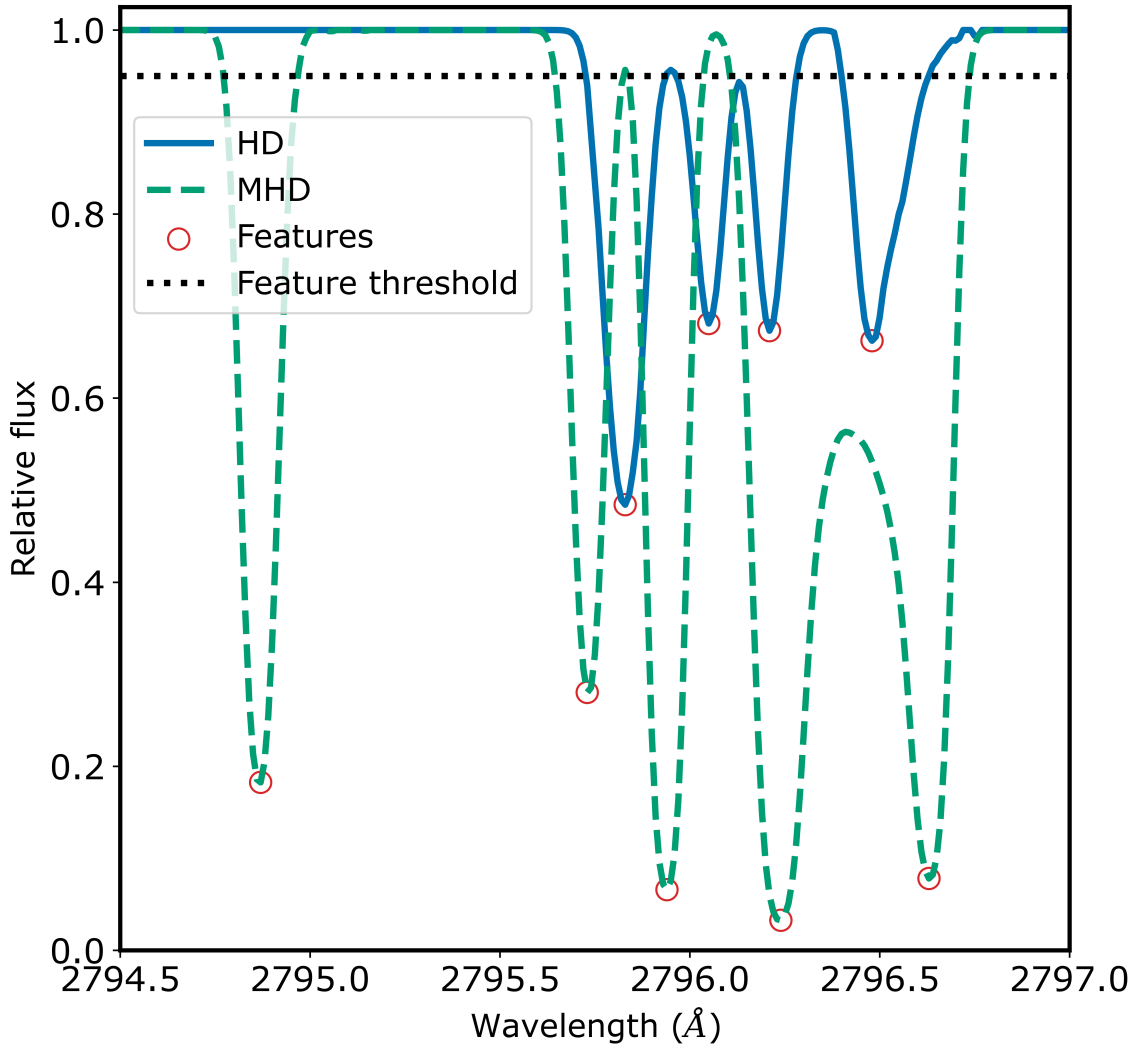

Figure 3.17: An example line-of-sight MgII 2796 Å absorption mock spectra with $\Delta\lambda = 0.01$Å, from the HD (blue solid line) and MHD (green dashed line) simulations with $\mathcal{M} = 0.5$ and $R_{\rm cl} = 310 l_{\rm shatter}$ (same as Fig. 3.16). The dotted black line shows the threshold of the minimum absorbed flux of a feature, and the red circles show the features that we consider for analysis. This figure is only for reference, as these are higher resolution spectra compared to the ones used in the analysis at $\Delta\lambda = 0.1$Å, which is closer to observational spectral resolution.

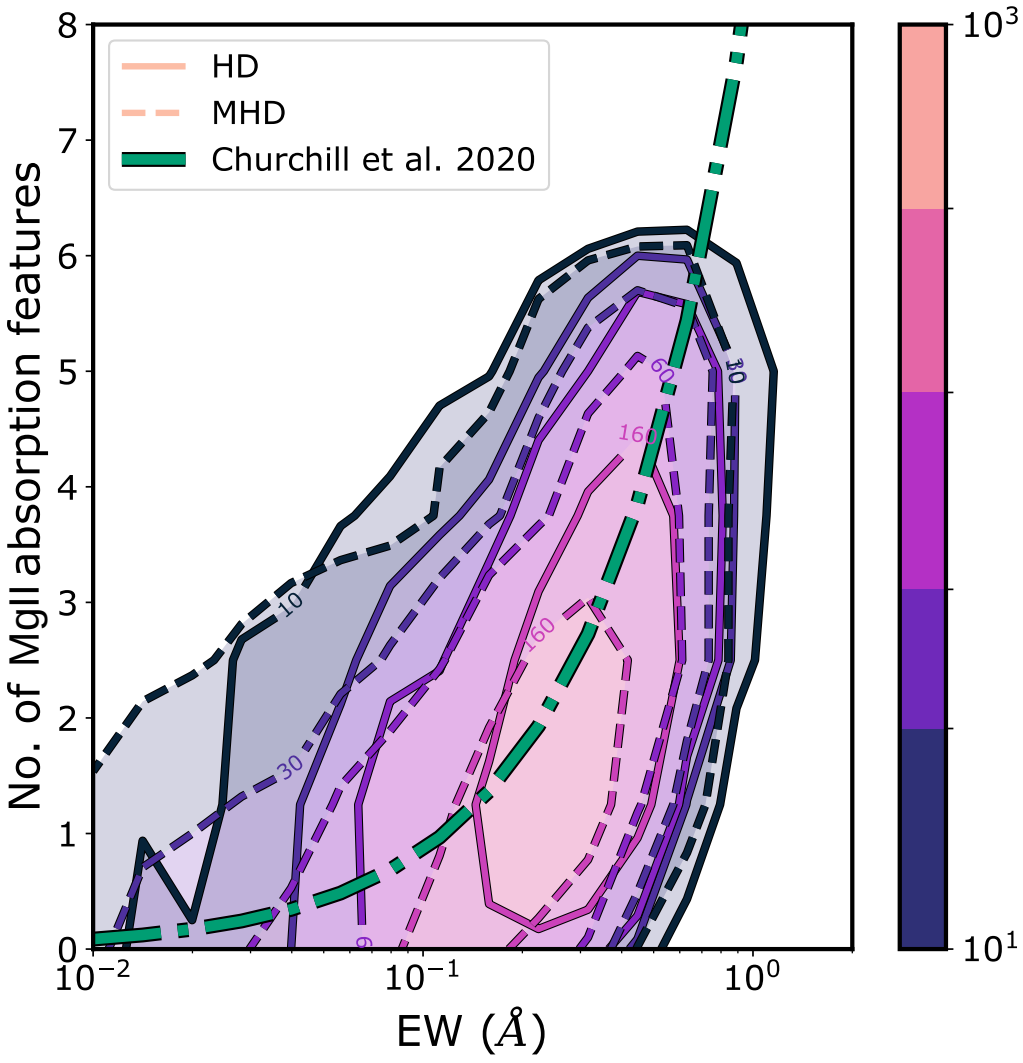

Figure 3.18: Contour plot of the 2D histogram of line-of-sight MgII absorption mock spectra in the number of absorption features vs. equivalent width space, for HD (solid contours) and MHD (dashed contours) simulations with $\mathcal{M} = 0.5$ and $R_{\rm cl} = 310 l_{\rm shatter}$ (same as Fig. 3.16 and 3.17). The dash-dotted green line shows the relation found in Churchill et al. (2020). This shows that there are only marginal differences in the overall distributions of HD and MHD simulations, despite the differences in Fig. 3.16. We also find that they agree quite well with the observed relations from Churchill et al. (2020).

and similar $v_{\rm turb}$ surrounding the cold gas means the new equilibrium magnetic field in the cold gas increases by $\sqrt{\rho_{\rm cold}/\rho_{\rm hot}}$. The flux-freezing causes a higher magnetic field in newly formed cold or mixed gas, and the other two processes amplify the existing magnetic field in the cold or mixed gas. As the magnetic fields reach equipartition values, they start to become stiff to the gas motions and start to back-react and influence the gas motions. This means the amplification value of $\chi^{1/2}B_0 \approx 10B_0$ at equipartition gives a rough upper limit on the amplification by all the processes. And, this agrees with our results in Fig. 3.14.

Out of the possible processes, turbulent local dynamo and magnetic draping are less likely due to a few reasons. For the magnetic fields to be amplified to $10B_0$ due to turbulent local dynamo, the turbulent velocity at cold gas cloud scales has to be similar to the hot gas turbulent velocity. But, due to the small scales of the cold gas clumps, the turbulent velocities at cloud scales will be much lower at $\sim v_{\rm turb}(l_{\rm clump}/L_{\rm box})^{2/3}$. Hence, the local dynamo will not be able to cause the calculated high amplifications.

For magnetic draping to amplify the fields, there needs to be a significant relative velocity ($v_{\rm rel}$) between the hot and cold gas, which generally is not the case, as we find a very similar VSF for hot and cold gas and low shear between the phases. This means, the $v_{\rm rel} \ll v_{\rm turb}$, hence the amplification of magnetic fields due to such process is probably insignificant. In addition, draping generally requires and leads to structured magnetic fields as they 'drape' around the clouds (Dursi & Pfrommer, 2008) – something we do not observe in our simulations.

This leaves flux-freezing and subsequent compression of magnetic fields as the only process that can cause significant amplification. Once, the amplification reaches a limit where the magnetic fields are stiff (trans/sub-Alfvénic), the gas continues to evolve along magnetic field lines, hence cold gas growth does not necessarily have to compress the magnetic fields.

Next, we consider the structure of the magnetic fields. In our study, we find that the extent of entanglement ($l_{\rm stream}/l$) of the magnetic field lines increases linearly with the length of the streamline (c.f. Fig. 3.15). This points to a structure where the longer the streamlines are, the more relatively small-scale structures are sampled. This is possible if the magnetic streamlines have a "fractal-like" structure that goes on until a fixed small-scale, which is the grid-scale in our simulations. Hence, the longer the streamlines are, the wider the range of perturbations that are included, leading to the increasing trend of entanglement.

This is analogous to the well-known problem of measuring a coastline, where the measured coastline length increases with decreasing length of the measuring stick. In this case, the roles are reversed. The measuring stick has a constant length, while we make the coastline longer. Assuming self-similarity, if we rescale this longer coastline, we effectively make the measuring stick smaller and we get back to the original coastline measuring problem. Let $\epsilon \propto 1/l_{\rm stream}$ be the effective length of the measuring stick. Hence, $L = l_{\rm stream}/l$ will be the rescaled coastline (streamline) length. We can use the relation found in Fig. 3.15 and the expression for the length of self-similar fractals, i.e. $L \propto \epsilon^{1-D}$ (Mandelbrot, 1967; Mandelbrot & Wheeler, 1983) to find the fractal dimension (D) of the magnetic field lines. We find that the magnetic field lines have

a fractal dimension, $D = 2$. Such naturally occurring fractal structures with a fractal dimension of 2 in 3D space are known to exist, with Brownian motion being one example (Falconer, 1985). Previous studies of TRMLs have also found fractal structures, for example, Fielding et al. (2020) show that the cooling layer in a TRML has a fractal dimension of 2.5, while Tan et al. (2021) find a slightly different value but note that measured values can differ.

We also find that a Γ distribution on logarithmic entanglement ($\log_{10} l_{\rm stream}/l$) matches fairly well with the computed distribution from the simulations for longer streamlines. The Γ distribution does a poorer job for very short streamlines, which might hint towards a transition to or altogether a different distribution for the entanglement. Or, this might possibly be due to higher resolution effects on the shorter streamlines.

We hope that this analytic form for magnetic field entanglement will be helpful in development of models for transport charged particles through magnetised multiphase turbulence.

3.4.3 Connection to observations

Multiwavelength studies now allow the joined observational study of multiphase astrophysical media. Of the many ways to probe the properties of the multiphase gas, the absorption lines are one of the widely used methods (e.g., Steidel et al., 2010; Crighton et al., 2015; Chen, 2017; Rubin et al., 2022). The different phases in the CGM of an intervening galaxy can deposit absorption features on the background quasar continuum. As the different sections of the absorbing medium can be moving with different velocities, these absorption features can be deposited at different Doppler-shifted positions near the line centre with different widths. Hence, the absorption features provide information about the kinematics and structure of the absorbing medium.

We find that there is no significant difference in mock absorption features of MgII 2796Å with and without magnetic fields. We, furthermore, show mock absorption spectra from both HD and MHD simulations agree with observed MgII absorption features from Churchill et al. (2003); Churchill et al. (2020), who established a relation between the number of 'absorbers' and the total equivalent width of the absorption. We also show in Appendix 6.5.3 that this agreement is approximately valid across spectral resolution and absorption lines.

As we found a universal clump mass distribution following $\mathrm{d}N/\mathrm{d}m \propto m^{-2}$ (cf. Fig. 3.10 and § 3.3.2) in both the HD and MHD cases (consistent with Gronke et al., 2022a), this suggests that the Churchill et al. (2020) is a direct consequence of the clump mass distribution, and similar probes might be used to constrain it providing an interesting avenue for future work.

In addition to absorption lines, there are many studies that investigate the emission lines from multiphase media. Li et al. (2022) look at the multiphase turbulence in the ram-pressure stripped tail of ESO 137-001 using different emission lines. They find a similar velocity structure function as ours (in Fig. 3.12) and many other simulations (Mohapatra et al., 2021, 2022a). This shows that both simulations and observations point towards a high extent of kinematic coupling between the different phases in astrophysical media.

3.4.4 Connection to previous studies

Due to the very high Reynolds number of astrophysical media, they are highly susceptible to turbulence. Hence, these media are expected to be turbulent in all the different scenarios in which energy is being injected into the medium, be it via supernovae, accretion or mergers. This turbulent nature of astrophysical medium has been studied before in previous studies (Schekochihin & Cowley, 2007; Lancaster et al., 2021; Hu et al., 2022; Li et al., 2022; Federrath, 2013; Elmegreen & Scalo, 2004; Wittor & Gaspari, 2020). There is also a plethora of studies that look at the different aspects of magnetohydrodynamic (MHD) turbulence, both in contexts related and unrelated to astrophysical mediums (see, e.g., review by Schekochihin, 2020).

Recently, there has been a significant focus on the multiphase nature of such turbulence, with or without magnetic fields. Previous studies like Mohapatra et al. (2022c) and Gronke et al. (2022a) have looked into hydrodynamic multiphase turbulence, while studies like Mohapatra et al. (2022b) and Mohapatra et al. (2022a) investigate the same with magnetic fields. And, studies like Seta & Federrath (2022) have looked at the evolution of magnetic fields in a multiphase medium. The key difference between these studies (except Gronke et al. (2022a)) and ours is the thermal instability of the ambient hot medium. In our setup, we mimic a heating source and turn off the cooling for gas hotter than $0.5T_{\rm amb}$, hence the ambient hot medium is thermally stable. Due to the absence of a thermally unstable ambient medium, mixing is the primary mechanism for creating the thermally unstable intermediate gas in our simulations. Still, results from our study will be relevant for the late evolution of simulations with thermally unstable hot medium, at which point, the further creation of cold gas is likely dominated by the cooling of mixed intermediate gas, rather than the less unstable hot medium. Importantly, the dynamics of a multiphase medium are quite different depending on which phase dominates the simulation domain. Since in most astrophysical media, the hot component is dominated by volume (see, e.g., Tumlinson et al., 2017, for the CGM), we choose to focus on the initial phase where this is also the case in our setup. Studying the full dynamic range, i.e., having a sufficiently large volume to sustain $f_{\rm V,c} \ll 1$ for an extended period of time while resolving the small-scale structure is unfortunately computationally prohibited.

Another similar system of turbulent boxes can be the stratified turbulent boxes, as studied by Mohapatra et al. (2021), Mohapatra et al. (2021) and Wang et al. (2023a). In such systems, the fundamental nature of turbulence can be different, depending on the extent of stratification. But, due to the presence of a similar hierarchy of structure and scales, we expect to see a similar growth or destruction of cold gas. In a stratified medium, there are two kinds of motions, one across the stratified layers, i.e. along the stratifying force ($F_{\rm strat}$), and the other along the layers, i.e. perpendicular to the $F_{\rm strat}$. The growth of cold gas within the layer itself would depend on the turbulent property in the layer, roughly perpendicular to $F_{\rm strat}$, while the transport and growth of cold gas among the stratified layers would depend on the gas motion along $F_{\rm strat}$. This kind of motion can be turbulent or buoyancy-driven where the cold gas falls "down". A stronger stratification can suppress the turbulent motions across the stratified layers, while the buoyant forces and motions can get amplified. Hence, even though some of our results are relevant to a stratified system, due to the complex interplay between these different flows, further study is needed to fully understand the rich physics in play.

Apart from explicitly turbulent boxes, turbulence shows up time and again in a lot of astrophysical simulations. An example of one such system are the 'cloud-crushing' simulations modelling cold gas-wind interactions. These set of simulations, designed to study multiphase galactic outflows, have been extensively studied (e.g., Klein et al., 1994a; Marinacci et al., 2010; Scannapieco & Brüggen, 2015; McCourt et al., 2015; Schneider & Robertson, 2017; Girichidis et al., 2021). Studies find that cold gas clouds that are bigger than a certain critical radius can not only survive against a fast-moving hot wind but even grow as they are being entrained in the wind (Gronke & Peng Oh, 2018; Li et al., 2020) with the details of the critical radius still under debate (Kanjilal et al., 2021; Farber & Gronke, 2021; Abruzzo et al., 2022a).

Initially, when hit with the hot wind, Kelvin-Helmholtz (KH) rolls are formed near the edges facing perpendicular to the wind, where the relative velocity is the highest. These KH rolls act as one of the initial sources of turbulent motions behind the cloud in its tail and cause mixing. As the cloud gets entrained and the shear decreases, this mechanism is unable to drive any further turbulence. Still, many of the previous studies mentioned above find that the cold gas mass continues to grow even after the cloud is entrained. This points to the presence of a substitute process for driving the turbulence at later times. The nature of this substitute process is still an open question, with some suggestions being the hot gas inflow due to cooling tail (Abruzzo et al., 2022a) or the pulsations of the cold clumps themselves (Gronke & Oh (2023), Gronke & Oh (2020b)). Regardless of the exact source of the late-time turbulence driving in the tails, as we show in this study, if the resulting turbulence in the tail is similar, the mixing and the cold gas evolution will be similar. Interestingly, studies with magnetic fields, like Gronke & Oh (2020a) and Hidalgo-Pineda et al. (2023) find a lack of significant difference between the growth rates of the cold gas with (MHD) and without (HD) magnetic fields. This result, in combination with what we find in our study, means that the presence of magnetic fields is not affecting the turbulence-driving mechanism. However, note that Hidalgo-Pineda et al. (2023) do find a significant difference in the survival criterion of clouds in a laminar flow with the inclusion of magnetic fields ($\sim$ 2 orders of magnitude with $\beta \sim 1$). To understand this, it is important to recall that the main difference to our turbulent setup is that for a wind tunnel setup the reduction of the drag time ($t_{\rm drag} \sim \chi v / r_{\rm cl} \sim \chi^{1/2} t_{\rm cc}$) in order to be comparable to the destruction time $t_{\rm cc}$ is sufficient for survival. Hidalgo-Pineda et al. (2023) attribute this reduction to a combination of draping (Dursi & Pfrommer, 2008; McCourt et al., 2015) and an altered χ due to compression of magnetic fields. On the other hand, in a turbulent setup, the cold gas is never fully entrained.

Another analogous set of systems is the Ram-pressure stripped galaxies, also called jellyfish galaxies. Similar to the cloud-crushing simulations, such galaxies have a multiphase tail. And, both simulations (Roediger & Brüggen, 2006; Tonnesen & Bryan, 2009) and observations (Boselli et al., 2022; Li et al., 2022; Luo et al., 2023) have shown the presence of turbulence in the tails of such galaxies. Results from this study will be quite relevant to the environment in such a tail, where the extent of the turbulence in the tail will dictate the overall evolution of the multiphase gas. Even though there are some strong parallels between jellyfish galaxies and cloud-crushing simulations, there are also many differences, like the difference in overdensity, presence of self-gravity, star-formation, feedback, etc. Hence, more detailed studies are required to fully understand these systems.

One of the major sources of turbulence in the circumgalactic medium (CGM) is the galactic outflows caused by the supernova feedback in the galactic disk. In our simulations, we vary the turbulent energy injection rate in order to get a similar turbulent velocity in both HD and MHD simulations. In a more realistic system, as in isolated galaxy simulations, the energy injection is dictated by the supernova rate, and indirectly by the star formation rate (SFR). Previous studies like Hopkins et al. (2019); van de Voort et al. (2021) found that changes to SFR, stellar mass and ISM mass due to the inclusion of magnetic fields are small. This means the energy injection rate into the CGM is roughly unaltered due to the inclusion of magnetic fields. As the magnetic fields in the CGM will act as an additional energy sink, the resulting turbulent velocity in the CGM due to the outflows is expected to be lower when magnetic fields are included. This reduced turbulent velocity in the CGM can be one of the possible reasons for the lower extent of mixing of metals in CGM, resulting in the stronger angular dependence of metallicity in simulations when the magnetic fields are included (van de Voort et al., 2021).

Closer to home, multiphase MHD turbulence is also seen in the solar atmosphere. The nature of MHD turbulence in the solar atmosphere is quite different, due to the very high magnetic field intensities, leading to sub-Alfvénic turbulence. In this case, the magnetic field tension is very high, and magnetic field lines are stiff to the gas flows. Still, as the mixing of multiphase gas is fundamentally tied only to the gas flows, and in the presence of the turbulent cascade of structures, our results suggest that the evolution of the multiphase gas would primarily be affected by the overall turbulent property. One of the sources for this turbulence can be the non-linear evolution of KH instability, which has been investigated in previous studies like Hillier et al. (2023).

3.4.5 Caveats / future directions

Below, we mention some caveats of the study and some directions that can be explored in future studies.

- *Resolution*: We use a lower resolution in our TRML simulations compared to that in Tan et al. (2021). This should not affect our results because, as Tan et al. (2021) show, it is enough to properly resolve the largest eddy to get converged cooling and mixing rates, which we do. Similarly, Gronke et al. (2022a) show that the growth rates and survival of cold gas clouds well within the survival regime, is converged if the cloud radius is well-resolved. As this criterion is satisfied in our simulations, we believe the results should be converged over similar resolutions. A lack of physical resistivity, viscosity or conduction means that in our simulations these are replaced by numerical resistivity, viscosity and conduction. A higher resolution will lead to a decrease in these but, as mentioned in section 3.4.1, the primary timescale in the problem is the turbulent eddy timescale of the largest eddy, which is unaffected by the resolution. This is similar to the analogous result in TRMLs which Tan et al. (2021) find in their study.
- *Turbulent driving*: In this study, we maintain a solenoidal to compressive driving ratio ($f_{\rm shear}$) of 0.3 across all turbulent box simulations. Previous studies find that different

$f_{\rm shear}$ in simulations can cause differences in the turbulent power spectrum (Federrath, 2013; Grete et al., 2018; Mohapatra et al., 2022c). But for our results, it is enough that the turbulent eddy timescale of the largest eddy is longer than that of smaller eddies, this remains unchanged with a different turbulent driving. The nature of turbulent driving can also affect the magnetic field amplification in MHD turbulence. The magnetic field in a turbulent box driven by an $f_{\rm shear} > 0$ is amplified much faster than a purely compressively-driven ($f_{\rm shear} = 0$) turbulent box. Still, this difference is well within an order of magnitude, and the results from our simulations should largely be applicable to the case of purely compressible turbulence.

- *Subsonic vs supersonic*: In this study, we restrict ourselves to the subsonic regime in both TRML and turbulent box simulations (to be more applicable to most astrophysical systems). Yang & Ji (2023) have looked at the behaviour of TRMLs with supersonic shear velocities, and find that for very high Mach numbers, the turbulent velocities in the mixing zone start to saturate with increasing shear velocities. This leads to a stagnation in the cooling rate, which is in agreement with our results from TRML simulations. Mohapatra et al. (2022b), in their simulations with supersonic turbulence, find that stronger turbulence can lead to higher compression and rarefactions in the medium. The stronger compression, along with shocks, might cause higher cold gas formation from the cooling of the ambient medium if the cooling is stronger than shock heating. This might also be valid for the supersonic multiphase turbulent boxes with non-cooling ambient medium, analogous to this study, where shocks passing through the medium might result in more efficient cooling of shocked intermediate gas regions. On the other hand, shocks in supersonic turbulence can also lead to the destruction of the cold gas, countering the additional cold gas formation. We see a hint of this more efficient destruction in our transonic ($\mathcal{M}_{\rm s} \approx 0.9$) turbulent simulations in Fig. 3.8, where the clouds larger than the subsonic critical radius get destroyed. Hence, the results in an analogous multiphase supersonic turbulent box might vary from the subsonic cases. This is further complicated by the presence of magnetic fields, where there are two kinds of shocks, and these can also lead to the amplification of the magnetic fields.

- *Super-Alfvénic vs Sub-Alfvénic*: Most of the large-scale astrophysical media like the ISM, CGM and ICM are usually super-Alfvénic ($\mathcal{M}_{\rm A} >1$) in nature. Even though, most of them start with a relatively high $\mathcal{M}_{\rm A}$, due to amplification of the magnetic fields the media reach a lower $\mathcal{M}_{\rm A}$, but usually not equipartition due to temporal evolution, and stay Super-Alfvénic. Similarly, in our simulations, we start well within the Super-Alfvénic regime but during the turbulent driving, we reach equipartition, before we introduce the cold gas cloud. That is, $\mathcal{M}_{\rm A} \gtrsim$ which is tran-Alfvénic to mildly super-Alfvénic. This setup works well to understand the above mentioned astrophysical media, but there are other multiphase environments like the Solar Corona where the medium is well within the sub-Alfvénic regime and our turbulent boxes may not be analogous anymore. On the other hand, our TRML simulations include simulations with trans-Alfvénic to mildly sub-Alfvénic motions. We find that our conclusion about the relation between turbulent velocity and mixing still holds. This means, given there are turbulent motions and a turbulent cascade, the mixing will only depend on the turbulent properties and not the presence or absence of the magnetic

fields. Still, we have not explicitly tested this in a turbulent box setup but can be a topic for future investigations.

- *Anisotropic conduction*: It is well-known that conduction is anisotropic in the presence of magnetic fields. But, as we do not have physical conduction in our simulations, the numerical conduction in the simulations is isotropic in both HD and MHD cases. While it has been shown by Tan et al. (2021); Tan & Oh (2021) that generally turbulent diffusion dominates over the laminar one (thus, explaining seemingly 'puzzling' convergence of larger scale studies such as ours), this has only recently been investigated with anisotropic conduction in an MHD setup by Zhao & Bai (2023a) who corroborate our results and find similar trend in suppression of cooling (see, however, Brüggen et al., 2023; Jennings et al., 2023, who included anisotropic conduction in their 'cloud-crushing' simulations and find similar mass growth rates as the pure hydro runs). This will add an additional layer of complexity, and can also be a future direction to explore.
- Other effects neglected in this study are *cosmic rays*, *viscosity*, and geometrical variations such as *stratification*. Our goal here was to study mixing in MHD in a simplified setup to which we will add additional layers of complexity in future work.

3.5 Conclusions

In this study, we investigate the influence of magnetic fields on the general phenomenon of mixing between the phases in a multiphase gas. For that purpose, we use two sets of simulations, turbulent radiative mixing layers (TRMLs) and turbulent boxes, with and without magnetic fields. First, we expand the parameter space for TRMLs explored in previous studies, to confirm the suppression of mixing for different cooling strengths (and hence different Damköhler numbers) at different initial magnetic field orientations. Second, we check for the effects of including magnetic fields in turbulent box simulations similar to Gronke et al. (2022a). We investigate for any differences in cold gas growth rates and survival. We also study the effects of magnetic fields on the morphology of the multiphase gas and magnetic fields and check for the subsequent observational consequences.

The following are the main conclusions from this study:

- We find that magnetic fields, in general, suppress the mixing in turbulent radiative mixing layers. The exception being some cases with magnetic fields are perpendicular to both shear and interface normal. This suppression is due to either amplification or the existence of strong magnetic fields along the shear, which stabilises the mixing layer.
- The inclusion of magnetic fields in TRML simulations only affects the generation of turbulence. We find that the relation between turbulent velocity in the mixing layer and mixing (hence cooling) rates from hydrodynamic simulations (Tan et al., 2021) still holds.
- We find that turbulent box simulations do not show significant differences in growth rates between identical cases with and without magnetic fields. Similarly, the survival criterion

of cold gas is also unaffected by the inclusion of magnetic fields.

- We show that this lack of difference, with and without magnetic fields, is in line with our results from TRML simulations where the relation between the turbulence and mixing is unaffected by the presence of magnetic fields. Given similar turbulent properties, we find that the mixing between phases in a multiphase medium will also be similar, regardless of the details of turbulence generation including the presence or absence of magnetic fields.
- We verify that the turbulent boxes with and without magnetic fields show similar clump size distribution ($N(> m) \propto m^{-1}$), which is in agreement with previous studies. But, we find that exact morphologies are different, with the clumps being more filamentary when magnetic fields are included.
- We find the cold phase to be generally well entrained with the hot phase with the MHD simulation reaching this entrained state faster than the HD one. This implies that 'shear-driven' mass transfer is not sufficient to explain the growth rates observed.
- We use mock absorption line observations of MgII to check the observational consequences of such differences in the morphology. While we do not find a significant difference between the statistics of the two cases with and without magnetic fields, both cases roughly agree with observations.
- We investigate the magnetic field structure in turbulent boxes. The cold gas phase has a higher mean magnetic field due to flux-freezing. We use the magnetic field streamlines to show the fractal nature of magnetic field lines and find an approximate distribution for the extent of magnetic field entanglement.

Our study reconciles the seemingly contradictory results of the effect of magnetic fields in turbulent mixing layers and a fully multiphase turbulent setup. This result also implies that the presence of cold gas in multiphase media can be explained through continuous mixing and cooling – and this channel is not hindered by the presence of magnetic fields. However, the topic of multiphase MHD turbulence still remains full of many unanswered questions, like the effect of cosmic rays, thermal conduction, viscosity, etc. which we hope to tackle in future work.

4 | MOGLI: Model for Multiphase Gas using Multifluid hydrodynamics

> A problem well stated is a problem half solved.
>
> — Charles Franklin Kettering

> The Copernican principle asserts that **I** do not occupy a unique or special position in the universe.
>
> — Arghyadeep Basu
> *First draft of his thesis*

This work has been resubmitted after the review process, to the Monthly Notices of the Royal Astronomical Society.

Multiphase gas dynamics is prevalent in various astrophysical media, from accretion disks to galactic outflows. There are observational (Tumlinson et al., 2017; Veilleux et al., 2020b), numerical and theoretical (McKee & Ostriker, 1977a; Donahue & Voit, 2022; Faucher-Giguère & Oh, 2023b) evidence for the multiphase nature of astrophysical media. The multiphase nature of the interstellar medium (ISM), circumgalactic medium (CGM) and intracluster medium (ICM) significantly affects the evolution of corresponding systems, like galaxies or galaxy clusters, via processes such as their baryon cycles or feedback processes (Veilleux et al., 2005; Péroux & Howk, 2020).

Recent observations have provided crucial insights into the structure of this multiphase gas, particularly in galactic halos. Studies have constrained the size of cold gas clouds in the CGM to be $\lesssim 10$ pc (Lan & Fukugita, 2017; Crighton et al., 2015; Schaye et al., 2007; Rauch et al., 1999; Chen et al., 2023b). This small-scale structure exists within large halos spanning tens to hundreds of kpc in radius (Tumlinson et al., 2017), creating a significant challenge for numerical simulations attempting to resolve these disparate scales – and leading to non-convergence of cosmological simulations in the halo gas content (e.g. Hummels et al., 2019; van de Voort et al., 2021).

Many theoretical studies use small-scale idealized simulation setups to better resolve and understand the small-scale gas structure. Some studies have focused on the in-situ formation of multiphase gas from the hot ambient phase via thermal instability (Field, 1965; Sharma et al., 2012; McCourt

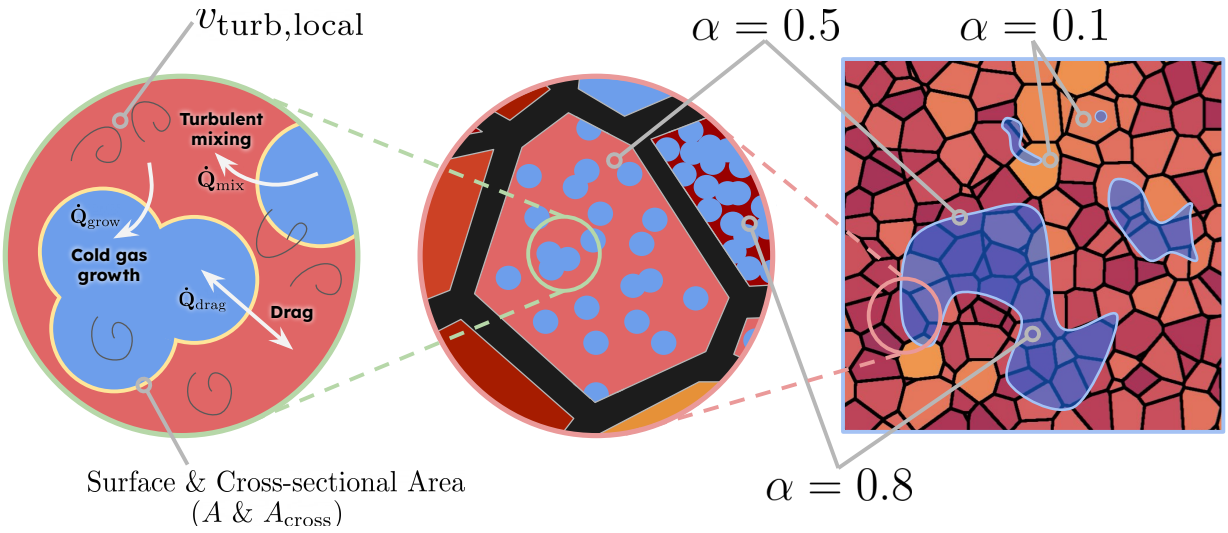

Figure 4.1: A schematic diagram showing the underlying picture of the multifluid method and the MOGLI model. The simulation domain on the right shows an example grid with different cold gas structures in blue, and marked volume-filling fractions (α). The zoomed-in view in the middle shows the model's assumption of the underlying cold gas structure, as numerous spheres. Zooming in further, the left panel shows the different interactions in the MOGLI model, along with other contributing variables, like the local turbulent velocity ($v_{\rm turb,local}$).

et al., 2012), and the effects of turbulence (Audit & Hennebelle, 2005; Mohapatra et al., 2022b), magnetic fields (Sharma et al., 2010; Ji et al., 2019), metallicity (Das et al., 2021a), density perturbations (Choudhury et al., 2019), rotation (Sobacchi & Sormani, 2019), cosmic rays (Butsky et al., 2020), and stratification (Mohapatra et al., 2020; Wang et al., 2023b). Other studies have examined the evolution of cold gas through mixing and subsequent cooling of the mixed intermediate temperature gas, particularly through cloud-crushing simulations where cold clouds are mixed and accelerated by hot outflow winds (e.g. Armillotta et al., 2016; Kanjilal et al., 2021; Abruzzo et al., 2022a; Hidalgo-Pineda et al., 2023) or cold streams flowing through a hot halo (e.g. Mandelker et al., 2020; Ledos et al., 2024).

Across these small-scale studies, it has been found that resolving length scales as small as sub-parsec is crucial for achieving convergence in even the most basic properties, such as the mass distribution across different phases (McCourt et al., 2018; Gronke & Peng Oh, 2018; Gronke et al., 2022b). This point has also been reiterated in larger scale simulations (Tonnesen & Bryan, 2021b; Tan & Fielding, 2023; Warren et al., 2024). However, accurately simulating these multiphase media in large-scale simulations, which are required to capture the dynamics and energetics of large-scale flows(Bustard et al., 2016; Fielding & Bryan, 2022; Nguyen & Thompson, 2022; Smith et al., 2024), and draw reasonable observational conclusions, remains a significant challenge due to the wide range of scales involved. For example, properly resolving the observed cold gas structures within a single galactic halo would require a resolution that remains computationally infeasible even for next-generation supercomputers.

There have been many approaches in astrophysical simulations to address this challenge through 'subgrid models' that incorporate processes occurring below the resolution limit. Notable examples include models for unresolved turbulence (Schmidt et al., 2006b; Schmidt & Federrath, 2011; Scannapieco & Brüggen, 2008), supernova feedback (e.g. Rosdahl et al., 2017; Martizzi et al., 2016), and star formation (e.g. Federrath & Klessen, 2012). Previous studies, such as Huang et al. (2020) and Smith et al. (2024) (cf. § 4.5.3 for an overview of previous multiphase subgrid models), have used Eulerian-Lagrangian methods for subgrid treatment of multiphase galactic outflows, where cold gas clouds are treated as particles interacting with the surrounding hot gas. Another possible approach is an Eulerian-Eulerian method, known as the 'multifluid' method.

The multifluid approach has been successfully applied to multiphase flows in various terrestrial contexts, including meteorology, combustion processes, and water flows. By tracking multiple fluids on the same grid, these methods allow for explicit representation of interactions between different phases (Prosperetti & Tryggvason, 2007). Recently, Butsky et al. (2024) implemented a subgrid model with a second pressureless cold fluid for unresolved cold gas clouds. In this study, we explore a different route by using an alternative implementation of the two-fluid method in the astrophysical code `AREPO` (Springel, 2010; Weinberger et al., 2020) by Weinberger & Hernquist (2023a) to create a subgrid model. Our approach advances the multifluid framework by allowing for arbitrary volume filling fractions of each fluid, the inclusion of physically motivated coupling terms between the phases, and a thorough testing against resolved multiphase simulations.

A major motivation behind the creation of a model with distinct physically-motivated and verified components is to make it usable for multiphase astrophysical systems in general. Although, different systems might need some setup-specific additions or modifications for numerical reasons, but the physical core of the model developed in this study and verified across a wide parameter space will still stay applicable, just like the physical theories that it draws upon. As the advances in computing resources will enable large-scale simulations to reach higher resolutions such simulations to start to better resolve the larger-scale cold gas structures. But, it will be insufficient to resolve the fractal-like smaller scale structures and physics. In such a regime, MOGLI will be applicable throughout the astrophysical gas. For instance, in the CGM or ICM, where it can keep track of the large regions in which the volume filling fraction of the cold phase is small (see, e.g., McCourt et al., 2018, and references therein) while also being able to model, e.g., resolved filaments feeding into the galaxies in which the cold gas is dominant (Dekel et al., 2009; Mandelker et al., 2020).

This paper is structured as follows. In § 4.1, we describe the numerical setup used to implement and validate our subgrid model, titled MOGLI. In § 4.2, we list and explain the ingredients that go into MOGLI before validating it in § 4.3 and § 4.4 using Kolmogorov scaling and local velocity gradients-based estimates for local turbulent velocities, respectively. We discuss these results in § 4.5 before we conclude in § 4.6. The visualisations related to this study can be found here.[1]

[1] http://hiteshkishoredas.github.io/research/mogli_subgrid.html

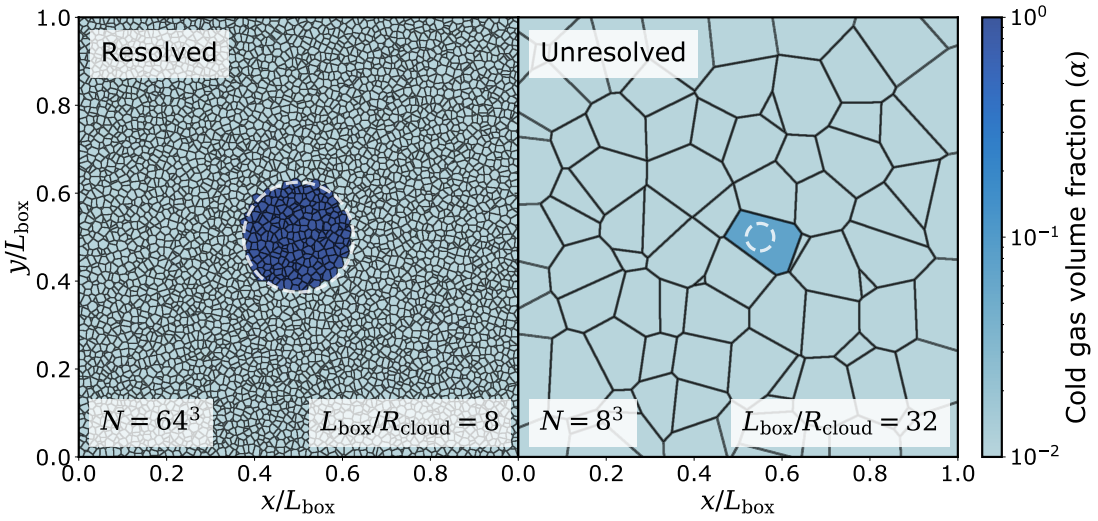

Figure 4.2: Initial cold fluid volume fraction slices for MOGLI simulations with resolved and unresolved cold gas clouds. The left panel shows an example of a resolved cold gas cloud with 64^3 cells and $L_{box}/R_{cloud} = 8$, where the cloud is bigger than the grid cells and grid cells inside the volume of the cloud have an $\alpha' = 1 - \alpha_{floor}$. On the other hand, the right panel shows the initial cold fluid volume fraction for MOGLI simulation with an unresolved cold gas cloud, with 8^3 cells and $L_{box}/R_{cloud} = 32$. As the cold gas cloud is unresolved, the volume fraction in the cell is set to $\alpha_{floor} + V_{cloud}/V_{cell}$, where V_{cloud} and V_{cloud} are the cloud and grid cell volumes. In both cases, the cells without any cold gas have a volume fraction, $\alpha' = \alpha_{floor} = 10^{-8}$. The dashed circles show the corresponding cold gas cloud size in the simulations.

4.1 Numerical Setup

We use two simulation setups: the high-resolution resolved single-fluid setup using `Athena++` (Stone et al., 2020b) and the analogous MOGLI simulations using multifluid `AREPO` (Springel, 2010; Weinberger et al., 2020) framework from Weinberger & Hernquist (2023a) with our new subgrid model MOGLI implemented.

4.1.1 Turbulent box simulations

We initialise a cubic computational domain, filled with isobaric hot gas of constant density, ρ_{hot}, at a temperature, $T_{hot} = 4 \times 10^6$K. Subsequently, we drive turbulence in this box at the largest scale, i.e. the box size (L_{box}), using the Ornstein-Uhlenbeck (OU) process (Eswaran & Pope, 1988b; Schmidt et al., 2006b) to reach a given turbulent velocity (v_{turb}) at steady-state. We let the turbulence driving proceed for about $7t_{eddy}$, where $t_{eddy} = L_{box}/v_{turb}$ is the eddy-turnover timescale. For the turbulence driving, we set the correlation timescale to $\sim t_{eddy}$, the driving timescale to $0.001t_{eddy}$ and the solenoidal to compressive fraction, $f_{sol} = 0.3$. Note that during the turbulence-driving of the initialisation phase, there is no radiative cooling in `Athena++` runs, and only a single fluid in MOGLI runs.

At the end of the initialisation phase, we restart the simulation after introducing a dense cold gas cloud with a radius $R_{\rm cloud}$, overdensity $\chi = 100$ and temperature $T_{\rm cold} = 4 \times 10^4$K, in the centre of the box. The introduction of cloud differs between the single-fluid `Athena++` and multifluid MOGLI runs, and the details are explained in Sec. 4.1.2 & 4.1.3. During the turbulence-driving in the initialisation phase, the temperature of the hot gas increases due to turbulence heating. Hence, before introducing the cloud, we rescale the temperature of each cell by a constant factor, to get the average temperature back to $T_{\rm hot}$. Due to the subsonic nature of turbulence, we find that the abrupt change in temperature does not have a noticable effect on the velocity and density distribution. We also repeat this two-step process, turbulent driving and the addition of cold cloud, with different random seeds for the turbulence driving to probe the stochasticity of the results.

4.1.2 Resolved single-fluid

For simulations with `Athena++` (Stone et al., 2020b), we use the default HLLC solver with Piecewise Linear Method (PLM) on primitive variables, RK2 time integrator, adiabatic equation of state (EOS) and cartesian geometry. Similar to Das & Gronke (2024b), we use the CIE cooling curve from Wiersma et al. (2009) at solar metallicity and implement the Townsend (2009b) radiative cooling algorithm with a 40-segment power-law fit on the cooling curve for calculating the radiative losses. We stop the cooling and enforce a temperature floor at $T_{\rm floor} = 4 \times 10^4$K.[2]

We include radiative cooling for one set of simulations (radiative mixing) and do not have radiative cooling for the rest (non-radiative mixing). For introducing the cold gas cloud with an overdensity of $\chi = 100$ in `Athena++` simulations, we set the density within the cloud region to $\chi\rho_{\rm hot}$ and temperature to $T_{\rm hot}/\chi$, while keeping the local pressure and kinetic energy unchanged. We resolve the dense cold gas cloud by at least 12 grid cells along its diameter, to have converged evolution (Gronke et al., 2022b; cf. Tan et al., 2021 for comparison to detailed turbulent mixing layer simulations). We vary the cloud radius ($R_{\rm cloud}$) as well as the $L_{\rm box}/R_{\rm cloud}$ for comparison with analogous multifluid simulations.

4.1.3 Subgrid multifluid

For MOGLI simulations with multifluid `AREPO`, we use the default exact hydrodynamic Riemann solver, time integration, and piecewise linear reconstruction with a variation to MUSCL-Hancock scheme (Pakmor et al., 2016). The details of the multifluid framework are presented in Weinberger & Hernquist (2023a). We use an adiabatic EOS for the hot fluid to allow for turbulent heating and cooling. In contrast, we use a quasi-isothermal EOS for the cold fluid, which resets the internal energy after each timestep, to emulate the temperature floor and fast cooling for cold gas in resolved single-fluid simulations[3]. We use a different (de)refinement criterion where we

[2] While the shape of $\Lambda(T)$ matters for the exact $\dot{m}$ (Abruzzo et al., 2022b), for the current theoretical focussed work the main decisive factor is the minimum cooling time (See also Farber & Gronke, 2021; Tan et al., 2021) which we have at the cloud temperature.

[3] Note that the bolometric luminosity of turbulent, multiphase media is dominated by the enthalpy flux (Ji et al., 2019; Gronke et al., 2022b). Hence, the energy radiated away by the cold medium is negligible (and highly dependent

assume the cell is filled with hot fluid, i.e. we refine depending on $m_{\rm refine} = \sum_k m_k \rho_{\rm hot}/\rho_k$, where k belongs to the set of fluids. We (de)refine the cell to match $m_{\rm refine}$ and a target mass resolution. This (de)refinement criterion ensures that the cells with more cold fluid are not excessively refined, and refinement occurs as if we only have the hot fluid. As with any other choice of (de)refinement criterion, this one also has some downsides, like worse resolution in cells filled with cold fluid, loss of the pseudo-Lagrangian nature in the case of source terms and its equivalence with equal spatial resolution.

In a multifluid simulation, we track hot and cold gas as two different fluids. Each cell has a quantity that refers to the fraction of cell volume occupied by the fluids. The right section of Fig. 4.1 shows a schematic diagram of different cases and corresponding cold gas volume fractions. As we only have two fluids in our setup, we only need to keep track of one volume fraction. We refer to the volume fraction of the cold fluid as α' and that of the hot fluid as $(1-\alpha')$. We enforce a floor of $\alpha_{\rm floor} = 10^{-8}$ on α' and $(1-\alpha')$ for numerical reasons. Hence, $\alpha' = \alpha_{\rm floor}$ for a cell filled with hot fluid and $\alpha' = 1 - \alpha_{\rm floor}$ for one filled with cold fluid. The $\alpha_{\rm floor}$ dictates the order of magnitude of the smallest amount of cold gas that can be tracked, so it has to be a sufficiently small number. We found that $\alpha_{\rm floor} = 10^{-8}$ is small enough, and further decrease does not have a significant effect on the results, apart from the slightly higher computational costs due to stricter source integration tolerances. Note that there is no single-phase radiative cooling for the hot fluid. This is in line with the assumptions of the single-fluid resolved simulations.

After rescaling the temperature (same as the `Athena++` setup; cf. Sec. 4.1.2 above), we take the single-fluid output at the end of the turbulence-driving in the initialisation phase and create the multifluid initial condition with the cloud. If the cloud is resolved, we fill the cells within the cloud region with cold fluid by setting $\alpha' = 1 - \alpha_{\rm floor}$. If the cloud is not resolved, we pick the cell closest to the centre of the box and increase the α' by the amount corresponding to the volume of the unresolved cloud. If $V_{\rm cell}$ and $V_{\rm cloud}$ are the volume of the cell and the cloud, respectively, the α' is set to $\alpha_{\rm floor} + V_{\rm cloud}/V_{\rm cell}$. Both fluids have the same velocity at the beginning of the simulations.

Fig. 4.2 shows the initial cold fluid volume fraction slices for MOGLI simulations with resolved and unresolved cold gas clouds. The left panel shows an example of a resolved cold gas cloud with 64^3 cells and $L_{\rm box}/R_{\rm cloud} = 8$, where the cloud is bigger than the grid cells and grid cells inside the volume of the cloud have an $\alpha' = 1 - \alpha_{\rm floor}$. On the other hand, the right panel shows the initial cold fluid volume fraction for MOGLI simulation with an unresolved cold gas cloud, with 8^3 cells and $L_{\rm box}/R_{\rm cloud} = 32$. As the cold gas cloud is unresolved, the volume fraction in the cell is set to $\alpha_{\rm floor} + V_{\rm cloud}/V_{\rm cell}$, where $V_{\rm cloud}$ and $V_{\rm cell}$ are the cloud and grid cell volumes. The dashed circles show the corresponding cold gas cloud size in the simulations.

on the heating source).

4.2 MOGLI: The subgrid model

Multifluid AREPO evolves multiple fluids on a common grid. This allows for the inclusion of terms for interactions between the fluids. In our case, the interaction terms are mass exchange ($\dot{m}$), momentum exchange ($\dot{\vec{p}}$) and energy exchange ($\dot{E}$) terms. The source terms are integrated using the Bader-Deuflhard semi-implicit integration (Bader & Deuflhard, 1983; Weinberger et al., in prep). The semi-implicit integrator takes the 10 conservative variables (mass, momenta and energy for each fluid) and integrates the source functions from the subgrid model to calculate the new values over a timestep. MOGLI consists of the model for the source terms for the interactions between the hot and cold gas fluids, which we explain in this section.

4.2.1 Definition of the source functions

Let $\mathbf{Q}$ and $\dot{\mathbf{Q}}$ denote the conservative variables and source functions, respectively, from the model.

$$\mathbf{Q} = \begin{bmatrix} m \\ \vec{p} \\ E \end{bmatrix}, \dot{\mathbf{Q}} = \begin{bmatrix} \dot{m} \\ \dot{\vec{p}} \\ \dot{E} \end{bmatrix} \tag{4.1}$$

where, m, $\vec{p}$ and E refer to mass, momentum and total energy in a cell.

We split the source functions into three components, which refer to contributions from three different physical processes. The first contribution, $\dot{\mathbf{Q}}_{\rm drag}$, is due to the hydrodynamic drag between fluids. The drag interaction does not lead to a mass exchange but can result in momenta and energy exchange. The second one, $\dot{\mathbf{Q}}_{\rm mix}$, is from the mixing between cold into hot fluid, and the third, $\dot{\mathbf{Q}}_{\rm grow}$, is from the cooling of the mixed gas from hot fluid to cold fluid. Both second- and third-source function contributions involve mass, momenta, and energy exchange. So, the full source function can be written as

$$\dot{\mathbf{Q}} = \dot{\mathbf{Q}}_{\rm drag} + \dot{\mathbf{Q}}_{\rm mix} + \dot{\mathbf{Q}}_{\rm grow}. \tag{4.2}$$

The left panel of Fig. 4.1 shows a schematic representation of the different source function contributions. While mass and momentum are conserved for all the different parts of the source functions, energy is only conserved for $\dot{\mathbf{Q}}_{\rm drag}$ and $\dot{\mathbf{Q}}_{\rm mix}$. For $\dot{\mathbf{Q}}_{\rm grow}$, the energy is not conserved as thermal energy is dissipated via radiative cooling and the difference between the energy exchange is given by $\dot{E}_{\rm cooling}$. We can write the conservation relations as

$$\dot{\mathbf{Q}}_{\rm drag,cold} = -\dot{\mathbf{Q}}_{\rm drag,hot}, \tag{4.3}$$

$$\dot{\mathbf{Q}}_{\rm mix,cold} = -\dot{\mathbf{Q}}_{\rm mix,hot}, \tag{4.4}$$

$$\dot{\mathbf{Q}}_{\rm grow,cold} = -\dot{\mathbf{Q}}_{\rm grow,hot} - \begin{bmatrix} 0 \\ 0 \\ \dot{E}_{\rm cooling} \end{bmatrix}. \tag{4.5}$$

From here onwards, we will denote elements of the 'cold' or 'hot' source functions with $_{\rm cold}$ or $_{\rm hot}$, respectively.

4.2.2 The cold gas volume filling fraction

As volume fraction is not part of the 10 conservative variables, we need to calculate the volume fraction from the conservative quantities.

$$\alpha' = \frac{m_{\rm cold} u_{\rm cold}}{m_{\rm cold} u_{\rm cold} + m_{\rm hot} u_{\rm hot}} \tag{4.6}$$

where $u_{\rm hot}$ and $u_{\rm cold}$ are the specific internal energy of the hot and cold fluid, respectively. As α has a floor and ceiling value, we redefine the volume fraction such that values between $\alpha_{\rm floor}$ and $\alpha_{\rm ceil}$ map linearly to their physical values in $[0, 1]$. So, a cell-filled with hot fluid and $\alpha' = \alpha_{\rm floor}$ corresponds to $\alpha = 0$, while a cell filled with cold fluid and $\alpha' = 1 - \alpha_{\rm floor}$ corresponds to $\alpha = 1$. This new mapped value is subsequently used for calculations in the source functions.

$$\alpha = \begin{cases} 0.0 & \text{for } \alpha' < \alpha_{\rm floor} \\ \dfrac{\alpha' - \alpha_{\rm floor}}{1 - 2\alpha_{\rm floor}} & \text{for } \alpha' \in [\alpha_{\rm floor}, 1 - \alpha_{\rm floor}] \\ 1.0 & \text{for } \alpha' > 1 - \alpha_{\rm floor} \end{cases} \tag{4.7}$$

4.2.3 Drag forces

One obvious change of momentum and energy stems from the hydrodynamic drag between the fluids in a cell, in the presence of a relative velocity $\Delta\vec{v}$ giving rise to $\dot{Q}_{\rm drag}$ in Eq. (4.2). The drag force between the two fluids in the cell will be

$$\dot{p}_{\rm drag,cold} = -\vec{F}_{\rm drag} = 0.5\, C_{\rm D}\, \rho_{\rm hot}\, A_{\rm cross}(\alpha)\, |\Delta\vec{v}|\Delta\vec{v} \tag{4.8}$$

where $C_{\rm D} = 0.5$ is the drag coefficient and $A_{\rm cross}(\alpha)$ is the cross-sectional area of the cold fluid in the direction of the relative velocity. We further discuss the functional form of $A_{\rm cross}$ (Eq. (4.33)) in Section 4.2.7.

Drag force also leads to an exchange of energy between the two fluids. The rate of energy exchange is set to,

$$\dot{E}_{\rm cold} = -\vec{F}_{\rm drag}.\vec{v}_i. \tag{4.9}$$

Here, $\vec{v}_i$ is the centre of mass velocity, which will be attained at equilibrium (Saurel & Abgrall, 1999), i.e.,

$$\vec{v}_{\rm i} = \frac{m_{\rm cold}\vec{v}_{\rm cold} + m_{\rm hot}\vec{v}_{\rm hot}}{m_{\rm cold} + m_{\rm hot}} = \frac{\vec{p}_{\rm cold} + \vec{p}_{\rm hot}}{m_{\rm cold} + m_{\rm hot}}. \tag{4.10}$$

As mentioned earlier, the drag force contribution does not cause mass exchange. Hence, the final form of $\dot{\mathbf{Q}}_{\rm drag,cold}$ is

$$\dot{\mathbf{Q}}_{\rm drag,cold} = \begin{bmatrix} 0 \\ -\vec{F}_{\rm drag} \\ -\vec{F}_{\rm drag}.\vec{v}_{\rm i} \end{bmatrix}. \tag{4.11}$$

Later, in Sec. 4.3.1 & 4.4 we include $\dot{\mathbf{Q}}_{\rm drag}$ and verify the MOGLI model.

4.2.4 Turbulent Mixing

Next, we consider the contribution to source functions from the turbulent mixing of cold gas into hot gas. This part of the source function contains mass, momenta and energy exchange and is captured by $\mathbf{Q}_{\rm mix}$ (cf. Eq. (4.2)).

To first order, we expect the turbulent mixing to destroy the cold gas on a characteristic timescale $t_{\rm destroy}$, i.e., $\dot{m}_{\rm cold\rightarrow hot} \sim m/t_{\rm destroy}$. From previous work as well as analytical considerations, we expect this destruction timescale to be the Kelvin-Helmholtz or Rayleigh-Taylor timescale of the cloud (e.g. Klein et al., 1994b; Gronke et al., 2022b)

$$t_{\rm destroy} = \frac{\chi^{1/2} l_{\rm cold}}{v_{\rm turb}}. \tag{4.12}$$

Here, $l_{\rm cold}$ is the effective size of the cold gas in the cell

$$l_{\rm cold} = \left(\frac{\alpha V_{\rm cell}}{4\pi/3}\right)^{1/3}, \tag{4.13}$$

$v_{\rm turb}$ is the turbulent velocity, and χ overdensity of a given cell

$$\chi \equiv \frac{\rho_{\rm cold}}{\rho_{\rm hot}} = \left(\frac{1}{\alpha} - 1\right)\frac{m_{\rm cold}}{m_{\rm hot}}. \tag{4.14}$$

Note that while χ is independent of α for a given cell, $l_{\rm cold}$ strongly depends on it and thus gives rise to a short destruction time for, e.g., a predominantly hot cell. We explicitly verified this destruction term in Sec. 4.3.1 & 4.4. While we calculate $l_{\rm cold}$ as the size of a monolithic cold cloud in the cell, it refers to the length-scale of the overall cold gas structure which we subsequently use to calculate destruction timescale, $t_{\rm destroy}$ in Eq. (4.12), it does not relate to the cold gas structure within the cell.

Within any cell, we expect the mass exchange to slow down and drop with increasing volume fraction of the cold fluid, due to the decrease in the interface area between the two fluids, over which the exchange can happen; for instance, we expect a cold gas cell surrounded by other gas cells with a ~ 1 cold gas volume fraction this mass exchange rate to be ~ 0 as the cell is entirely 'shielded' from the hot medium. We include an extra multiplicative factor, i.e. the area factor, of

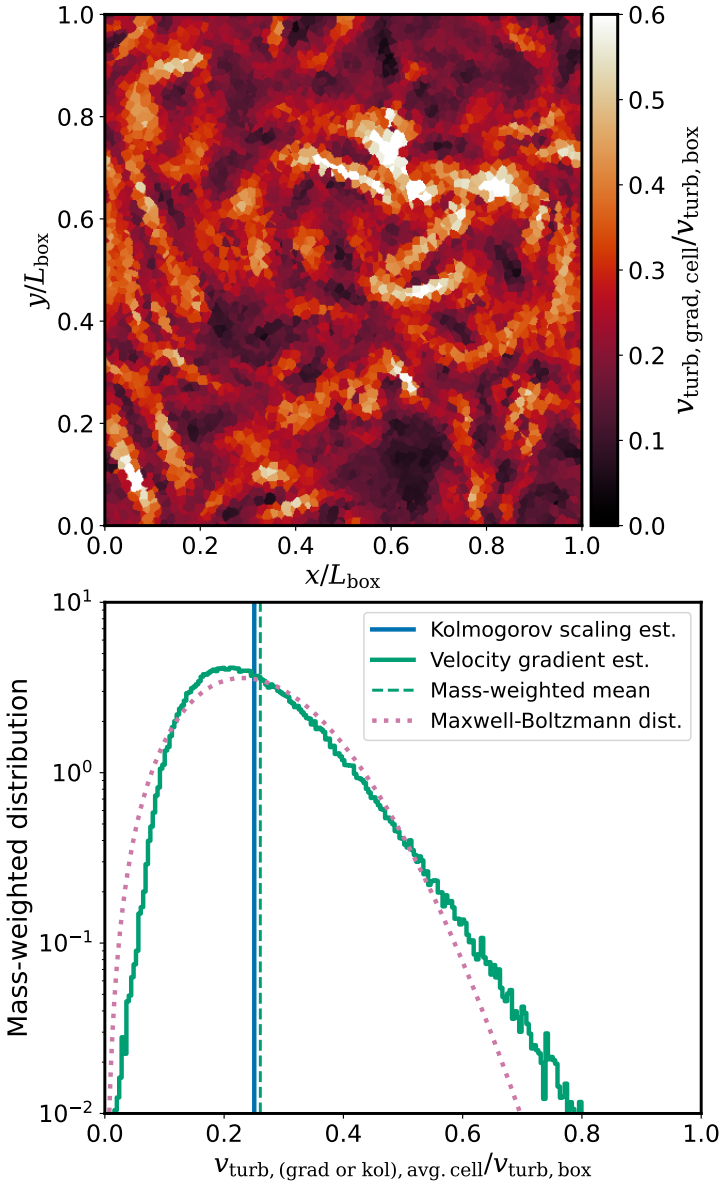

Figure 4.3: *Top panel* shows a slice of $v_{\rm turb,grad}$ from a simulation with a turbulent Mach number, $\mathcal{M}_{\rm turb,box} = 0.5$ at the box scale. It shows how the velocity gradient-based estimation (`grad`) can capture the spatial variation in the local velocity dispersion, in other words, the local turbulent velocity. *Bottom panel* shows, in solid lines, the distribution of the local turbulent velocity, at the scales of average cell size instead of local cell size, in the same snapshot as the top panel. We find that while the mass-weighted mean of from `grad` method, shown as the dashed green line, agrees with the estimate from `kol`, shown as the solid blue line. The pink dotted line shows the expected Maxwell-Boltzmann distribution with the same mean as the mass-weighted mean from `kol` method. Even though the mean turbulent velocity from the two simulations are very similar, the distribution of velocities is drastically different, with the `kol` method leading to a fixed value for a fixed length scale, and the `grad` method matching the expected Maxwell-Boltzmann distribution.

$2h(\alpha)$ to account for this dependence on the interface area. This factor essentially encodes the details of the subgrid cold gas structure. The exact form of this factor is derived and discussed in § 4.2.7[4].

We find that the variation of surface area, via the area factor of, $2h(\alpha)$), is inadequate to suppress the cold gas destruction in cells which have a high cold fluid mass fraction, $\alpha_{\rm mass} = m_{\rm cold}/(m_{\rm cold} + m_{\rm hot})$, especially for cases with resolved cold gas. We find that the cells in the interior of a resolved cold gas structure have spuriously high mass fluxes. In resolved single-fluid simulations, these cells are 'shielded' from mixing with the hot gas, as they are mostly also surrounded by other predominantly cold gas cells preventing their destruction. To account for this extra 'shielding' in resolved simulations, we introduce the first of the two free-parameters in the model, where the mass exchange from cold to hot occurs only in cells that possess a mass fraction $\alpha_{\rm mass}$ less than a threshold. We find that a $\alpha_{\rm mass}$ threshold of 0.15 works well across all tests (§ 4.3.1), i.e.,

$$\dot{m}_{\rm cold\rightarrow hot} = \begin{cases} 2h(\alpha)\dfrac{m_{\rm cold}}{t_{\rm destroy}} & \alpha_{\rm mass} < 0.15 \\ 0 & \text{otherwise.} \end{cases} \tag{4.15}$$

The momenta and energy exchange are the corresponding fluxes caused by the mass exchange. Hence, we get a source function contribution due to mixing,

$$\dot{\mathbf{Q}}_{\rm mix,cold} = \begin{bmatrix} -\dot{m}_{\rm cold\rightarrow hot} \\ -\vec{v}_{\rm cold}\dot{m}_{\rm cold\rightarrow hot} \\ -\frac{1}{2}\dot{m}_{\rm cold\rightarrow hot}v_{\rm cold}^2 - \dot{m}_{\rm cold\rightarrow hot}u_{\rm cold} \end{bmatrix} \tag{4.16}$$

4.2.5 Cold gas growth

Finally, we include the source function contribution due to the cooling of mixed gas to create more cold gas. Previous studies like Gronke et al. (2022b) have shown that for cases that are well within the growth regime, the cold gas mass follows an exponential growth, with a characteristic timescale of $t_{\rm grow} \sim \chi(t_{\rm cool} l/v_{\rm turb})^{1/2}$, i.e., characterised by the geometric mean of the cold gas mixing and cooling time, and where l refers to the cold gas structure lengthscale and $v_{\rm turb}$ is the turbulent velocity at the lengthscale l. Note that this growth time is backed up by analytical arguments of combustion theory and numerically verified using small-scale simulations (Tan et al., 2021). We can rewrite the expression for $t_{\rm grow}$ in terms of the local cell properties as,

$$t_{\rm grow} = \chi(t_{\rm destroy} t_{\rm cool,cold})^{1/2}\alpha^{1/9} \tag{4.17}$$

where the additional factor $\alpha^{1/9}$ arises to account for the effective cold gas size within a cell, i.e. $(R_{\rm cloud}/L_{\rm box})^{1/3}$.

[4]Note that we deliberately did not absorb the factor 2 into the fudge factor to facilitate comparison with prior work; cf. § 4.2.7

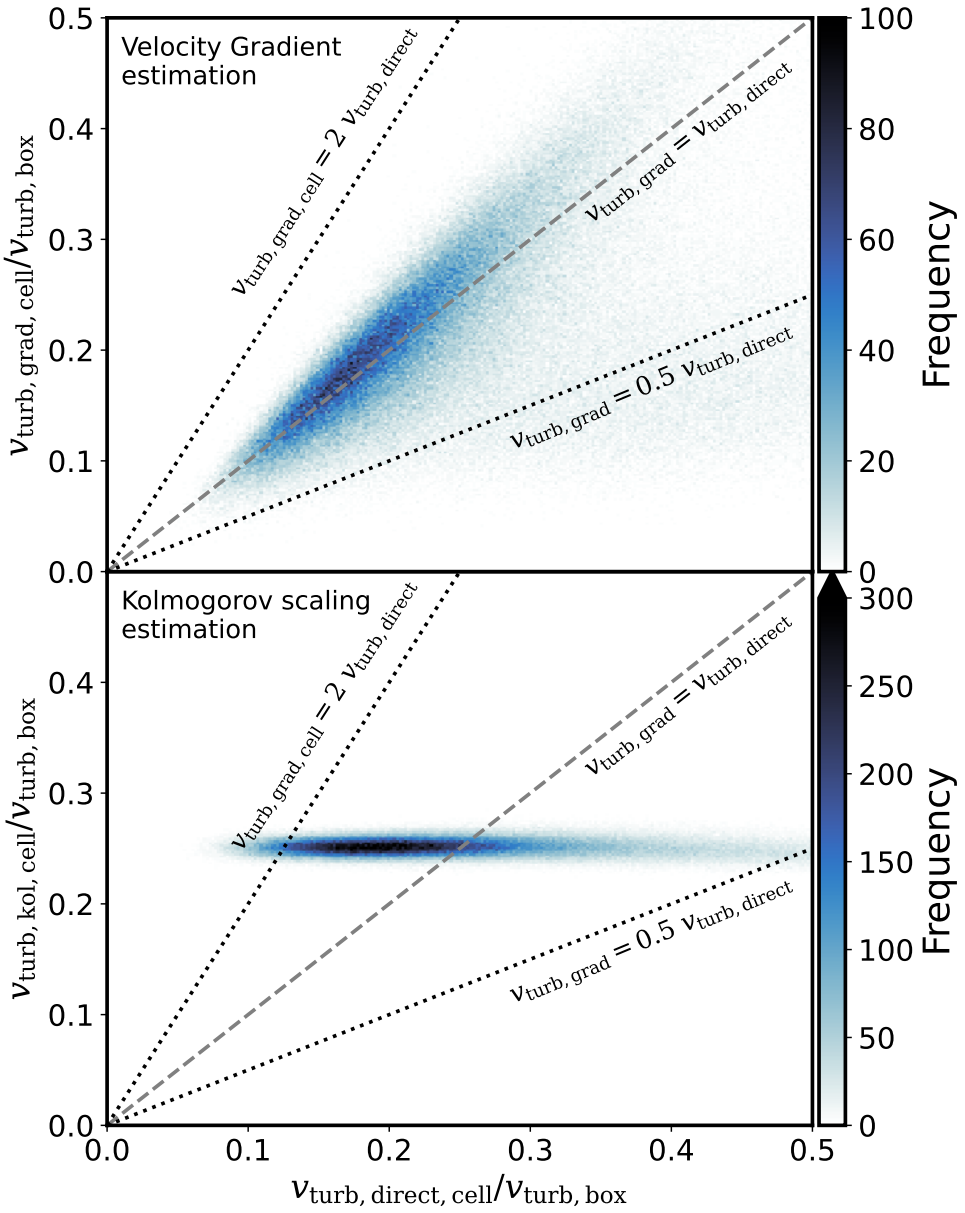

Figure 4.4: The comparison between the directly calculated velocity dispersion ($v_{\mathrm{turb,direct}}$) and the approximated local velocity dispersions using both estimation methods. The top panel shows the comparison with the velocity gradient-based method (`grad`) and the bottom panel show the comparison with the Kolmogorov spectrum-based method (`kol`).

Both $t_{\rm destroy}$ and $t_{\rm cool,cold}$ can be calculated from local grid cell properties, but in our tests, we consider a fixed value of $t_{\rm cool,cold}$. We use the value of cloud-crushing timescale, i.e. $t_{\rm cc} = \chi^{1/2} R_{\rm cloud}/v_{\rm turb}$ and the ratio $t_{\rm cool,cold}/t_{\rm cc}$ for the benchmark `Athena++` simulation to obtain the corresponding value of $t_{\rm cool,cold}$ for MOGLI runs. We also include the area factor of $2h(\alpha)$ for this interaction, same as Eq. (4.15), which gives the hot to cold fluid mass exchange rate,

$$\dot{m}_{\rm hot\to cold} = 2h(\alpha)\frac{m_{\rm cold}}{t_{\rm grow}} \tag{4.18}$$

As mentioned earlier, the energy across the system is not conserved during cold gas growth. Any increase in the specific internal energy is quickly radiated away. One major contribution to this is the difference in internal energy during the mass exchange from hot to cold fluid is radiated away and hence subtracted

$$\dot{E}_{\rm cooling} = \dot{m}_{\rm hot\to cold}(u_{\rm hot} - u_{\rm cold}). \tag{4.19}$$

Note that there will be additional cooling of the thermalised kinetic energy. While the exact amount of this radiated energy is uncertain and depends on the details of geometry and momentum exchange (see Appendix 6.5.3), it is self-consistently removed by the quasi-isothermal EOS.

Including the momentum exchange due to mass exchange, we obtain the expression for the source function contribution due to cold gas growth

$$\dot{\mathbf{Q}}_{\rm grow,cold} = \begin{bmatrix} \dot{m}_{\rm hot\to cold} \\ \vec{v}_{\rm hot}\dot{m}_{\rm hot\to cold} \\ \frac{1}{2}\dot{m}_{\rm hot\to cold}v_{\rm hot}^2 + \dot{m}_{\rm hot\to cold}u_{\rm hot} \end{bmatrix} - \begin{bmatrix} 0 \\ 0 \\ \dot{E}_{\rm cooling} \end{bmatrix}. \tag{4.20}$$

4.2.6 Turbulent velocity estimation

Turbulence is key in mixing hot and cold material, and thus, the expressions in $\dot{\mathbf{Q}}_{\rm mix}$ and $\dot{\mathbf{Q}}_{\rm grow}$ depend on the local turbulent velocity at the scale of cold fluid in the cell, as $v_{\rm turb} = v_{\rm turb,cell}(l_{\rm cold}/l_{\rm cell})^{1/3}$, where $l_{\rm cell}$ is the cell size. The most accurate way to accomplish this is to have a turbulence model that keeps track of the subgrid turbulence (akin to Schmidt et al., 2006b or Semenov, 2024). As the implementation of such a model in a moving-mesh code like `AREPO` is out of the scope of this study, we use two methods to approximate the turbulence at the grid cell scales.

Estimation by Kolmogorov Scaling (`kol`)

The first method (`kol`) assumes that the turbulence is fully developed and follows the Kolmogorov spectrum to the subgrid scales. So, by scaling the box-scale turbulent velocity ($v_{\rm turb,box}$) down to the grid cell scale, we can estimate the local turbulence.

$$v_{\rm turb,kol,cell} = v_{\rm turb,box}\left(\frac{l_{\rm cell}}{L_{\rm box}}\right)^{1/3} \tag{4.21}$$

This method is feasible for setups with fully developed turbulence at a resolved scale, like our turbulent box simulations. However, it is not appropriate in simulations with significant spatial and/or temporal variation in turbulence.

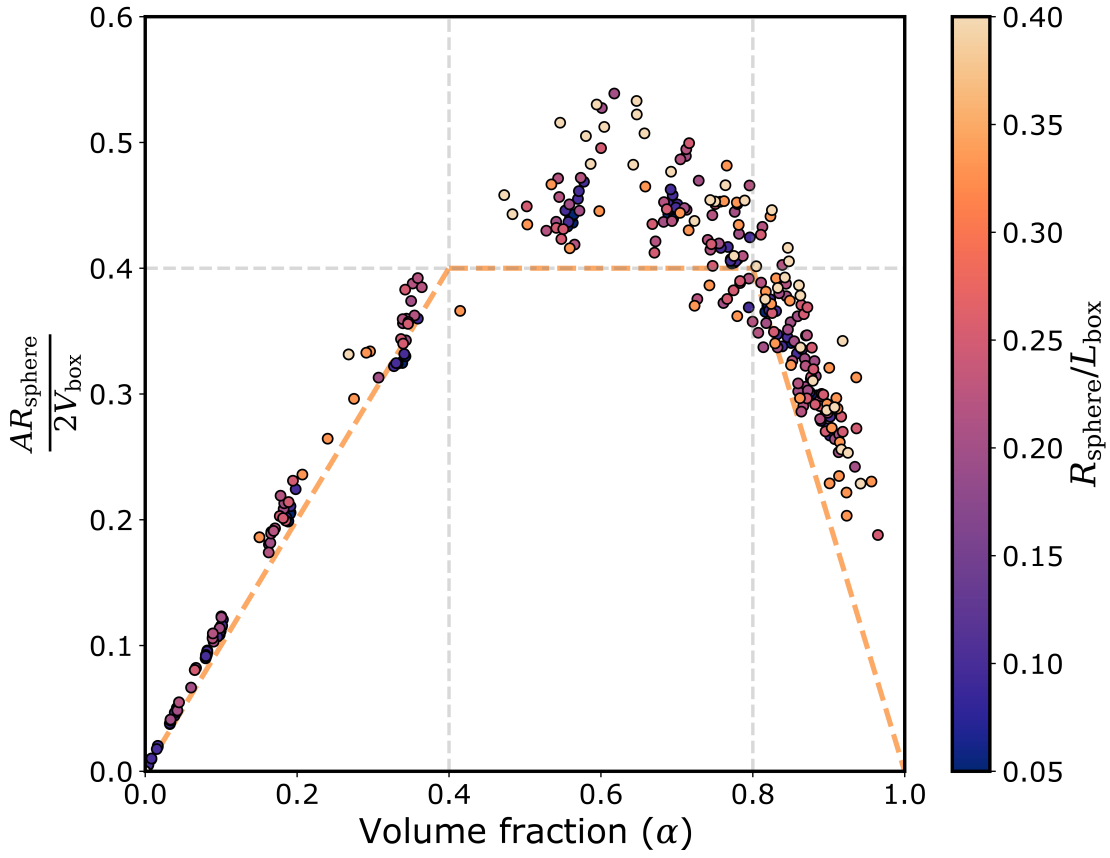

Figure 4.5: Variation of $AR/(2V_{\text{box}})$ with volume fraction (α) in a 3D box. The colour of the points shows the size of the individual spheres, relative to the box size and the orange lines correspond to the approximate fit for the points, i.e. $\alpha h(\alpha)$ (Eq. (4.30)).

Estimation by velocity gradients (grad)

The second method of local turbulence estimation (grad) avoids the problems of the kol method by estimating the local velocity dispersion at any given time. We use the Jacobian of the velocity vector ($\mathbf{J}[a,b] = \partial\ \vec{v}[a]/\partial\ \vec{x}[b]$), to estimate velocity dispersion at the grid scale ($\sigma_{\vec{v},\mathrm{cell}}$), and assume a fully-developed Kolmogorov spectrum on smaller scales to estimate the turbulent velocity at the subgrid cold gas scale (l_{cold}) from the calculated grid-scale. The subscript to different quantities refers to their relation to the fluid cell. For example, $\vec{\rho}_i$ refers to the density in the i^{th} cell.

As explained in Pakmor et al. (2016), in AREPO, the gradient of a quantity ϕ, in the i^{th} cell, i.e. $\vec{\nabla}_i\phi$) is calculated such that it gives the best fit for Eq. (4.22) when written for the quantity in all neighbouring cells (ϕ_j). Let the i^{th} cell have n_{ngb} neighbouring cells, each denoted by a subscript j, at a displacement of $\vec{x}_{ji}$,

$$\phi_j = \phi_i + \vec{\nabla}_i\phi \cdot \vec{x}_{ji}. \tag{4.22}$$

We use Eq. (4.22) to calculate the mean of ϕ over the neighbouring cells in n_{ngb} including the i^{th} cell,

$$\mu_i(\phi_j) = \phi_i + \vec{\nabla}_i\phi \cdot \mu_i(\vec{x}_{ji}). \tag{4.23}$$

Subsequently, we use the Eq. (4.23) for the mean to calculate the standard deviation for ϕ, σ^2_ϕ.

$$\sigma^2_\phi = \frac{1}{n_{\mathrm{ngb}}+1}\sum_j^{n_{\mathrm{ngb}}}\left[\vec{\nabla}_i\phi \cdot \left(\vec{x}_{ji} - \mu_i(\vec{x}_{ji})\right)\right]^2 \tag{4.24}$$

To evaluate the Eq. (4.24) further, we need to make some assumptions. First, we assume that the neighbouring cells are uniformly distributed around the current cell. Hence, the weighted average of the displacements, $\mu_i(\vec{x}_{ji})$ is expected to have a marginal magnitude and can be ignored. Next, we assume that the neighbouring cells are at roughly equal distances of x_{ngb} from the current cell, and we can replace $\vec{x}_{ji}$ with $x_{\mathrm{ngb}}\hat{x}_{ji}$. Here, $\hat{x}_{ji}$ refers to the unit vector in the direction of $\vec{x}_{ji}$, i.e. $\hat{x}_{ji} = \vec{x}_{ji}/|x_{ji}|$. This simplifies Eq. (4.24) to

$$\sigma^2_\phi = \frac{x^2_{\mathrm{ngb}}}{n_{\mathrm{ngb}}+1}\sum_j^{n_{\mathrm{ngb}}}\left[\vec{\nabla}_i\phi \cdot \hat{x}_{ji}\right]^2. \tag{4.25}$$

Eq. (4.25) shows that the velocity dispersion is related to the root-mean-square value of the component of gradient towards the neighbouring cells. The exact value of this quantity will depend on the relative position and number of the neighbouring cells. Hence, to further simplify the Eq. (4.25), we postulate that this value is close to the value at the limit of $n_{\mathrm{ngb}} \to \infty$, with all the neighbouring cells uniformly distributed around the current cell. This allows us to rewrite Eq. (4.25) in its integral form and to obtain the value at the limit by evaluating the integral,

$$\sigma_{\phi,n_{\mathrm{ngb}}\to\infty} = \sqrt{\frac{1}{3}}\, x_{\mathrm{ngb}}|\nabla_i\phi| \tag{4.26}$$

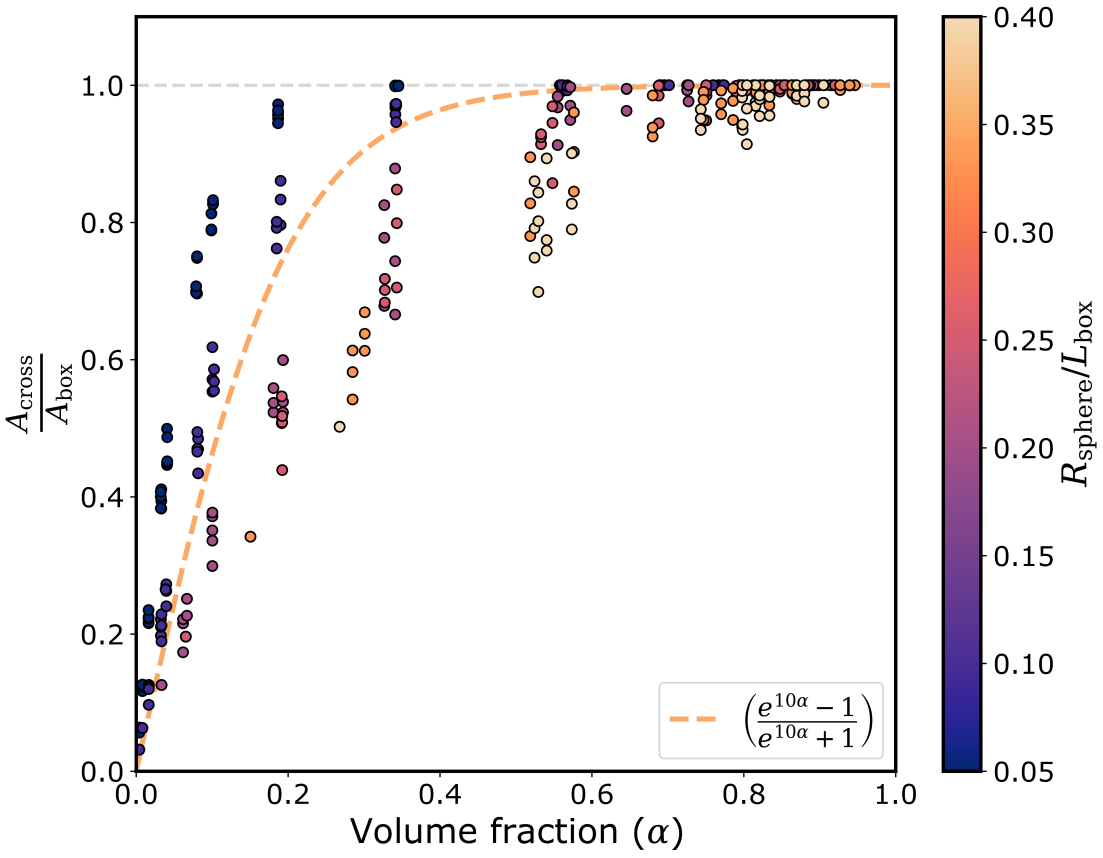

Figure 4.6: Variation of A/A_{box} with volume fraction (α) in a 3D box. The colour of the points shows the size of the individual spheres, relative to the box size and the orange lines correspond to the approximate fit for the points (Eq. (4.33)).

To replace ϕ with v_x,v_y and v_z [5] in Eq. (4.26), we use the approximation $x_{\rm ngb} \approx V_{\rm cell}^{1/3}$. This yields an estimate of the local turbulence

$$v_{\rm turb,grad,cell} = (\sigma^2_{v_x} + \sigma^2_{v_y} + \sigma^2_{v_z})^{1/2} = V_{\rm cell}^{1/3} \sqrt{\frac{1}{\xi} \sum_{i,j}^{3} \left(\frac{\partial v_j}{\partial x_i}\right)^2} \tag{4.27}$$

where, $\xi = 3$. Here, we replace 3 with ζ as a free parameter, which we verify and modify in the next section. For multifluid simulations, if there are n_k fluids, we evaluate the local turbulent velocity with Eq. (4.27) for each fluid separately and take the mass-weighted average as the final turbulent velocity estimate per cell, i.e.,

$$v_{\rm turb,grad,cell} = \frac{1}{m_{\rm cell}} \sum_{k}^{n_k} m_k v_{\rm turb,grad,k}. \tag{4.28}$$

Comparison and validation of the methods

The top panel of Fig. 4.3 shows a slice of $v_{\rm turb,grad,cell}$ from a simulation with a turbulent Mach number, $\mathcal{M}_{\rm turb,box} = 0.5$ at the box scale using $N_{\rm cells} = 64^3$ resolution elements. It shows how the velocity gradient-based estimation (`grad`) can capture the spatial variation in the local velocity dispersion, in other words, the local turbulent velocity. The bottom panel shows, in solid lines, the estimation for local turbulent velocity at the lengthscale of the average cell size ($l_{\rm cell,avg} = (V_{\rm box}/N_{\rm cell})^{1/3}$) in the same snapshot as the top panel. As the `kol` only depends on the lengthscale, it returns a fixed local turbulent velocity for a fixed lengthscale. The blue solid line shows the `kol` method estimate for the $l_{\rm cell,avg}$. The green solid line shows the distribution of the `grad` estimates for local turbulent velocities at scale of $l_{\rm cell}$, and the green dashed line shows the corresponding mass-weighted mean. We find that the estimate from `kol` and mass-weighted mean from `grad` agree very well with each other, and the expected value $\bar{v}_{\rm turb} \approx v_{\rm turb,box}/N_{\rm cells}^{1/3}$.

As the turbulence velocities along each basis directions ($v_{{\rm turb},x}$, $v_{{\rm turb},y}$, $v_{{\rm turb},z}$) roughly follow gaussian distribution, the turbulent velocity magnitude $v_{\rm turb} = (v^2_{{\rm turb},y} + v^2_{{\rm turb},y} + v^2_{{\rm turb},z})^{1/2}$ is expected to follow a Maxwell-Boltzmann distribution. In Fig. 4.3, the pink dotted line shows the expected Maxwell-Boltzmann distribution, with the same mean as the the mass-weighted mean from `grad` method. We find that the distribution of local turbulent velocity estimate from `grad` matches well with the Maxwell-Boltzmann distribution, with some deviations at small and large velocity magnitudes. The deviations at small velocity magnitudes are likely due to the resolution limit and lack of small scales, while the deviations at the larger velocities are probably due to slope-limiting for the gradients.

We want to test how well Eq. (4.28) can approximate the local velocity dispersion. Hence, we directly calculate the velocity dispersion at grid cell size in the neighbourhood for each grid

[5] Note that the velocity gradients used in the MOGLI simulations are the slope-limited gradients that are used in the finite-volume solver.

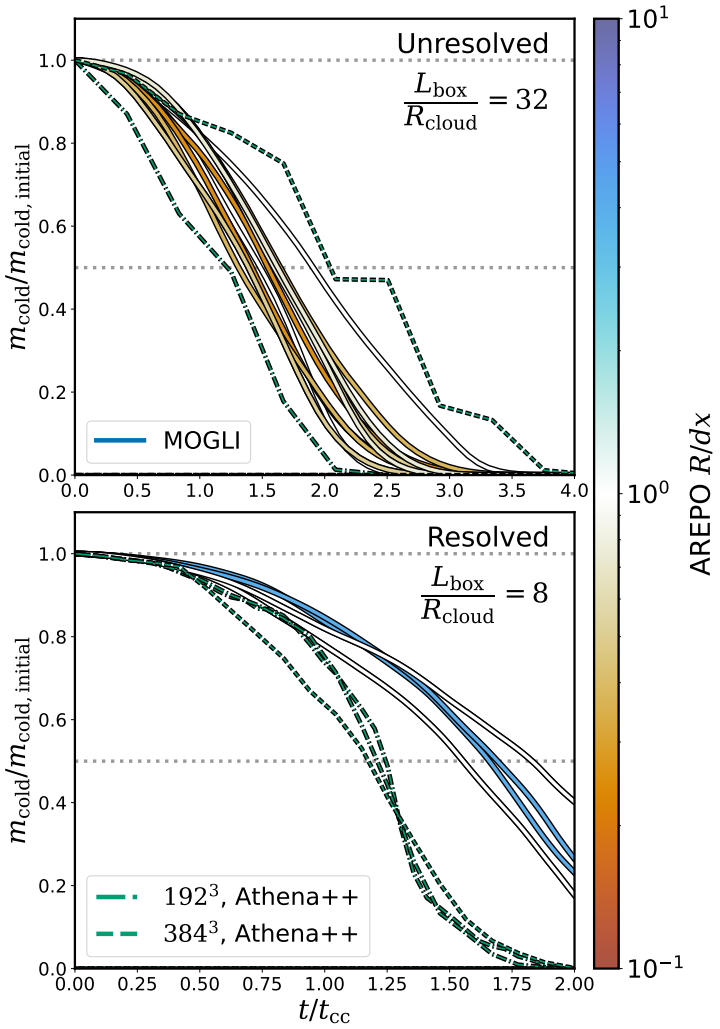

Figure 4.7: Cold gas evolution in non-radiative MOGLI runs with time, normalised to the initial cloud-crushing time ($t_{\rm cc} = \chi^{1/2} R_{\rm cloud}/v_{\rm turb}$), with $\mathcal{M}_{\rm turb} = 0.5$. The solid lines show the cold gas evolution, as the total mass of the cold fluid, with the colour of the line denoting the initial $R_{\rm cloud}/dx$. The dot-dashed and dashed lines show the cold gas evolution in the benchmark `Athena++` simulations, with resolutions 192^3 and 384^3 respectively. *Top panel* shows the evolution for simulations with unresolved initial cloud $L_{\rm box}/R_{\rm cloud} = 32$ and *bottom panel* shows the same for resolved initial cloud $L_{\rm box}/R_{\rm cloud} = 8$. This shows that the cloud destruction timescales in MOGLI are in agreement with the timescales in benchmark `Athena++`.

cell in the simulation, $\sigma_{\rm turb,ngb}$ and use it as the benchmark we want to approximate. As the directly calculated velocity dispersion is over the whole neighbourhood with a volume $V_{\rm ngb} = \sum_{\rm ngb} V_{\rm cell,j}$, we use the Kolmogorov scaling to scale it down to the grid cell size as $v_{\rm turb,direct} = \sigma_{\rm turb,ngb}(V_{\rm cell}/V_{\rm ngb})^{1/9}$ where the latter term introduces corrections of order unity.

Fig. 4.4 shows the comparison between the directly calculated velocity dispersion ($v_{\rm turb,direct}$) and the approximated local velocity dispersions using both estimation methods. The top panel shows the comparison with the velocity gradient-based method (`grad`) and the bottom panel show the comparison with the Kolmogorov spectrum-based method (`kol`). For the bulk of the cells, $v_{\rm turb,direct}$ and $v_{\rm turb,grad}$ agree well with each other and are within a factor of 2 between each other. The slight deviations from $v_{\rm turb,direct}$ are likely due to the assumptions involved in obtaining the Eq. (4.27). On the other hand, the $v_{\rm turb,kol}$ from the `kol` method is unable to capture the spatial variations in the $v_{\rm turb,direct}$.

During our non-radiative turbulent mixing tests, explained later in Sec. 4.4, we find a $\xi = 2$ works better in matching with the benchmark Athena++ simulations. Hence, we use $\xi = \xi_{\rm MOGLI} \equiv 2$ in MOGLI runs,

$$v_{\rm turb,grad,cell,MOGLI} = V_{\rm cell}^{1/3} \sqrt{\frac{1}{\xi_{\rm MOGLI}} \sum_{i,j}^{3} \left(\frac{\partial v_j}{\partial x_i}\right)^2}. \tag{4.29}$$

Even though the analytical expression with $\xi = 3$ can estimate the local velocity dispersion or local turbulent velocity, the estimated turbulent velocity is not high enough to match the turbulent mixing in the resolved Athena++ simulations. One potential cause for this can be the proximity to the dissipation scales, which can be rectified in future with better subgrid turbulence models. [6] Later, in Sec. 4.3 and 4.4 we test our MOGLI model with both Kolmogorov scaling-based (`kol`) and velocity gradient-based (`grad`) methods for local turbulent velocity estimation, respectively. See Appendix 6.5.3 for a more general version Eq. (4.29), which can also be applied to 2D geometries.

4.2.7 Cold gas surface and cross-sectional area

Both the mass exchange from hot to cold and cold to hot medium naturally depend on the exposure of the two media, and thus crucially depend on the size of the interface area in any given cell. As shown in the middle and left panel of Fig. 4.1, in order to account for non-spherical and overlapping cold gas structures, we use two area factors in the model introduced in Sec. 4.2.4 & 4.2.5 (cf. Eq. (4.15) & (4.18)).

The first area factor, $2h(\alpha)$, corresponds to the dependence on the interface area between the two fluids. The second area factor, $A_{\rm cross}(\alpha)$, is for the cross-sectional area along the relative velocity of the fluid.

[6] Also note this scheme will also interpret laminar viscous flows with velocity gradients as turbulent velocity, although such cases might be unlikely due to the very high Reynolds number of astrophysical gas.

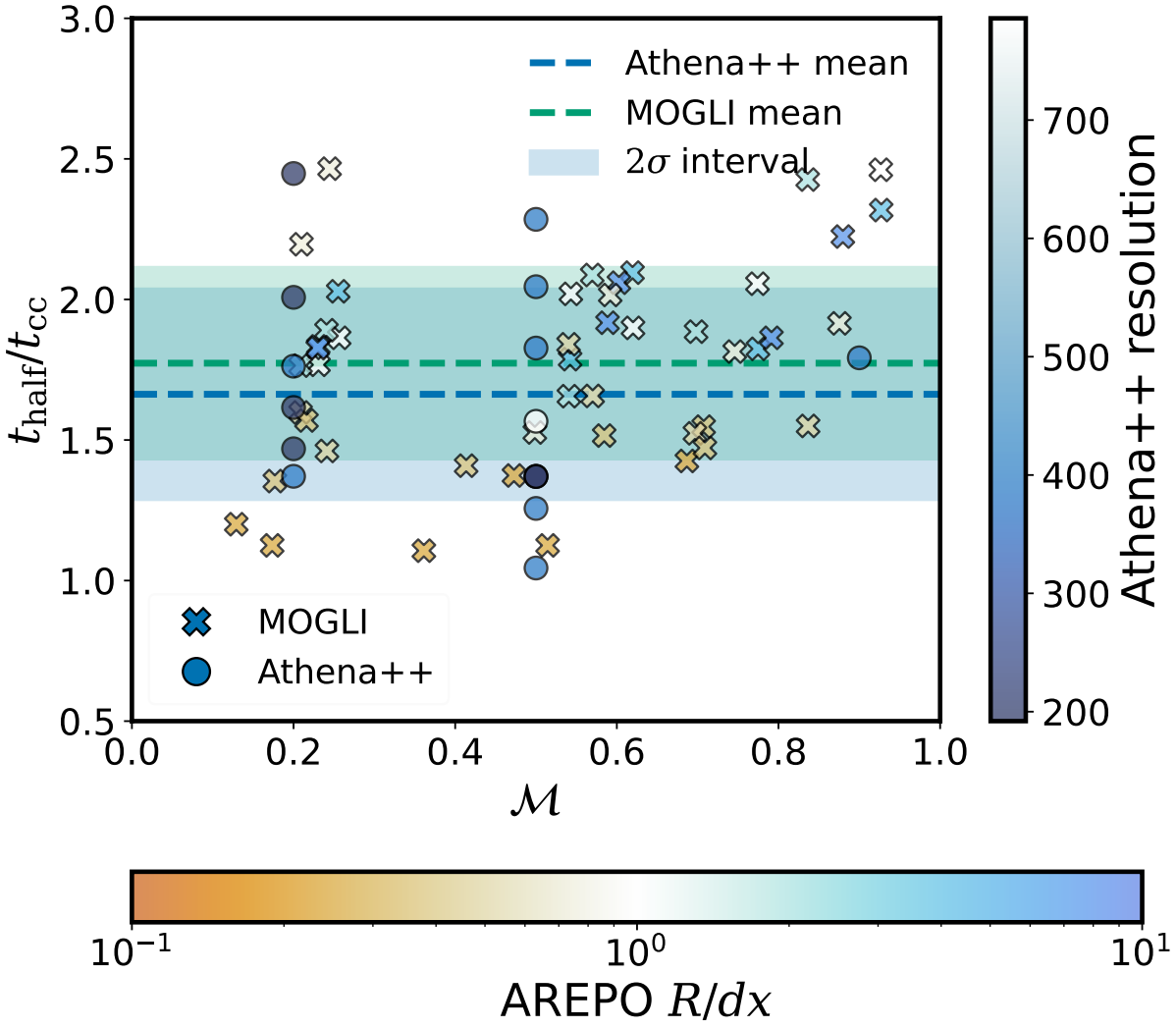

Figure 4.8: Scatter plot of the half mass time ($t_{\rm half}$) normalised to the initial cloud-crushing timescale ($t_{\rm cc} = \chi R_{\rm cloud}/v_{\rm turb}$), for different turbulent Mach numbers. `Athena++` simulations with different resolutions (192^3, 384^3, and 768^3, represented by the colour of the point) and turbulence random seeds to capture the inherent stochasticity of cold gas destruction in a turbulent medium.

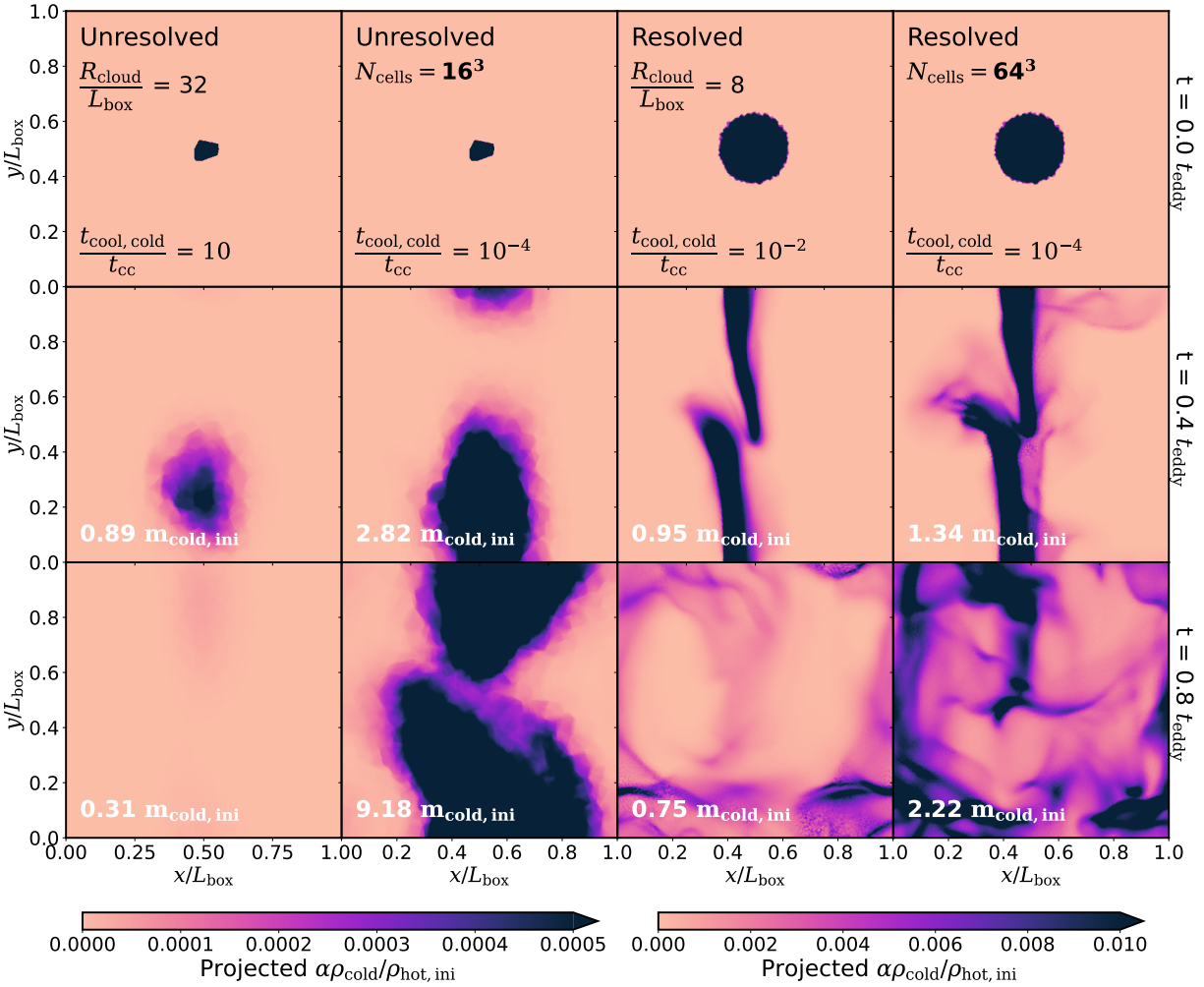

Figure 4.9: Projected $\alpha\rho_{\rm cold}/\rho_{\rm hot,ini}$, i.e. $\int_{\rm los} \alpha(\rho_{\rm cold}/\rho_{\rm hot,ini})dz/L_{\rm box}$, plots at different times for MOGLI runs with $\mathcal{M} = 0.5$ different $t_{\rm cool,cold}/t_{\rm cc}$ values. Two columns on the left show the evolution of an unresolved ($L_{\rm box}/R_{\rm cloud} = 32$) initial cloud and two columns on the right show the evolution of a resolved initial ($L_{\rm box}/R_{\rm cloud} = 8$) cold cloud for destruction and survival regimes. We find that the clouds with short cooling timescales, i.e. $t_{\rm cool,cold} = 10^{-4} t_{\rm cc}$ survive and grow, while clouds with long cooling timescales, i.e. $t_{\rm cool,cold} = \{10, 10^{-2}\} t_{\rm cc}$ end up losing cold gas and get destroyed, as expected from the results of previous studies (Gronke et al., 2022b).

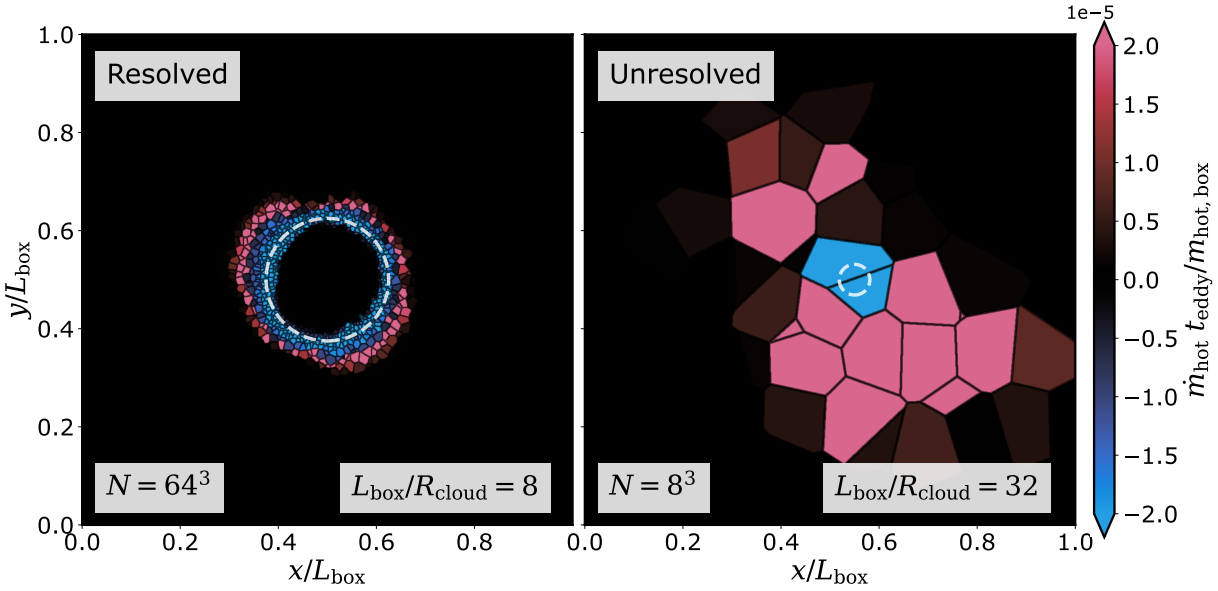

Figure 4.10: Early-time hot fluid mass flux ($\dot{m}_{hot}$) slices, normalised with ratio of total hot fluid mass and eddy-turnover time ($m_{hot,box}/t_{eddy}$), for MOGLI simulations with resolved and unresolved cold gas clouds, at $\mathcal{M} = 0.5$. The left panel shows an example of a resolved cold gas cloud with 64^3 cells and $L_{box}/R_{cloud} = 8$, where the cloud is bigger than the grid cells and grid cells inside the volume of the cloud have an $\alpha = 1 - \alpha_{floor}$. On the other hand, the right panel shows the slice for MOGLI simulation with an unresolved cold gas cloud, with 8^3 cells and $L_{box}/R_{cloud} = 32$. This shows how the model is able to distinguish between the interior and exterior of the resolved cloud and the mass exchange only occurs at the interface around the cloud. The dashed circles show the corresponding initial cold gas cloud size in the simulations.

We take a Monte-Carlo approach to approximate these area factors. We generate a fixed grid box with a varying number of equally sized, spheres, allowing for overlapping spheres[7]. We calculate the surface area (A) of the resulting ensemble of spheres using the `scikit-learn`'s marching cubes algorithm (Pedregosa et al., 2011; Lorensen & Cline, 1987), and volume fraction (α) as the ratio of the volume of encapsulated cells and grid volume (V_{box}). We repeat this exercise with different radii of spheres (R_{sphere}).

We find, as shown in Fig. 4.5, that the quantity $AR_{sphere}/(2V_{box})$ seems to follow a general relation with the volume fraction.

$$\frac{AR_{sphere}}{2V_{box}} = \alpha h(\alpha) = \begin{cases} \alpha & \text{if } \alpha \in [0, 0.4) \\ 0.4 & \text{if } \alpha \in [0.4, 0.8) \\ 2 - 2\alpha & \text{if } \alpha \in [0.8, 1] \end{cases} \tag{4.30}$$

[7]We also tried different sphere size distributions but did not find any major impact on the results while significantly increasing the number of free parameters.

where $h(\alpha)$ is a function of volume fraction, which we define for convenience in later derivations[8].

Assuming that the spheres are composed of cold gas, with an overdensity of χ and density of $\chi\rho_{\rm hot}$, we obtain a relation for the interface area as a function of the volume fraction,

$$A = \frac{2h(\alpha)\alpha V_{\rm box}}{R_{\rm sphere}} = \frac{2h(\alpha)m_{\rm cold}}{\chi\rho_{\rm hot}R_{\rm sphere}}. \tag{4.31}$$

Substituting the area (A) from Eq. (4.31) in the expression for mass exchange (e.g., Tan et al., 2021) we obtain

$$\dot{m}_{\rm cold} = A\rho_{\rm hot}v_{\rm flux} = \frac{m_{\rm cold}}{\chi R_{\rm sphere}/v_{\rm flux}}2h(\alpha) = 2h(\alpha)\frac{m_{\rm cold}}{t_{\rm flux}} \tag{4.32}$$

which introduces the cold gas surface area factor of $2h(\alpha)$. Here, $t_{\rm flux} \sim \chi R_{\rm sphere}/v_{\rm flux}$ is the naive mass doubling/halving time of a spherical object. Note that the factor of 2 along $h(\alpha)$ can explain the fudge factor 0.5 used in $t_{\rm grow}$ in (Gronke et al., 2022b). At low cold gas volume fractions, Eq. (4.32) reduces to the empirical exponential growth rate expression observed in previous studies like (Gronke et al., 2022b).

We take a similar approach to approximate the dependence of cross-sectional area in the direction of relative velocity, on the volume fraction. Assuming an isotropic distribution of the spheres, the cross-sectional area should be independent of the direction of the relative velocity. We calculate the cross-sectional area ($A_{\rm cross}$) and volume fraction (α) of a varying number of randomly distributed spheres along the three axes of the grid and repeat it for different radii of the spheres ($R_{\rm sphere}$). Fig. 4.6 shows the dependence of $A_{\rm cross}$ normalised to the grid's cross-sectional area, i.e. $A_{\rm box} = L_{\rm box}^2$, on the volume fraction of the spheres. There is a scatter, where larger individual spheres lead to a lower cross-sectional area for the same volume fraction. However, the trend converges with smaller individual clouds, and we use a sigmoid function to approximate this relation.

$$A_{\rm cross}(\alpha) = V_{\rm cell}^{2/3}\left(\frac{e^{10\alpha}-1}{e^{10\alpha}+1}\right) \tag{4.33}$$

where, we replace $A_{\rm box}$ with $V_{\rm cell}^{2/3}$. Although we observe a $R_{\rm sphere}/L_{\rm box}$ dependence, we do not expect there to be a significant effect in final behaviour, as $A_{\rm cross}$ is only used for the drag force, which turns out to have a minor contribution to the momentum exchange.

With this, we have the complete and fully-defined MOGLI model and can move to verifying this model in the next section.

4.3 Verification: With Kolmogorov turbulence estimation

As the turbulent velocity estimation is a fundamental part of the model, we verify the two estimates separately and present the results in two sections. In this section, we test MOGLI with

[8]We also tested similar fits to the points in Fig. 4.5, including higher order ones, but it does not change the results significantly.

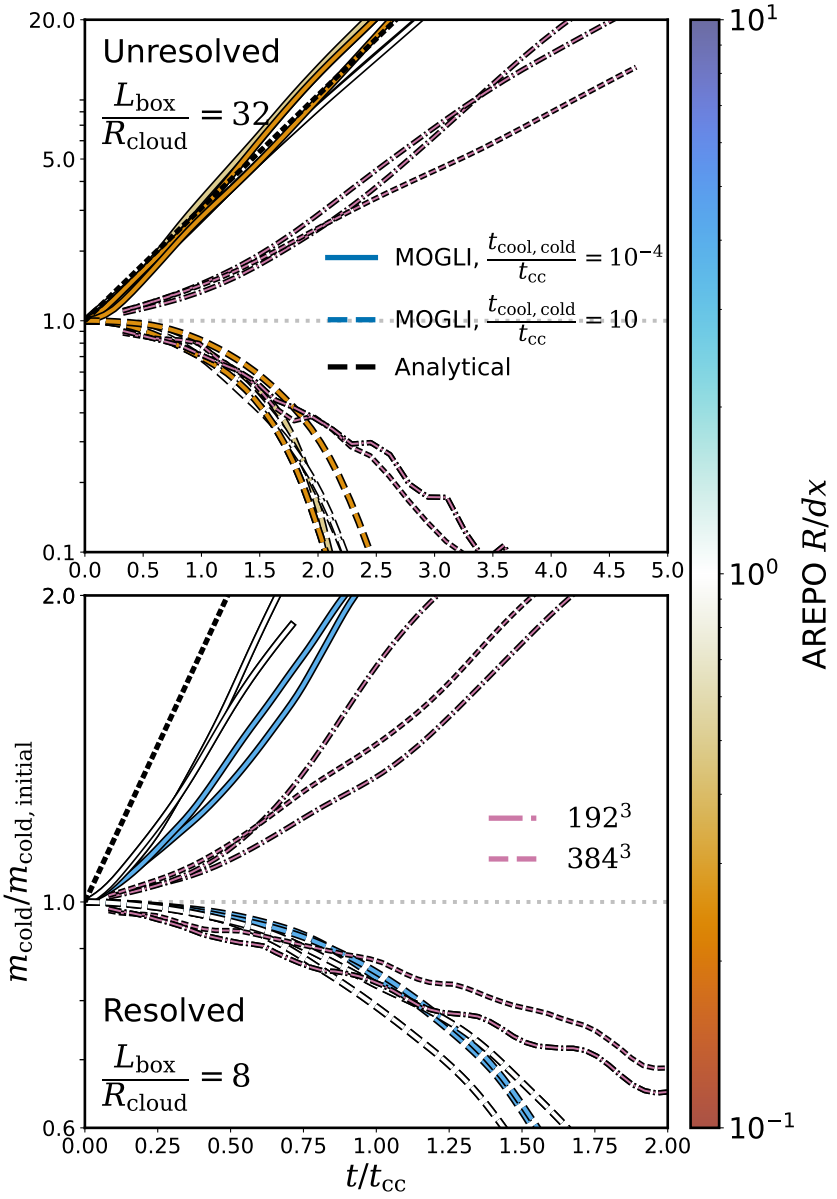

Figure 4.11: Cold gas evolution in MOGLI runs with time, normalised to the initial cloud-crushing time ($t_{\rm cc}$), with $\mathcal{M}_{\rm turb} = 0.5$. The two groups of solid and dashed curves correspond to $t_{\rm cool,cold}/t_{\rm cc} = \{10^{-4}, 10\}$. These lines show the cold gas evolution, as the total mass of the cold fluid, with the colour of the line denoting the initial $R_{\rm cloud}/dx$. *Top panel* shows the evolution for simulations with unresolved initial cloud $L_{\rm box}/R_{\rm cloud} = 32$ and *bottom panel* shows the same for resolved initial cloud $L_{\rm box}/R_{\rm cloud} = 8$. The black dashed line shows the expected exponential growth of the simulations which grow, with the growth time ($t_{\rm grow}$) calculated using Eq. (5.11). The purple dot-dashed and dashed lines show the cold gas evolution from analogous Athena++ benchmark runs, with 192^3 and 384^3 cells, respectively. We find a good agreement between the analytically expected growth rates and MOGLI runs.

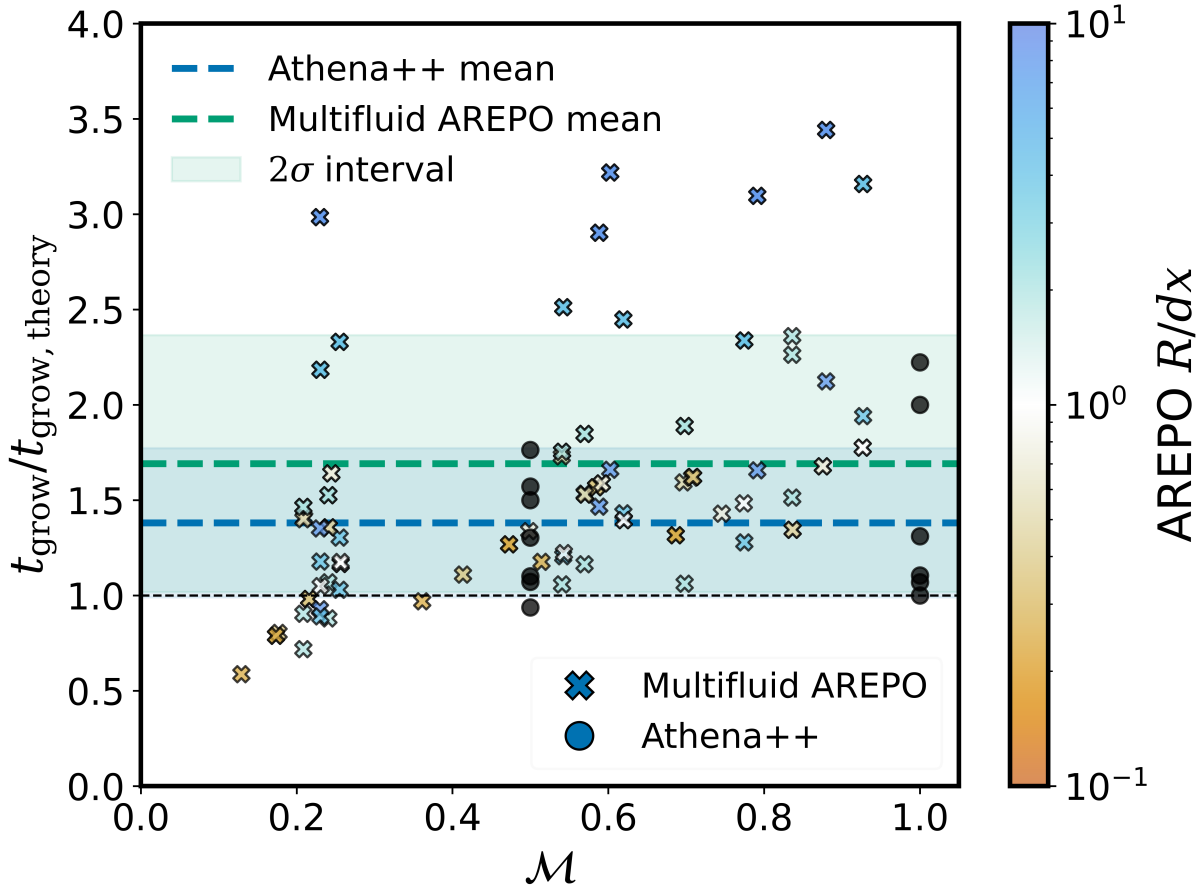

Figure 4.12: Scatter plot of the ratio of the $t_{\rm grow}$ from the simulations and the analytical $t_{\rm grow,theory}$ (Eq. (5.11)), across different turbulent Mach number ($\mathcal{M}$). Crosses show the values from the MOGLI runs, with the colours denoting their "Resolvedness" (R/dx), while the black circles show the values from benchmark `Athena++`. The set of points for benchmark `Athena++` include values calculated from simulations from Gronke et al. (2022b); Das & Gronke (2024b). We also show the means as dashed lines and 2σ intervals as shaded regions of the benchmark `Athena++` and MOGLI runs. The comparison shows only a marginal difference between the benchmark `Athena++` and MOGLI runs in the means with significant overlap between the scatter.

the Kolmogorov scaling-based turbulent velocity estimate. We use high-resolution Athena++ turbulent box simulations with resolved initial cold gas cloud as the benchmark to compare the multifluid simulations with the MOGLI subgrid model. For a model to be declared operational, we require the multifluid simulation to agree with the benchmark Athena++ simulations, even if the

- initial cold gas clump is resolved or unresolved, i.e., $R_{\rm cloud}/dx > 1$ or < 1, respectively.[9],
- resolution of the simulation is varied (dx), regardless of the "resolvedness" of the cloud,
- turbulent velocity is changed ($\mathcal{M}$),
- random driving of the turbulence is different.

In the next sections, we test the different parts of the model across this parameter space. First, we only add the contributions from drag and turbulent mixing of cold gas and verify this reduced version of MOGLI with the benchmark Athena++ simulations in Sec. 4.3.1. In Sec. 4.3.2, we verify the full MOGLI model again with small-scale high-resolution Athena++ simulations and results.

4.3.1 Non-radiative Mixing

We start with testing a reduced version of the MOGLI model. This is to independently verify the different parts of the model. For the first set of tests, we only include the contributions from $\dot{\mathbf{Q}}_{\rm drag}$ and $\dot{\mathbf{Q}}_{\rm mix}$, i.e. $\dot{\mathbf{Q}}_{\rm non-rad} = \dot{\mathbf{Q}}_{\rm drag} + \dot{\mathbf{Q}}_{\rm mix}$. This setup is analogous to the turbulent mixing of cold and hot gas in a non-radiative box, i.e. without radiative cooling.

We run the Athena++ turbulent box simulations and introduce a cold cloud after driving the turbulence, without radiative cooling. In the absence of cooling of the mixed gas, inevitably, the cold cloud loses mass at an approximately exponential rate. Fig. 4.7 shows the evolution of $m_{\rm cold}/m_{\rm cold,initial}$ with time normalised to initial cloud crushing timescale ($t_{\rm cc} = \chi^{1/2} R_{\rm cloud}/v_{\rm turb}$)[10]. We find that the mass evolution happens at approximately similar time-scales, in the MOGLI simulations using $\dot{\mathbf{Q}}_{\rm non-rad}$ and Athena++ benchmark simulations, with differences well within a factor of 2. We vary the $L_{\rm box}/R_{\rm cloud}$ in the range $[8, 64]$, resolution per direction in $[8, 64]$, turbulent Mach number, $\mathcal{M}$ in $[0.2, 0.75]$ and random seed for turbulence driving. Note that an exact match between the MOGLI runs and Athena++ benchmark runs is infeasible due to stochasticity of turbulence and differences in the numerical methods

In Athena++, we define cold gas mass as the total mass of gas cells with temperature below 8×10^4K and in MOGLI, the cold gas mass is the total mass of the cold fluid in the box. We calculate this for the snapshots separately and find the time taken for the total cold gas mass to reach half its initial value, i.e. $t_{\rm half}$. Fig. 4.8 shows a scatter plot of the half mass time ($t_{\rm half}$)

[9]Note that throughout the text, we use $R_{\rm cloud}$ refers to the size of the initial cold gas cloud. $l_{\rm cold}$ in the previous section refers to the cold gas length scale inside a particular grid cell.

[10]Throughout the text, $t_{\rm destroy}$ refers to the cold gas destruction timescale within the cell (cf. Eq. 4.12), while $t_{\rm cc}$ refers to the cloud destruction timescale of the initial cold gas cloud.

normalised to the initial cloud-crushing timescale, for different turbulent Mach numbers. As a benchmark, we use resolved Athena++ simulations with different resolutions (192^3, 384^3 and 768^3, represented by the colour of the point) and turbulence random seeds to capture the inherent stochasticity of cold gas destruction in a turbulent medium. Due to this inherent stochasticity, we show the mean and 2σ interval around the mean for the benchmark Athena++ and corresponding MOGLI simulations. For the MOGLI runs, the colour of the point in Fig. 4.8 shows how resolved or unresolved the initial cloud is via the ratio of the cloud radius and grid cell size (R/dx).

We find that the mean and scatter of the cold gas destruction from the subgrid model with the Kolmogorov turbulent velocity estimation agree well with the benchmark Athena++ and both cluster with a factor of ~ 2 near the analytical value of $\sim t_{\rm cc}$. This verifies that the source function contribution for mixing, $\dot{\mathbf{Q}}_{\rm mix}$ is working as expected and leads to a physically consistent behaviour.

4.3.2 Radiative mixing

Next, we include the remaining source function contribution for the growth of cold gas via mixing, $\dot{\mathbf{Q}}_{\rm grow}$. This gives us the full subgrid model for radiative mixing with $\dot{\mathbf{Q}} = \dot{\mathbf{Q}}_{\rm drag} + \dot{\mathbf{Q}}_{\rm mix} + \dot{\mathbf{Q}}_{\rm grow}$. With the full subgrid model, the MOGLI simulations are analogous to resolved turbulent box simulations with radiative cooling, similar to simulations in Das & Gronke (2024b); Gronke et al. (2022b).

We run the MOGLI simulations with different turbulent Mach numbers ($\mathcal{M}$) in [0.2, 0.75], multiple resolutions per direction in [8, 64], two different random seeds for turbulent driving and different values of $t_{\rm cool,cold}/t_{\rm cc}$. We calculate the value of $t_{\rm cool,cold}$ from the $t_{\rm cc} = \chi^{1/2} R_{\rm cloud}/v_{\rm turb}$ and required value of their ratio. We use our Athena++ runs with different resolutions, turbulent Mach numbers random turbulence seeds, and cold cloud sizes ($R_{\rm cloud}$) as the benchmark for comparison. This includes our simulations and the results from Gronke et al. (2022b); Das & Gronke (2024b).

Morphology

Fig. 4.9 shows the 2D maps of projected $\alpha\rho_{\rm cold}$ ($\int_{\rm los} \alpha\rho_{\rm cold} dz/L_{\rm box}$) plots at different times, for MOGLI runs with $\mathcal{M} = 0.5$ different $t_{\rm cool,cold}/t_{\rm cc}$ values. Two columns on the left show the evolution of an unresolved ($L_{\rm box}/R_{\rm cloud} = 32$) initial cloud and two columns on the right show the evolution of a resolved initial ($L_{\rm box}/R_{\rm cloud} = 32$) cold cloud for destruction and survival regimes. We find that the clouds for runs with short $t_{\rm cool,cold}$ show growth of cold gas, while the clouds in runs with longer $t_{\rm cool,cold}$ get destroyed, as expected from the results of previous studies (Gronke et al., 2022b).

Fig. 4.10 shows the early-time hot fluid mass flux ($\dot{m}_{\rm hot}$) slices, normalised with ratio of total hot fluid mass and eddy-turnover time ($m_{\rm hot,box}/t_{\rm eddy}$), for radiative MOGLI simulations with resolved and unresolved cold gas clouds, at $\mathcal{M} = 0.5$. The left panel shows a case of a resolved

cold gas cloud with 64^3 cells and $L_{\rm box}/R_{\rm cloud} = 8$, where the cloud is bigger than the grid cells and grid cells inside the volume of the cloud have an $\alpha = 1 - \alpha_{\rm floor}$. It is clear that cells located within the cloud lose hot mass and gain cold mass ($\dot{m}_{\rm hot} < 0$), while cold gas is being mixed into cells located just outside the cloud which thus gain hot mass and lose cold mass ($\dot{m}_{\rm hot} > 0$).

On the other hand, the right panel of Fig. 4.10 shows the slice from a MOGLI simulation with an unresolved cold gas cloud, 8^3 cells and $L_{\rm box}/R_{\rm cloud} = 32$. This shows how the model can distinguish between the interior and exterior of the resolved cloud and ensures that the mass exchange only occurs at the interface around the cloud. The dashed circles show the corresponding initial cold gas cloud size in the simulations.

Cold gas growth and survival

We use the same definition of cold gas as in Section 4.3.1, for both benchmark `Athena++` runs and MOGLI runs to calculate the cold gas mass in different snapshots and obtain the evolution of cold gas mass with time. Fig. 4.11 shows the temporal evolution of the cold gas, normalised to the initial cold gas mass, in MOGLI runs with $\mathcal{M} = 0.5$. We include simulations with two different cold cloud sizes ($L_{\rm box}/R_{\rm cloud}$), two values for $t_{\rm cool,cold}/t_{\rm cc} = \{10^{-4},\ 10\}$, two values for turbulence random seed and multiple resolutions. We only show the evolution till $m_{\rm cold,box} < 0.9 m_{\rm total,box}$, as beyond that point the growth of the cold gas stagnates due to the deficiency of hot gas in the box and the theoretical predictions from previous studies do not apply anymore. The colour of the lines shows how "Resolved" ($R/dx > 1$) or "Unresolved"($R/dx < 1$) the initial cold gas cloud is. We find that the MOGLI runs, regardless of the varied degrees of resolutions, also show growth of cold gas when $t_{\rm cool,cold} \ll t_{\rm cc}$ and destruction when $t_{\rm cool,cold} \gg t_{\rm cc}$, in agreement with the previous results using resolved single-fluid simulations (Gronke et al., 2022b; Das & Gronke, 2024b).

We run benchmark Athena++ simulations with the corresponding $t_{\rm cool,cold}/t_{\rm cc}$ and different resolutions and random instances of turbulence. Fig. 4.11 shows the benchmark Athena++ cold gas evolution in Fig. 4.11 for comparison. We find that even though the early evolution might vary marginally, the late-time growth rates are similar between the benchmark Athena++ and MOGLI runs, within the range of turbulent stochasticity and factor of 2. In Fig. 4.11, we also show the corresponding analytical, cold gas growth curve as black dashed lines, and the MOGLI runs agree well with the predicted exponential growth curve. The analytical growth timescale, $t_{\rm grow,theory}$, is given by (Gronke et al., 2022b)

$$\frac{t_{\rm grow,theory}}{t_{\rm cc}} = 0.5\,\chi \left(\frac{t_{\rm cool,cold}}{t_{\rm cc}}\right)^{1/2} \left(\frac{L_{\rm box}}{R_{\rm cloud}}\right)^{1/6}. \tag{4.34}$$

Note that while this equation is of the same form as the implemented Eq. (4.17), on a per-cell basis, it is important to point out that whether our simulations recover the correct global growth rate is far from obvious. This is due to undecidability problem of complex systems, like cellular automata (Kari, 1994), where the existence of a simpler set of rules that result in an intended emergent behaviour is not necessary.

Next, we quantitatively compare the cold gas growth rates between the benchmark Athena++ and the MOGLI runs. We calculate the cold gas mass doubling time and use it to calculate the $t_{\rm grow}$. Fig. 4.12 shows the ratio of the $t_{\rm grow}$ from the simulations and the analytical $t_{\rm grow,theory}$ from Eq. (5.11), across different turbulent Mach number ($\mathcal{M}$). Crosses denote the values from the MOGLI runs, with the colours denoting their "Resolvedness" (R/dx), while the black circles show the values from benchmark Athena++. The set of points for benchmark Athena++ include values of data from Gronke et al. (2022b); Das & Gronke (2024b). We also show the mean values as dashed lines and 2σ intervals as shaded regions, in blue for the benchmark Athena++ and in green for MOGLI runs. The comparison shows only a marginal difference in the means with significant overlap between the scatter of values from benchmark Athena++ and MOGLI runs. This verifies that the MOGLI subgrid model accurately captures the growth of cold gas to a reasonable extent.

Apart from growth rates, a working subgrid model should consistently agree with the survival criterion of cold gas clouds obtained in previous studies using resolved single-fluid simulations (Gronke et al., 2022b). In Fig. 4.13, we reproduce the survival plot from Gronke et al. (2022b) with MOGLI runs. It shows the survival or destruction of cold gas in the MOGLI runs, in a parameter space of $t_{\rm cool,mix}/t_{\rm cc}$ and turbulent Mach number ($\mathcal{M}$), where $t_{\rm cool,mix}$ refers to the cooling time of the intermediate mixed gas,

$$t_{\rm cool,mix} = t_{\rm cool}(T_{\rm mix}, \rho_{\rm mix}) \tag{4.35}$$

where the $T_{\rm mix} = \sqrt{T_{\rm cold} T_{\rm hot}}$ and $\rho_{\rm mix} = \sqrt{\rho_{\rm cold}\rho_{\rm hot}}$ are the temperature and density of the intermediate mixed gas (Begelman & Fabian, 1990b).

As the MOGLI runs only use the cold gas cooling time ($t_{\rm cool,cold}$), unlike our Athena++ runs which use a full cooling function, we assume the CIE cooling curve from Wiersma et al. (2009) (as used in the benchmark Athena++ runs) to evaluate $t_{\rm cool,mix} = \chi t_{\rm cool,cold}\Lambda(T_{\rm mix})/\Lambda(T_{\rm cold})$. For our choice of $T_{\rm cold}$, χ this results in $t_{\rm cool,mix} \approx 64 t_{\rm cool,cold}$

The circles in Fig.4.13 denote runs with “resolved” ($R/dx > 1$) initial cold clouds and crosses represent the “unresolved” ($R/dx \leq 1$) initial cold clouds and the colour of the points show the final cold gas mass, averaged over the last 10 snapshots and normalised with the initial cold gas mass. We show the survival criterion found in Gronke et al. (2022b) and confirmed in Das & Gronke (2024b) as a dashed black line along with annotation for the survival and destruction regimes. As there are a large number of points with very similar parameters, we randomly displace the points vertically by a factor of 1.5, for clarity. We find that the resolved MOGLI runs agree well with the survival criteria, while the unresolved runs agree within an order of magntude and show the expected trend. We also see some stochasticity in simulations that lie close to the criterion. This is an expected behaviour seen in resolved single-fluid simulations due to the inherent randomness of turbulence. This verifies the ability of the subgrid model to accurately reproduce the survival and destruction of cold gas as an emergent behaviour.

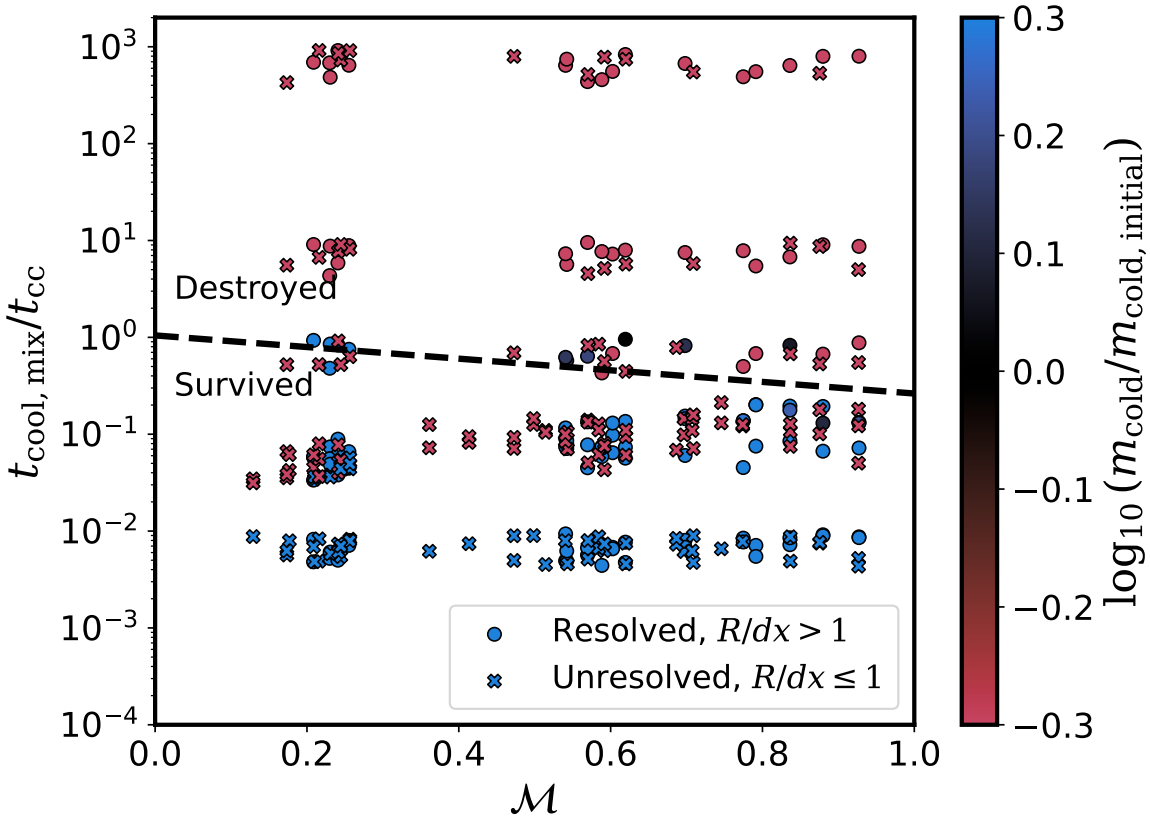

Figure 4.13: Scatter plot of survival or destruction of cold gas in the MOGLI runs, in a parameter space of $t_{\mathrm{cool,mix}}/t_{\mathrm{cc}}$ and turbulent Mach number, $\mathcal{M}$, where $t_{\mathrm{cool,mix}}$ (c.f. Eq. (4.35)). The circles show the points from resolved ($R/dx > 1$) MOGLI simulations, while crosses denote the unresolved ($R/dx < 1$) simulations. The colour of the points denotes the ratio of total final cold fluid mass, averaged over the last 10 snapshots, normalised to the initial value. The black dashed line shows the survival criterion from Gronke et al. (2022b), and we find that MOGLI can reproduce this survival criterion as an emergent behaviour. Note that the points are randomly shifted vertically by a factor of 1.5 for clarity.

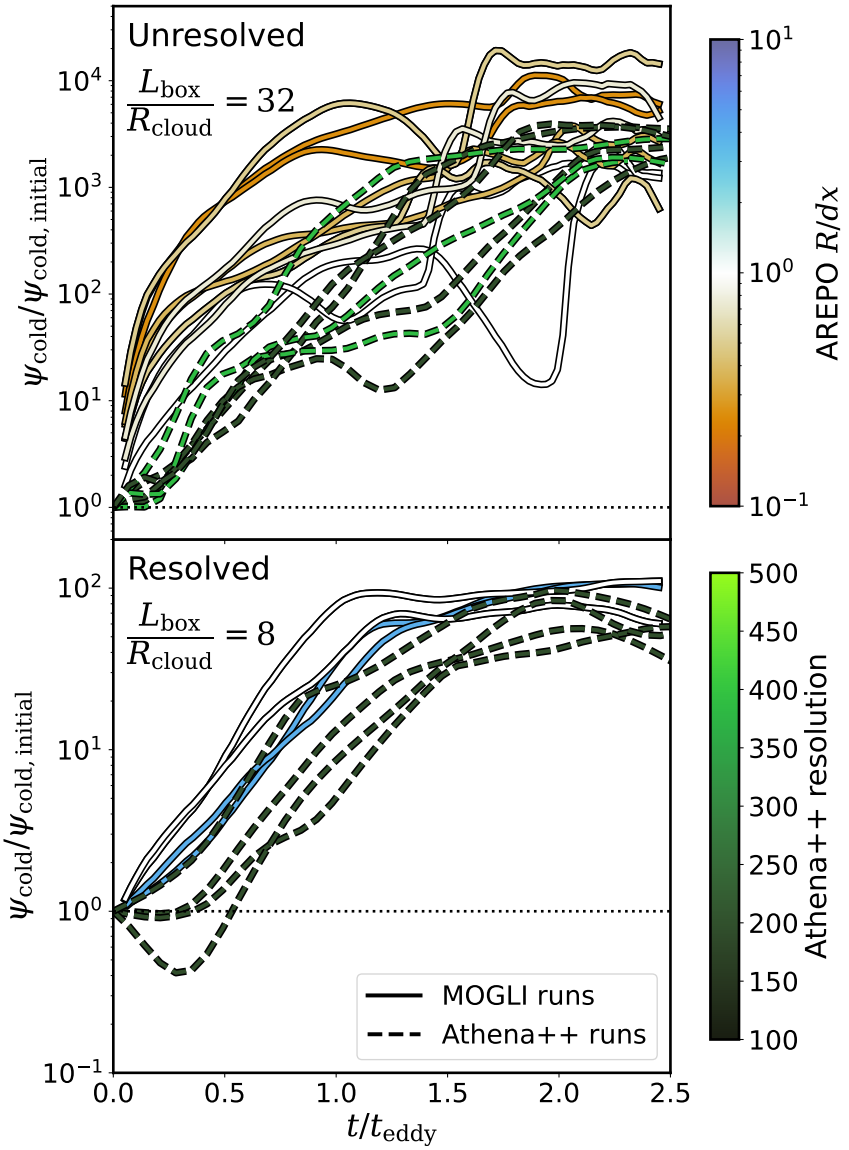

Figure 4.14: Evolution of the cold gas spatial dispersion, normalised to its initial value, in the benchmark `Athena++`, as dashed lines, and MOGLI runs, as solid lines, with time normalised with turbulent eddy turnover time. The colour of dashed lines shows the resolution of the `Athena++` simulations, while the colour of the solid lines shows the "resolvedness" of the initial cold cloud in the MOGLI runs, i.e. R/dx. *Left panel* shows the evolution of MOGLI runs with resolved initial clouds at $L_{\rm box}/R_{\rm cloud} = 8$, and the corresponding `Athena++` runs. *Right panel* shows the same but for MOGLI runs with unresolved initial cloud at $L_{\rm box}/R_{\rm cloud} = 32$, and the `Athena++` runs.

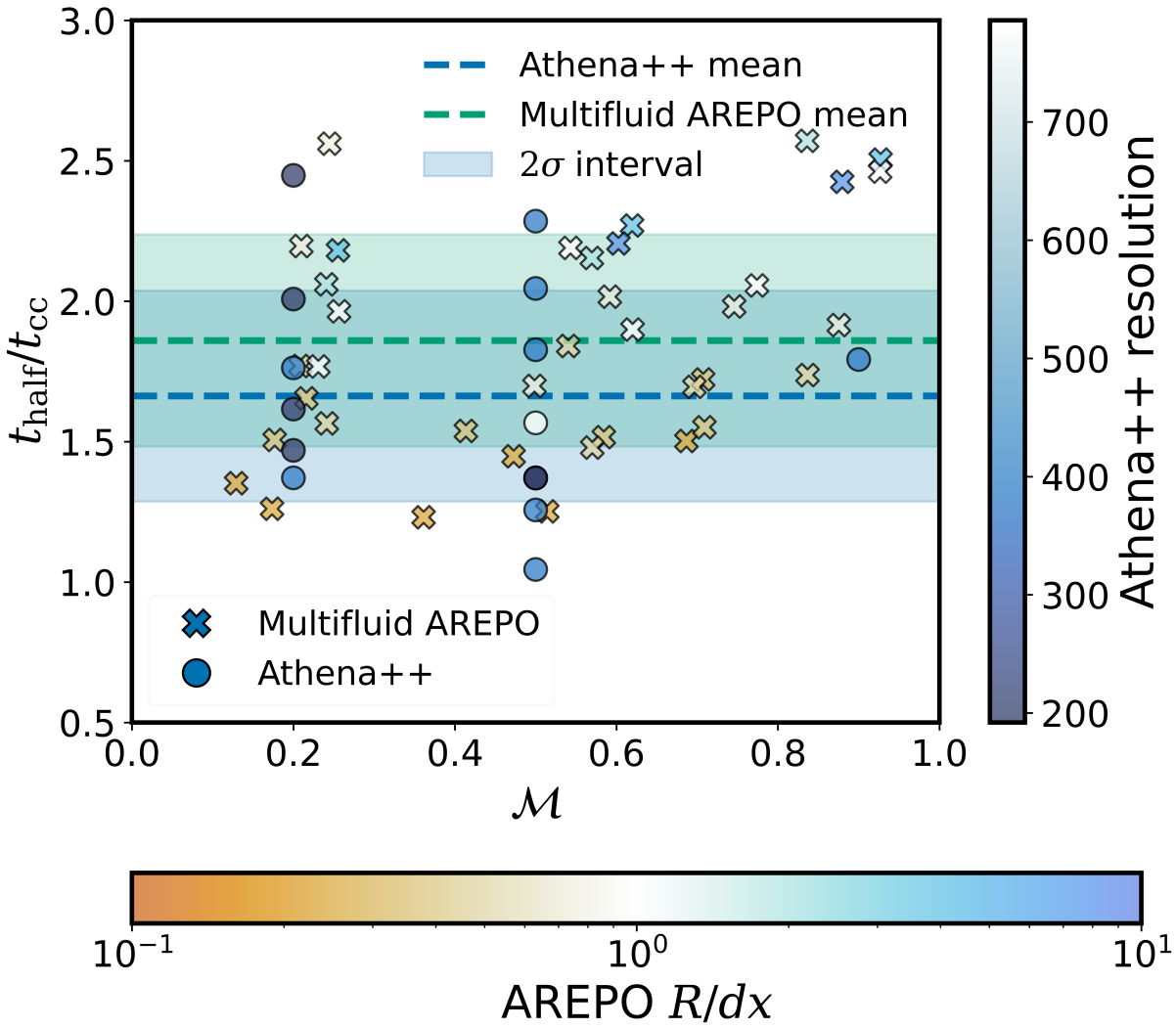

Figure 4.15: Same as Fig. 4.8 but with the gradient-based local turbulence estimation. Scatter plot of the half mass time ($t_{\rm half}$) normalised to the initial cloud-crushing timescale ($t_{\rm cc} = \chi R_{\rm cloud}/v_{\rm turb}$), for different turbulent Mach numbers. `Athena++` simulations with different resolutions (192^3, 384^3, and 768^3, represented by the colour of the point) and turbulence random seeds to capture the inherent stochasticity of cold gas destruction in a turbulent medium.

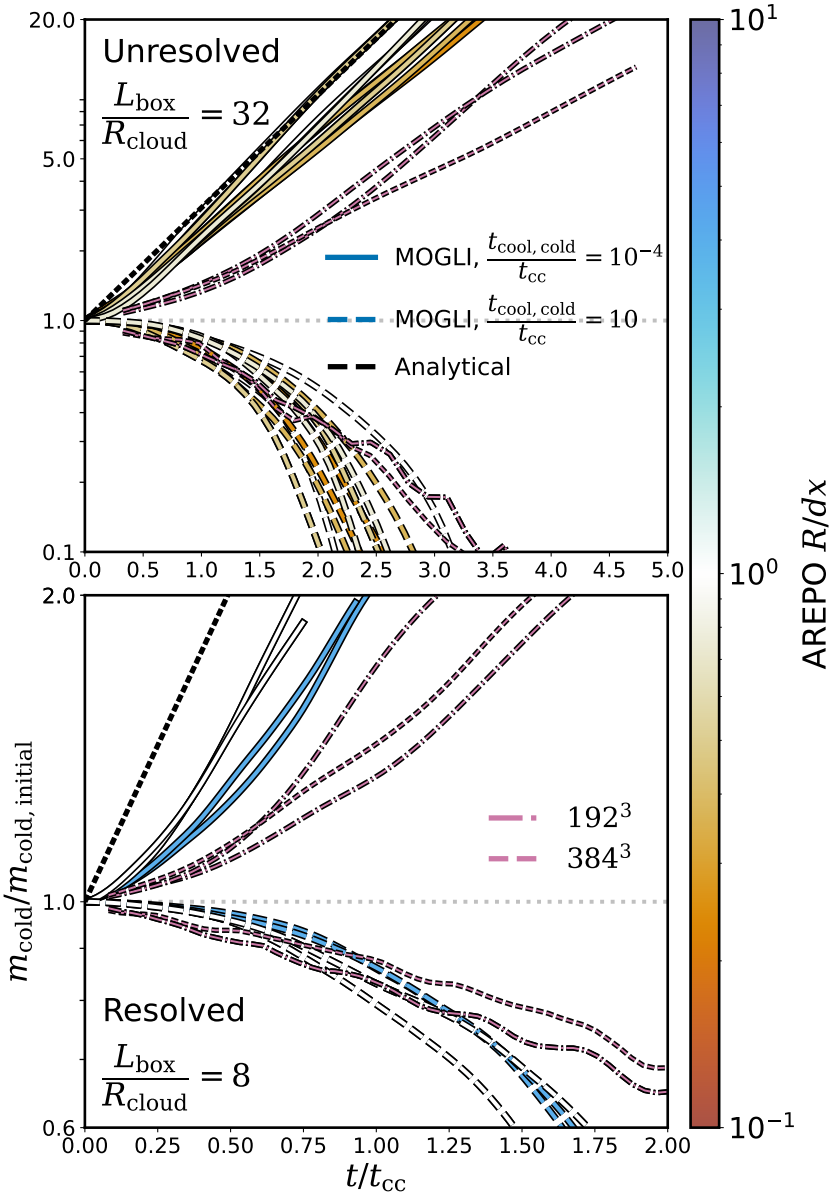

Figure 4.16: Same as Fig. 4.11 but with the gradient-based local turbulence estimation. Cold gas evolution in MOGLI runs with time, normalised to the initial cloud-crushing time ($t_{\rm cc}$), with $\mathcal{M}_{\rm turb} = 0.5$. The two groups of solid and dashed curves correspond to two different values of $t_{\rm cool,cold}/t_{\rm cc} = \{10^{-4}, 10\}$. The solid lines show the cold gas evolution, as the total mass of the cold fluid, with the colour of the line denoting the initial $R_{\rm cloud}/dx$. *Top panel* shows the evolution for simulations with unresolved initial cloud $L_{\rm box}/R_{\rm cloud} = 32$ and *bottom panel* shows the same for resolved initial cloud $L_{\rm box}/R_{\rm cloud} = 8$. The black dashed line shows the expected exponential growth of the simulations which grow, with the growth time ($t_{\rm grow}$) calculated using Eq. (5.11). The purple dot-dashed and dashed lines show the cold gas evolution from analogous Athena++ benchmark runs, with 192^3 and 384^3 cells, respectively. We find a good agreement between the analytically expected growth rates and MOGLI runs.

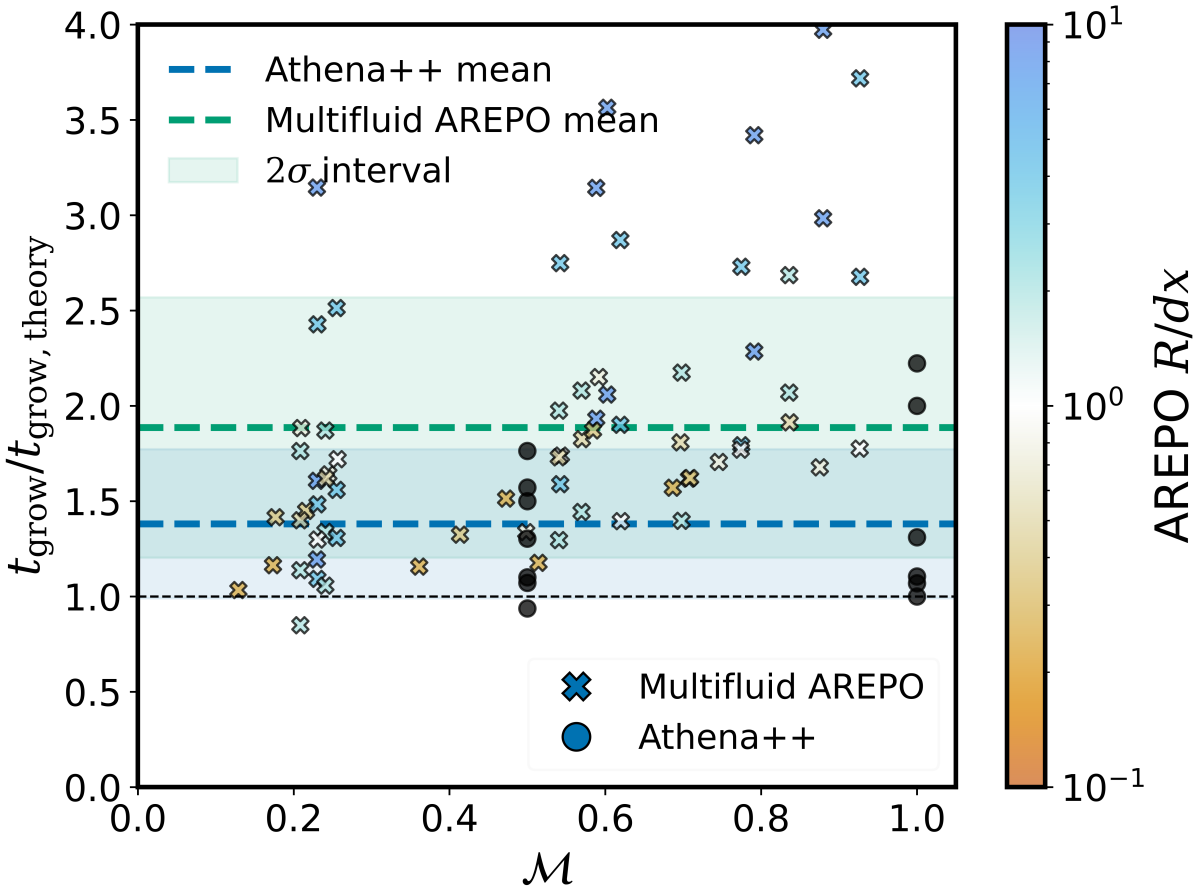

Figure 4.17: Same as Fig. 4.12 but with the gradient-based turbulence estimation. Scatter plot of the ratio of the $t_{\rm grow}$ from the simulations and the analytical $t_{\rm grow,theory}$ (Eq. 5.11), across different turbulent Mach number ($\mathcal{M}$). Crosses show the values from the MOGLI runs, with the colours denoting their "Resolvedness" (R/dx), while the black circles show the values from benchmark `Athena++`. The set of points for benchmark `Athena++` include values calculated from simulations from Gronke et al. (2022b); Das & Gronke (2024b). We also show the means as dashed lines and 2σ intervals as shaded regions of the benchmark `Athena++` and MOGLI runs. The comparison shows only a marginal difference between the benchmark `Athena++` and MOGLI runs in the means with significant overlap between the scatter.

Cold gas spatial dispersion

As the simulation evolves, the cold gas is expected to get progressively more spatially dispersed with time and can be an important mechanism for the transport of cold gas in large-scale simulations. We test for differences in the dispersion of cold gas in the benchmark Athena++ and MOGLI simulations. We define a quantity, ψ, as a proxy for the spatial dispersion of cold gas,

$$\psi_{\rm cold} = \prod_{i=[1,2,3]} \left[\frac{\sum_{\rm cold} m_{\rm cold}\ \delta x_{i,\rm com}}{\sum_{\rm cold} m_{\rm cold}} \right] \tag{4.36}$$

where, $\delta x_{i,\rm com} = |x_{i,\rm cell} - x_{i,\rm com,cold}|$ is the distance, along $i^{\rm th}$ axis, between the cold gas/fluid centre-of-mass and cell centre, in a periodic box. We run benchmark Athena++ and the corresponding MOGLI runs with initial $R_{\rm cloud} = 310\ c_{\rm s,cold} t_{\rm cool,cold}$, varying resolution and different turbulent random seed. We repeat this calculation on the snapshots from Athena++ and MOGLI runs to obtain the temporal evolution of the cold gas dispersion ($\psi_{\rm cold}$). Fig. 4.14 shows the temporal evolution of the $\psi_{\rm cold}$, normalised to its initial value, in the benchmark Athena++ as dashed lines, and MOGLI runs as solid lines. The colour of dashed lines shows the resolution of the Athena++ simulations, while the colour of the solid lines shows the "resolvedness" of the initial cold cloud in the MOGLI runs, i.e. initial R/dx. The top panel shows the evolution of MOGLI runs with unresolved initial clouds at $L_{\rm box}/R_{\rm cloud} = 32$, and the corresponding Athena++ runs. The bottom panel shows the same but for MOGLI runs with unresolved initial cloud at $L_{\rm box}/R_{\rm cloud} = 8$, and the Athena++ runs.

In general, in both "resolved" and "unresolved" cloud cases, while the cold gas dispersion is higher in MOGLI runs, the growth of dispersion follows qualitatively similar evolution with similar timescales[11]. The higher dispersion is likely due to the poorer resolution for the highly unresolved, i.e. low R/dx, which leads to higher numerical diffusion in volume fraction. This can be improved in future with a higher-order solver in the multifluid code, but the differences fall within an acceptable range for the current study.

With the above tests, we verify that the MOGLI model, with the Kolmogorov turbulence estimation, can capture all the different facets of cold gas behaviour, i.e. the survival, destruction rates, growth rates and cold gas dispersion in a turbulent medium, in an emergent way. In the next section, we repeat the verification tests from this section for MOGLI model with our new gradient-based local turbulence estimation method (grad).

4.4 Verification: With Velocity gradient-based turbulence estimation

As the Kolmogorov estimation method (kol) assumes isotropic and steady-state turbulence over the simulation domain, it cannot be applied in setups with evolving or strongly varying turbulence. For more general scenarios with temporal and/or spatial variation in turbulence, we need a method

[11] Interestingly, we find good agreement even though the cold gas has one bulk velocity per cell.

to estimate the local turbulent velocity from the local fluid properties. We implement the `grad` method for local turbulence estimation based on velocity gradients to get around this limitation of the `kol` method. As described in Sec. 4.2.6, we use the local velocity gradient calculated using neighbouring cells in `AREPO` (Pakmor et al., 2016) to estimate the velocity dispersion in the neighbourhood. Once we know the turbulent velocity in this neighbourhood, we scale it to the cold gas scales by assuming a fully developed Kolmogorov turbulence below those grid scales.

We repeat our verification tests from Section 4.3 to confirm the accuracy of MOGLI with the gradient-based turbulent velocity estimation. We start with checking the non-radiative turbulent mixing rates. Fig. 4.15, analogous to Fig. 4.8, shows the cold gas half time for non-radiative MOGLI runs ($\dot{\mathbf{Q}} = \dot{\mathbf{Q}}_{\rm drag} + \dot{\mathbf{Q}}_{\rm mix}$) with the `grad` method. For the `grad` method, we find a slightly higher separation between the mean of the benchmark `Athena++` and MOGLI runs, and a wider scatter in both cases when compared to the `kol` method of estimation. The differences are minimal and within acceptable limits. So, we can conclude that the `grad` method works well for non-radiative mixing.

For the full model, i.e., including radiative mixing, first, we check the evolution of cold gas mass evolution in Fig. 4.16, analogous to Fig. 4.11. It shows the same behaviour where, regardless of the resolution, the clouds with faster cooling time, i.e. $t_{\rm cool,cold}/t_{\rm cc} \ll 1$, grow at expected rates while the clouds with slow cooling, i.e. $t_{\rm cool,cold}/t_{\rm cc} \gg 1$, get destroyed. Subsequently, we repeat the quantitative verification of the growth rates in Fig. 4.17, similar to the comparison made in Fig. 4.12. We find marginally higher differences in the mean value of $t_{\rm grow}/t_{\rm grow,theory}$ (cf. Sec. 4.3.2) of the benchmark `Athena++` runs and MOGLI runs, in comparison to the differences with `kol` method, while the standard deviation is similar.

Next, we verify the emergent survival criterion from MOGLI with the `grad` estimation. In Fig. 4.18, we show the survival and destruction of the cold cloud, analogous to Fig. 4.13. We find that the MOGLI runs still agree well with the survival criterion from Gronke et al. (2022b), albeit slightly worse than the `kol` method.

Finally, we check for any differences in the dispersion of cold fluid using the local turbulent estimator. Fig. 4.19 shows the evolution of cold gas dispersion $\psi_{\rm cold}$ (cf. Eq. 4.36 in Sec. 4.3.2), analogous to Fig. 4.14 for `kol` method. We find that the cold gas dispersion follows an almost identical evolution with `grad` method, in Fig. 4.19 as with `grad` in Fig. 4.14.

With the series of tests above, we can conclude that MOGLI model with the velocity gradient-based local turbulence estimation (`grad`) method also accurately captures the subgrid behaviour of cold gas with a good agreement with the benchmark `Athena++` and analogous MOGLI runs with the `kol` simulations. Since the average turbulence estimates are consistent and the agreement between MOGLI and the resolved `Athena++` runs was demonstrated in the previous section, this outcome is unsurprising. However, this assumption does not hold for simulations focused on local measures (e.g., local dispersion) or where gas flows vary significantly, making a 'global' concept of turbulence inapplicable. In summary, we find the `grad` method to be more suitable for most astrophysical applications and thus adopt it as the default in MOGLI. Nonetheless, the initial comparison with the simpler `kol` method provides a valuable opportunity to isolate and

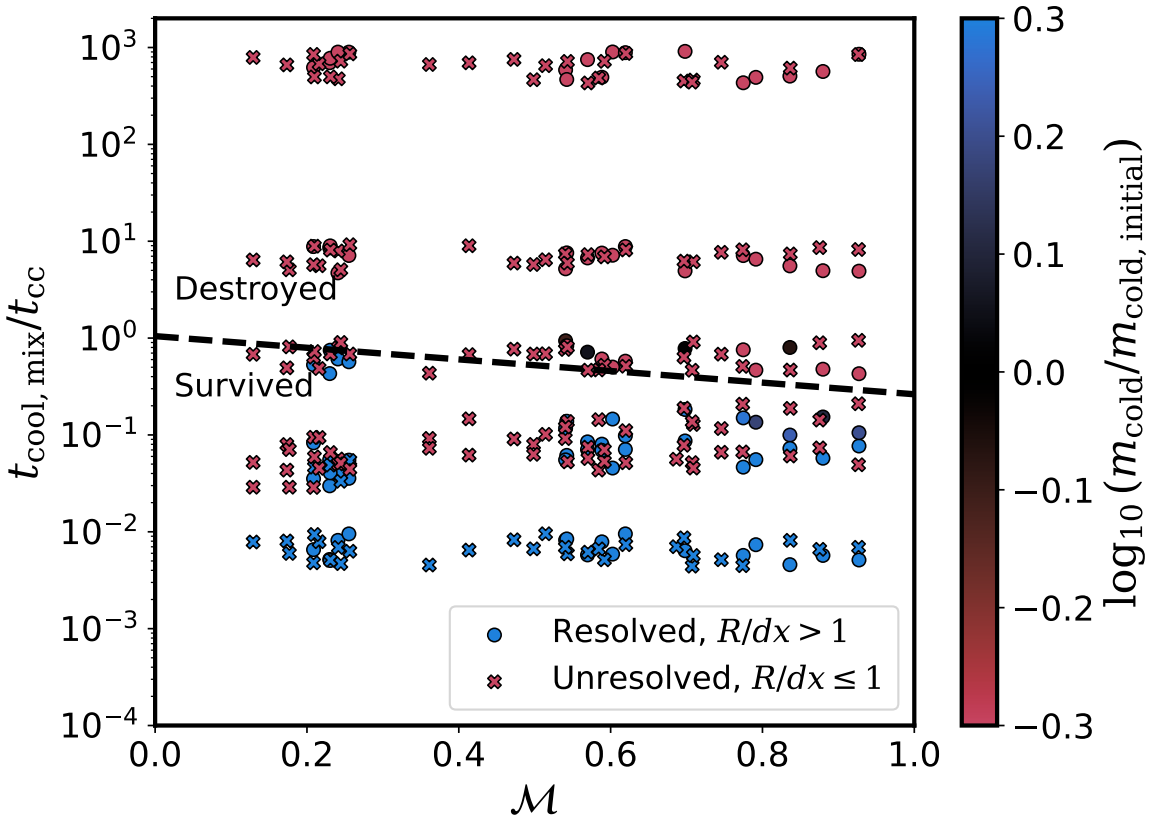

Figure 4.18: Same as Fig. 4.13 but with the gradient-based turbulence estimation. Scatter plot of survival or destruction of cold gas in the MOGLI runs, in a parameter space of $t_{\mathrm{cool,mix}}/t_{\mathrm{cc}}$ and turbulent Mach number, $\mathcal{M}$, where $t_{\mathrm{cool,mix}}$ (c.f. Eq. (4.35)). The circles show the points from resolved ($R/dx > 1$) MOGLI simulations, while crosses denote the unresolved ($R/dx < 1$) simulations. The colour of the points denotes the ratio of total final cold fluid mass, averaged over the last 10 snapshots, normalised to the initial value. The black dashed line shows the survival criterion from Gronke et al. (2022b), and we find that MOGLI can reproduce this survival criterion as an emergent behaviour. Note that the points are randomly shifted vertically by a factor of 1.5 for clarity.

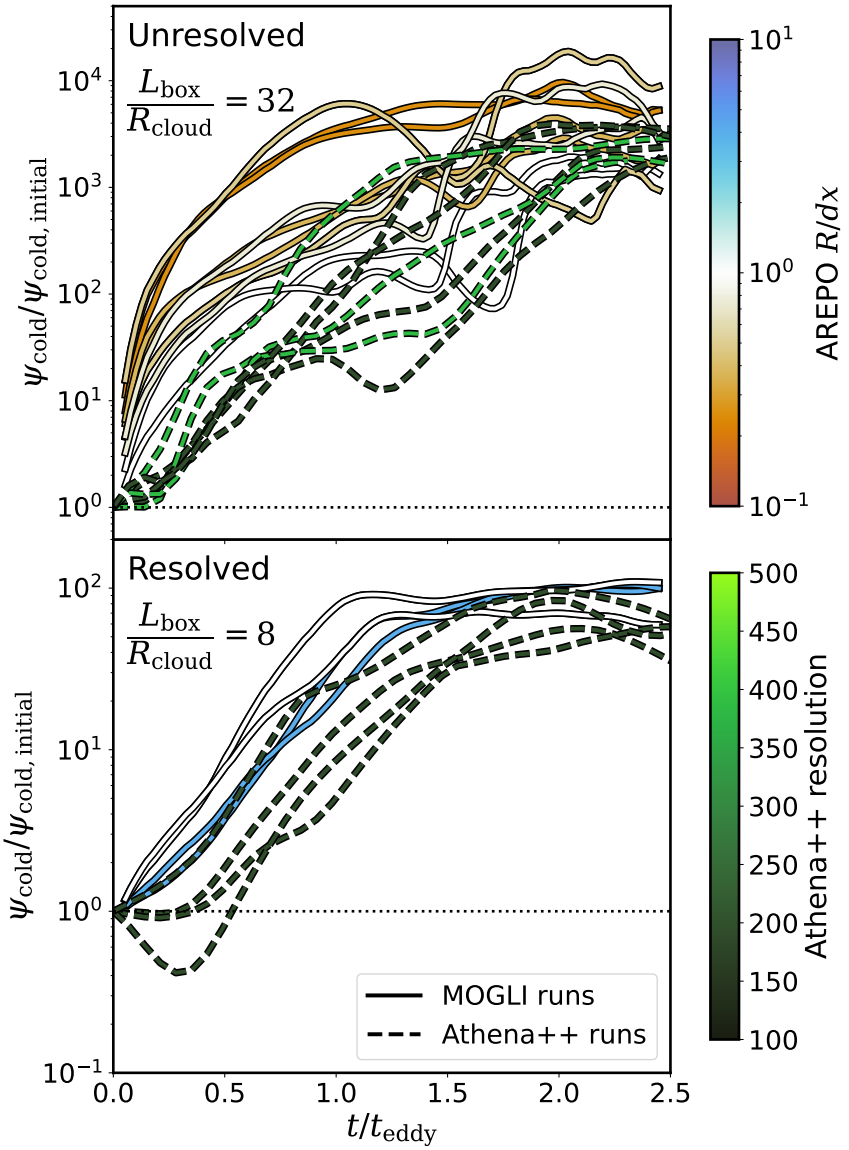

Figure 4.19: Same as Fig. 4.14 but with gradient-based turbulence estimation. Evolution of the cold gas dispersion, normalised to its initial value, in the benchmark `Athena++`, as dashed lines, and MOGLI runs, as solid lines, with time normalised with turbulent eddy turnover time. The colour of dashed lines shows the resolution of the `Athena++` simulations, while the colour of the solid lines shows the "resolvedness" of the initial cold cloud in the MOGLI runs, i.e. R/dx. *Top panel* shows the same but for MOGLI runs with unresolved initial cloud at $L_{\rm box}/R_{\rm cloud} = 32$, and the `Athena++` runs. *Bottom panel* shows the evolution of MOGLI runs with resolved initial clouds at $L_{\rm box}/R_{\rm cloud} = 8$, and the corresponding Athena++ runs.

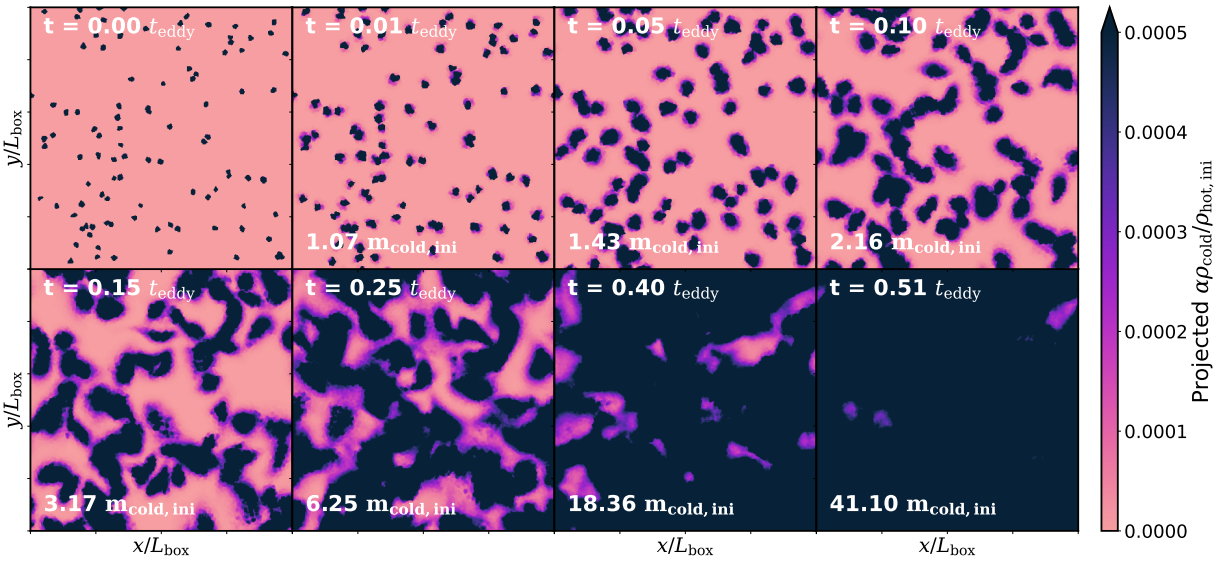

Figure 4.20: Evolution of projected $\alpha\rho_{\rm cold}/\rho_{\rm hot,ini}$ for a turbulent box with MOGLI, `grad` method, 64^3 cells, 100 unresolved clouds with a radius $L_{\rm box}/256$, where $L_{\rm box}$ is the box size, and $t_{\rm cool}/t_{\rm cc} = 5\times10^{-4}$. The unresolved clouds grow and subsequently fill the box due to its finite size. We will need a box with $\sim 3000^3$ cells to run an analogous simulation in a single-fluid code without a subgrid model.

understand the underlying physical mechanisms.

4.5 Discussion

4.5.1 Model showcase

After the testing and verification of the MOGLI model in Sec. 4.3 & 4.4, we can use it to simulate a setup to show the strengths of such a model. We simulate a turbulent box with 64^3 cells and $\mathcal{M} = 0.5$, and introduce 100 unresolved clouds with a radius of $L_{\rm box}/256$, where $L_{\rm box}$ is the box size. To run an analogous setup in a single-fluid simulation code without a subgrid model, we need to resolve the individual clouds with around 10 cells across their radius, hence requiring a single-fluid simulation with $\sim 3000^3$ cells. Such single-fluid simulations require a considerable computational cost, while our analogous MOGLI multifluid simulation can capture the relevant cold gas evolution with just a 64^3 cells simulation with negligible computational cost. Fig. 4.20 shows the evolution projected $\alpha\rho_{\rm cold}/\rho_{\rm hot,ini}$ for the showcase simulation using our MOGLI model with the `grad` local turbulence estimation method.

This shows the potentially massive savings in computational times with the MOGLI model, over a brute force method of resolving the cold gas structures in a single-fluid code without a subgrid model allowing for configurations infeasible with traditional single-fluid simulations. We plan to study several such scenarios in future work.

4.5.2 The need for a multiphase subgrid model

With the ISM, CGM, and ICM, multiphase media are ubiquitous in and around galaxies and, thus, crucial to our understanding of galaxy formation and growth. Not only is the new fuel for star-formation channelled through the multiphase galactic halos (see reviews by Donahue & Voit, 2022; Faucher-Giguère & Oh, 2023b) but gas is also expelled from galaxies through multiphase galactic winds (Veilleux et al., 2020b; Heckman & Thompson, 2017). Even the gas within the galaxy is highly multiphase with a much wider range of temperatures, from $\sim 10^2$K gas in molecular gas to $> 10^7$K gas in supernova ejecta. Thus, correctly modelling multiphase gas dynamics is the foundation of accurately modelling gas transport, its conversion into stars and their subsequent impact on the galaxy when they end in supernovae and lead to feedback. Hence, understanding multiphase gas is a cornerstone of understanding the wider baryon cycle.

While great strides are being made to model the interstellar medium including its multiphase nature correctly in dedicated, small domain simulations (Walch et al., 2015; Kim & Ostriker, 2017), this is much more problematic in a larger scale, cosmological simulations. Nevertheless, modern large-scale cosmological simulations using 'zoom in' and adaptive techniques, based on targeting a mass resolution, manage to reach a parsec-scale resolution in certain dense regions within the ISM while at the same time capturing the effects of the larger environment.

However, the same techniques cannot be applied to the halo of galaxies spanning ~ 100 kpc in radius (for a Milky Way-sized galaxy at $z \sim 0$; Tumlinson et al., 2017). In these large volumes, recent observations constrain the upper limit to the size of this cold gas to be $\lesssim 10$ pc (Lan & Fukugita, 2017; Crighton et al., 2015; Schaye et al., 2007; Rauch et al., 1999). This implies that simulation of a single halo would require at least $(100,000)^3$ resolution elements – a task infeasible even for the next generation of supercomputers. For example, modern cosmological simulations require tens of millions of CPU hours to simulate $\sim 10^9$ particles/cells (e.g., `THESAN`, Kannan et al., 2022). Extrapolating this figure to $(100,000)^3$ cells, we would need $\sim 10^7$ million core hours. Thus, even an optimally parallelised run on one million cores (approximately the number of CPU cores on the exascale supercomputer El Capitan) such a run would take 10^7 hours, i.e. ~ 1000 years. Of course, this is a simplified approximation; however, it still illustrates the point that even next-generation exascale machines will not be able to resolve the CGM structure observed to date.

The inability of modern cosmological simulations to achieve the resolution needed to model the (observed) cold gas structures found in the halos directly comes from the fact they are non-converged in even the most basic cold gas properties such as the amount of $\sim 10^4$ K gas found (see extensive discussion of this in the literature, e.g., Faucher-Giguère & Oh, 2023b; van de Voort et al., 2021; Hummels et al., 2024; Ramesh & Nelson, 2024a; Peeples et al., 2019). This implies that when comparing such simulations to CGM observables, it is impossible to know whether a (mis)match is due to the physics implemented in this simulation (e.g., the feedback mechanisms, and star formation models) or if this is a transient agreement that would vanish with a higher resolution.

In addition, while the simulation projects mentioned above can significantly increase the number

of resolution elements in the CGM, it is important to note that all these projects start with cosmological zoom simulations of individual halos in which memory usage is not as much of an issue. However, to study cold gas microphysics across the galaxy population, this technique would have to be applied to a large number of halos, posing significant additional requirements on the available memory. Since modern uniform mass resolution galaxy formation simulations are limited not solely by compute resources but also by memory, such an undertaking would only allow very limited increases in the number of resolution elements per halo, with no prospects to resolve the required spatial scales any time soon.

This limitation due to a highly multiscale problem is not new to astrophysics. For about two decades now, we have known that supernovae feedback – taking place on initially minuscule scales – is crucial to shaping galaxy morphology (e.g. Naab & Ostriker, 2017). The way these indispensable 'feedback' processes are modelled in astrophysical simulations is through a 'subgrid model', that is, by including their effects on larger scales through (empirical) source and sink terms.

Our model MOGLI is exactly such a subgrid model but for a two-phase multifluid medium. While it is not the first model of this kind (cf. § 4.5.3 for a comparison to previous work), it includes *(i)* a solid Eularian-Eularian numerical framework common in engineering (Weinberger & Hernquist, 2023a) implemented in the popular code `AREPO` (Weinberger et al., 2020; Springel, 2010), and *(ii)* coupling terms between the phases based on and verified with small-scale simulations and combustion inspired theory (Tan et al., 2021; Gronke et al., 2022b).

This solid foundation implies that the number of free parameters in our model is at a bare minimum, i.e. it includes only two free parameters. Only in Eq. (4.15), the $\dot{m}_{\mathrm{cold}\rightarrow\mathrm{hot}}$ includes a fudge parameter for the α_{mass} threshold, and in Eq. (4.29), $v_{\mathrm{turb,grad,MOGLI}}$ includes ξ_{MOGLI} (which is within a factor of ~ 2 of the theoretically expected value). Such a low number of free parameters is important, in general, for a subgrid model to preserve the predictive power of the simulations – but especially for a multiphase subgrid model such as MOGLI, as all cells are affected by it. Thus, allowing for more degrees of freedom by, for example, altering directly the amount of cold gas found in the halo would diminish the predictive power rapidly.

Naturally more work is required (cf. § 4.5.4) but this work is a strive in the right direction to ultimately model the multiphase gas in and around galaxies in a converged manner.

4.5.3 Previous work

As multiphase media are common in terrestrial applications, numerical tools to model them are extensively developed and widely used in various engineering disciplines, such as chemical, mechanical, and civil engineering. For example, in chemical engineering, they are critical for simulating processes like distillation, fluidized bed reactors, and mixing in multiphase reactors. In mechanical engineering, they enable the design and optimization of cooling systems involving liquid-vapor interactions, such as in heat exchangers and condensers. In civil engineering, they play a key role in understanding and managing subsurface flows, including groundwater contamination, oil recovery, and sediment transport in rivers (Prosperetti & Tryggvason, 2007).

In astrophysics, however, dedicated methods to model multiphase flows are less used – with some notable exceptions. Semelin & Combes (2002), for instance, already included a 'warm' ($> 10^4$ K) and a 'cold', pressureless phase as two separate fluids in their SPH scheme (alongside stars and dark matter) with the colder one being modelled via a 'sticky particle scheme' (Levinson & Roberts, 1981), thus, allowing the particles to inelastically collide with each other. They include the possibility for 'warm' particles to cool down and turn into 'cold' ones, and vice-versa to evaporate 'cold' particles due to supernovae feedback. Using this scheme, Semelin & Combes (2002) successfully perform a simulation of an isolated disk galaxy and study its evolution. While their source/sink terms are relatively large-scale and simplified, their approach represents a pioneering step toward incorporating multiphase processes in galaxy modelling (also see Berczik et al., 2003 for a similar implementation or Harfst et al., 2004 for an extension to three phases).

A similar approach is followed by Scannapieco et al. (2006), who instead of using two different particle types in their SPH scheme, 'decouple' particles with low entropy (essentially corresponding to a cold phase), thus, allowing neighbouring particles with different thermal properties. This implementation is meant to address the 'overcooling problem' where the energy of a supernova ejected in the dense medium is instantly lost (e.g. Kim & Ostriker, 2015; Smith et al., 2018). While the multiphase implementation of Scannapieco et al. (2006) is not specifically targeting galactic winds, their supernovae feedback implementation results in a separation of nearby particles into 'hot' and 'cold' ones, and, thus leads to an efficient wind launching. Their algorithm can thus be seen to be more in line with the more recent developments of SN ejected winds where particles are also decoupled (Springel & Hernquist, 2003; Okamoto et al., 2005; Oppenheimer & Davé, 2006).

More recently, the multiphase nature of galactic winds has led to the development of several Eulerian-Lagrangian subgrid models where the cold phase is represented by particles within a hot gas cell (Huang et al., 2020; Smith et al., 2024). In these models, physically motivated source and sink terms between the phases akin to the ones used in this study have been implemented[12].

Our work can be seen as a continuation of these efforts using different numerical means. While the previous astrophysical work mentioned above has focused on a colder phase represented via a particle, we have created a two-phase (a $\sim 10^4$ K and a 'hot' $\gtrsim 10^6$ K phase) Eulerian-Eulerian subgrid model using the multifluid implementation of Weinberger & Hernquist (2023a) and coupling terms inspired by combustion theory which was validated previously using a range of small-scale numerical simulations (Ji et al., 2019; Tan et al., 2021; Gronke et al., 2022b; Tan et al., 2023). This implementation has the advantage that it can especially capture multiphase, turbulent media – which are ubiquitously found in astrophysics, such as in the CGM, ICM and galactic winds – as well as the cold gas disperses naturally.

In this regard, our approach is similar to the two-fluid model implemented in `ENZO` by Butsky et al. (2024) during the work on this model. Note, however, that our cold fluid is represented as a compressible second fluid while their cold phase is assumed to be pressureless. While both

[12]Note that subgrid model of Huang et al. (2020) does not include cold gas mass growth whereas the Smith et al. (2024) model does.

should yield the same result in the case of vanishing volume filling fractions and temperature of the cold phase, a pressureless fluid can only represent unresolved cold clouds. The transition to marginally resolved or even fully resolved clouds where the pressure of the cold fluid displaces the hot fluid, i.e. the main focus of this work, cannot be modelled in the pressureless approach. This also results in differences in source terms: their coupling terms between the phases are inspired by the classical 'cloud crushing' problem, i.e., the interaction of a laminar hot wind and a cold cloud (e.g., Klein et al., 1994b) with the individual cold gas cloudlets radii being $r_{\rm cl} \approx \min(c_{\rm s} t_{\rm cool})$ inspired by the 'shattering' scenario (McCourt et al., 2018). In contrast, the presented work allows full flexibility in the respective volume filling fractions and allows, specifically, also the case where the typical length and timescales of unresolved and resolved processes are comparable. Thus, we needed to generalise the source terms to account for the finite availability of hot gas, of 'shielding' of inner layers of resolved cold clouds and geometric considerations of the change in surface area when a substantial fraction of a cell is filled with cold gas and generally cannot assume an instantaneous equilibration of the cold gas into a universal cloud radius or cloud mass function.

Both Eulerian-Eulerian and Eulerian-Lagrangian multifluid models have advantages and disadvantages. Notably, in the Eulerian-Lagrangian approach the particles representing the cold phase have zero extents. Thus, reproducing the dispersion of the cold medium (cf. § 4.3.2) would require particle splitting/merging which is currently not implemented in these models. This is in particularly crucial since multiphase gas exhibits a large amount of fragmentation and dispersion (cf. § 4.3.2, also Gronke et al., 2022b; Mohapatra et al., 2022b; Fielding et al., 2023a) leading commonly to large areal covering fractions observed, e.g., in the CGM (see, e.g., review by Tumlinson et al., 2017). On the other hand, Lagrangian-Eulerian subgrid models can represent several bulk flows within one cell which might be advantageous in modeling fountain flows[13].

The different subgrid implementations found in the literature do not just differ in the exact numerical implementation but also in terms of their goals and philosophy. While most of the above discussed aim directly for a large-scale application, no comparison of the emergent behavior to smaller-scale resolved hydrodynamical simulations is done – as was carried out here (as well as in Butsky et al., 2024). While such a comparison is somewhat tedious, it is crucial to ensure robustness a while keeping the amount of free parameters to a minimum.

4.5.4 Limitations and future directions

Although our model MOGLI takes a step in the direction of capturing the rich physics of small-scale cold gas structures, many aspects of the multiphase gas are still open questions and remain to be investigated in both small-scale simulations and subgrid modelling. Some of such aspects are:

- *Magnetic fields*: Although magnetic fields can suppress mixing via hydrodynamical instabilities like Kelvin-Helmholtz instabilities (Chandrasekhar, 1961; Ji et al., 2019),

[13] When considering different levels of fluid discretization, one must also account for realistic turbulent diffusion, which often dominates in multiphase systems (e.g. Tan et al., 2021).

as shown in Das & Gronke (2024b), the mixing properties depend only on the turbulent velocities. Hence, MOGLI model should remain unchanged with or without magnetic fields.

- *Thermal conduction*: In the turbulent mixing of cold gas, the eventual mixing of cold gas is via thermal conduction at molecular diffusion scales. Such small scales are not resolved in our simulations, but as shown in Tan et al. (2021), the turbulent mixing is rate-limited at the scales of the largest eddy, and is converged with the largest eddy scales are well resolved. Although, in our simulations, the thermal conduction is numerical, due to the rate-limiting nature of the largest scale, we expect the multiphase gas behaviour to be unchanged.

- *Viscosity*: Similar to thermal conduction, viscosity operates at very small scales and can change the small-scale turbulent properties. Even though we have numerical viscosity in our simulations, due to the same rate-limiting nature of largest eddies in turbulent mixing, with grid cells larger than the viscous scales, the multiphase gas properties are expected to be unaffected. While viscosity can potentially change the microturbulent properties of the 'laminar' cooling front on small scales, and thus, affect the form of our coupling terms (cf. Tan et al., 2021), it has recently been shown in small-scale simulations that even strong viscosity has a weak effect on the mass transfer rate due to the competing effect of cooling (Marin-Gilabert et al., 2025).

Apart from the limitations mentioned above, there are many directions the MOGLI can be improved and expanded in future studies. One such improvement can be to include a more sophisticated subgrid turbulence model (Schmidt & Federrath, 2011; Semenov, 2024). Currently, MOGLI does not account for in-situ formation of cold gas from hot gas via processes like thermal instability (Field, 1965; McCourt et al., 2018; Sharma et al., 2010). This will enable the creation of the initial seed cold gas which can later grow further via turbulent mixing included in the MOGLI model.

Another avenue for refining the model is the inclusion of other phases. It is clear from observations that colder (< 8000K) gas exists (McKee & Ostriker, 1977a; Cox, 2005), which points to the existence of a three-phase gas, with much more rich physics and complex interactions among the phases (Farber & Gronke, 2021; Chen & Oh, 2024). Three-phase turbulent gas is still a relatively unexplored system and detailed investigations with small-scale simulations are required before a theory can be developed to be included in MOGLI.

While several ingredients are still missing, this work represents a first step for multi-fluid cosmological simulations. These next generation of large-scale simulations would overcome the vexing converging issue in particular in the CGM that current models suffer (see discussion in § 4.5.2). In contrast – as demonstrated in § 4.3.2 – the total cold gas mass of MOGLI is independent of resolution, and thus can lead to converged large-scale simulations and a robust comparison to observations. To do so, however, it is important to recall that multi-fluid simulations are not as easily interpretable as single-phase ones. For instance, the sub-resolution morphology and kinematics have to be defined as both absorption (Hummels et al., 2017; Singh Bisht et al., 2024; Rudie et al., 2019) as well as emission (e.g. Gronke et al., 2016; Hansen & Oh, 2006;

Chang & Gronke, 2024) crucially depends on them. While some results (such as the clump mass distribution; Gronke et al., 2022b; Tan & Fielding, 2023) are already known, and more small-scale simulations are needed to parametrize this information. This information can then be used to alter tools such as `Trident` (Hummels et al., 2017) to make them aware of the subgrid details in a multi-fluid simulation.[14]

4.6 Conclusions

In this study, we introduce our new MOGLI subgrid model to account for the subgrid cold gas behaviour, using multifluid hydrodynamics. We use the theoretical framework developed and confirmed in previous work (Fielding et al., 2020; Tan et al., 2021; Gronke et al., 2022b; Das & Gronke, 2024b), and the multifluid implementation (Weinberger & Hernquist, 2023a) in `AREPO` (Springel, 2010; Weinberger et al., 2020). First, we present the details of our models which consists of,

- Mass, momentum and energy fluxes ($\dot{\mathbf{Q}}$), from drag forces ($\dot{\mathbf{Q}}_{\rm drag}$), turbulent mixing ($\dot{\mathbf{Q}}_{\rm mix}$), and cold gas growth ($\dot{\mathbf{Q}}_{\rm grow}$).
- A local turbulent velocity estimation methods ($v_{\rm turb}$) based on a Kolmogorov scaling-based method ($v_{\rm turb,kol}$), or a velocity gradient-based approach ($v_{\rm turb,grad}$).
- an estimate of the cold gas surface and cross-sectional area ($2h(\alpha)$ and ($A_{\rm cross}(\alpha)$, respectively).

Second, we separately verify the different parts of the MOGLI model for the two local turbulence estimates. We compare the MOGLI runs with resolved benchmark single-fluid `Athena++` simulations for verification. We test the quantities across different turbulent Mach numbers, resolved/unresolved initial cold clouds, resolution and random seeds for turbulent driving, for a robust comparison. The following are the main conclusions from our verification and tests in this study:

- We show that the reduced version of the MOGLI model for non-radiative mixing, i.e. $\dot{\mathbf{Q}}_{\rm non-rad} = \dot{\mathbf{Q}}_{\rm drag} + \dot{\mathbf{Q}}_{\rm mix}$, matches the benchmarks non-radiative `Athena++`, both qualitatively and quantitatively, in terms of the destruction timescales, across all different parameters, with very similar mean and scatter in $t_{\rm half}/t_{\rm cc}$,
- We find that MOGLI model leads to physically consistent interaction between the phases in both resolved and unresolved cold gas structures, where the mass exchange only happens at the interfaces when the cold gas is resolved and throughout the structure when unresolved,
- The full MOGLI model for radiative mixing, shows the expected behaviour of cold gas growth at short cooling timescales and cold gas destruction for long cooling timescales, across all different parameters,

[14] Ultimately, evolving some morphological parameters (e.g., clump size distribution) alongside the fluid quantitites is also possible. However, to do so the set of equations have to be developed and thoroughly tested.

- We verify that the full MOGLI model for radiative mixing, quantitatively matches the expected cold gas mass growth timescales, with very similar mean and scatter in $t_{\rm grow}/t_{\rm grow,theory}$ between the benchmark `Athena++` runs and MOGLI runs. In both, we find the mean $t_{\rm grow}$ to be $\sim 1.5 t_{\rm grow,theory}$,
- The full MOGLI model for radiative mixing, also recreates the cold gas survival criterion from Gronke et al. (2022b), as an emergent process, i.e., while 'survival' is not explicitly implemented in MOGLI, it can recover this larger scale result.
- We show that the cold gas dispersion is similar between the full MOGLI model for radiative mixing and analogous benchmark `Athena++` runs. The agreement is better in case of a resolved, initial cold gas cloud, compared to the unresolved initial cold gas cloud,
- All the verification tests hold true, regardless of the local turbulent velocity estimation method,
- We demonstrate the strength of the MOGLI model by running a 64^3 cells simulation using MOGLI with 100 unresolved clouds, which would require $\sim 3000^3$ cells in a single-fluid code without a subgrid model.

Our study presents our new physically motivated, multifluid subgrid model MOGLI. We have extensively tested and verified the model across a wide range of possible simulation parameters, to ensure a robust and consistent model. This work will be a useful development towards running converged large-scale simulations with subgrid prescriptions for the unresolved cold gas. However, this MOGLI has many avenues for improvement like the inclusion of the molecular phase, in-situ cold gas formation, subgrid turbulence prescription, etc, which we hope to tackle in future work.

5 | Cold gas creation and survival in a turbulent ISM

> When we think we know, we cease to learn.
>
> — Sarvapalli Radhakrishnan

> Who are we, if not explorers?
>
> — Rahul Ramesh & Anshuman Acharya

This work is being prepared for submission to The Astrophysical Journal.

5.1 Introduction

The formation and persistence of cold gas in turbulent, radiatively cooling astrophysical media is central to understanding a range of astrophysical media, like the interstellar (ISM), circumgalactic (CGM) and intracluster medium (ICM) (Field et al., 1969). In particular, cold gas plays a pivotal role in regulating star formation, fueling feedback cycles, and governing the thermodynamic state of extended gaseous halos (Tumlinson et al., 2017). While the importance of cold gas is widely recognised, the physical mechanisms responsible for its condensation and survival within a turbulent, hot environment remain areas of active investigation.

Turbulence introduces significant complexity into this problem (Mohapatra et al., 2022b). By generating fluctuations in density and temperature, turbulence can both promote and suppress the condensation of cold gas. The timescales for cooling and mixing become intimately linked, with gas in intermediate temperature regimes often occupying thermally unstable states. Whether a multiphase medium develops depends sensitively on the balance between turbulent eddy turnover times and local cooling times. Prior studies have shown that under certain conditions, a small seed of cold gas can grow via turbulent mixing and subsequent radiative cooling (e.g., Gronke & Peng Oh, 2018; Gronke et al., 2022a; Das & Gronke, 2024a). The presence of the seed cold gas is usually explained by the external influences like galactic outflows (Tumlinson et al., 2017) or in-situ cold gas formation from hot phase via thermal instability (Field, 1965; Sharma et al., 2010; Mohapatra & Sharma, 2019).

In the previous studies, the in-situ cold gas formation (or condensation) of cold gas from an

thermally unstable hot gas and its subsequent growth via mixing were investigated separately, due to the separation in relevant timescales, i.e. cooling timescale of hot ($t_{\rm cool,hot}$) and cold phase ($t_{\rm cool,cold}$) respectively, in CGM and ICM. In ISM, this does not hold true anymore, where the cooling time of the hotter phase ($T_{\rm hot} = 10^4$K) is comparable to the cooling time of the cold phase ($T_{\rm cold} = 100$K). Hence, in the ISM, both processes can act together and be important in different circumstances.

In this chapter, we systematically investigate the ISM-like turbulent system, with an unstable hot phase (10^4K). We study (1) the criterion for turbulent cold gas condensation from the hot phase, and (2) subsequent cold cloud survival in a stable hot phase. We begin with analytical considerations that motivate a new condensation criterion based on the cooling time of turbulently compressed gas parcels. We then describe our simulation setup and methods, before presenting results on cold gas morphology, mass evolution, and phase structure. Finally, we compare our proposed criterion against previous models and discuss the broader implications for cold gas in multiphase astrophysical systems.

5.2 Analytical considerations

In this section, we review the relevant timescales, lengthscales, and criteria.

The phenomenon of turbulence has its own inherent timescales and lengthscales. In a turbulent box, the turbulent eddies of size l evolve on the eddy-turnover timescale, $t_{\rm eddy}(l) = l/u$, where u is the turbulent velocity on that scale. Assuming a Kolmogorov spectrum and turbulent velocity of $v_{\rm turb}$ at the scales of the box, i.e. $L_{\rm box}$, we can rewrite $t_{\rm eddy}(l) \sim t_{\rm eddy,box}(l/L_{\rm box})^{2/3}$, where $t_{\rm eddy,box} = L_{\rm box}/v_{\rm turb}$ is the eddy turnover time at the box scale.

In this study, we aim to study the behaviour of turbulent gas with radiative cooling. The process of radiative cooling introduces its own timescales, namely the cooling time, defined for gas at a density ρ and temperature T as

$$t_{\rm cool}(\rho, T) = \frac{k_{\rm B}T/(\gamma-1)}{\rho\Lambda(T)} \tag{5.1}$$

where, $\Lambda(T)$ is the cooling function and $\mathcal{L}_{\rm cool} = \rho^2\Lambda$ is the cooling rate. From henceforth, Λ_x will refer to $\Lambda(\rho_x, T_x)$.

We also define a second cooling timescale ($t'_{\rm cool}$), including the effect of the heating function, $\Gamma(T)$, defined as

$$t'_{\rm cool}(\rho, T) = \frac{k_{\rm B}T/(\gamma-1)}{\rho\Lambda(T) - \Gamma(T)} \tag{5.2}$$

where $\rho\Gamma$ is the heating rate. As we maintain an average energy equilibrium in the hot gas phase in the box, to avoid the box from cooling or heating as a whole, heating terms balance cooling for average conditions, i.e. $\Gamma/\rho_{\rm hot} = \Lambda_{\rm hot}$. The previous cooling time, i.e. $t_{\rm cool}$ is comparatively easier to calculate than $t'_{\rm cool}$, hence we use $t_{\rm cool}$ during our simulation setup.

Different characteristic density and temperature pairs have their corresponding cooling times, like cooling time for (ρ, T) pairs for cold and hot gas phase, $(\rho_{\rm cold}, T_{\rm cold})$ and $(\rho_{\rm hot}, T_{\rm hot})$ correspond to the cooling times $t_{\rm cool,cold}$ and $t_{\rm cool,hot}$. The other important cooling time is the cooling time of the 'mixed' gas, $t_{\rm cool,mix}$, at a density and temperature of $(\rho_{\rm mix}, T_{\rm mix})$, where $\rho_{\rm mix} = \sqrt{\rho_{\rm cold}\rho_{\rm hot}}$ and $T_{\rm mix} = \sqrt{T_{\rm cold}T_{\rm hot}}$ (Begelman & Fabian, 1990a).

Previous work has shown that using the ratio of a 'destruction time' to $t_{\rm cool,mix}$ can explain the survival of cold gas in a laminar 'wind tunnel' (Gronke & Peng Oh, 2018; Kanjilal et al., 2021) as well as in a turbulent box (Gronke et al., 2022a; Das & Gronke, 2024a). Specifically, these authors used

$$\frac{t_{\rm cool,mix}}{t_{\rm cc}} < 1 \tag{5.3}$$

where $t_{\rm cc} \sim \chi^{1/2} r_{\rm cl}/v$ is the 'cloud crushing' timescale (Klein et al., 1994a) of a cold cloud of size $r_{\rm cl}$ and overdensity $\chi \equiv \rho_{\rm cl}/\rho_{\rm hot}$ being impinged by a hot flow with velocity v – which in the turbulent medium is $v \sim v_{\rm turb}$. We will connect our work to these previous studies on cold gas survival, and in particular, investigate the validity of Eq. (5.3) for lower temperatures. However, we will also study the condensation of a cold phase from an initially purely hot, turbulent gas.

Putting radiative cooling and turbulence together results in modification of cooling timescales as the density and temperature distributions broaden due to turbulent fluctuations. Next, we want to calculate the cooling time of the turbulently compressed gas, $t_{\rm cool,comp}$. We know that the Eulerian density in a turbulent box at steady-state roughly follows a log-normal distribution (Federrath, 2013). So, if $s = \ln(\rho/\rho_{\rm hot})$ is the log-density, the probability density function (PDF) of s is given by a normal distribution, $\mathcal{N}(\mu_s = 0, \sigma_s)$, where μ_s and σ_s are the mean and standard deviation of the normal distribution. As shown in Federrath (2013), the value of σ_s depends on the turbulent mach number ($\mathcal{M}$) and a constant parameter (b) that changes with forcing, as

$$\sigma_s^2 = \ln\left(1 + b^2\mathcal{M}^2\right) \tag{5.4}$$

where $b \approx 0.38$ (Mohapatra et al., 2022b).

As s is normally distributed, the probability of highly compressed or rarified gas decreases exponentially away from the mean value. We assume a threshold of $s_{\rm comp} = k\sigma_s$ for the high-end of the log-density corresponding to compressed gas, where k is a constant free parameter. We rewrite this threshold to calculate density of the compressed gas $\rho_{\rm comp}$ corresponding to $s_{\rm comp}$ as

$$\rho_{\rm comp} = \rho_{\rm hot} e^{k\sigma_s} = \chi^{-1/2}\rho_{\rm mix} e^{k\sigma_s} \tag{5.5}$$

and, assuming adiabaticity of the turbulence

$$T_{\rm comp} = T_{\rm hot} e^{(\gamma-1)k\sigma_s} = \chi^{1/2} T_{\rm mix} e^{(\gamma-1)k\sigma_s}. \tag{5.6}$$

Now, we can use Eq. 5.1 to calculate the ratio

$$\frac{t'_{\rm cool,comp}}{t_{\rm cool,mix}} = \left(\frac{\rho_{\rm mix}}{\rho_{\rm comp}}\right)\left(\frac{T_{\rm comp}}{T_{\rm mix}}\right)\left(\frac{\Lambda_{\rm mix}}{\Lambda_{\rm comp} - (\rho_{\rm hot}/\rho_{\rm comp})\Lambda_{\rm hot}}\right) \tag{5.7}$$

$$= \chi e^{(\gamma-2)k\sigma_s}\left(\frac{\Lambda_{\rm mix}}{\Lambda_{\rm comp} - \Lambda_{\rm hot}e^{-k\sigma_s}}\right). \tag{5.8}$$

If we postulate that condensation from a turbulent hot gas occurs if $t_{\rm cool,comp}$ is short enough compared to $t_{\rm eddy}$, which timescale over which a gas parcel samples a significant portion of the density distribution (Scannapieco et al., 2024). Hence, assuming another free parameter, A, we can write a condensation criterion as

$$\frac{t'_{\rm cool,comp}}{t_{\rm eddy}} < A \implies \frac{t_{\rm cool,mix}}{t_{\rm eddy}} < A\left(\frac{e^{(2-\gamma)k\sigma_s}}{\chi}\right)\left(\frac{\Lambda_{\rm comp} - \Lambda_{\rm hot}e^{-k\sigma_s}}{\Lambda_{\rm mix}}\right) \tag{5.9}$$

5.3 Method

We use the ATHENA++ code (Stone et al., 2020a) for our simulations. We run the code with the default HLLC solver, Piecewise Linear Method (PLM) on primitive variables, second-order Runge-Kutta time-integrator, adiabatic equation of state (EOS) on a Cartesian grid, and periodic boundary conditions.

5.3.1 Turbulence and cold cloud

We adopt a setup similar to that used in Das & Gronke (2024a) for hydrodynamic turbulent box simulations. The domain is initialised as a cubic box filled with isobaric gas at uniform density and temperature ($T_{\rm hot} = 10^4$ K), assuming solar metallicity and hydrogen abundance. Turbulence is driven at the largest scale ($k = 2\pi/L_{\rm box}$) using an Ornstein–Uhlenbeck (OU) process (Eswaran & Pope, 1988a; Schmidt et al., 2006a). We set the driving timescale to 0.001 $t_{\rm eddy}$, with a correlation timescale of approximately $t_{\rm eddy} = L_{\rm box}/v_{\rm turb}$, and a solenoidal-to-compressive forcing ratio of $f_{\rm sol} = 0.3$. All simulations use a box-to-cloud size ratio of $L_{\rm box}/R_{\rm cloud} = 20$[1]

We drive the turbulence for up to 7 $t_{\rm eddy}$ in the presence of radiative cooling, allowing the system sufficient time to either reach a statistical steady state with saturated kinetic energy or to undergo cold gas condensation. If no condensation occurs within this period, we restart the simulation by introducing a dense cloud at the centre of the box. The cloud has an overdensity of $\chi = 100$, a radius $R_{\rm cloud}$, and is initialised while conserving the total kinetic energy densities. This results in an isobaric, cold, dense cloud with density $\rho_{\rm cold} = \chi\,\rho_{\rm hot}$ and temperature $T_{\rm cold} = 10^2$ K $= T_{\rm floor}$.

Our fiducial simulations have a resolution of 64^3 cells, with a subset of runs at 128^3 resolution for testing convergence. We explore a range of Mach numbers spanning both subsonic and

[1]This is smaller than the ratio $L_{\rm box}/R_{\rm cloud} = 40$ used in Das & Gronke (2024a), chosen here to maintain the same number of resolution elements per cloud radius at reduced overall resolution. The trade-off is a more rapid filling of the box with cold gas as condensation progresses.

supersonic regimes ($\mathcal{M} \in [0.1, 2.5]$) and vary the hot gas density $\rho_{\rm hot}$ to systematically probe different values of the cooling-to-dynamical timescale ratio, $t_{\rm cool,mix}/t_{\rm eddy}$.

5.3.2 Radiative cooling and heating

We implement radiative cooling using the algorithm of Townsend (2009a), which enables accurate integration of stiff cooling source terms. We adopt a cooling curve $\Lambda(T)$ at solar metallicity, from Wiersma et al. (2009) $T > 10^4$K and Koyama & Inutsuka (2002) for $T \leq 10^4$K, and approximated using 70 piecewise power-law segments spanning the temperature range 10^2 K to 10^8 K. We enforce a temperature floor of $T_{\rm floor} = 10^2$ K throughout the simulations.

To study cold gas condensation from the hot phase, we do not suppress cooling in the hot medium, unlike in Gronke et al. (2022a) and Gronke & Peng Oh (2018). However, the absence of external heating can lead to net cooling or turbulent heating of the bulk gas. To maintain approximate global energy balance, we include a uniform heating/cooling density term, $\mathcal{H}_{\rm extra}$. We assume that the kinetic energy injected to drive turbulence, $\dot{E}_{\rm turb}$, is fully dissipated as heat. This rate is estimated using the box size $L_{\rm box}$ and ambient density $\rho_{\rm hot}$ as

$$\dot{E}_{\rm turb} = \frac{1}{2}\rho_{\rm hot} L_{\rm box}^2 v_{\rm turb}^3$$

(see, e.g., Lemaster & Stone, 2009). If $\mathcal{L}_{\rm cool}$ denotes the volumetric cooling rate for gas at constant density $\rho_{\rm hot}$ and temperature $T_{\rm hot}$, then the global energy balance can be written as

$$\mathcal{H}_{\rm extra} = \mathcal{L}_{\rm cool} - \dot{E}_{\rm turb}/L_{\rm box}^3 = \rho_{\rm hot}^2 \left[\Lambda(T_{\rm hot}) - \frac{1}{2}\frac{v_{\rm turb}^3}{\rho_{\rm hot} L_{\rm box}}\right] \tag{5.10}$$

Figure 5.1 shows the resulting equilibrium temperatures at the end of the turbulence driving phase. The inclusion of $\mathcal{H}_{\rm extra}$ effectively regulates the thermal state of the gas, maintaining the hot phase within a narrow temperature range centered around $T_{\rm hot} = 10^4$ K.

5.4 Results

As mentioned in Section. 5.3, we run the turbulent box simulations in two stages. The first stage involves driving the turbulence in the hot medium, with radiative cooling. If during the first stage, no cold gas condensation occurs and the box reaches a steady state, we introduce a cold dense cloud. In the upcoming sections, we explore the behaviour of cold gas in both stages of simulations across a parameter space of turbulent Mach number ($\mathcal{M}$) and $t_{\rm cool,mix}/t_{\rm eddy}$. In this work, we define the cold phase as the gas with temperature $T < 200$K and the hot phase as the temperature $T > 5000$K.

5.4.1 Cold gas morphology and behaviour

Over the parameter space spanned by different values of $t_{\rm cool}/t_{\rm eddy}$ and $\mathcal{M}$, the evolution of cold gas falls into three distinct categories. In Fig. 5.2, we illustrate representative simulations from

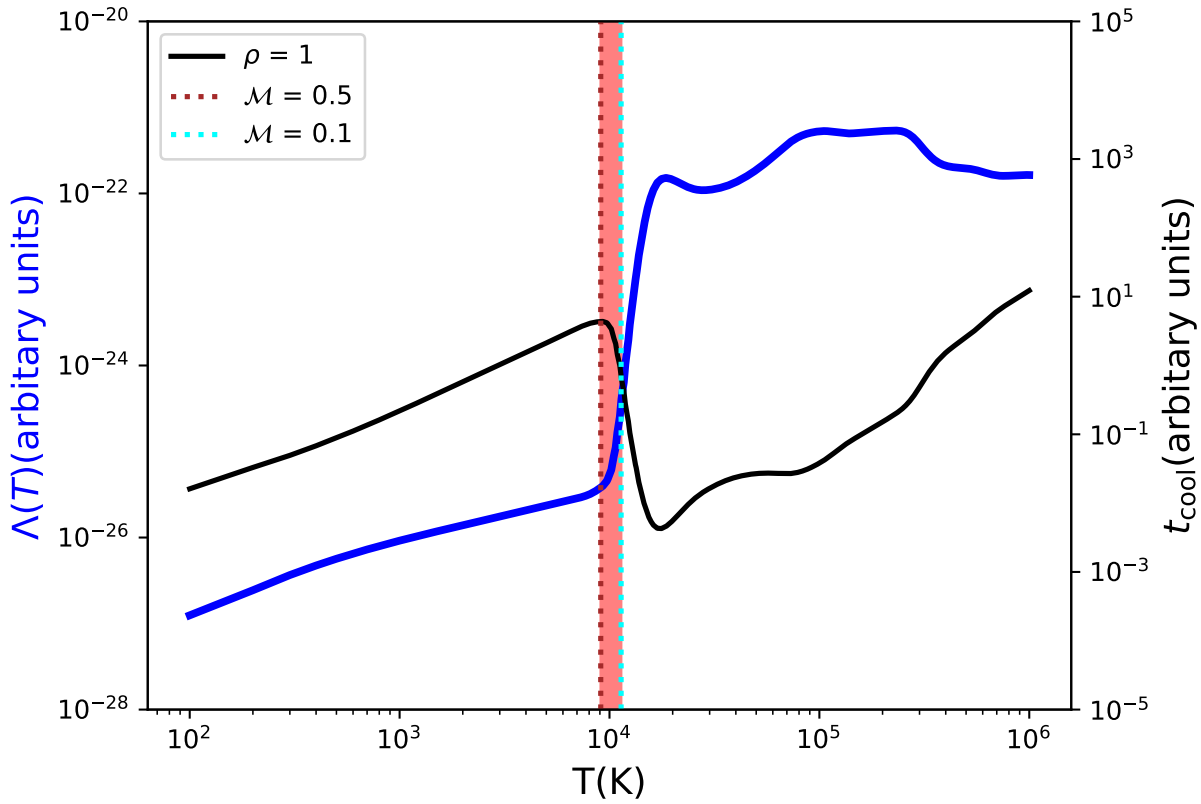

Figure 5.1: The cooling function ($\Lambda(T)$) and cooling time ($t_{\rm cool}$) for different temperatures and $\rho_{\rm hot} = 1$. The blue curve shows $\Lambda(T)$ and the black curve shows the $t_{\rm cool}$. The red regions mark the temperature region of the equilibrium temperature in our simulations with the global energy balance with Eq. 5.10.

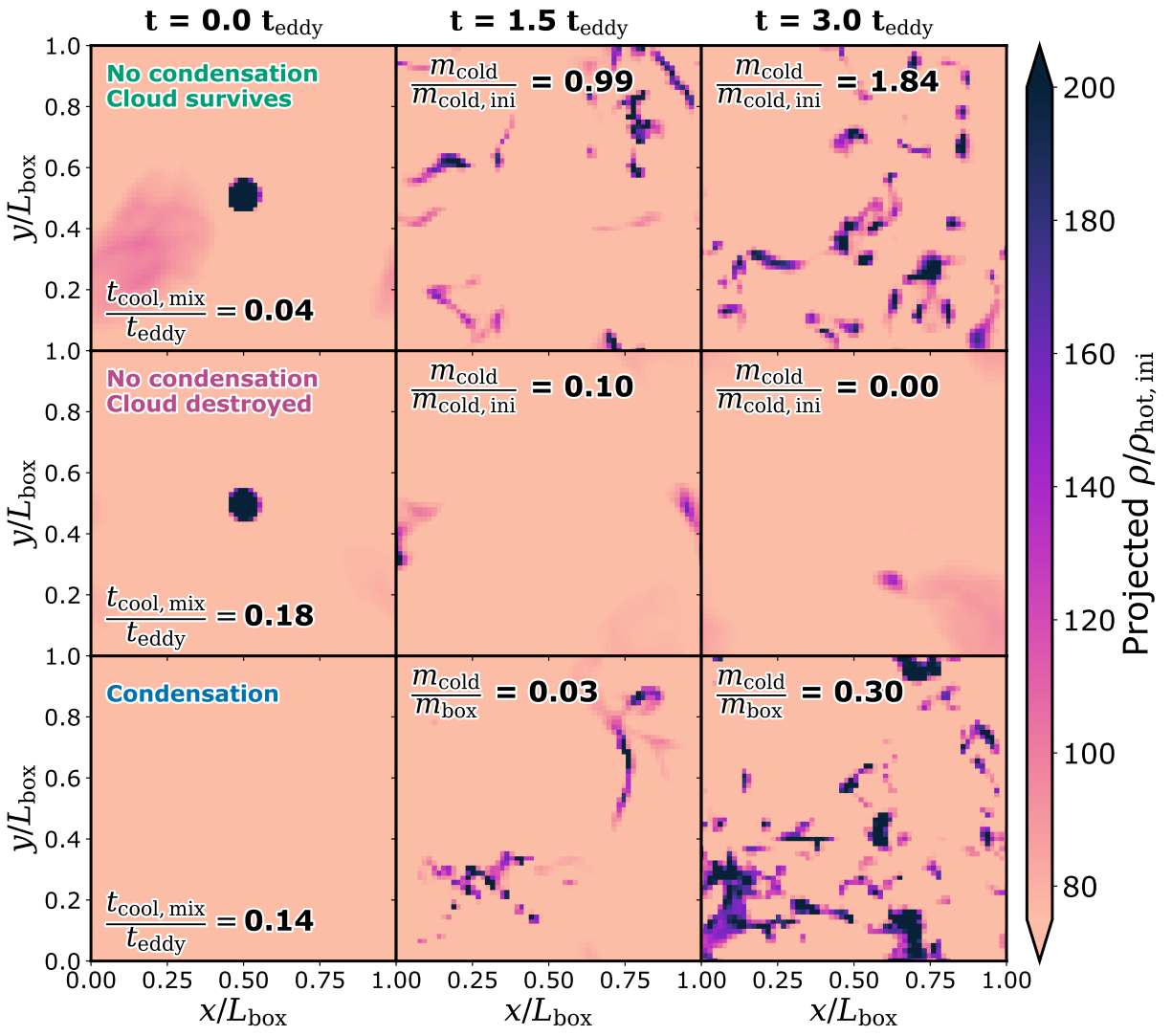

Figure 5.2: Density projections of turbulent box simulations with $\mathcal{M} \sim 0.5$, at three different times across columns, and for the three different cold gas behaviours across the rows. The different regimes of behaviour are *bottom row*: turbulent condensation, *middle row*: no turbulent condensation but cold cloud survival and *top row*: no turbulent condensation and cold cloud destruction. The two regimes where the end state contains cold gas show a similar fragmented cold gas structure.

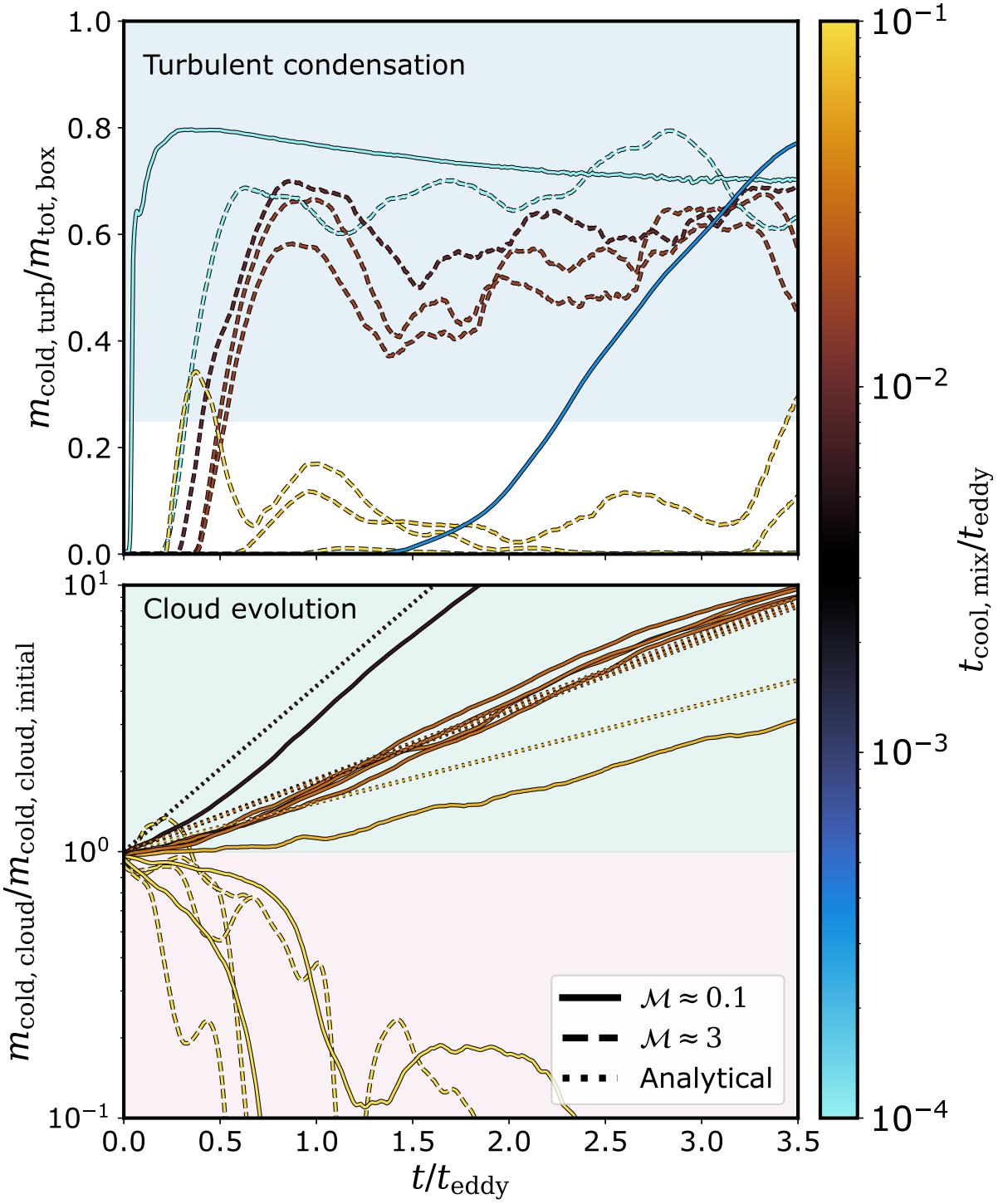

Figure 5.3: Cold gas mass evolution in the two stages of simulations, for $\mathcal{M} \sim [0.5, 3]$. *Top panel* shows the cold gas evolution during the turbulent condensation stage. The blue shaded region marks the region where we consider a simulation is have turbulent condensation. The *bottom panel* shows the cold gas mass evolution after the introduction of a cold cloud in simulations without condensation. The green and red shaded regions show the regimes of cold gas survival and destruction. The dotted lines show the expected cold gas growth ($m_{\rm cold,cloud} = m_{\rm cloud,cloud,initial} e^{t/t_{\rm grow}}$) with the analytical growth rate ($t_{\rm grow}$ using the Eq. 5.11 from Gronke et al. (2022a)

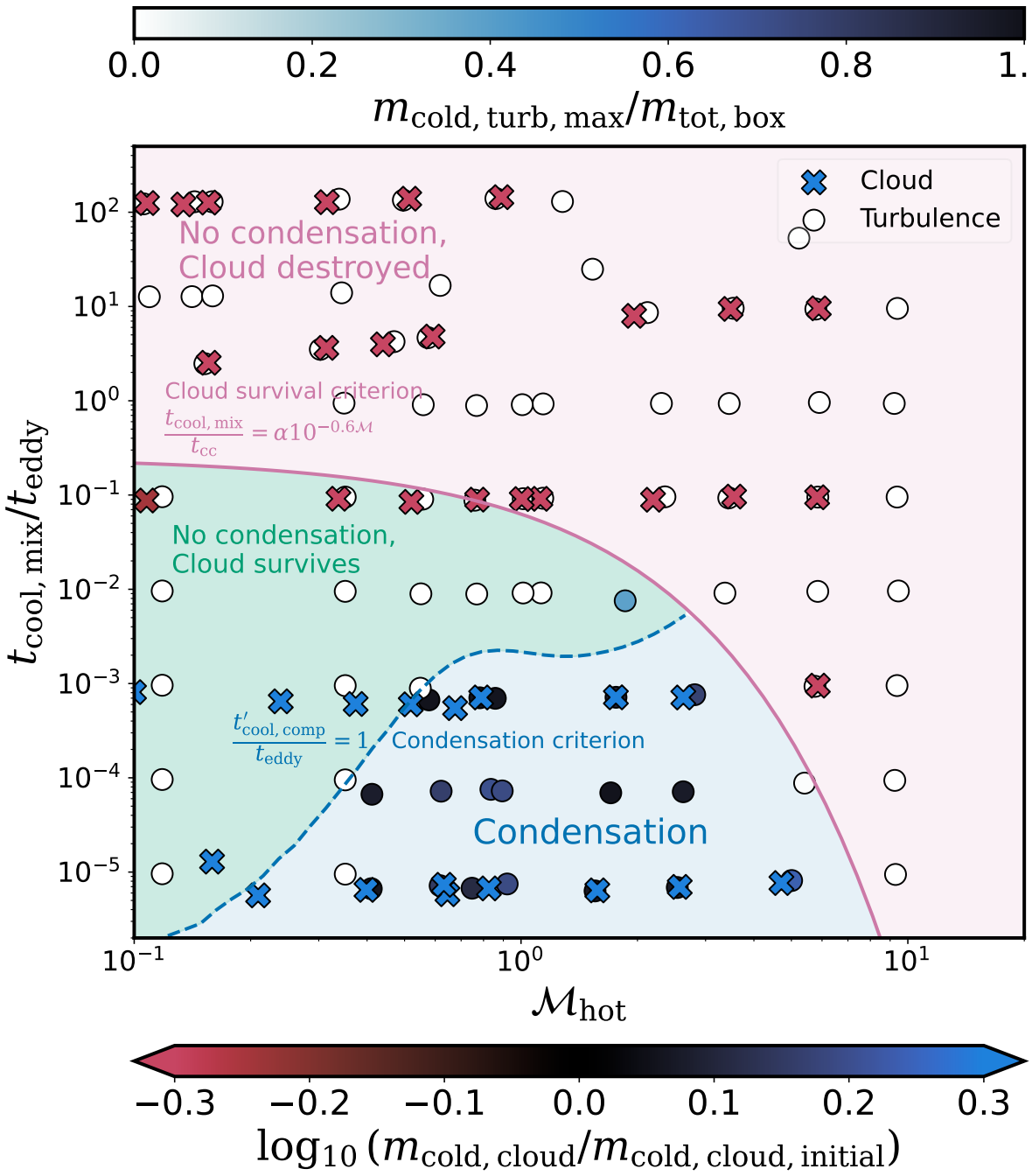

Figure 5.4: The fate of cold gas during the two stages of simulations across the parameter space of $(t_{\mathrm{cool}}/t_{\mathrm{eddy}})$ vs. $\mathcal{M}$. The circles denote the first stage of simulations with turbulence driving, while the crosses show the second stage where a cold cloud is introduced in simulations without condensation. The colour of the points denotes the corresponding final cold gas mass. We show the three different regimes of cold gas behaviour, namely, **blue regime** where simulations with turbulent condensation, **green regime** where simulations without turbulent condensation, but show survival of cold gas cloud, and finally **red regime** with simulations without turbulent condensation and which also show cold cloud destruction. The regimes are separated by the turbulent condensation criterion as blue dashed line, from Eqn. 5.9 and cold cloud survival criterion from Gronke et al. (2022a).

each regime. The figure shows density projections ($\rho/\rho_{\rm hot,initial}$) integrated along a coordinate axis, with time increasing from left to right.

In the first category, where the turbulent hot medium is thermally unstable, cold gas condenses out of the background and fragments, forming structures across a range of length scales (bottom row of Fig. 5.2). In the second and third categories, the background is thermally stable, and we introduce a cold, dense cloud. In the second case, the cloud survives and grows despite the lack of ambient thermal instability (top row), whereas in the third, it is destroyed by turbulent mixing (middle row). In the two regimes with cold gas in the end state, we find similar multiscale fragmented cold gas structures, showing parallels between the two channels of cold gas creation.

The regime with no turbulent condensation and cold cloud survival is of particular interest. This shows that even in the thermally stable regime, an externally introduced cold gas can persist and grow. This highlights that thermal instability and multiphase mixing affect the cold gas behaviour independently. This emphasises the importance of mixing and non-linear dynamical processes in shaping the multiphase structure.

5.4.2 Temporal cold gas mass evolution

Next, we take a quantitative look at the cold gas evolution across our simulations. We compute the total mass of cold gas ($T < 200\,{\rm K}$) in each snapshot to track its temporal evolution.

The top panel of Fig. 5.3 shows the cold gas mass as a function of time (normalised to $t_{\rm eddy}$) during the initial turbulence driving phase. Condensation occurs on different timescales depending on the ratio $t_{\rm cool,mix}/t_{\rm eddy}$ with some stochastic variation. The blue-shaded region marks the threshold for turbulent condensation: simulations with their time-averaged cold gas mass (over the final $0.5\ t_{\rm eddy}$) below this region are classified as not exhibiting turbulent condensation. For these, we proceed to inject a cold, dense cloud to study its evolution.

The bottom panel shows the evolution of cold gas after such a cloud is introduced. In agreement with earlier studies, clouds grow when $t_{\rm cool,mix}/t_{\rm eddy}$ is small, and are disrupted when this ratio is large. We show both subsonic and supersonic examples, with cold gas survival and destruction. We compare the cold gas evolution from simulations with the expected cold gas growth, i.e. $m_{\rm cold} = m_{\rm cold,ini} e^{t/t_{\rm grow}}$, where $t_{\rm grow}$ refers to the analytical growth rates from Gronke et al. (2022a), given by

$$t_{\rm grow} \equiv \alpha\chi\mathcal{M}_{\rm hot}^{-1/2}\left(\frac{R_{\rm cloud}}{l_{\rm shatter}}\right)^{1/2}\left(\frac{R_{\rm cloud}}{L_{\rm box}}\right)^{-1/6} t_{\rm cool,cold} \tag{5.11}$$

where, $\alpha = 0.5$ is a fudge factor. The analytic predictions are shown only for subsonic cases, as cold gas does not survive in the supersonic regime. We find that the analytical growth rates agree well with the cold gas mass evolution in these simulations.

In simulations that do produce condensation, the cold gas typically grows rapidly and reaches a quasi-steady state, often dominating the mass budget due to the finite volume and periodic boundaries of the simulation box. This saturation is likely numerical rather than physical. We

also see stochasticity in the time of condensation between simulations with similar $t_{\rm cool,mix}/\,t_{\rm eddy}$ values, e.g. yellow dashed lines with $t_{\rm cool,mix}/\,t_{\rm eddy} \sim 0.1$. We attribute this to the stochastic nature of turbulence.

Some simulations exhibit transient condensation, where the cold gas initially grows but then declines to a much lower, steady level. To differentiate between cases with and without turbulent condenstation, we adopt a criterion: if the maximum cold gas mass remains below 25% of the total box mass, we classify it as not sustaining significant condensation. We find that cold gas clouds can survive in thermally stable turbulence only if the turbulence is subsonic. None of the supersonic runs without in-situ condensation support the survival of the introduced cold gas clouds, indicating that cloud longevity in such regimes is tightly linked to the presence of condensation.

5.4.3 Condensation, survival and destruction of cold gas

Next, we take a look at the parameter scan of simulations with varying Mach numbers ($\mathcal{M} = 0.1$ to 3) and different $t_{\rm cool,mix}/t_{\rm eddy}$ ratios. The analysis proceeds in two stages, as before: first, we test for turbulent cold gas condensation during the driving phase; if no condensation is observed, we introduce a cold cloud to assess its survival. We use the corresponding cold gas mass evolution of the simulations, similar to Fig. 5.3, and take the average cold gas mass over the final $0.5\,t_{\rm eddy}$ to ascertain the fate of cold gas in the simulation.

Figure 5.4 summarises the outcomes across this parameter space. Circles indicate whether condensation occurred during the driving phase, with colours representing the final cold gas mass normalised to the total box mass. As mentioned in the previous section, we use a threshold of $0.25\,m_{\rm tot,box}$ to classify turbulent condensation. For simulations lacking condensation, additional runs track the fate of an introduced cold cloud. These are marked with crosses, with the colour denoting the final cold gas mass normalised to the initial cloud mass. The solid pink line represents the survival threshold from Gronke et al. (2022a), and the blue line represents the our condensation criterion, Eq. 5.9 from Section. 5.2, with a $k = 3$ and $A = 10^{-5}$ as a free-parameters, based on whether the cooling time of compressed gas, $t_{\rm cool,comp}$, is comparable to $t_{\rm eddy}$[2]. Three distinct regimes emerge, indicated by shaded regions:

- **Blue**: Turbulent condensation during the first stage of simulation,
- **Green**: No turbulent condensation, but the cold clouds survive,
- **Red**: No turbulent condensation and the cold clouds are destroyed.

As we show in Fig. 5.4, cloud survival without turbulent condensation is limited to subsonic turbulence.

[2]We compare this with alternative criteria from previous work in the appendix.

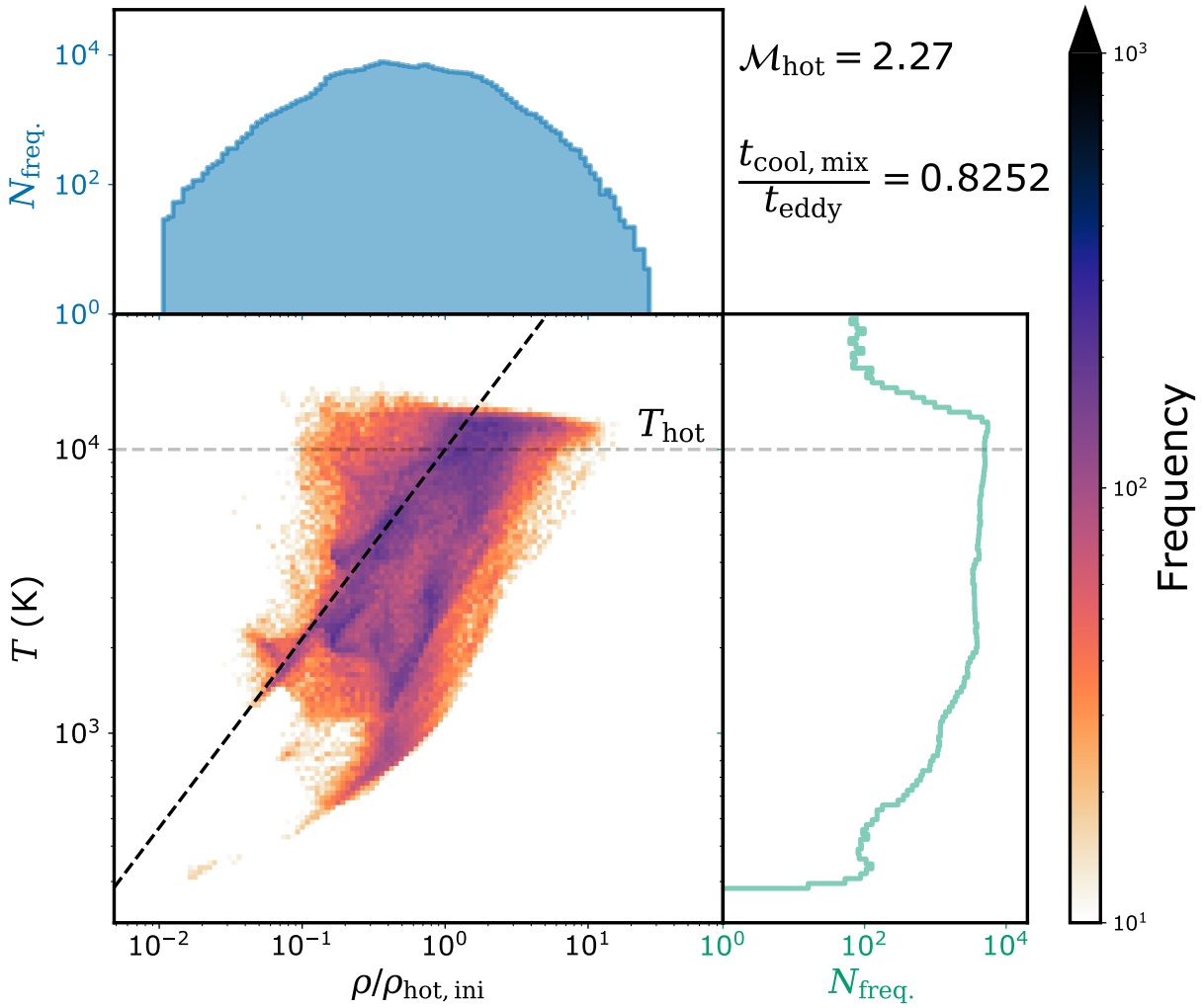

Figure 5.5: Density-temperature ($\rho/\rho_{\rm hot,ini} - T$) histogram of a supersonic turbulence simulation, at $\mathcal{M} = 2.27$ and $t_{\rm cool,mix}/t_{\rm eddy} = 0.8252$, without cold gas condensation. Figures on the top and right show the distribution of $\rho/\rho_{\rm hot,ini}$ and T respectively. The black dashed line shows an adiabatic curve set to the initial entropy.

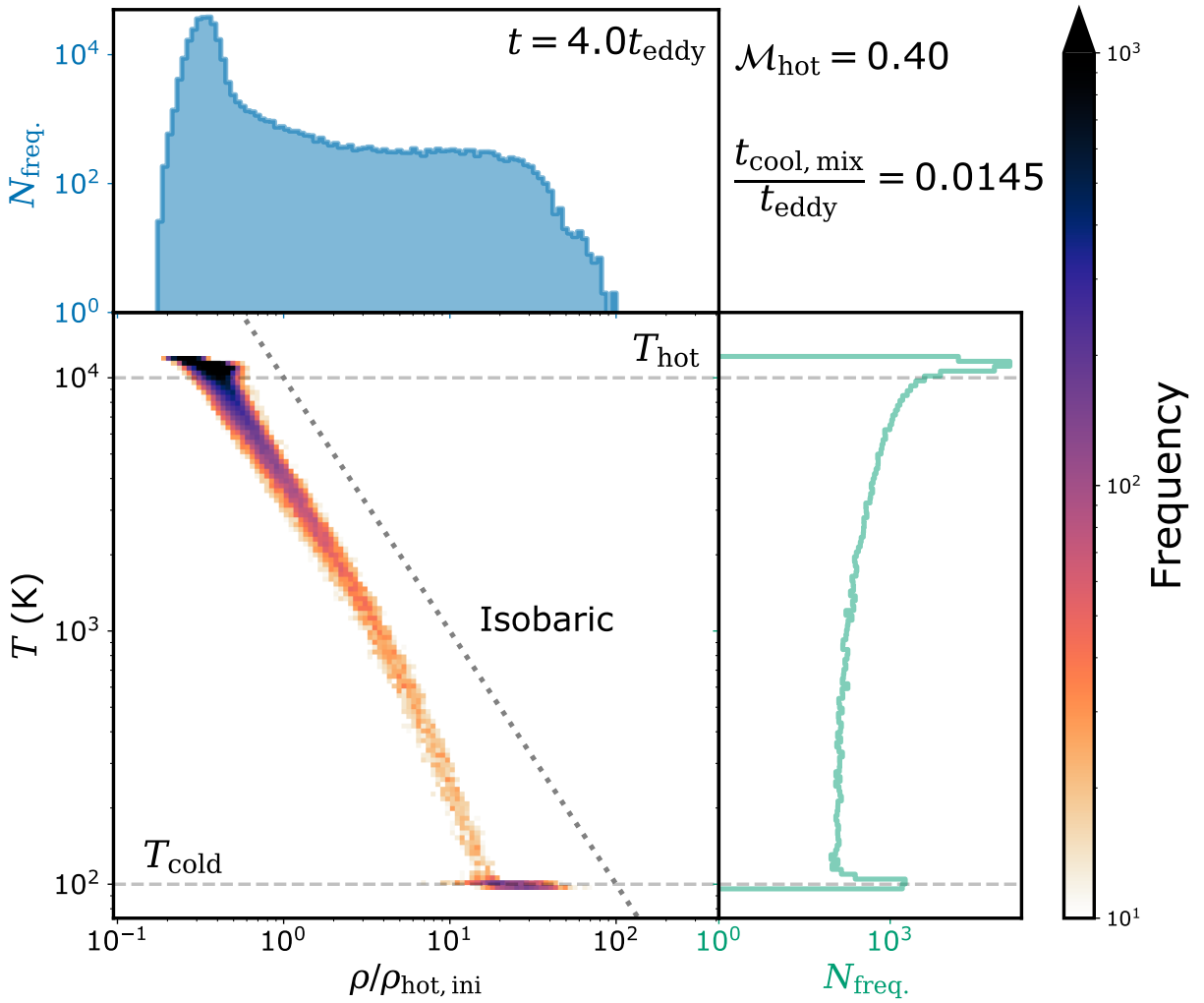

Figure 5.6: Density-temperature ($\rho/\rho_{\rm hot,ini} - T$) histogram of a subsonic turbulence simulation, at $\mathcal{M} = 0.4$ and $t_{\rm cool,mix}/\,t_{\rm eddy} = 0.0145$, with cold gas condensation. Figures on the top and right show the distribution of $\rho/\rho_{\rm hot,ini}$ and T respectively. The black dotted line shows an isobaric curve set to the initial pressure.

5.4.4 Phase plot of the gas

To further understand turbulent condensation, we examine the phase structure of the simulations during the first stage of turbulent driving with radiative cooling. We focus exclusively on this phase, as the second stage involving an externally introduced cold cloud has already been explored in previous studies (Kanjilal et al., 2021). To analyse the phase structure, we calculate the 2D volume-weighted histograms of the simulation snapshots, showing the distribution of gas cells in temperature–density space, with the density normalised to the initial hot gas density. Alongside the 2D histogram, we also present the corresponding 1D histograms of the volume-weighted density and temperature distributions, on the top and right side.

Figure 5.5 shows the 2D and corresponding 1D histograms of density and temperature for a turbulent box simulation with supersonic turbulence ($\mathcal{M} = 2.27$) and $t_{\rm cool,mix}/t_{\rm eddy} = 0.8252$, a case with no cold gas condensation. We find that the phase structure broadly follows an adiabatic relation, shown as the black dashed line in the figure. This supports the assumption of adiabatic evolution in our derivation of the cold gas condensation criterion in Section. 5.2. We also find a broad density distribution, consistent with previous studies (Federrath, 2013). The temperature histogram similarly spans a wide range, roughly following the adiabatic curve.

Next, we examine a case where the turbulent hot gas undergoes cold gas condensation. In Fig. 5.6, we show the phase diagram for a subsonic turbulent box with $\mathcal{M}_{\rm hot} = 0.4$ and $t_{\rm cool,mix}/t_{\rm eddy} = 0.0145$, where a clear transition from the hot to the cold phase is observed. The resulting density and temperature distributions are bimodal, characteristic of a multiphase medium. Between the two stable phases, we observe a trace population of gas cooling from the hot to the cold phase. This gas approximately follows an isobaric trajectory, deviating only near the cold end where the cooling becomes increasingly rapid.

5.5 Conclusions and Discussion

- **Condensation criterion**: The criterion from Mohapatra et al. (2022b), expressed as $t_{\rm TI,hot}/t_{\rm eddy} = c_2\, e^{c_1 \sigma_s}$, where σ_s is the standard deviation of the logarithmic density field and, $[c_1, c_2]$ are empirical constants. $t_{\rm TI}$ refers to the thermal instability timescale defined as,

$$t_{\rm TI} = \frac{\gamma t_{\rm cool}}{2 - (d\ln\Lambda/d\ln T) - \alpha}$$

  where $\alpha = 1$ depends on the details of the heating.

  For our simulations, as the $(d\ln\Lambda/d\ln T)|_{T=T_{\rm hot}} \approx 6$, the hot phase is linearly stable to thermal instability. Hence, according to the criterion from Mohapatra et al. (2022b), the hot phase should be indefinitely stable, which we do not find in our simulations. While this discrepancy can stem from differing definitions of condensation and variations in simulation setup, in contrast, our criterion shows good agreement with the simulation outcomes.

  A more detailed comparison between condensation criteria would benefit from a controlled suite of simulations with standardised setups, which we defer to future work.

- **Onset of cold gas condensation**: While the onset of cold gas condensation has a dependence on $t_{\rm cool}/t_{\rm eddy}$, we see that there is also some stochastic variation among simulations with similar $t_{\rm cool}/t_{\rm eddy}$. This variation is likely due to the stochastic nature of turbulence.
- **Cold gas creation, survival and destruction**: We find three different regimes of cold gas behaviour. One with turbulent cold gas condensations, two others where the hot phase is stable and does not condense. In the latter two regimes, we see one where the cold cloud survives upon introduction, and one where it is destroyed. The regime of particular interest is the one where the hot phase is stable to turbulent condensation but lets the cloud grow if introduced externally.

  This implies the existence of regions of ISM, where cold gas can only appear if a seed cold gas was embedded by an external source.
- **Caveats** ISM is home to rich physics with many different processes contributing to the overall behaviour of the multiphase gas. In this study, we only account for a handful of them. Some of the missing components are viscosity, thermal conduction, magnetic fields, partial ionisation, etc. Inclusion of these processes can be important, and will be revisited in a future study.

6 | Conclusions and outlook

> To see a world in a grain of sand
> And a heaven in a wild flower,
> Hold infinity in the palm of our hand
> And eternity in an hour.
>
> — William Blake, *Auguries of Innocence*

> Gravity do be a cruel mistress.
>
> — Aniket Bhagwat

6.1 Creation of multiphase gas

The first step in the evolution of multiphase gas is its creation. One of the possible origins for multiphase gas is the in-situ formation from hot gas due to thermal instability. The theory of the linear evolution of thermal instability has been an active field of research since the 1950s (Field, 1965; Parker, 1953), with more and more physics getting included. At the same time, significant interest has arisen in non-linear evolution, too.

We expect the hot plasma to be highly turbulent due to its very high Reynolds number. As mentioned in Chapter 5, we investigat how supersonic turbulent fluctuations can seed thermal instability, lead to the creation of a multiphase ISM and mix the phases in such a multiphase ISM.

6.2 Survival of multiphase gas

In recent years, a lot of development has occurred in establishing a firm theory of multiphase gas (McCourt et al., 2018; Gronke & Peng Oh, 2018; Sharma et al., 2010; Butsky et al., 2020; Ji et al., 2019; Fielding et al., 2023b; Gronke et al., 2022b). Also, thanks to analogies to the field of turbulent combustion, these efforts led to a solid understanding of the mixing and transport of the different phases (Tan et al., 2021). This is crucial for implementing small-scale physics in larger-scale simulations and for interpreting observed data. However, all these efforts might be for nothing because of the neglect of magnetic fields. We not only know that magnetic fields exist in astrophysical plasmas, but also that magnetic fields inhibit the mixing of phases. This can affect a big chunk of the theory developed to date for the existence and survival of multiphase

gas, and resolving this tension has been a big puzzle.

To tackle this puzzle, in Chapter 3, we investigated the interplay of magnetic fields, turbulence, and radiative cooling in Das & Gronke (2024b). we show that just the presence of a magnetic field does not inherently affect the mixing or growth of cold gas. Rather, the extent of turbulence in the medium dictates the evolution in a multiphase medium. We confirm this new picture of the turbulent mixing of multiphase gas using the turbulent radiative mixing layer (TRML) simulations. Since then, these results have been confirmed in other studies with varying simulation setups (Hidalgo-Pineda et al., 2024; Zhao & Bai, 2023b). We also show that even though magnetic fields do not affect cold gas mass or volume distribution, they result in significantly more elongated cold gas structures. Using these simulations, we test for observable differences with or without magnetic fields with synthetic absorption spectra for MgII and CIV and find a good agreement with observed MgII absorption spectra statistics from HST-COS observations (Churchill et al., 2020), regardless of the presence or absence of magnetic fields.

In summary, our study in Chapter 3 explains the puzzling fact that magnetic fields present in (turbulent) astrophysical media do not alter the mixing processes between the phases and thus puts the prior theory of small-scale gas dynamics on a solid foundation.

6.3 Bridging the large and small scales

Large-scale simulations have been a potent tool to compare our theoretical understanding and observations. But often, deviations from observation start to appear when looked at closely. Current large-scale simulations manage to reach, at best, a resolution of a few tens of parsecs in the CGM (Hopkins et al., 2018; Grand et al., 2017; Pillepich et al., 2019; Ramesh & Nelson, 2024b). On the other hand, many small-scale studies have shown that we need to resolve scales at least as small as 10^{-2}pc, if not smaller, to capture the small-scale structure accurately (Gronke & Oh, 2020b; Das et al., 2021b; McCourt et al., 2018; Gronke & Oh, 2020a; Das & Gronke, 2024b). Achieving such resolutions in large-scale simulations by brute computational power is infeasible. Hence, there is a need to bridge this gap in scales between the large and small scales, and subgrid models are one way to do so.

Using the recently developed novel AREPO Multifluid Framework (Weinberger & Hernquist, 2023b), as shown in Chapter. 4 we developed a new subgrid model that consistently accounts for the evolution of cold gas, both smaller and bigger than grid cells (Das et al. (2024)). The model consists of source and sink terms for mass, momentum, and energy, quantifying the interactions between the cold and hot gas phases. As these are based on first principles or small-scale simulations based on first principles, the subgrid model does not require any free parameters to capture the unresolved cold gas dynamics. The model was rigorously tested and verified using the resolved small-scale simulations. For this testing and verification, we perform a large grid of over 200 simulations on various HPC systems. We show that the model accurately predicts cold gas growth, survival, and destruction, regardless of the resolution, extent of turbulence, and across the whole parameter space. Even though the model only uses the local properties, without

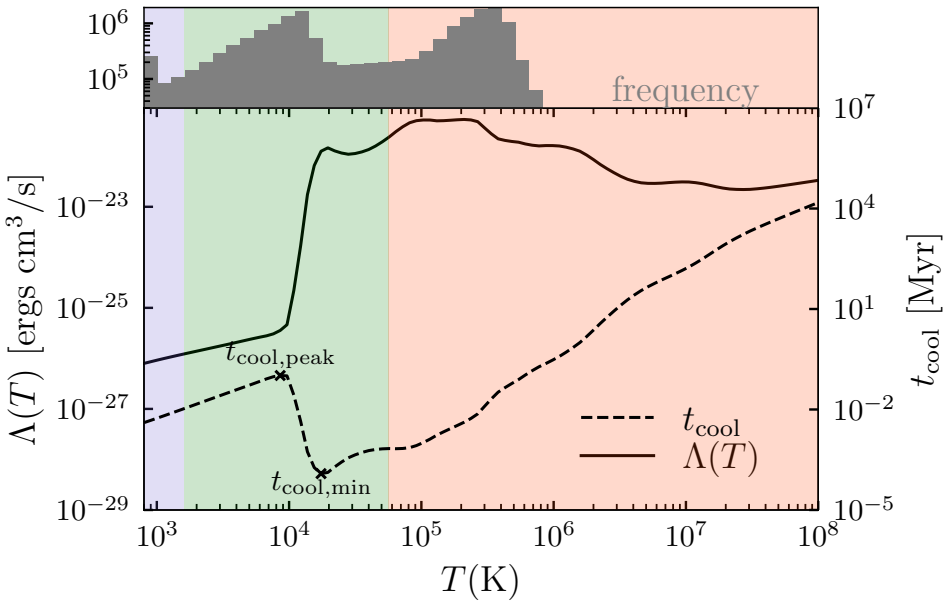

Figure 6.1: The cooling function $\Lambda(T)$ (*solid line, left axis*), and the cooling time $t_{\rm cool}$ (*dashed, right axis*) of a particular cloud crushing setup with floor temperature $T_{\rm floor}$ = 800K and hot gas density $\rho_{\rm hot}$ = 0.1 mp/cm^3. The local peak $t_{\rm cool,peak}$ and minimum $t_{\rm cool,min}$ of the cooling time are labelled. The three shaded regions mark the temperature range for the cold $T_{\rm cloud} < T < 2\times T_{\rm cloud}$ (*blue*), warm $2 \times T_{\rm cloud} < T < T_{\rm mix}$ (*green*), and hot gas temperatures $T_{\rm mix} < T < T_{\rm ceil}$ (*red*) used in this study. These correspond to the temperature distribution of a simulation snapshot shown on top of the figure, where the three stable phases are clearly separated.

any tuning of free parameters, we find that cold gas destruction rates, growth rates, and survival criteria of cold clouds are produced as an emergent behaviour with the subgrid model.

As the model also requires the local turbulent velocity, we develop a novel analytic method to estimate local turbulent velocity which re-uses the velocity gradients calculated for the flux calculations. We verify that this method accurately captures the local turbulent velocity and allows the implementation of this subgrid model to more general large-scale simulations. To showcase the advantages of this model, we simulate $\sim$ 100 tiny "unresolved" cold clouds with just $\mathbf{64^3}$ resolution elements, which would have required $\mathbf{5000^3}$ without the subgrid model.

This effort now paves the way for fully converged, large-scale, cosmological simulations.

6.4 Other works: 3-phase turbulent medium

Until now, studies of multiphase mixing and cold/warm gas survival, relevant to CGM and ICM, have been mostly limited to the investigation of 2-phase media. The justification behind this assumption is the presence of a UV background which inhibits the cooling below 10^4K. But, the

self-shielding in a dense 10^4K gas cloud can shield against the UV background heating and allow the core of such clouds to cool to lower temperatures ($< 10^4$K). This makes 3-phase medium a possibility with cold phase (800K), warm phase (8000K) and hot phase ($\gtrsim 4 \times 10^6$K) in a CGM environment.

To study such a 3-phase turbulent medium, in this study, we use a simulation setup similar to that in Chapter 3. We lower the floor temperature to 800K to allow for the formation of cold gas (800K), in addition to the warm phase (8000K).

Fig. 6.1 shows the cooling function ($\Lambda(T)$) from Wiersma et al. (2009) and Koyama & Inutsuka (2002) on the left y-axis as the solid line and an example of cooling timescale ($t_{\rm cool}$) on the right y-axis as the dashed line, between 800K and 10^8K. We assume isobaricity and a hot gas density of $\rho_{\rm hot} = 0.1$ mp/cm^3 at $T_{\rm hot} = 4 \times 10^6$K. The temperature range is split into three regimes, corresponding to the three phases of gas. We define cold gas phase as gas with temperature in $[T_{\rm cloud}, 2 \times T_{\rm cloud}]$, shown in blue, warm gas phase with temperature in $[2 \times T_{\rm cloud}, T_{\rm mix}]$, shown in green, and hot gas phase with temperature above $T_{\rm mix}$, shown in red. Here, $T_{\rm mix}$ refers to the geometric mean of the cold and hot gas temperature, i.e. $\sqrt{T_{\rm cold} T_{\rm hot}}$ (Begelman & Fabian, 1990a). The top panel of Fig. 6.1 shows the number distribution of the temperature distribution at an intermediate snapshot from one of our simulations. It clearly shows the three peaks corresponding to the three stable gas phases. We also annotate two physically relevant cooling times, namely the local cooling time peak for warm gas phase ($t_{\rm cool,peak}$) and the minimum cooling timescale ($t_{\rm cool,min}$).

Next, we look at the temperature distributions of different gas phases. We plot the temperature slices of the four different behaviours corresponding to the four cases of survival-destruction, to better understand the physical distribution of cold gas. Figure 6.2 shows the morphology of cold gas and warm gas in the four clouds with different initial radii at different stages of evolution. The cold phase is shown in blue, and the warm phase in pink.

As the initial size of the cloud increases from left to right panels, there is more cold gas formation. However, the warm gas is almost always limited to the interface between the cold and hot. For any clump of cold gas, it is always covered by a thin envelope of warm gas. This is consistent with recent conclusions of Blackburn & Farber (2024), who also see “intermediate mixing layers" in their simulations. The presence of the intermediate warm gas layer decreases the mixing timescale of cold gas due to the temperature dependence $t_{\rm cc} = \frac{\chi_{\rm cl}^{1/2} R_{\rm cl}}{v_{\rm turb}}$, where $\chi_{\rm wc} = \frac{T_{\rm warm}}{T_{\rm cold}}$. This timescale is mediated by the newly formed warm layer, which is faster than otherwise with direct interaction between hot and cold, due to the decreased $\chi_{\rm wc} < \chi_{\rm hw} < \chi_{\rm hc}$.

This work will be important for extending our 2-phase subgrid model, from Chapter 4, to a more general framework.

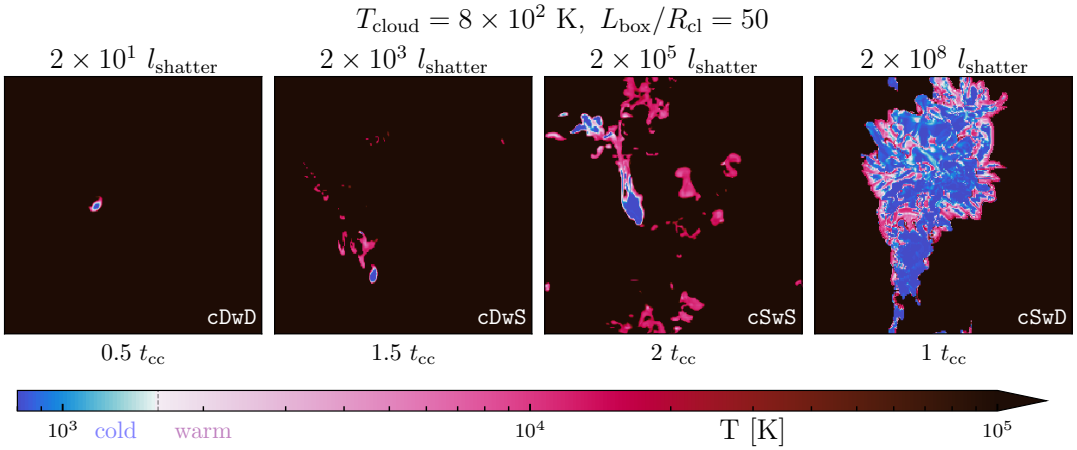

Figure 6.2: Temperature slices of four 800K boxes, initialized with clouds of different initial radii (from $R_{\rm cl} \sim 20 l_{\rm shatter}$ to $\sim 2 \times 10^8 l_{\rm shatter}$) and temperature ratio $\chi \approx 5000$ in the turbulent medium with $\mathcal{M} = 0.4$ and box 50 times the cloud size, again representing the four cases of survival-destruction. The slices are taken at snapshots which best demonstrate the evolution of cold gas, with corresponding $t_{\rm cc}$ values shown on the bottom. The diverging colorbar is drawn in a way that shows the different phases of gas. Going left to right, we see an overall growth of cold medium with the increasing cloud size. Regardless of this, the cold cloud (blue) is always enveloped in layers of warm gas (red), separated from the surrounding hot medium (black).

6.5 Future directions

In recent years, observations have expanded their horizons to a wider range of redshifts, higher spectral and spatial resolutions, and wider surveys, resulting in many new and unexpected discoveries. Given ongoing and future surveys by HST/COS, JWST, VLT, ELT, Gemini, Keck, LSST, TMT, and GMT, this pace of discovery can only accelerate - which is one of the reasons why this topic of 'Cosmic Ecosystems' was selected by the US National Academies in their Astro2020 decadal survey as one out of only three "Key Scientific Challenges for the Next Decade" highlighting its importance for the field. While the observational side of this field is making huge strides, our theoretical models are challenged by the multiphase and multiscale nature of astrophysical gas and, as a result, cannot even reproduce basic observed properties such as the amount of cold gas, let alone make robust predictions. For this reason, there are three directions in which the work of this thesis can be taken forward:

1. pushing the boundaries of theoretical understanding of small-scale physics by including the missing components,

2. developing numerical methods, like subgrid models, to model these small-scale effects and run the next generation of large-scale simulations using them,

3. creating the tools for improved observational predictions from the new generation of

simulations.

6.5.1 A more complete picture of Multiphase gas dynamics

The range of scales for astrophysically relevant processes is vast. From the AU-scale gyro-radius of cosmic ray particles to the Mpc-scale gas flow in the circumgalactic medium (CGM), this makes capturing all the relevant physics in a single simulation computationally infeasible. This has led to efforts towards understanding smaller-scale idealised simulations that include a subset of relevant physics, in an attempt to understand the complex behaviour of astrophysical media. The interaction between different physical processes further complicates this problem. Almost all astrophysical media are highly multiphase, with hot gas, cold gas, molecular gas, and dust. For a long time, the complex interactions between these phases and the computational cost of simulating all the relevant physics had been a bottleneck in studying such multiphase gas. Only in recent years, with better computational resources and advances in the understanding of simpler systems, has it finally become feasible to do a complete and exhaustive investigation with all the different relevant pieces included.

This work can be further extended to study the interplay between all the stable phases of a turbulent astrophysical media, namely: Hot gas ($> 10^6$K), cold gas ($\sim 10^4$K), molecular gas ($< 10^4$K), and dust. This means the simulation will have a vast range in temperatures, from 10^7K to 10K, and this will be the first time any small-scale resolved simulation has captured such a vast range in temperatures.

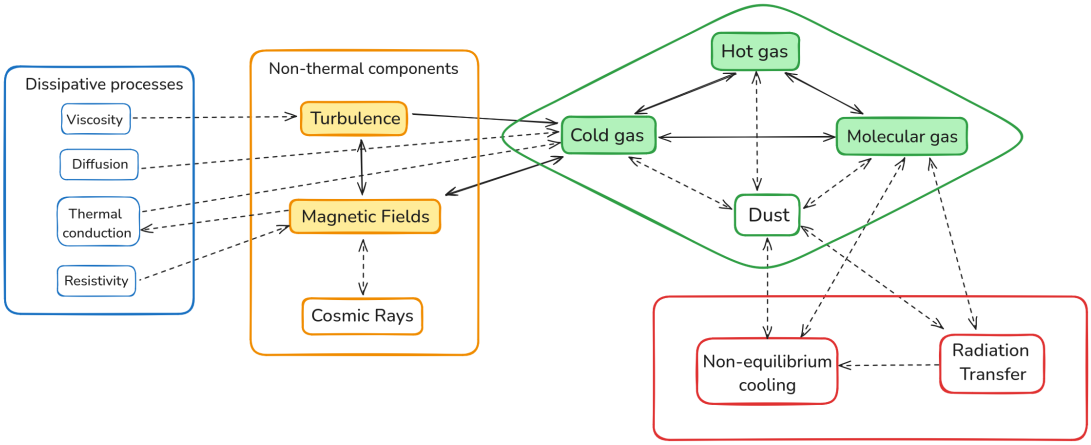

Figure 6.3: The three boxes represent different aspects of multiphase gas dynamics, and the shaded boxes are the currently explored areas. It shows the chain of rich physics needed for better understanding and observational predictions of multiphase gas.

As the gas properties can be very different across this wide range of temperatures, the relevant physical processes also change dramatically depending on the temperature. Three such processes that used to be neglected in a subrange of temperatures but have to be included for this setup are: radiative transfer, non-equilibrium cooling, and magnetic fields. These three processes can

interact in complex ways that can only be properly studied in a small-scale simulation where the required resolution conditions can be satisfied.

6.5.2 Subgrid models and Next-generation large-scale simulations

As mentioned in the previous section, the small-scale effects, as the name suggests, operate at very short length and time scales. Many of the previous studies reaffirm the necessity to resolve scales that are, at the very least, significantly sub-parsec in scale. This multiphase, multiscale nature makes the extended media like CGM and ICM extremely challenging to model, and thus far, all prior simulations are not converged in even the first-order gas properties such as the amount of cold gas, let alone quantities that can directly be compared to observations, such as the gas covering fractions. This is where subgrid models take centre stage. A subgrid model takes into account a small-scale phenomenon occurring at scales smaller than those resolved in a simulation and ensures that the large-scale behaviour is as if those subgrid scales are resolved. One well-known example is the attempt towards a subgrid model of turbulence, to account for the turbulent cascade to scales smaller than the resolved scales of a simulation.

The next generation of large-scale simulations will need to include such subgrid models to accurately capture the small-scale physics of multiphase gas, which is almost entirely missing in the current simulations. The other potential development can be towards filling this gap with an extension to the current work onthe 2-phase MOGLI subgrid model, from Chapter 4.

Our ongoing work into 3-phase gas (hot, cold, and molecular gas) behavior from Sec. 6.4 (Wu, Z., Das, H. K. & Gronke (2025)[in prep.]) and in-situ formation of multiphase gas from hot gas (Das et al. (2021b), Das & Gronke (2025) [in prep.]) can provide the required theoretical backing for the development of a 3-phase subgrid model.

6.5.3 Towards better observational predictions

Apart from acting as a laboratory for controlled experiments and helping us better understand the relevant physics, simulations also serve as a predictive tool to make sense of the observations and test our theoretical understanding. Current simulations cannot predict baryonic observations such as quasar absorption features, because they lack the resolution or methods needed to capture the baryonic physics. So, it is imperative to test the next generation of large-scale simulations rigorously. Hence, another possible avenue for further work can be the test of the predictive ability of large-scale simulations, with subgrid models, to reproduce the recent abundance of absorption and emission observations from both space and ground-based observatories.

We can develop methods to create synthetic quasar line-of-sight (QSO) absorption observations and extended dust emissions from such large-scale simulations, which consistently track the small-scale multiphase structure with subgrid models. As these converged simulations capture the small-scale gas behaviour and structures, such mock observations will allow an apples-to-apples comparison with the observations at greater fidelity and farther into the extended CGM and ICM (Péroux & Howk, 2020). In the future, these datasets can be further extended to include other

emission features observed in and around galaxies (Green et al., 2014; Reichardt Chu et al., 2022).

Bibliography

Abruzzo M. W., Fielding D. B., Bryan G. L., 2022a, arXiv e-prints

Abruzzo M. W., Bryan G. L., Fielding D. B., 2022b, The Astrophysical Journal, 925, 199

Ade P. A. R., et al., 2015, Astronomy & Astrophysics, 576, A104

Adrian R. J., Christensen K. T., Liu Z. C., 2000, Experiments in Fluids, 29, 275

Antiochos S. K., MacNeice P. J., Spicer D. S., 2000, Astrophysical Journal, 536, 494

Antolin P., 2020, Plasma Physics and Controlled Fusion, 62, 014016

Antolin P., Froment C., 2022, Frontiers in Astronomy and Space Sciences, 9, 820116

Armillotta L., Fraternali F., Marinacci F., 2016, Monthly Notices of the Royal Astronomical Society, 462, 4157

Ashley T., Fox A. J., Lockman F. J., Wakker B. P., Richter P., French D. M., Moss V. A., McClure-Griffiths N. M., 2024, Astrophysical Journal, 961, 94

Audit E., Hennebelle P., 2005, A&A, 433, 1

Bader G., Deuflhard P., 1983, Numerische Mathematik, 41, 373

Begelman M. C., Fabian A. C., 1990a, Monthly Notices of the Royal Astronomical Society, 244, 26P

Begelman M. C., Fabian A. C., 1990b, Monthly Notices of the RAS, 244, 26P

Berczik P., Hensler G., Theis C., Spurzem R., 2003, Astrophysics and Space Science, 284, 865

Best P. N., von der Linden A., Kauffmann G., Heckman T. M., Kaiser C. R., 2007, Monthly Notices of the RAS, 379, 894

Blackburn M. G., Farber R. J., 2024, Research Notes of the American Astronomical Society, 8, 94

Boselli A., Fossati M., Sun M., 2022, Astronomy and Astrophysics Reviews, 30, 3

Bourouiba L., 2016, New England Journal of Medicine, 375, e15

Brandenburg A., Nordlund A., 2011, Reports on Progress in Physics, 74, 046901

Brereton G. J., Kodal A., 1994, Physics of Fluids, 6, 1775

Brüggen M., Scannapieco E., Grete P., 2023, arXiv e-prints, p. arXiv:2304.09881

Burkhart B., et al., 2020, The Astrophysical Journal, 905, 14

Bustard C., Zweibel E. G., D'Onghia E., 2016, Astrophysical Journal, 819, 29

Butsky I. S., Fielding D. B., Hayward C. C., Hummels C. B., Quinn T. R., Werk J. K., 2020, The Astrophysical Journal, 903, 77

Butsky I. S., Hummels C. B., Hopkins P. F., Quinn T. R., Werk J. K., 2024, Monthly Notices of the RAS, 535, 1672

Chandrasekhar S., 1961, Hydrodynamic and hydromagnetic stability

Chang S.-J., Gronke M., 2024, Monthly Notices of the RAS, 532, 3526

Chen H.-W., 2017, in Knapen J. H., Lee J. C., Gil de Paz A., eds, Astrophysics and Space Science Library Vol. 434, Outskirts of Galaxies. p. 291, doi:10.1007/978-3-319-56570-5_9

Chen Z., Oh S. P., 2024, Monthly Notices of the Royal Astronomical Society, 530, 4032

Chen M. C., et al., 2023a, MNRAS, 518, 2354

Chen H.-W., et al., 2023b, Astrophysical Journal, Letters, 955, L25

Choudhury P. P., Sharma P., Quataert E., 2019, Monthly Notices of the Royal Astronomical Society, 488, 3195

Churchill C. W., Vogt S. S., Charlton J. C., 2003, Astronomical Journal, 125, 98

Churchill C. W., Evans J. L., Stemock B., Nielsen N. M., Kacprzak G. G., Murphy M. T., 2020, The Astrophysical Journal, 904, 28

Clarke T. E., Kronberg P. P., Böhringer H., 2001, The Astrophysical Journal, 547, L111

Consolandi G., Gavazzi G., Fossati M., Fumagalli M., Boselli A., Yagi M., Yoshida M., 2017, Astronomy and Astrophysics, 606, A83

Corrsin S., 1951, Journal of Applied Physics, 22, 469

Cox D. P., 2005, Annual Review of Astron and Astrophys, 43, 337

Crighton N. H. M., Hennawi J. F., Simcoe R. A., Cooksey K. L., Murphy M. T., Fumagalli M., Prochaska J. X., Shanks T., 2015, Monthly Notices of the Royal Astronomical Society, 446, 18

Damköhler G., 1940, Zeitschrift für Elektrochemie und angewandte physikalische Chemie, 46, 601

Das H. K., Gronke M., 2024a, Monthly Notices of the RAS, 527, 991

Das H. K., Gronke M., 2024b, Monthly Notices of the RAS, 527, 991

Das H. K., Gronke M., 2025, In prep.

Das H. K., Choudhury P. P., Sharma P., 2021a, Monthly Notices of the Royal Astronomical Society, 502, 4935

Das H. K., Choudhury P. P., Sharma P., 2021b, Monthly Notices of the RAS, 502, 4935

Das H. K., Gronke M., Weinberger R., 2024, arXiv e-prints, p. arXiv:2412.03751

Dekel A., Sari R., Ceverino D., 2009, Astrophysical Journal, 703, 785

Dimopoulos K., Davis A.-C., 1997, Physics Letters B, 390, 87

Donahue M., Voit G. M., 2022, Physics Reports, 973, 1

Dreher J. W., Carilli C. L., Perley R. A., 1987, The Astrophysical Journal, 316, 611

Dubinski J., 1998, Astrophysical Journal, 502, 141

Dubner G., Castelletti G., Kargaltsev O., Pavlov G. G., Bietenholz M., Talavera A., 2017, Astrophysical Journal, 840, 82

Dursi L. J., Pfrommer C., 2008, The Astrophysical Journal, 677, 993

Elmegreen B. G., Scalo J., 2004, Annual Review of Astronomy and Astrophysics, 42, 211

Esquivel A., Benjamin R. A., Lazarian A., Cho J., Leitner S. N., 2006, The Astrophysical Journal, 648, 1043

Eswaran V., Pope S. B., 1988a, Computers & Fluids, 16, 257

Eswaran V., Pope S., 1988b, Computers & Fluids, 16, 257

Fabian A. C., Johnstone R. M., Sanders J. S., Conselice C. J., Crawford C. S., Gallagher III J. S., Zweibel E., 2008, Nature, 454, 968

Faeth G., 1996, Symposium (International) on Combustion, 26, 1593

Falceta-Gonçalves D., Kowal G., Falgarone E., Chian A. C.-L., 2014, Nonlinear Processes in Geophysics, 21, 587

Falceta-Gonçalves D., de Gouveia Dal Pino E. M., Gallagher J. S., Lazarian A., 2010, Astrophysical Journal, Letters, 708, L57

Falconer K. J., 1985, The Geometry of Fractal Sets. Cambridge University Press, doi:10.1017/CBO9780511623738, https://www.cambridge.org/core/product/identifier/9780511623738/type/book

Farber R. J., Gronke M., 2021, arXiv e-prints, 17, 1

Faucher-Giguere C.-A., Oh S. P., 2023a, arXiv e-prints, p. arXiv:2301.10253

Faucher-Giguère C.-A., Oh S. P., 2023b, Annual Review of Astron and Astrophys, 61, 131

Federrath C., 2013, Monthly Notices of the Royal Astronomical Society, 436, 1245

Federrath C., Klessen R. S., 2012, Astrophysical Journal, 761, 156

Field G. B., 1965, Astrophysical Journal, 142, 531

Field G. B., Field G. B., 1965, The Astrophysical Journal, pp 531–567

Field G. B., Goldsmith D. W., Habing H. J., 1969, Astrophysical Journal, Letters, 155, L149

Fielding D. B., Bryan G. L., 2022, Astrophysical Journal, 924, 82

Fielding D. B., Ostriker E. C., Bryan G. L., Jermyn A. S., 2020, The Astrophysical Journal, 894, L24

Fielding D. B., Ripperda B., Philippov A. A., 2023a, The Astrophysical Journal Letters, 949, L5

Fielding D. B., Ripperda B., Philippov A. A., 2023b, Astrophysical Journal, Letters, 949, L5

Fossati M., Fumagalli M., Boselli A., Gavazzi G., Sun M., Wilman D. J., 2016, Monthly Notices of the RAS, 455, 2028

Fox A. J., et al., 2016, Astrophysical Journal, Letters, 816, L11

Girichidis P., Naab T., Walch S., Berlok T., 2021, Monthly Notices of the RAS, 505, 1083

Grand R. J. J., et al., 2017, Monthly Notices of the RAS, 467, 179

Green A. W., et al., 2014, Monthly Notices of the RAS, 437, 1070

Grete P., O'Shea B. W., Beckwith K., Schmidt W., Christlieb A., 2017, Physics of Plasmas, 24, 092311

Grete P., O'Shea B. W., Beckwith K., 2018, The Astrophysical Journal, 858, L19

Gronke M., Oh S. P., 2020a, Monthly Notices of the Royal Astronomical Society, 492, 1970

Gronke M., Oh S. P., 2020b, Monthly Notices of the Royal Astronomical Society: Letters, 494, L27

Gronke M., Oh S. P., 2023, Monthly Notices of the Royal Astronomical Society, p. stad1874

Gronke M., Peng Oh S., 2018, Monthly Notices of the Royal Astronomical Society: Letters, 480, L111

Gronke M., Dijkstra M., McCourt M., Oh S. P., 2016, Astrophysical Journal, Letters, 833, L26

Gronke M., Oh S. P., Ji S., Norman C., 2022a, Monthly Notices of the Royal Astronomical Society, 511, 859

Gronke M., Oh S. P., Ji S., Norman C., 2022b, Monthly Notices of the RAS, 511, 859

Hansen M., Oh S. P., 2006, Monthly Notices of the RAS, 367, 979

Harfst S., Theis C., Hensler G., 2004, Publications of the Astronomical Society of Australia, 21, 228

Heckman T. M., Thompson T. A., 2017, arXiv e-prints, p. arXiv:1701.09062

Hester J. J., 2008, Annual Review of Astron and Astrophys, 46, 127

Hidalgo-Pineda F., Farber R. J., Gronke M., 2023, arXiv e-prints, p. arXiv:2304.09897

Hidalgo-Pineda F., Farber R. J., Gronke M., 2024, Monthly Notices of the RAS, 527, 135

Hillier A., Polito V., 2018, Astrophysical Journal, Letters, 864, L10

Hillier A., Snow B., Arregui I., 2023, Monthly Notices of the Royal Astronomical Society, 520, 1738

Hopkins P. F., et al., 2018, Monthly Notices of the RAS, 480, 800

Hopkins P. F., et al., 2019, Monthly Notices of the Royal Astronomical Society, 492, 3465

Hu H., Qiu Y., Gendron-Marsolais M.-L., Bogdanović T., Hlavacek-Larrondo J., Ho L. C., Inayoshi K., McNamara B. R., 2022, The Astrophysical Journal Letters, 929, L30

Huang S., Katz N., Scannapieco E., Cottle J., Davé R., Weinberg D. H., Peeples M. S., Brüggen M., 2020, Monthly Notices of the RAS, 497, 2586

Hummels C. B., Smith B. D., Silvia D. W., 2017, The Astrophysical Journal, 847, 59

Hummels C. B., et al., 2019, The Astrophysical Journal, 882, 156

Hummels C. B., Rubin K. H. R., Schneider E. E., Fielding D. B., 2024, Astrophysical Journal, 972, 148

Inutsuka S.-i., 2009, Proceedings of the International Astronomical Union, 5, 444–445

Jáchym P., Combes F., Cortese L., Sun M., Kenney J. D. P., 2014, Astrophysical Journal, 792, 11

Jáchym P., et al., 2019, Astrophysical Journal, 883, 145

Jennings F., Beckmann R. S., Sijacki D., Dubois Y., 2023, Monthly Notices of the RAS, 518, 5215

Ji S., Oh S. P., McCourt M., 2018, Monthly Notices of the Royal Astronomical Society, 476, 852

Ji S., Oh S. P., Masterson P., 2019, Monthly Notices of the Royal Astronomical Society, 487, 737

Kaaret P., Prestwich A. H., Zezas A., Murray S. S., Kim D. W., Kilgard R. E., Schlegel E. M., Ward M. J., 2001, Monthly Notices of the RAS, 321, L29

Kanjilal V., Dutta A., Sharma P., 2021, Monthly Notices of the Royal Astronomical Society, 501, 1143

Kannan R., Garaldi E., Smith A., Pakmor R., Springel V., Vogelsberger M., Hernquist L., 2022, Monthly Notices of the Royal Astronomical Society, 511, 4005

Kari J., 1994, Journal of Computer and System Sciences, 48, 149

Kempski P., Fielding D., Quataert E., Galishnikova A. K., Kunz M. W., Philippov A. A., Ripperda B., 2023, MNRAS, 000, 1

Kim C.-G., Ostriker E. C., 2015, Astrophysical Journal, 802, 99

Kim C.-G., Ostriker E. C., 2017, Astrophysical Journal, 846, 133

Kim K. T., Kronberg P. P., Dewdney P. E., Landecker T. L., 1990, The Astrophysical Journal, 355, 29

Klein R. I., McKee C. F., Colella P., 1994a, The Astrophysical Journal, 420, 213

Klein R. I., McKee C. F., Colella P., 1994b, Astrophysical Journal, 420, 213

Kolmogorov A., 1941, Akademiia Nauk SSSR Doklady, 30, 301

Koyama H., Inutsuka S.-i., 2002, Astrophysical Journal, Letters, 564, L97

Kuo K. K.-y., Acharya R., 2012, Fundamentals of turbulent and multiphase combustion. John Wiley & Sons

Kwak K., Shelton R. L., 2010, The Astrophysical Journal, 719, 523

Lan T.-W., Fukugita M., 2017, Astrophysical Journal, 850, 156

Lancaster L., Ostriker E. C., Kim J.-G., Kim C.-G., 2021, The Astrophysical Journal, 914, 89

Larkin C. J. K., Mackey J., Haworth T. J., Sander A. A. C., 2025, arXiv e-prints, p. arXiv:2503.01272

Ledos N., Takasao S., Nagamine K., 2024, Monthly Notices of the RAS, 527, 11304

Lemaster M. N., Stone J. M., 2009, The Astrophysical Journal, 691, 1092

Levinson F. H., Roberts W. W. J., 1981, Astrophysical Journal, 245, 465

Li J.-T., Hodges-Kluck E., Stein Y., Bregman J. N., Irwin J. A., Dettmar R.-J., 2019, Astrophysical Journal, 873, 27

Li X., Chang P., Levin Y., Matzner C. D., Armitage P. J., 2020, Monthly Notices of the Royal Astronomical Society, 494, 2327

Li Y., Luo R., Fossati M., Sun M., Jáchym P., 2022, MNRAS, 000, 1

Lopez-Rodriguez E., Guerra J. A., Asgari-Targhi M., Schmelz J. T., 2021, The Astrophysical Journal, 914, 24

Lorensen W. E., Cline H. E., 1987, in Proceedings of the 14th Annual Conference on Computer Graphics and Interactive Techniques. SIGGRAPH '87. Association for Computing Machinery, New York, NY, USA, p. 163–169, doi:10.1145/37401.37422, https://doi.org/10.1145/37401.37422

Luo R., et al., 2023, Monthly Notices of the RAS, 521, 6266

Mandelbrot B., 1967, Science, 156, 636

Mandelbrot B. B., Wheeler J. A., 1983, American Journal of Physics, 51, 286

Mandelker N., Nagai D., Aung H., Dekel A., Birnboim Y., van den Bosch F. C., 2020, Monthly Notices of the Royal Astronomical Society, 494, 2641

Marin-Gilabert T., Gronke M., Oh S. P., 2025, arXiv e-prints, p. arXiv:2504.15345

Marinacci F., Binney J., Fraternali F., Nipoti C., Ciotti L., Londrillo P., 2010, Monthly Notices of the Royal Astronomical Society, 404, 1464

Martizzi D., Fielding D., Faucher-Giguère C.-A., Quataert E., 2016, Monthly Notices of the RAS, 459, 2311

Matsubayashi K., Konami S., Sofue Y., Tsuru T. G., Matsushita K., Seta M., Kimura M., Ohyama Y., 2013, Shedding Light on the Power of M82's Superwinds, https://subarutelescope.org/en/results/2013/01/18/2437.html

McCourt M., Sharma P., Quataert E., Parrish I. J., 2012, Monthly Notices of the RAS, 419, 3319

McCourt M., O'Leary R. M., Madigan A.-M., Quataert E., 2015, Monthly Notices of the Royal Astronomical Society, 449, 2

McCourt M., Oh S. P., O'Leary R., Madigan A.-M., 2018, Monthly Notices of the Royal Astronomical Society, 473, 5407

McKee C. F., Ostriker J. P., 1977a, The Astrophysical Journal, 218, 148

McKee C. F., Ostriker J. P., 1977b, The Astrophysical Journal, 218, 148

Mccourt M., Sharma P., Quataert E., Parrish I. J., 2012, Monthly Notices of the Royal Astronomical Society, 419, 3319

Merluzzi P., et al., 2013, Monthly Notices of the RAS, 429, 1747

Mohapatra R., Sharma P., 2019, Monthly Notices of the Royal Astronomical Society, 484, 4881

Mohapatra R., Federrath C., Sharma P., 2020, Monthly Notices of the Royal Astronomical Society, 493, 5838

Mohapatra R., Federrath C., Sharma P., 2021, Monthly Notices of the Royal Astronomical Society, 500, 5072

Mohapatra R., Jetti M., Sharma P., Federrath C., 2022a, Monthly Notices of the Royal Astronomical Society, 510, 2327

Mohapatra R., Jetti M., Sharma P., Federrath C., 2022b, Monthly Notices of the Royal Astronomical Society, 510, 3778

Mohapatra R., Federrath C., Sharma P., 2022c, Monthly Notices of the Royal Astronomical Society, 514, 3139

Mufson S. L., McCollough M. L., Dickel J. R., Petre R., White R., Chevalier R., 1986, Astronomical Journal, 92, 1349

NASA/CXC/SAO JHU STScI 2006, Multiwavelength Image of the Starburst Galaxy M82, NASA Chandra X-ray Observatory Public Image Archive, https://chandra.harvard.edu/photo/2006/m82/

Naab T., Ostriker J. P., 2017, Annual Review of Astron and Astrophys, 55, 59

Nakagawa Y., 1970, Solar Physics, 12, 419

Nguyen D. D., Thompson T. A., 2022, The Astrophysical Journal Letters, 935, L24

Oboukhov A. M., 1949, Isv. Geogr. Geophys. Ser., 13, 58

Okamoto T., Eke V. R., Frenk C. S., Jenkins A., 2005, Monthly Notices of the RAS, 363, 1299

Olivares V., Picquenot A., Su Y., Gaspari M., Gendron-Marsolais M.-L., Polles F. L., Nulsen P., 2025, Nature Astronomy, 9, 449

Oppenheimer B. D., Davé R., 2006, Monthly Notices of the RAS, 373, 1265

Pakmor R., Springel V., Bauer A., Mocz P., Munoz D. J., Ohlmann S. T., Schaal K., Zhu C., 2016, Monthly Notices of the RAS, 455, 1134

Pakmor R., et al., 2020, Monthly Notices of the Royal Astronomical Society, 498, 3125

Parenti S., 2014, Living Reviews in Solar Physics, 11, 1

Parker E. N., 1953, Astrophysical Journal, 117, 431

Pedregosa F., et al., 2011, Journal of Machine Learning Research, 12, 2825

Peeples M. S., et al., 2019, Astrophysical Journal, 873, 129

Péroux C., Howk J. C., 2020, Annual Review of Astronomy and Astrophysics, 58, 363

Pillepich A., et al., 2019, Monthly Notices of the RAS, 490, 3196

Pope S. B., 2000, Turbulent Flows

Prosperetti A., Tryggvason G., 2007, Computational Methods for Multiphase Flow. Cambridge University Press

Putman M. E., Peek J. E. G., Joung M. R., 2012, Annual Review of Astron and Astrophys, 50, 491

Ramesh R., Nelson D., 2024a, Monthly Notices of the RAS, 528, 3320

Ramesh R., Nelson D., 2024b, Monthly Notices of the RAS, 528, 3320

Rathjen T.-E., Naab T., Walch S., Seifried D., Girichidis P., Wünsch R., 2023, Monthly Notices of the RAS, 522, 1843

Rauch M., Sargent W. L. W., Barlow T. A., 1999, Astrophysical Journal, 515, 500

Reichardt Chu B., et al., 2022, Monthly Notices of the RAS, 511, 5782

Reynolds O., 1883, Philosophical Transactions of the Royal Society of London, 174, 935

Roediger E., Brüggen M., 2006, Monthly Notices of the RAS, 369, 567

Rosdahl J., Schaye J., Dubois Y., Kimm T., Teyssier R., 2017, Monthly Notices of the RAS, 466, 11

Rubin K. H. R., et al., 2022, Astrophysical Journal, 936, 171

Rudie G. C., Steidel C. C., Pettini M., Trainor R. F., Strom A. L., Hummels C. B., Reddy N. A., Shapley A. E., 2019, Astrophysical Journal, 885, 61

Ruszkowski M., Pfrommer C., 2023, arXiv e-prints, p. arXiv:2306.03141

Salomé P., et al., 2006, Astronomy and Astrophysics, 454, 437

Sardina G., Picano F., Gualtieri P., Casciola C. M., 2011, in Kuerten H., Geurts B., Armenio V., Fröhlich J., eds, Direct and Large-Eddy Simulation VIII. Springer Netherlands, Dordrecht, pp 213–218

Saurel R., Abgrall R., 1999, Journal of Computational Physics, 150, 425

Scalo J., Elmegreen B. G., 2004, Annual Review of Astron and Astrophys, 42, 275

Scannapieco E., Brüggen M., 2008, Astrophysical Journal, 686, 927

Scannapieco E., Brüggen M., 2015, The Astrophysical Journal, 805, 158

Scannapieco C., Tissera P. B., White S. D., Springel V., 2006, Monthly Notices of the Royal Astronomical Society, 371, 1125

Scannapieco E., Pan L., Buie II E., Brüggen M., 2024, Science Advances, 10, eado3958

Schaye J., Carswell R. F., Kim T.-S., 2007, Monthly Notices of the RAS, 379, 1169

Schekochihin A. A., 2020, arXiv e-prints, p. arXiv:2010.00699

Schekochihin A. A., Cowley S. C., 2007, Turbulence and Magnetic Fields in Astrophysical Plasmas (arXiv:astro-ph/0507686)

Schekochihin A., Cowley S., Maron J., Malyshkin L., 2001, Physical Review E, 65, 16305

Schmidt W., Federrath C., 2011, Astronomy and Astrophysics, 528, A106

Schmidt W., Hillebrandt W., Niemeyer J. C., 2006a, Computers & Fluids, 35, 353

Schmidt W., Niemeyer J. C., Hillebrandt W., 2006b, Astronomy and Astrophysics, 450, 265

Schneider E. E., Robertson B. E., 2017, The Astrophysical Journal, 834, 144

Schneider E. E., Ostriker E. C., Robertson B. E., Thompson T. A., 2020, The Astrophysical Journal, 895, 43

Semelin B., Combes F., 2002, Astronomy & Astrophysics, 388, 826

Semenov V. A., 2024, arXiv e-prints, p. arXiv:2410.23339

Seta A., Federrath C., 2022, Monthly Notices of the RAS, 514, 957

Seta A., Federrath C., Livingston J. D., McClure-Griffiths N. M., 2023, Monthly Notices of the RAS, 518, 919

Sharma P., Parrish I. J., Quataert E., 2010, Astrophysical Journal, 720, 652

Sharma P., Mccourt M., Quataert E., Parrish I. J., 2012, Monthly Notices of the Royal Astronomical Society, 420, 3174

Singh Bisht M., Sharma P., Duttta A., Nath B. B., 2024, arXiv e-prints, p. arXiv:2411.17173

Slavin J. D., Shull J. M., Begelman M. C., 1993, The Astrophysical Journal, 407, 83

Smith M. C., Sijacki D., Shen S., 2018, Monthly Notices of the RAS, 478, 302

Smith M. C., Fielding D. B., Bryan G. L., Bennett J. S., Kim C.-G., Ostriker E. C., Somerville R. S., 2024, arXiv e-prints, p. arXiv:2408.15321

Sobacchi E., Sormani M. C., 2019, Monthly Notices of the Royal Astronomical Society, 486, 205

Spitzer L., 1962, Physics of Fully Ionized Gases

Springel V., 2010, Monthly Notices of the RAS, 401, 791

Springel V., Hernquist L., 2003, Monthly Notices of the RAS, 339, 289

Steidel C. C., Erb D. K., Shapley A. E., Pettini M., Reddy N., Bogosavljević M., Rudie G. C., Rakic O., 2010, Astrophysical Journal, 717, 289

Stokes G. G., 1851, Transactions of the Cambridge Philosophical Society, 9, 8

Stone J. M., Tomida K., White C. J., Felker K. G., 2020b, The Astrophysical Journal Supplement Series, 249, 4

Stone J. M., Tomida K., White C. J., Felker K. G., 2020a, The Astrophysical Journal Supplement Series, 249, 4

Subramanian K., 2015, arXiv e-prints, p. arXiv:1504.02311

Sun M., Donahue M., Roediger E., Nulsen P. E. J., Voit G. M., Sarazin C., Forman W., Jones C., 2010, Astrophysical Journal, 708, 946

Sun M., et al., 2021, Nature Astronomy, 6, 270

Tan B., Fielding D. B., 2023, MNRAS, 000, 1

Tan B., Oh S. P., 2021, Monthly Notices of the Royal Astronomical Society: Letters, 508, L37

Tan B., Oh S. P., Gronke M., 2021, Monthly Notices of the Royal Astronomical Society, 502, 3179

Tan B., Oh S. P., Gronke M., 2023, Monthly Notices of the RAS, 520, 2571

Taylor G. B., Perley R. A., 1993, The Astrophysical Journal, 416, 554

Tonnesen S., Bryan G. L., 2009, The Astrophysical Journal, 694, 789

Tonnesen S., Bryan G. L., 2021a, Astrophysical Journal, 911, 68

Tonnesen S., Bryan G. L., 2021b, Astrophysical Journal, 911, 68

Townsend R. H., 2009a, Astrophysical Journal, Supplement Series, 181, 391

Townsend R. H. D., 2009b, Astrophysical Journal, Supplement, 181, 391

Tumlinson J., Peeples M. S., Werk J. K., 2017, Annual Review of Astronomy and Astrophysics, AA, 1

Turk M. J., Smith B. D., Oishi J. S., Skory S., Skillman S. W., Abel T., Norman M. L., 2011, The Astrophysical Journal Supplement Series, 192, 9

Veilleux S., Cecil G., Bland-Hawthorn J., 2005, Annual Review of Astronomy and Astrophysics, 43, 769

Veilleux S., Maiolino R., Bolatto A. D., Aalto S., 2020a, The Astronomy and Astrophysics Review, 28, 2

Veilleux S., Maiolino R., Bolatto A. D., Aalto S., 2020b, Astronomy and Astrophysics Reviews, 28, 2

Vidal-García A., et al., 2021, Monthly Notices of the Royal Astronomical Society, 506, 2551

Villermaux E., 2019, Annual Review of Fluid Mechanics, 51, 245

Virtanen P., et al., 2020, Nature Methods, 17, 261

Vollmer B., Cayatte V., Balkowski C., Duschl W. J., 2001, Astrophysical Journal, 561, 708

Wakker B. P., van Woerden H., 1997, Annual Review of Astron and Astrophys, 35, 217

Walch S., et al., 2015, Monthly Notices of the RAS, 454, 238

Wang C., Oh S. P., Ruszkowski M., 2023a, Monthly Notices of the Royal Astronomical Society, 519, 4408

Wang C., Oh S. P., Ruszkowski M., 2023b, Monthly Notices of the RAS, 519, 4408

Warren O., Schneider E. E., Mao S. A., Abruzzo M. W., 2024, arXiv e-prints, p. arXiv:2410.11747

Waters T., Proga D., 2019, The Astrophysical Journal, 875, 158

Weinberger R., Hernquist L., 2023a, Monthly Notices of the RAS, 519, 3011

Weinberger R., Hernquist L., 2023b, Monthly Notices of the RAS, 519, 3011

Weinberger R., Springel V., Pakmor R., 2020, Astrophysical Journal, Supplement, 248, 32

Westmeier T., 2018, Monthly Notices of the RAS, 474, 289

Wiersma R. P. C., Schaye J., Smith B. D., 2009, Monthly Notices of the RAS, 393, 99

Wittor D., Gaspari M., 2020, Monthly Notices of the Royal Astronomical Society, 498, 4983

Wu, Z., Das, H. K. Gronke M., 2025, In prep.

Yang Y., Ji S., 2023, Monthly Notices of the Royal Astronomical Society, 520, 2148

Zhao X., Bai X.-N., 2023a, arXiv e-prints, p. arXiv:2307.12355

Zhao X., Bai X.-N., 2023b, Monthly Notices of the RAS, 526, 4245

van de Voort F., Bieri R., Pakmor R., Gómez F. A., Grand R. J. J., Marinacci F., 2021, Monthly Notices of the Royal Astronomical Society, 501, 4888

List of Figures

Appendix

MHD Turbulence

Comparison of methods to calculate u'

There are different ways to calculate the turbulent velocity (u') in TRML simulations, and it is important to ensure that our conclusions are not sensitive to the choice of the method. In this section, we compare two methods of calculating u'. The first method is the one we use for the analysis in this paper and is the same method used in Tan et al. (2021). The second method is employing Gaussian filtering (e.g. Brereton & Kodal, 1994; Adrian et al., 2000; Abruzzo et al., 2022a). Fig 4 shows the same analysis as Fig 3.5 but using the two methods, and Fig 5 shows the same analysis as the Fig 3.6 but using the u' calculated using the Gaussian filtering method.

We find that our results are robust across the two methods and are insensitive to the differences between these two methods of calculating u'.

Quantification of filamentariness

As mentioned in § 3.3.2, we use neighbourhood graphs for each cold gas clump to calculate the measure of filamentariness. The following are the different steps we take to calculate the measure, after we use a clump-finding method to identify the cold gas clumps:

1. Calculate the adjacency matrix for each gridcell inside the clump. If a speedup is needed, construct another adjacency matrix for each n^{th}.
2. Construct the neighbourhood graphs from all the adjacency matrices constructed in the previous step.
3. Calculate the shortest path between each node in the smallest of the neighbourhood graphs created in the previous step.
4. Find the longest of the set of calculated shortest paths and note the nodes corresponding to that path.
5. Recalculate the length of the longest "shortest" path between the nodes from the previous step, using the largest neighbourhood graph.

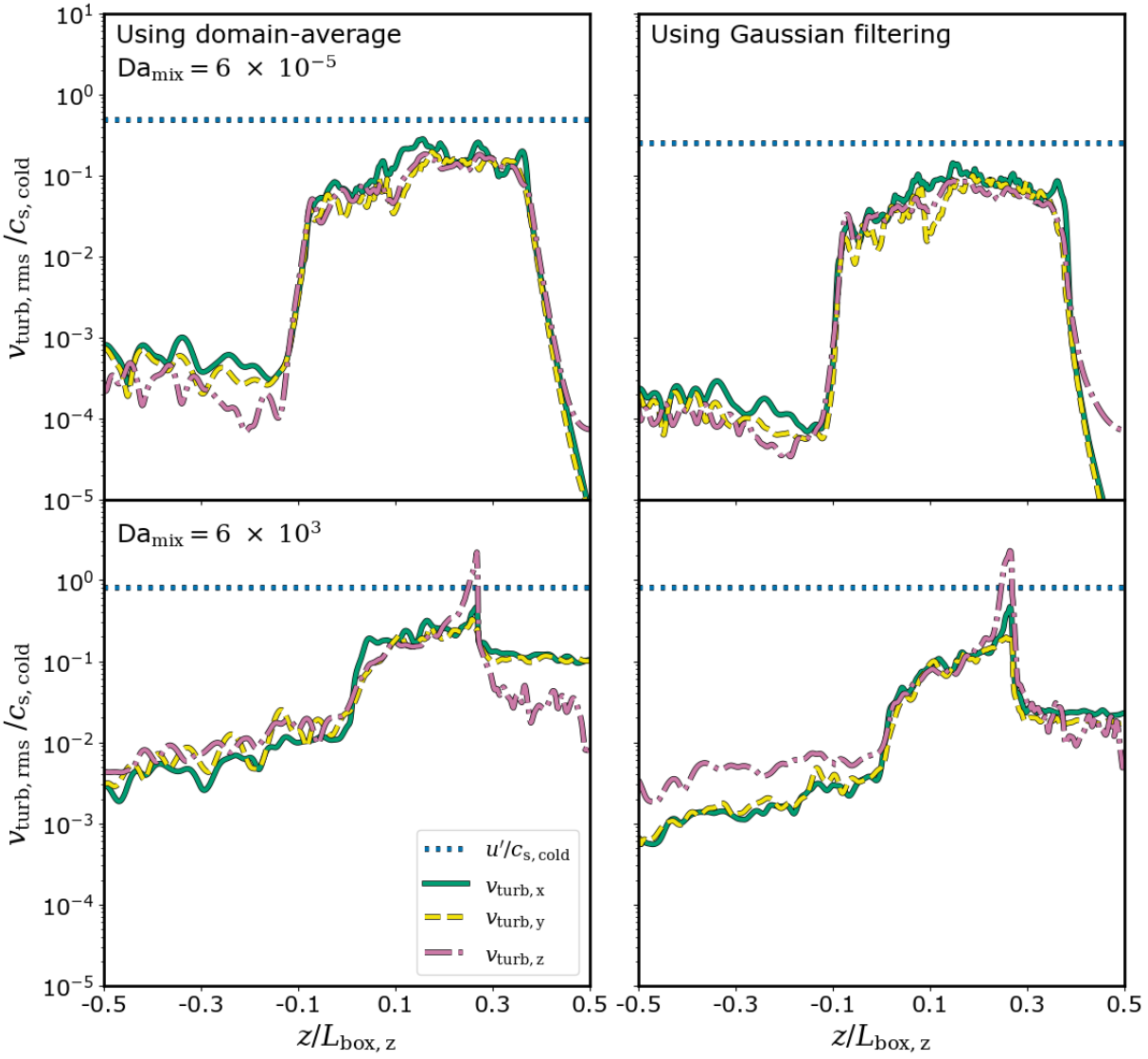

Figure 4: u' profiles for two different methods. The left panel shows the averaging method used in Tan et al. (2021), and the right panel shows the Gaussian filtering method used in Abruzzo et al. (2022a). We find only minor differences between the two methods which, at worst, stay within an order of magnitude.

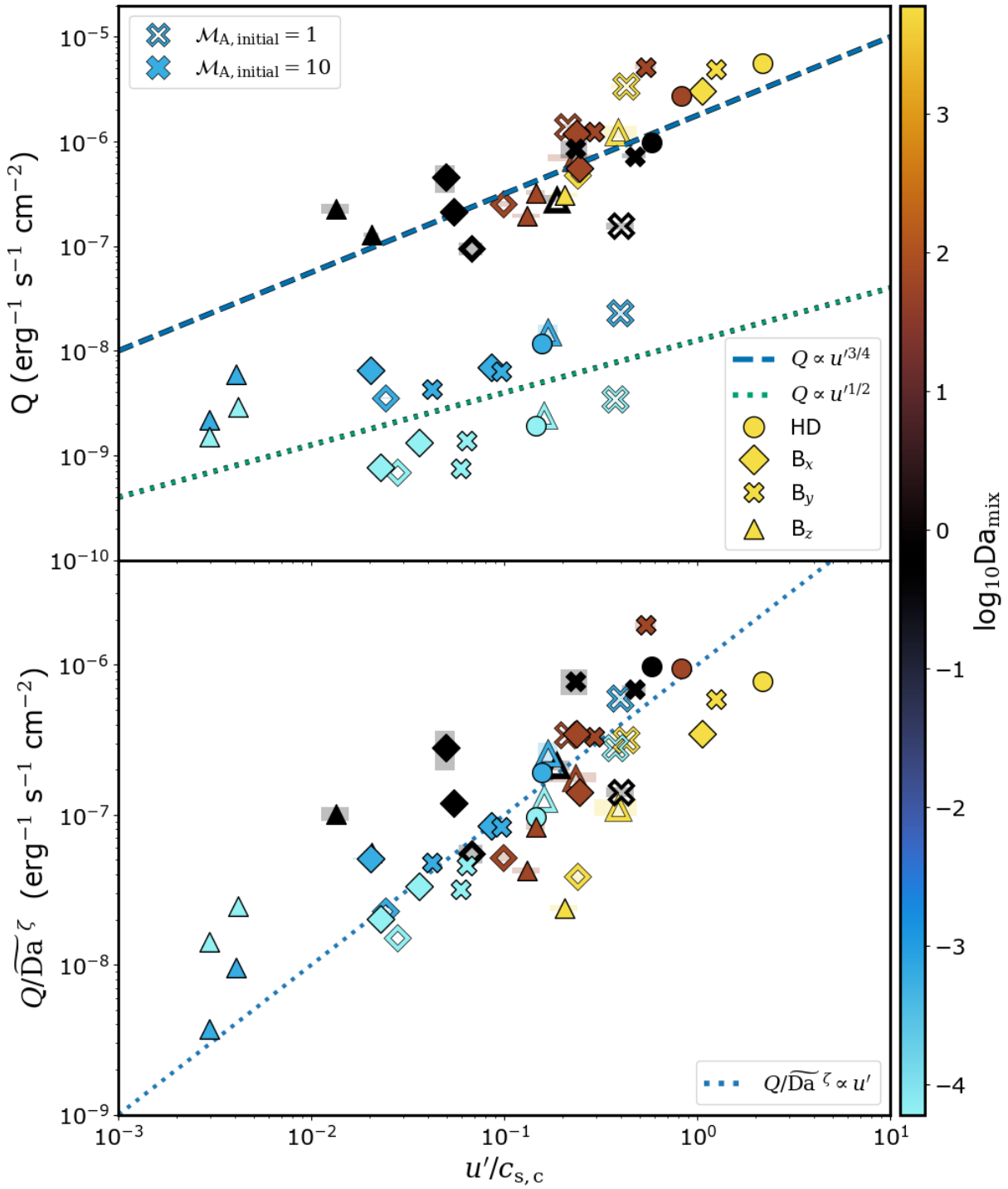

Figure 5: Same figure as Fig 3.6, but the u' is calculated using the Gaussian filtering method from Abruzzo et al. (2022a). This shows that the results in Fig 3.6 are not sensitive to the method used to calculate the turbulent velocity.

6. The length from the previous step gives a rough measure of the filament length in the clump. Repeat the steps for all clumps.

We tested the above method for different numbers of skipped points for calculating the shortest paths. We find a negligible difference in the calculated length of large clumps even up to the point where every 20^{th} point is considered. We see major deviations only when the skipped points are a big majority of the points and the resulting neighbourhood graph is not representative of the clump anymore.

In this work, we only skip every 4^{th} point in the clump. Fig. 6 shows an example of the calculated filament length for a clump in an MHD turbulent box simulation.

Mock spectra

As mentioned in § 3.3.5 and 3.4.3, we find only marginal differences between the statistics of the MgII mock absorption spectra of the HD and MHD simulations, despite significant differences in the column densities. This can be due to the specific property of the MgII 2796Å absorption line, like the curve of growth flattening around similar column densities, which can lead to smaller differences. Another possible reason for this lack of difference can also be the spectral resolution. To address both these points, we first increase the spectral resolution of the mock spectra tenfolds to $\Delta\lambda = 0.01$Å and recreate the same MgII 2796Å mock absorption spectra analysis as Fig. 3.18. Secondly, we repeat the same analysis for CIV 1551Å at the higher resolution. As a significant fraction of the CIV mock absorption lines are saturated, we use a more relaxed constraint for the minimum (0.01) and maximum (0.95) absorbed flux. Fig. 7 and 8 show the results from the analysis of higher spectral resolution MgII 2796Å and CIV 1551Å mock absorption spectra.

We find that the increase in spectral resolution of mock MgII absorption spectra shifts the relation between the number of features and total equivalent width, but it roughly follows the same slope as the observed relation from Churchill et al. (2020). Surprisingly, the statistics of the mock CIV 1551Å absorption spectra also seem to agree with the observed MgII relation, and the HD-MHD differences are wider as expected, but to the lower number of unsaturated mock spectra, it is harder to draw concrete conclusions.

This apparent robustness of the observed relation might hint towards a more fundamental origin of the relation, like the clump distribution. But, we leave it to future studies to investigate this further.

Effect of stochasticity

The stochastic nature of the turbulence can cause variations in the evolution of quantities in a turbulent environment. Gronke et al. (2022a) found that this stochasticity affects the cold gas mass evolution in hydrodynamic turbulent boxes with an intermediate-sized initial cold cloud. In this regime, they saw both survival and destruction of the cold cloud for different choices of random seeds for turbulent driving. This was attributed to the higher significance of the exact turbulent velocity field in the intermediate regime between cloud survival and destruction.

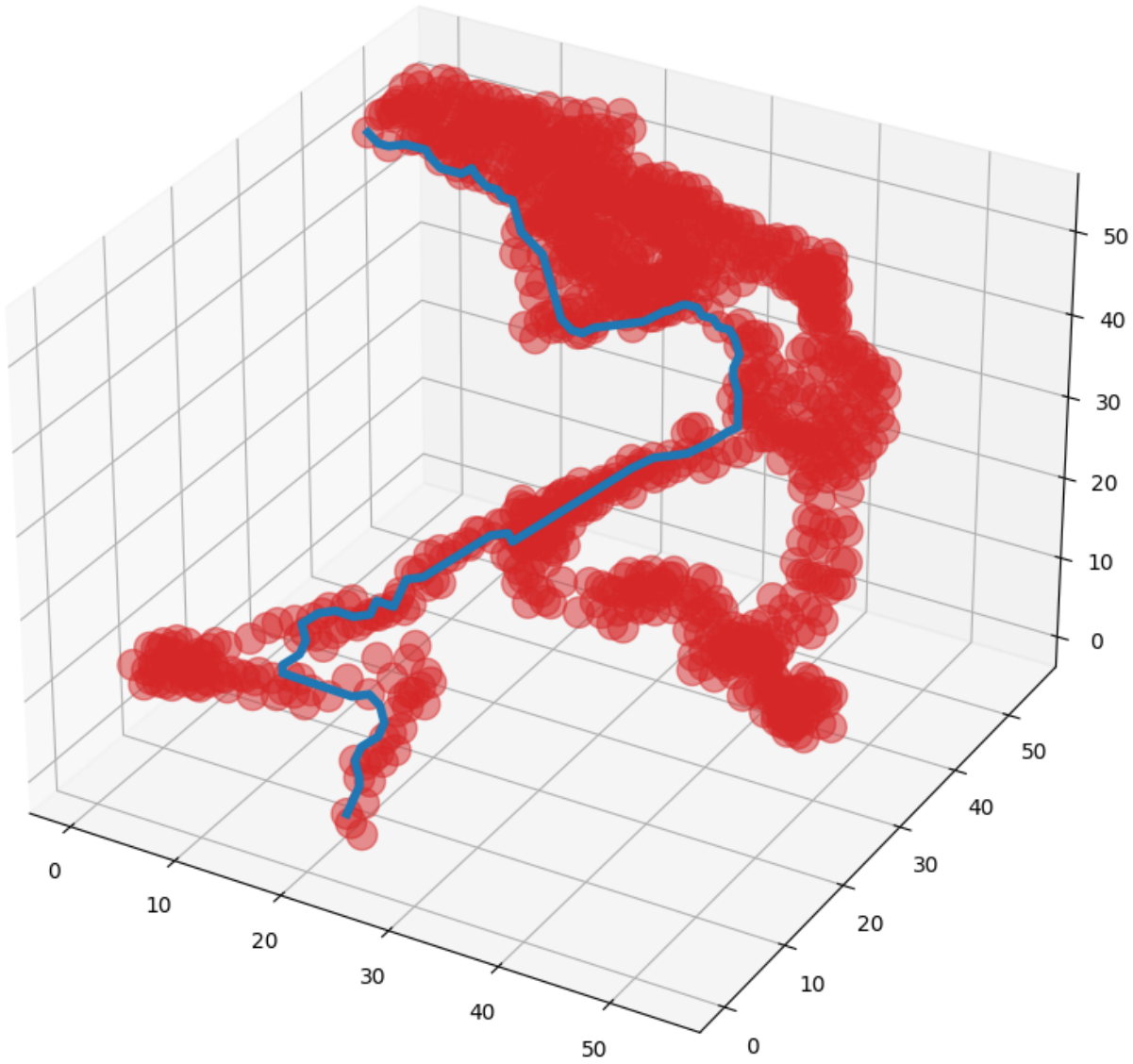

Figure 6: Red points show the points from the skipped graph of a single clump, and the blue solid line shows the calculated filament length using every 4^{th} point. Axis labels correspond to the number of gridcells.

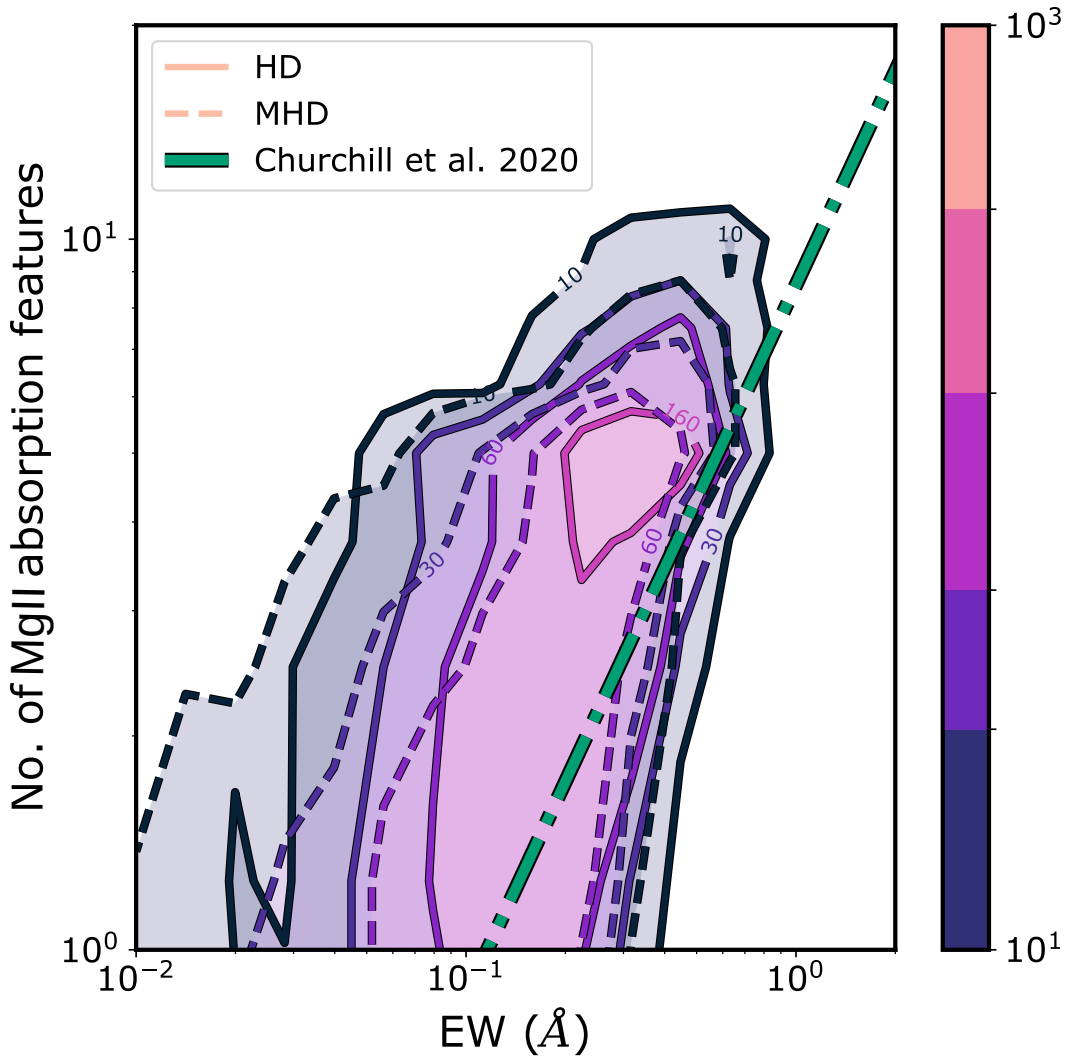

Figure 7: Same as Fig. 3.18 but for high resolution MgII 2796 Å absorption spectra with $d\lambda = 0.01$Å

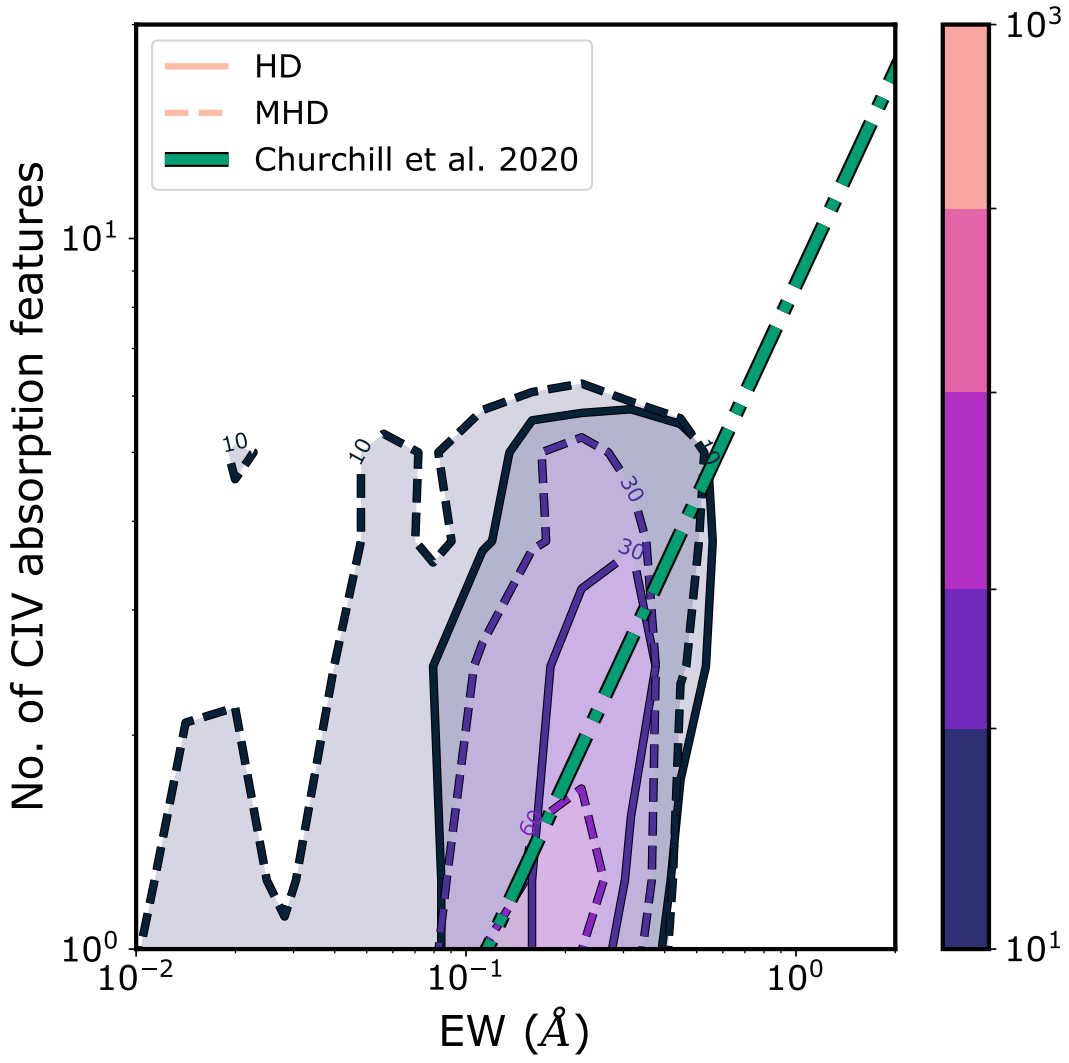

Figure 8: Same as Fig. 3.18 but for high resolution CIV Å absorption spectra with $d\lambda$ = 0.01Å

We repeat this test for our simulations, with and without magnetic fields. We run turbulent box simulations with 3 different random seeds at $\mathcal{M} = 0.5$ and introduce clouds of different sizes to check for the effect of stochasticity of the turbulence. We use a $L_{\rm box}/R_{\rm cl} = 20$, instead of 40, due to its lower computational costs.

Fig. 9 shows the cold gas mass evolution for the different cases. We find that the cold gas mass growth/destruction rate for cold gas clouds in intermediate and destruction regimes is sensitive to the exact choice of the random seed. We also find that this is true for both HD and MHD and with no clear order of growth rate between the HD and MHD counterparts. This high dependence on stochasticity in these regimes is due to the lack of cold gas mass. This results in a very stochastic sampling of turbulence, hence making the evolution very stochastic in nature.

On the other hand, in the survival regime, the MHD simulations seem to have a slightly lower growth rate, compared to their HD counterparts, although still a much lower difference compared to the order of magnitude difference observed in TRML simulations. We attribute this minor difference to some unavoidable systematic differences between the HD and MHD simulations. The biggest of them is the difference in dissipation rate between MHD and HD, due to the extra dissipation of magnetic energy via numerical resistivity. This higher dissipation results in a slightly hotter medium in a fully developed turbulent box, in turn resulting in a slightly deviated density distribution. These slight deviations affect the evolution via a slight difference in overdensity, mixed gas temperature, etc.

Still, as Fig. 9 shows, this difference is minor and it gets even more trivial when we take the spread due to stochasticity into account.

MOGLI: Multiphase subgrid model

Local Turbulence estimation in 2D

We can generalise the expression for 2D geometries. In 2D, the limits of the integral are different, along with a different definition of the cell volume, leading to a slight variation in Eq. (4.27),

$$v_{\rm turb,grad,2D} = (\sigma^2_{v_x} + \sigma^2_{v_y})^{1/2} = V_{\rm cell}^{1/2} \sqrt{\frac{1}{\xi_{\rm 2D}} \sum_{i,j}^{2} \left(\frac{\partial v_j}{\partial x_i}\right)^2} \tag{1}$$

where, $\xi_{\rm 2D} = 4$.

During our non-radiative turbulent mixing tests, explained later in Sec. 4.4, we find a $\xi_{3D} = 2$ works better in matching with the benchmark Athena++ simulations. Hence, we use a $\xi_{3D} = 2$ in MOGLI runs. We can also combine both Eq. (4.27) & (1) into a single expression for D

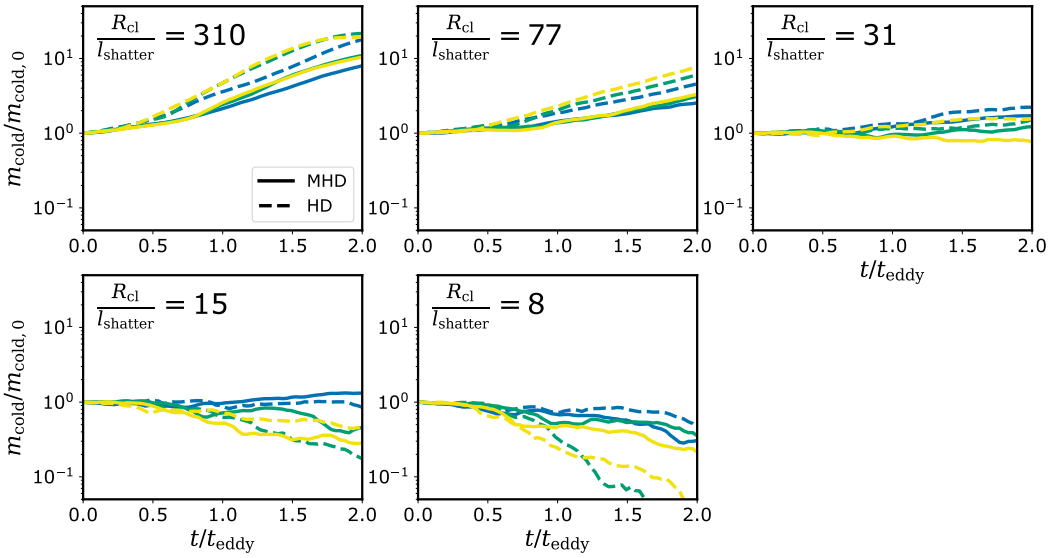

Figure 9: Cold gas mass evolution for simulations with the same parameters but different random instances of turbulence. The different panels refer to different $R_{\rm cl}/l_{\rm shatter}$ in a turbulent medium with $\mathcal{M} = 0.5$. The different colours denote simulations with varying random seeds for turbulent driving. The solid and dashed lines show the evolution of simulations with and without magnetic fields, respectively.

dimensions,

$$v_{\text{turb,grad,D}} = V_{\text{cell}}^{1/D} \sqrt{\frac{1}{\xi_{\text{D}}} \sum_{i,j}^{D} \left(\frac{\partial v_j}{\partial x_i}\right)^2}$$
$$\text{where, } \xi_{\text{D}} = \begin{cases} 4 & \text{if } D = 2 \\ 3 & \text{if } D = 3 \text{ Analytical} \\ 2 & \text{if } D = 3 \text{ MOGLI} \end{cases} \tag{2}$$

Heating due to inelastic mass exchange

We start with the assumption of conservation of total energy (E_{total}) during mass exchange, i.e. $\dot{E}_{\text{total,hot}} + \dot{E}_{\text{total,cold}} = 0$. The total energy further consists of the total energy into thermal and kinetic energy. We denote the cold fluid mass and hot fluid mass as m_{cold} and m_{hot} respectively. Similarly, $u_{\text{cold/hot}}$ and $v_{\text{cold/hot}}$ for the corresponding cold/hot fluid specific thermal and kinetic energy. We assume that the cold fluid cools rapidly back to stay at u_{cold}, and we account for radiated energy as $\dot{E}_{\text{rad}}$. As mass is converged during this process, $\dot{m}_{\text{cold}} = -\dot{m}_{\text{hot}}$, which leads to

$$\dot{m}_{\text{cold}}(u_{\text{hot}} - u_{\text{cold}}) + \frac{1}{2}\dot{m}_{\text{cold}}(v_{\text{hot}}^2 - v_{\text{cold}}^2) = \tag{3}$$
$$(\dot{E}_{\text{rad}} + m_{\text{hot}}\dot{u}_{\text{hot}}) + m_{\text{cold}}v_{\text{cold}}\dot{v}_{\text{cold}} + m_{\text{hot}}v_{\text{hot}}\dot{v}_{\text{hot}}$$

Next, we rearrange the conservation relation for total momentum, i.e. $\dot{p}_{\text{hot}} + \dot{p}_{\text{cold}} = 0$ and multiply v_{hot} to obtain,

$$m_{\text{hot}}v_{\text{hot}}\dot{v}_{\text{hot}} = \dot{m}_{\text{cold}}v_{\text{hot}}(v_{\text{hot}} - v_{\text{cold}}) - m_{\text{cold}}v_{\text{hot}}\dot{v}_{\text{cold}} \tag{4}$$

We plug this relation back into Eq. 4, and further decompose the mass and momentum flux into two components of the bidirectional exchange. After simplifying the expression further, we obtain

$$\dot{E}_{\text{rad}} + m_{\text{hot}}\dot{u}_{\text{hot}} = (\dot{m}_{\text{hot}\to\text{cold}} + \dot{m}_{\text{cold}\to\text{hot}})\,\frac{(\Delta v)^2}{2} + \dot{m}_{\text{cold}}\Delta u \tag{5}$$

where $\Delta u = (u_{\text{hot}} - u_{\text{cold}})$ and $\Delta v = (v_{\text{hot}} - v_{\text{cold}})$.

The left-hand side (LHS) of Eq. 5 represents the total heating in both the fluids. The first term in right-hand side (RHS) refers to heating from the thermalised kinetic energy. On the other hand, the second term of RHS gives the heating due to thermal energy exchange. While the second term in the RHS can be divided between the fluids, the separation of first term will depend on the details of the geometry and momentum exchange, as these affect how much of the lost kinetic energy was thermalised in each fluid.

If we assume a fudge factor, $\Omega \in (0, 1)$, denoting the fraction of lost energy thermalised in the cold fluid, we can separate the two terms in LHS as,

$$\begin{aligned}\dot{E}_{\rm rad} &= \Omega \left(\dot{m}_{\rm hot\to cold} + \dot{m}_{\rm cold\to hot}\right) \frac{(\Delta v)^2}{2} \\ &\quad + \dot{E}_{\rm cooling} \\ m_{\rm hot}\dot{u}_{\rm hot} &= (1-\Omega) \left(\dot{m}_{\rm hot\to cold} + \dot{m}_{\rm cold\to hot}\right) \frac{(\Delta v)^2}{2} \\ &\quad - \dot{m}_{\rm cold\to hot}\Delta u\end{aligned}$$

As MOGLI keeps track of the total energy consistently while imposing quasi-isothermal EOS for the cold fluid, it is unaffected by this uncertainty of Ω.

Acknowledgements

Writing a PhD thesis often feels like captaining a rickety ship through turbulent waters, with no map, no exact destination, and many late-night log entries. But no ship sails alone, and I have been incredibly lucky with the crew that helped keep this vessel afloat and enabled it to reach the current destination.

First and foremost, I would like to thank Max Gronke, my advisor, the sponsor and navigator of this voyage. Max steered me into amazing regions of exciting science, provided wise counsel through rough seas and calm, and made sure I did not drift too far into the weeds. His guidance, curiosity, and support were an indispensable push for this journey. Coming to the rest of the current and previous Multiphase Gas crew: Seok-Jun, Silvia, Fernando, Caitlin, Tirso, Benedikt, Gitanjali, Ryan and Jason. I would like to thank them for making the deck a livelier place with thoughtful discussions, jokes, and just the right amount of distraction. Seok-Jun, always present to support, help and push me up, scientifically and otherwise. Silvia, as a co-sailor going through the same journey, was always all ears for discussions. Tirso, honorary crewmember and co-explorer of Multiphase crew, was always up for those long discussions where we were both lost on a confusing problem.

Next up are the other crew members of the ship. I want to thank Anshuman for keeping me fed, caffeinated, and vaguely organised, and for decoding the German bureaucracy. I am grateful to Abinaya and Arghyadeep for keeping the ship sane with coffee-fueled rants and reality checks. Bo, for holding fast to the other end of the climbing rope, being up for any crazy mountain adventure that I come up with and for our many science conversations (along with Iker) that reminded me how much more there is to explore. Fulvio, Matteo, Julian, Benedikt, Pavan, Alankar, Ritali, Gitanjali, Aakash, Iliya, Abinaya, Arghyadeep, Geza, Christoph, and many more, thank you for keeping morale high with foosball, table tennis and board games. Geza, I owe you at least half this thesis for your coffee-bribed writing sessions. Joanne, Akash, Silvia, Katyayani, Ivan, and the whole meme council, thank you for the laughs and the group therapy. Also, thanks to Johannes and Andrija, you made our office the best one at MPA (this is not up for debate). To all the friends who made MPA a home: Aniket, Miha, Matteo, Iker, Lazaros, Benedetta, Teresa, and many more, thank you for the lunches, the parties, and the everyday chaos that made this time not only bearable but joyful. You're the wind that filled the sails when I needed it most. Some extra thanks to Miha, Fulvio and everyone who joined for Weekly After-Work (WAW) beers, for adding the cherry on top for all the long workweeks. And a lot of gratitude to the administrative

and IT staff at MPA, especially Gabi, Maria, Sonja, Cornelia, Andi, Goran, Zubanova, Sonia, Solvejg, Isabel and Marzia, for making the rough seas of bureaucracy much smoother.

Finally, to the home port, my family. I am eternally grateful to my mom, Sumitra, for trying valiantly (and mostly unsuccessfully) to stop me from doing crazy things, and for always reminding me that I have a support fleet behind me. To my dad, Raja, the steady keel and the weight that keeps everything balanced, thank you for always being there with calm and strength. And to my grandmother, Satya, for her unconditional love and grounding wisdom, you are the anchor that connects every journey to its roots.

To all of you, thank you for crewing this improbable voyage. This thesis has my name on the cover, but your fingerprints are on every page.

And so it goes...

— Kurt Vonnegut, in *Slaughterhouse-Five*